AIX-MARSEILLE UNIVERSITÉ

PHYSIQUE ET SCIENCE DE LA MATIÈRE (352)

LABORATOIRE D'ASTROPHYSIQUE DE MARSEILLE

Thèse présentée pour obtenir le grade universitaire de docteur

Discipline: Physique et Science de la Matière
Spécialité: Astrophysique et Cosmologie

Thomas RONNET

Origin and Formation of the Regular Satellites around Planets

Soutenue le 01/10/2018 devant le jury composé de:

Anders JOHANSEN	Lund Observatory	Rapporteur
Alessandro MORBIDELLI	Observatoire de la côte d'Azur	Rapporteur
Michel BLANC	Observatoire Midi-Pyrénées	Examinateur
Magali DELEUIL	LAM	Examinateur
Jonathan LUNINE	Cornell University	Examinateur
Peter WURZ	Universität Bern	Examinateur
Olivier MOUSIS	LAM	Directeur de thèse
Pierre VERNAZZA	LAM	Directeur de thèse

Numéro national de thèse/suffixe local: 2018AIXM0331/041ED352

Remerciements

Je tiens à débuter ce manuscrit par l'expression de ma gratitude envers toutes les personnes qui m'ont permis d'aller au bout de ces trois années de thèse, à commencer par mes deux encadrants, Olivier Mousis et Pierre Vernazza. Vous avez tous les deux un engouement inspirant pour la recherche que vous avez su me transmettre. Votre dynamisme et votre bonne humeur ont fait de ces trois dernières années une période à la fois productive et agréable. Vous êtes tous les deux intéressés et à l'affût des dernières découvertes dans de nombreux aspects de l'étude du Système Solaire et cela a largement participé à mon ouverture et intérêt pour différents sujets que j'ai pris plaisir à étudier. Merci à Olivier de m'avoir offert l'opportunité de faire cette thèse à Marseille et aussi d'avoir toujours pensé à l'étape d'après, au futur. Merci à Pierre pour toutes nos discussions qui m'ont toujours poussées à me questionner et à élargir le contexte de mes recherches. Ce fut un plaisir de travailler avec vous. J'espère qu'il a été partagé et que cette fin de thèse marque aussi le début de futures collaborations. Enfin, vous avez su m'offrir un environnement propice à mon développement et épanouissement en tant que chercheur débutant. J'ai eu la chance de rencontrer et discuter avec nombre de vos collaborateurs, de participer à des conférences internationales, workshops, et écoles d'hiver. Pour tout ça, je vous suis reconnaissant.

J'ai une pensée particulière pour tous les membres de l'équipe systèmes planétaires du laboratoire. Je garderai un bon souvenir de chacun d'entre vous et de nos discussions. Ces trois années n'auraient pas été les mêmes sans les étudiants et postdocs de l'équipe qui m'ont rendu la vie plus agréable à la fois au laboratoire et en dehors. Je remercie également Frédérique et Solange pour les bons moments passés ensemble, et Françoise pour sa gentillesse et son aide précieuse lors de mon arrivée au laboratoire.

Je tiens aussi à remercier les membres de mon jury de thèse, Alessandro et Anders pour leurs efforts sur la lecture de mon manuscript et leurs commentaires, Jonathan pour être venu d'outre-atlantique pour la soutenance, et également Michel et Peter d'avoir accepté l'invitation et montré tant d'enthousiasme pour mes travaux. Un grand merci à Magali d'avoir présidé ce jury, c'était un plaisir pour moi.

Je n'en serais pas arrivé là sans le soutien de mes parents et de ma famille tout au long de mes études. Merci d'avoir cru en moi et en mes choix. Le chemin a été long mais vous avez toujours été là pour moi, et je sais que vous le serez encore. Je suis fier de vous avoir à mes côtés et j'espère faire honneur à votre soutien.

Je suis très heureux d'avoir pu commencer et finir cette thèse en compagnie de Bastien, mon collègue de bureau pour un temps et maintenant ami (pour longtemps j'espère !). Mille fois merci pour ton oreille attentive, ton soutien et ton enthousiasme. Que ce soit au laboratoire ou autour d'un verre (sans oublier le fromage et la charcuterie qui vont avec), à la cafétéria ou au 'Mexicain', au karaté ou dans un canoë, tous ces bons moments passés ensemble sont pour moi indissociables du souvenir de ces trois années de thèse.

Enfin, merci à celle qui partage ma vie depuis 7 ans maintenant. Je ne peux imaginer le chemin parcouru, ni le chemin à parcourir, sans toi à mes côtés Althéa. Merci de m'avoir accompagné tout ce temps et de continuer à m'accompagner. Je sais la chance que j'ai, et je n'ai pas les mots pour te remercier assez et exprimer tout ce que tu es pour moi. Sans toi, je ne suis pas moi.

Résumé

L'origine du Système Solaire et de ses planètes est un vaste sujet ayant intéressé nombre de scientifiques depuis plusieurs siècles. L'hypothèse de la *nébuleuse primitive*, selon laquelle les planètes se formeraient lors du refroidissement d'un disque gazeux entourant le jeune Soleil, fut émise par Pierre Simon Laplace (1749–1827) et Emmanuel Kant (1724–1804) au 18ème siècle. Cette première formulation de la théorie de la formation des planètes postulait déjà que ces dernières sont un produit naturel de la formation des étoiles et constitue encore aujourd'hui la base des théories modernes de l'origine des systèmes planétaires.

Depuis, le scénario proposé par Kant et Laplace a été raffiné au moyen d'observations de plus en plus détaillées et de formulations théoriques de plus en plus poussées, aujourd'hui largement appuyées par le développement d'ordinateurs à la puissance de calcul croissante. L'observation du voisinage solaire a révélé que les étoiles se forment dans des régions "denses" du milieu interstellaire, appelées nuages moléculaires. Certaines portions de ces nuages s'effondrent sur elles-même sous l'effet de leur propre gravité. La pression et la température augmentent de manière importante lors de la contraction du nuage, particulièrement en son centre où une proto-étoile est finalement formée. La conservation du moment angulaire lors de l'effondrement entraine la formation d'un disque dans le plan perpendiculaire à l'axe de rotation. Les disques entourant les jeunes étoiles sont communément appelés disques proto-planétaire en référence au fait qu'ils sont le lieu de naissance des planètes. Ils sont de nos jours observés avec de grandes précisions qui permettent d'en distinguer les nombreuses structures (anneaux, bras spiraux, lobes et bien d'autres). Le temps de vie observé de ces disques autours d'étoiles de type solaire, qui est estimé à quelques millions d'années, contraint les échelles de temps de formation des planètes (tout du moins de celles ayant une atmosphère primordiale massive, comme les géantes gazeuses, qui a dû être attirée avant la dissipation du disque).

Une théorie cohérente de l'accrétion des planètes fut développée dans les années 50 et 60 par le théoricien russe Viktor Safronov et résumée dans son livre *L'évolution du nuage proto-planétaire.* Selon son hypothèse, la formation des planètes procède

par l'accrétion d'objets plus petits, nommés planétésimaux, dont les populations de petits corps du Système Solaire, tels les astéroïdes et les comètes, seraient les représentants. Sur cette base, une théorie de l'accrétion des planètes géantes, commençant par la formation d'un noyau solide et suivie par l'accrétion d'une massive enveloppe gazeuse, fut construite. Les planètes telluriques sont quant à elles supposées s'être formées à la suite d'un épisode plus chaotique de violents impacts entre des embryons de masses similaires après la dispersion du disque proto-planétaire. Le mécanisme de formation de planètes par l'accrétion de planétésimaux permit ainsi de développer un scénario cohérent de la formation des planètes du Système Solaire.

Les planètes de notre système sont généralement accompagnées d'un ou plusieurs satellites naturels (également appelés lunes, par analogie avec le satellite naturel de la Terre). Parmi ces satellites, les satellites dits réguliers orbitent largement à l'intérieur de la sphère d'influence gravitationnelle de leur planète parente avec une eccentricité et une inclinaison, relative au plan équatorial de cette dernière, relativement faibles. Il est largement reconnu aujourd'hui que ces propriétés reflètent le fait que ces satellites se sont formés *in situ*. À l'opposé, des satellites irréguliers orbitent, de manière prograde aussi bien que rétrograde, autour des quatre planètes géantes du Système Solaire à de plus grandes distances orbitales, avec de larges eccentricités et inclinaisons. Ces objets ont certainement été capturés par les planètes depuis des orbites héliocentriques. Il est intéressant de noter que seules Mercure et Vénus ne possèdent pas de satellites réguliers connus à ce jour. La faible période de révolution de ces planètes ainsi que leur proximité au Soleil induiraient d'importantes forces de marées sur de putatifs satellites qui auraient de ce fait pu tomber à la surface de leur planète hôte il y bien longtemps. Il apparaît donc que la présence de satellites soit la règle plutôt que l'exception pour les planètes du Système Solaire. Il s'ensuit qu'une théorie valable de la formation des planètes doit aussi rendre compte de l'existence des satellites (ici et dans la suite de ce manuscrit, le terme satellite ou lune fait référence aux satellites réguliers des planètes).

Les systèmes satellitaires présentent une grande diversité aussi bien dans leur architecture que dans leurs propriétés physiques et il est donc difficile de concevoir que des événements et mécanismes similaires sont à l'origine de leur formation. Les théories actuelles semblent néanmoins converger sur un fait: la formation des satellites prend place dans les phases finales de l'accrétion des planètes et implique des disques circum-planétaires (ces derniers peuvent être consitués de débris solides ou être majoritairement gazeux). Dans le cas des planètes telluriques, les violents impacts qui se produisent lors de la collision d'embryons massifs peuvent arracher une partie de leur manteau, donnant naissance à un disque de débris au sein duquel une ou plusieurs lunes peuvent se former. En ce qui concerne les planètes géantes, les théories furent d'abord développées pour Jupiter et la formation de ses satellites dits Galiléens, au nombre de quatre. Les propriétés de ce système (présentées au Chapitre 2) ont depuis longtemps fait émerger l'idée qu'il constitue sous de nombreux aspects un Système Solaire miniature, et donc que les satellites se seraient formés dans un disque majoritairement gazeux, par analogie avec l'hypothèse de la nébuleuse de la formation planétaire. Dans les instants finaux de la formation de Jupiter, lorsque la planète s'est suffisamment refroidie et contractée, le moment angulaire du matériau qu'elle accrète est trop élevé pour que celui-ci tombe directement dans son enveloppe. Ce matériau forme au contraire un disque d'accrétion au sein duquel les lunes se forment. Appliquer cette théorie à Saturne (ainsi qu'Uranus et Neptune) se révèle compliqué étant donnée l'architecture très différente de son système de satellite et le fait que la composition de ces derniers semble décorrélée de leur distance orbitale, contrairement aux satellites Galiléens. Bien qu'on ne sache pas si les systèmes satellitaires des planètes géantes se sont tous formés dans un disque gazeux entourant leur planète hôte, le modèle développé par Robin Canup et William Ward au début des années 2000, dans lequel l'accrétion des satellites est régulée par l'apport de matériel accrété par la planète géante, a été assez largement accepté comme un scénario plausible de leur origine.

La découverte en 1995 par Michel Mayor et Didier Queloz de la première planète orbitant autour d'une autre étoile que le Soleil, ainsi que la quantité d'objets détectés depuis, ont levé le voile sur la grande diversité des systèmes planétaires extrasolaires. Il semble que les planètes les plus communes dans notre galaxie soient des super-terres, ayant des tailles une à quatre fois supérieures à celle de la Terre et des périodes orbitales typiquement inférieures à une centaine de jours. Il est notable qu'il n'existe dans notre Système Solaire aucun analogue à ces planètes, mais plus particulièrement, ces découvertes ont révélé que nous sommes encore loin d'avoir un cadre cohérent de la formation des planètes qui puisse rendre compte de la diversité des systèmes observés. Ce constat a motivé de nombreuses études théoriques de la formation des planètes, ainsi que des observations plus détaillées des disques proto-planétaires et la construction de nouveaux modèles de leur évolution. De larges progrès ont été réalisés lors des deux dernières décennies dans la compréhension de la formation des planétésimaux et les processus d'accrétion des planètes. Plus récemment encore, la vision largement acceptée de l'évolution des disques proto-planétaires a été remise en question, avec potentiellement de profondes conséquences pour notre compréhension de la formation des planètes et de leur évolution dynamique précoce. Néanmoins, les théories de formation des satellites furent peu révisées.

Le présent manuscrit expose, en anglais, les travaux réalisés au cours de trois années de thèse, tandis que chacun des chapitres est résumé ci-dessous en français.

Les études présentées dans ce document concernent principalement l'origine et la formation des satellites Galiléens et des satellites martiens Phobos et Deimos. Ces lunes sont les cibles de futures missions d'exploration spatiale dédiées spécifiquement à leur caractérisation, motivant ainsi l'intérêt particulier porté à ces objets durant cette thèse.

Chapitre 1

Ce chapitre d'introduction commence par une mise en contexte générale qui reprend essentiellement le texte ci-dessus, avec l'addition de quelques détails ainsi que des illustrations.

La suite du chapitre introduit des notions importantes pour la compréhension de la formation des planètes et de leur(s) satellite(s). Dans un premier temps, la structure des disques proto-planétaires et leur évolution sont présentées. Ces disques sont majoritairement constitués d'hydrogène moléculaire et d'hélium gazeux, les éléments plus lourds représentant uniquement une fraction d'environ un centième de leur masse. Le gaz est en rotation quasi-képlérienne autour de l'étoile centrale (une légère déviation est induite par le gradient de pression dans le disque) et la pression et la température du disque diminuent avec la distance à l'étoile. Le corps central accrète continuellement du matériel venant du disque, impliquant un transport de moment angulaire. Ce transport est généralement modélisé comme un processus visqueux. Néanmoins, la viscosité moléculaire étant bien trop faible dans les disques proto-planétaires, une viscosité effective est introduite dont l'origine, mal comprise, viendrait des mouvements turbulents à l'intérieur du disque. Quelques éléments de remise en question de ce modèle sont discutés.

Dans un second temps, l'évolution des poussières dans ces disques, qui sont à la base de la formation des planètes, est discutée. La dynamique des grains de poussière est contrôlée par leur couplage aérodynamique avec le gaz et dépend donc de leur taille. Les grains de poussière peuvent grossir par coagulation mais seulement jusqu'à une taille typiquement de l'ordre du millimètre au centimètre. En effet, plusieurs barrières s'opposent à la croissance des grains. Au-delà d'une certaine taille, la collision entre les poussières aura tendance à les fragmenter. Un autre effet vient de la dynamique des grains. Ces derniers ont tendance à spiraler vers l'étoile centrale et cette dérive radiale peut être plus rapide que l'échelle de temps typique sur laquelle les grains coagulent, limitant ainsi leur croissance. La formation de planétésimaux par l'effondrement de denses filaments de poussière dans les disques est brièvement discutée.

Dans la suite, un mécanisme d'accrétion de planètes, appelé "pebble accretion", récemment découvert et étudié est présenté. Celui-ci consiste à attirer les grains de poussières qui spiralent vers l'étoile centrale. La combinaison de la friction avec le gaz et de l'attraction gravitationnelle de l'objet qui grossit permet d'étendre très significativement la section efficace de l'accrétion comparée à la simple section géométrique. L'important flux radial de grains à travers le disque permet de former rapidement des objets massifs tels que les noyaux des planètes géantes. La croissance de proto-planètes via ce mécanisme est stoppée au-delà d'une masse critique au-dessus de laquelle la perturbation gravitationnelle de la proto-planète est suffisament importante pour altérer significativement le profil de densité du disque. Cette perturbation agit comme une barrière à la dérive des grains qui restent piégés à l'extérieur de l'orbite de la proto-planète. Comme présenté plus tard, ceci a également d'importantes conséquences pour la formation des lunes des planètes géantes.

Finalement, le chapitre termine par une discussion sur l'évolution dynamique des planètes géantes. Plusieurs mécanismes peuvent modifier l'orbite des planètes pendant ou après leur formation. Ce processus, appelé migration planétaire, joue un rôle essentiel dans l'architecture d'un système planétaire et la distribution des petits corps comme les astéroïdes.

Chapitre 2

Le second chapitre s'intéresse aux satellites Galiléens, Io, Europe, Ganymède et Callisto, orbitant Jupiter, l'origine de ces derniers constituant le propos principal de ce manuscrit. Les principales contraintes sur les conditions de formation de ces lunes sont passées en revue. Premièrement, les quatre Galiléens possèdent des masses globalement similaires. Le plus massif, Ganymède, a une masse environ trois fois supérieure à Europe, le moins massif des quatre satellites. La masse totale du système Galiléen ne représente qu'une infime fraction de la masse de Jupiter ($\approx 2.1 \times 10^{-4}$). Si les Galiléens se sont formés dans un disque de composition solaire (c'est à dire avec un ratio de masse de matériaux solides comparé au gaz d'environ 0.01), alors un minimum d'environ 0.02 fois la masse de Jupiter est nécessaire à leur assemblage. Une autre des propriétés du système satellitaire est sa compacité. Alors que la sphère d'influence gravitationnelle de Jupiter a un rayon d'environ 744 rayons jovien et que la taille typique du disque circum-planétaire est supposée être de plusieurs centaines de rayons joviens, Callisto, le satellite Galiléen le plus éloigné de Jupiter, est à une distance orbitale d'à peine 26 rayons joviens. La densité des satellites décroît monotoniquement en fonction de leur distance orbitale, suggérant un gradient de la quantité d'eau contenue dans ces satellites. Finalement, il apparaît que Callisto est un corps seulement partiellement différencié, impliquant un temps de formation assez long pour éviter un chauffage trop important de son intérieur qui aurait entrainé une différentiation totale.

La seconde partie du chapitre présente une revue des principaux modèles de formation des satellites Galiléens. Ceux-ci sont généralement de l'une ou l'autre des catégories de modèle de "minimum mass subnebula" (MMSN) ou "gas-starved disk". Dans la première catégorie, il est supposé que le disque circum-jovien possède initialement la masse requise pour former les satellites. Ceci résulte en des disque assez denses et chauds autour de Jupiter et l'accrétion des lunes se fait dans un système isolé. Au contraire, dans les modèles "gas-starved", il est considéré que Jupiter accrète constamment du matériel à ses alentours ce qui nourrit le disque circum-planétaire durant la formation des satellites. De ce fait, plutôt que d'être présente à un même moment, la masse nécessaire à l'assemblage des satellites est fournie à mesure qu'ils se forment sur de longues échelles de temps. Dans ces modèles, la densité et la température du disque sont beaucoup plus faibles que dans les modèles MMSN. Alors qu'il apparaît difficile de reproduire la masse et l'architecture du système Galiléen avec les modèles MMSN, les modèles "gas-starved" ont eu plus de succès. Il serait même possible de former plusieurs générations de satellites dans le contexte de ces derniers modèles, les premières générations étant perdues dans Jupiter par migration des satellites dans le disque, et les satellites observés aujourd'hui seraient en fait les derniers survivants. Bien que ce scénario soit attractif, les chapitre 3 et 4 de ce manuscrit pointent du doigt des hypothèses de ce modèle qui semblent injustifiées ou erronées au regard de la compréhension actuelle de la formation planétaire.

Chapitre 3

Ce chapitre est le premier présentant des travaux originaux réalisés au cours de la thèse. Il présente l'étude de l'évolution de particules solides dans le disque circum-jovien et discute de l'accrétion des satellites Galiléens à partir des grains qui dérivent rapidement dans le disque, comme présenté au chapitre 1.

Pour cette étude, un modèle de transport de particules, incluant la force de gravité du corps central, les forces de friction avec le gaz et la diffusion turbulente, a été développé. Un modèle thermodynamique permet quant à lui de suivre l'évolution de la température de surface des particules et d'en estimer le taux de sublimation. Ceci permet de suivre l'évolution dynamique des particules en fonction de leur taille ainsi que l'évolution de leur composition globale en terme de rapport de masse entre glace d'eau et roches. Les résultats sont discutés par rapport à la composition supposée des satellites Galiléens.

Les résultats révèlent que les corps les plus larges (avec une taille $\gtrsim 10\,\mathrm{km}$) sont capable de retenir d'importante quantité d'eau même dans les régions chaudes du disque où la glace d'eau est thermodynamiquement instable. Ceci est dû d'une part au fait que l'échelle de temps d'ablation d'un corps à une température donnée est proportionnelle à son rayon, et d'autre part au fait que la sublimation de l'eau, qui a une importante chaleur latente, est un processus endothermique qui refroidit efficacement la température de surface et rallonge l'échelle de temps d'ablation. Si les satellites Galiléens se sont assemblés à partir de tels objets, il est très probable que chacun d'entres eux ait accrété une quantité importante d'eau. Ceci impliquerait que Io, qui ne contient pas d'eau aujourd'hui, et Europe, qui contient moins de 10 % d'eau en masse, aient perdu de l'eau durant leur évolution suivant leur formation. Les particules avec une taille centimétrique à métrique sont quant à elles assez petites pour être complètement asséchées dans les régions internes du disque, bien que leur rapide dérive dans le disque leur permette de perdre graduellement cette eau le long de leur trajet dans le disque. Les particules de cette taille définissent ainsi trois régions bien distinctes en termes de composition qui peuvent directement correspondre à celle des satellites Galiléens.

Ce dernier résultat est intéressant dans le cadre d'un modèle "gas-starved". En effet, malgré l'hypothèse souvent considérée dans ces modèles que la croissance des satellites procède par l'accrétion d'objets assez larges (10–100 km de rayon), le disque circum-jovien est supposé être réapprovisionné par du matériel majoritairement gazeux et qui contient de petites poussières (probablement de tailles bien inférieures au millimètre). Dans ces conditions, il est difficile d'imaginer que les poussières puissent grossir en de larges corps de plusieurs dizaines de kilomètres, comme nous le montrons dans ce chapitre. Les poussières pourraient grossir jusqu'à des tailles de quelques centimètres à quelques mètres et dériveraient rapidement vers Jupiter due à la friction avec le gaz. Le mécanisme de "pebble accretion" est donc une bien meilleure description de la croissance des lunes dans le contexte d'un scénario "gas-starved". L'efficacité de la "pebble accretion" dans le système jovien est estimée, et il s'avère que tout au plus une dizaine de pourcents des "pebbles" qui dérivent seraient accrétés par les lunes. Cette faible efficacité augmente de manière significative la masse totale nécessaire à l'assemblage des lunes et rend l'hypothèse de la formation de multiples générations de satellites, comme pensé précédemment, très peu probable. Il devient au contraire nécessaire de stopper la migration des satellites dans le disque, ce qui conforte l'idée d'un disque tronqué par une cavité magnétique interne comme proposé par plusieurs auteurs auparavant. Plusieurs hypothèses sur lesquelles se basent les résultats présentés sont discutées.

Chapitre 4

Ce chapitre s'intéresse aux mécanismes d'approvisionnement de matériaux solides nécessaires à la formation des Galiléens dans le disque entourant Jupiter. Dans le contexte des modèles "gas-starved" de la formation des satellites, il est considéré que le gaz accrété par Jupiter dans les derniers instants de sa formation contient également des poussières qui vont permettre la croissance des lunes. Ceci fait des lunes un produit naturel de la formation des géantes gazeuses et l'on devrait trouver des systèmes assez semblables au système jovien autour de toutes les géantes gazeuses. Bien que Saturne, qui possède également un cortège de satellites réguliers dont Titan, une lune assez semblable aux satellites glacés de Jupiter, semble corroborer cette hypothèse, la compréhension actuelle de la formation des planètes géantes et de l'évolution des poussières dans les disques permet de douter sérieusement du mécanisme proposé. Les simulations numériques hydrodynamiques actuelles montrent que le matériel accrété par une planète d'une masse comparable à celle de Jupiter vient des hauteurs du disque et tombe verticalement vers la planète et son disque. D'un autre côté, la coagulation des grains de poussière et les forces de friction avec le gaz entrainent leur sédimentation vers le plan médian du disque proto-planétaire. Comme exposé dans le premier chapitre, dans le plan médian, la perturbation induite par la proto-planète agit comme une barrière pour la dérive des grains qui se trouvent stoppés. Le gaz accrété par Jupiter au moment de la formation de ses satellites devait donc être fortement appauvri en poussières et ce ne peut être la source principale des matériaux nécessaires à la formation des lunes Galiléennes.

Une autre source potentielle de solides dans le disque circum-jovien est la capture de planétésimaux depuis des orbites héliocentriques. Les planétésimaux qui passent assez près de Jupiter peuvent être freinés par friction avec le gaz en traversant le disque circum-planétaire et ainsi se retrouver sur une orbite liée à la planète géante. Plusieurs auteurs ont étudié ce phénomène auparavant. Néanmoins, ces études considèrent l'évolution de planétésimaux qui se trouvent dans le proche entourage de Jupiter, ce qui n'est pas très réaliste. En effet, bien avant l'époque supposée de la formation des satellites Galiléens, Jupiter a dû nettoyer son voisinage sous l'effet de son influence gravitationnelle.

Ici, nous proposons qu'un réservoir potentiellement massif de planétésimaux s'est créé à l'endroit où la dérive des grains est stoppée par la perturbation du disque gazeux induite par Jupiter. Ce réservoir est néanmoins situé trop loin de la planète pour que les planétésimaux soient efficacement capturés autour de Jupiter. Cependant, nous montrons que la formation du noyau de Saturne au sein de ce réservoir, ou bien sa migration dans le disque en direction de Jupiter, a pu disperser les objets du réservoir, permettant ainsi à une fraction d'entres eux d'être capturés dans le disque circum-jovien. Les objets peuvent être capturés en orbites prograde ou retrograde, à de larges distances orbitales et avec initialement de très grandes eccentricités. La friction avec le gaz en rotation quasi-Keplerienne autour de Jupiter fait rapidement spiraler les corps en orbite retrograde vers la surface de la planète géante. En revanche, les corps en orbite prograde voient leur eccentricité ainsi que leur demi-grand axe graduellement réduits par les forces de friction et finissent par avoir des orbites circulaires à des distances orbitales qui correspondent bien à l'extension actuelle des satellites Galiléens.

Contrairement à l'approvisionnement du disque en poussières, le mécanisme proposé dans ce chapitre lie la formation de lunes massives autour des planètes géantes à la présence d'autres objets massifs à proximité et prévoit donc que toutes les planètes géantes ne possèdent pas nécessairement de satellites comparables aux Galiléens. De plus, les simulations présentées dans ce chapitre révèlent que certains planétésimaux initialement dans le réservoir sont injectés dans le Système Solaire interne. Il est donc possible que certaines propulations d'astéroïdes glacés de la ceinture principale soient les représentants des briques élémentaires des satellites Galiléens. Comparer les données collectées par les futures missions spatiales JUICE et Europa Clipper avec les données précises fournies par les météorites collectées sur Terre pourrait permettre de tester la validité de ce lien entre astéroïdes et satellites joviens.

Chapitre 5

Dans ce chapitre, la question de l'origine des lunes de Mars, Phobos et Deimos, est abordée. Cette question est controversée car différentes propriétés de ces lunes pointent vers des conclusions contradictoires concernant leur origine. D'un côté, ces deux lunes possèdent des orbites quasi-circulaires et alignées dans le plan équatorial de Mars. De ce point de vue, ces objets sont donc des satellites réguliers qui se seraient formés autour de Mars. De l'autre côté, ces deux lunes ont des formes irrégulières et leurs spectres de réflectance ressemblent beaucoup à ceux d'astéroïdes primitifs que l'on peut trouver dans la ceinture principale. Leurs propriétés physiques pointent donc plutôt vers le fait que ces objets sont deux astéroïdes qui furent capturés intacts par Mars.

Plusieurs auteurs ont pointé les difficultés de réconcilier la capture de Phobos et Deimos avec leurs orbites actuelles. Une formation suite à un impact sur Mars, de manière analogue à l'événement supposé avoir donné naissance à la Lune, semble être le meilleur scénario de l'origine des lunes martiennes d'un point de vue dynamique et a reçu une attention grandissante ces dernières années. Cependant, il reste à expliquer pourquoi Phobos et Deimos ont des spectres semblables à des astéroïdes primitifs.

Une étude de la composition minéralogique des lunes qui se formeraient suite à un impact géant sur Mars ainsi que de la probable texture de ces minéraux est présentée. Les spectres de Phobos et Deimos, qui ne présentent aucune bande d'absorption dans le visible et le proche infrarouge, sont incompatibles avec la formation des lunes de Mars par un processus exactement similaire à celui de la formation de la Lune. Le fait qu'aucune bande d'absorption ne soit visible dans le spectre des lunes suggère que leur surface est dominée par des grains extrêmement fins, avec des tailles probablement inférieures au micromètre. En effet, si les grains à la surface sont beaucoup plus petits que la longueur d'onde dans lequel le spectre est mesuré, aucune bande d'absorption ne sera visible, quelle que soit la composition de ces grains. La présence de grains si fins est compatible avec la formation de Phobos et Deimos dans les régions externes du disque de débris formé suite à l'impact, où la faible pression a pu conduire à la condensation de matériaux vaporisés durant l'impact en grains de poussières fins. Ce type de condensation conduit généralement à la formation de grains avec des tailles typiques de quelques centaines de nanomètres. La ressemblance des lunes martiennes avec des astéroïdes primitifs serait ainsi dûe au fait que leurs spectres sont dominés par la présence de grains micro- ou sous-micrométriques à leur surface plutôt qu'à une composition similaire. Ce scénario permettrait ainsi de réconcilier les caractéristiques physiques et orbitales des lunes de Mars.

Chapitre 6

Les travaux menés durant la thèse ont permis de contribuer à des études concernant la composition des glaces cométaires, et particulièrement l'origine de l'oxygène moléculaire dans la coma de la comète 67P/Churyumov-Gerasimenko, cible de la mission Rosetta de l'agence spatiale européenne. Ce chapitre présente en particulier une étude sur la formation d'oxygène moléculaire par radiolyse de la glace d'eau de grains exposés aux radiations cosmiques.

En utilisant le modèle de transport de grains présenté au chapitre 3, couplé à une paramétrisation de la dose d'énergie reçue en fonction de la densité de colonne de gaz au-dessus d'un grain, un taux de production d'oxygène par radiolyse de l'eau dans les disques proto-planétaires est estimé. Ce taux est néanmoins extrêmement faible, alors même que l'hypothèse très favorable que toute l'énergie reçue servait à produire de l'oxygène a été utilisée. La conclusion la plus probable est que la radiolyse des grains de la comète 67P/C-G a principalement eu lieu dans l'environnement peu dense du milieu interstellaire, avant la formation de la nébuleuse protosolaire. Ces grains ont "survécu" à l'effondrement du nuage protosolaire, c'est-à-dire qu'ils n'ont pas été exposés à des températures supérieures à la température de stabilité de la glace d'eau, en gardant emprisonnées les molécules d'oxygène.

Chapitre 7

Ce dernier chapitre résume les travaux réalisés durant la thèse et leurs implications. Beaucoup de questions restent cependant en suspens, et certaines pistes à explorer dans le futur sont brièvement discutées.

Annexes

Les publications dans des journaux à comités de lecture sorties durant la thèse, au nombre de trois en tant que premier auteur et trois en tant que co-auteur, sont compilées dans les annexes et rangées par ordre chronologique de leur date de publication.

Contents

1 Introduction **18**

1.1 Context . . . 18

1.2 Mechanisms of planetary formation . . . 23

1.2.1 Protoplanetary disks . . . 23

1.2.2 The evolution of dust . . . 27

1.2.3 Growth of planets : the new paradigm of pebble accretion . . . 34

1.2.4 Dynamical evolution of the giant planets . . . 40

1.3 Organization of this manuscript . . . 45

2 Conditions of formation of the Galilean satellites **48**

2.1 Introduction . . . 48

2.2 Constraints on the formation of the Galilean system . . . 48

2.3 Formation in a circum-planetary disk . . . 50

2.3.1 The Minimum Mass models . . . 50

2.3.2 The Gas Starved model . . . 57

2.4 Concluding remarks . . . 61

3 Pebble accretion in the Galilean System **64**

3.1 Introduction . . . 64

3.2 Methods . . . 65

3.2.1 Gas dynamics . . . 65

3.2.2 Particles dynamics and thermodynamics . . . 68

3.3 Results . . . 73

3.4 Discussion . . . 78

3.4.1 Constraints on the size of the building blocks of the Galilean satellites . . . 78

3.4.2 Growing the Galilean satellites through pebble accretion . . . 79

3.4.3 Model assumptions and limitations . . . 84

3.5 Conclusions . . . 86

4 Delivery of solids to the circum-jovian disk **88**
4.1 Introduction 88
4.2 Sources of solid material 89
4.2.1 Inflow of small dust grains 90
4.2.2 Capture of large planetesimals 92
4.2.3 Existence of a reservoir of planetesimals close to Jupiter . . . 93
4.3 Delivering planetesimals from the reservoir 94
4.3.1 Case 1 : Growth of Saturn at the edge of Jupiter's gap 98
4.3.2 Case 2 : Migration of Saturn toward Jupiter 103
4.4 Evolution of captured planetesimals 105
4.5 Discussion 109
4.5.1 Implantation of planetesimals in the asteroid belt 109
4.5.2 Effect of the surface density of the CPD 111
4.5.3 Influence of Saturn's growth track 112
4.5.4 Formation of Saturn's satellite system 113
4.5.5 Implications for the formation of extrasolar moons 113
4.6 Summary 113

5 Origin of the two martian moons Phobos and Deimos **115**
5.1 A controversial origin 115
5.2 Formation from a cooling magma 117
5.2.1 Methods 118
5.2.2 Results 118
5.3 Formation in an extended gaseous disk 122
5.4 Discussion 125

6 Other contributions. Investigation of the origin of molecular oxygen in cometary ices **130**
6.1 Context 130
6.2 Irradiation of grains 131
6.3 Discussion 135

7 Conclusions and perspectives **136**

Chapter 1

Introduction

1.1 Context

The origin of the Solar System and its planets is a vast subject that have attracted the interests of many scientists over centuries. The *nebula hypothesis* was proposed by Pierre Simon Laplace (1749–1827) and Immanuel Kant (1724–1804) in the 18th century. They postulated that the atmosphere of the Sun was once much more extended and then substantially cooled down and contracted. The planets would then have condensed out of this cooling gas and rotate around the Sun due to conservation of angular momentum. This early formulation of the theory of the formation of planets already stated that these latter are naturally formed around stars and still constitutes the basis of modern theories of the origin of planetary systems.

The scenario proposed by Kant and Laplace has been refined over the past centuries with the help of more and more detailed observations, as well as theoretical efforts which have been supported by the development of increasingly powerful computers since the second half of the 20th century. It has been observed that stars are born in overdense regions of the interstellar medium, known as molecular clouds (figure 1.1 shows a picture of the Orion nebula, one such region where star formation is ongoing). Parts of these massive clouds collapse under the effect of their own gravity. The pressure and temperature increase upon the contraction of the cloud, especially at the center where the protostar is eventually found. The conservation of angular momentum during the collapse results in the formation of a disk in the plane perpendicular to the rotation axis. The disks surrounding young stars are generally referred to as protoplanetary disks as they are the birth place of planets and are nowadays observed at increasing resolution, unveiling their many features (rings, spiral arms and lobes; see figure 1.2 for an example). Around solar mass stars, protoplanetary disks have a typical mass of a few 10^{-2} to 10^{-1} that of

Figure 1.1: The Orion nebula, one of the most famous star forming regions in the vicinity of the Sun, as imaged by the Hubble Space Telescope.

their primary and a lifetime of a few million years before being (probably) blown away by their central star from the inside out, constraining the timescale of planet formation (at least those planets with a substantial primordial atmosphere, such as gas giants).

The theory of planetary accretion, starting from dust to planetesimals (e.g., $\sim$km sized objects) and massive planets, was laid out by Viktor Safronov during the 1950s and 1960s and summarized in his book, *The evolution of the protoplanetary cloud*. The core accretion model for giant planets formation was constructed within this framework over the following decades, where a solid core builds up first, followed by the accretion of a massive envelope of gas. On the other hand, the final assemblage of the terrestrial planets is thought to proceed through a more chaotic phase of giant impacts among roughly similar sized embryos after the dispersal of the protoplanetary disk. Overall, the mechanism of planetary growth through the accretion of smaller planetesimals provided a good understanding of the formation of the Solar System's planets (although Safronov pointed out already that the growth of Neptune at an orbital distance of 30 astronomical units–au, defined as the orbital distance of the Earth $\sim 1.5 \times 10^{11}$ m–would be unacceptably long).

Within the Solar System, the planets are usually accompanied by one or several satellites (or moons). Among these satellites, the regular satellites are those which

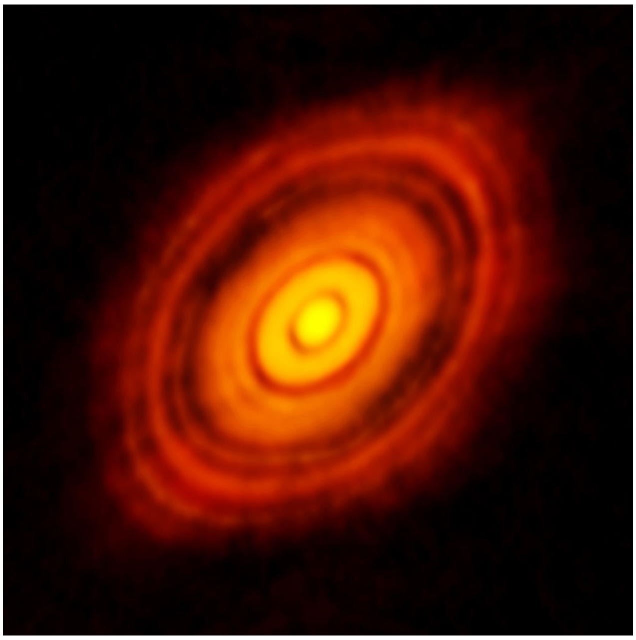

Figure 1.2: Image of the disk around the young star HL Tauri from the ground based Atacama Large Millimeter/submillimeter Array (ALMA) telescope. This image released on November 2014 revealed for the first time small scale ringed structures of a protoplanetary disk.

orbit well within the gravitational sphere of influence of their parent planets with relatively low eccentricities and low inclinations with respect to the equatorial plane of their primary (figure 1.3; not to scale). These characteristics are believed to reflect the fact that these satellites formed *in situ* on such low inclination and eccentricity orbits. Irregular satellites, on the other hand, are found around all giant planets of the Solar System on wider, either prograde or retrograde orbits, with generally high eccentricities and inclinations, and are thus believed to be captured objects. It is worthwhile to note that Mecury and Venus are the only planets that do not possess regular satellites but tidal interactions of any existing moons with these planets would have driven their rapid orbital decay towards the surface of their primary (see, e.g., Burns 1973). Therefore, the ubiquitous presence of regular satellites around the planets of our Solar System entails that any good theory for the formation of planets must account for the existence of their satellites (unless otherwise specified, the subsequent use of the term satellite or moon will refer to regular satellites of the planets).

The satellite systems exhibit a wide diversity in their architecture and properties and it is then difficult to conceive that the exact same events and mechanisms are responsible for their formation. The current theories however seem to converge on one fact, satellites formation takes place in the final stages of accretion of the planets and involves circum-planetary disks (these latter might be mainly constituted of

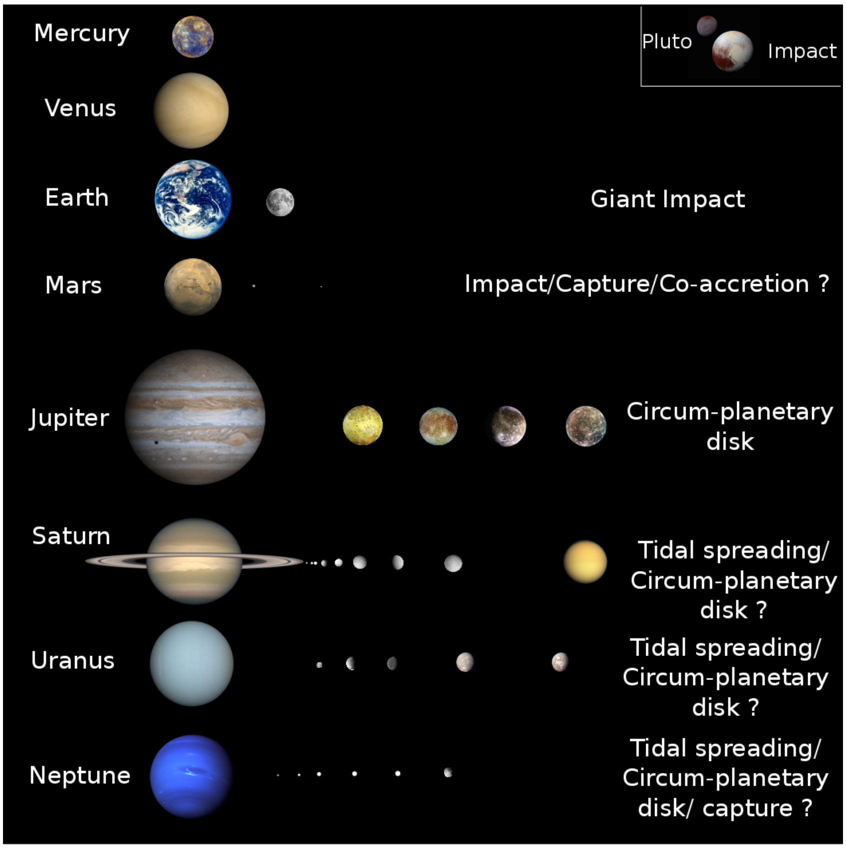

Figure 1.3: An overview of the planets of the Solar System (and Pluto) and their regular satellites systems. On the right of each system, the putative formation mechanism of the satellites is mentioned. Planets and satellites are not to scale but satellites are roughly to scale with one another. The distance relative to the center of the planet is approximately the orbital distance of the moons expressed in radii of their primary, except for the Moon which orbits far from the Earth and could not fit. Neptune's system includes outermost Triton although this satellite is thought to be a captured object due to its retrograde motion.

solid debris or dominated by gaseous material). In the case of terrestrial planets[1], the violent impacts among massive embryos in the final stages of their accretion can strip part of the mantles of the target and the impactor, resulting in a disk of debris out of which one or several moons can form. In the case of giant planets, theories were first developed for Jupiter and the Galilean system of satellites (shown on figure 1.3). The properties of this system (see Chapter 2) has led to the idea that it is in many regards a miniature Solar System, hence the satellites would have formed out of a mainly gaseous disk, similarly to the *nebula hypothesis* of planetary formation. In the last stages of Jupiter's formation, as the planet substantially cooled down and contracted, the angular momentum of the material accreted by the giant planet prevented its direct fall onto Jupiter's envelope and it would instead form an accretion disk within which the satellites formed. Applying this theory to Saturn has proven difficult given the very different architecture of its satellite system and the fact that the composition of the satellites do not seem to correlate with their orbital distance. We note in this regard that recent theories propose that moons can be tidally spread out of planetary rings, resulting in an architecture which is consistent with the satellite systems of Saturn, Uranus and Neptune. The origin of rings that are massive enough to account for the present day satellites remains however elusive in this scenario. Despite the fact that the origin of the different architectures of the satellite systems of the giant planets is unclear if they all formed within a gaseous disk surrounding their parent planet, the framework developed by Robin Canup and William Ward in the early 2000s, where the growth of satellites is regulated by the inflow of the material accreted by the giant planet, has been well accepted.

The discovery of the first planet orbiting an other star than the Sun in 1995 by Michel Mayor and Didier Queloz, and the plethora of objects detected since then, unveiled the great diversity of extrasolar planetary systems. It seems that the most common type of planets are the so-called super-earths, with sizes 1–4 times that of the Earth and orbital periods that are usually shorter than about a hundred days. It is notable that we have no analogues of these planets in the Solar System but most of all, these discoveries pointed out to the fact that we are far from having a consistent picture of planetary formation that can account for the observed diversity of systems. This renewed the interest in planet formation theories and motivated the observation of protoplanetary disks and better models of their evolution. Several breakthroughs have been made over the past two decades regarding mechanisms of planetesimal formation and planets growth. More recently, the admitted picture of protoplanetary disks evolution has been questioned, which might have profound implications for our understanding of planet formation and

[1] The controversial case of the martian moons is discussed in the Chapter 5.

their early dynamical evolution. In spite of this, theories for satellites formation remained mostly untouched.

In the remainder of this chapter, we provide further details on topics relevant to the formation of planets, with special emphasis on giant planets, as the formation of their moons is tightly linked to their own accretion history.

1.2 Mechanisms of planetary formation

In this section, the main theories for the formation of planets are presented with an emphasis on the most recent theories of accretion and the formation of giant planets, which are of peculiar interest to understand the formation of their satellite systems. Some of the caveats of these theories are also briefly discussed.

1.2.1 Protoplanetary disks

Planets form in disks surrounding young stars in the earliest phases of their formation. These protoplanetary disks, which are now routinely observed (e.g., Dutrey et al. 2014), are mainly gaseous with hydrogen (in its molecular form H_2) and helium (He) being their main components and only a small fraction of their masses (of the order of 1%) being heavier elements that might be found in condensed form (e.g., dust and ice) and will eventually build solid planets. Young stars are observed to accrete material from their disk (see Hartmann et al. 2016, for a review), implying transport of angular momentum within the disks and revealing that protoplanetary disks evolve with time. Understanding the structure and evolution of protoplanetary disks is crucial to the understanding of many aspects of planetary formation. However, modelling the detailed physics that drive the evolution of disks has proven difficult and the mechanism of angular momentum transport in protoplanetary disks, although being the subject of extensive research, remains elusive (Turner et al. 2014).

Some simplified models try to capture the main effects of the evolution of disks, namely the evolution of the mass and temperature which are of primary interest for the formation of planets, with all the detailed physics hidden behind some parameters that may be varied. The most widely used of such models is the α-viscous disk. The interest in viscous disks comes from the fact that the gas in the disk is approximately rotating around the central star at Keplerian speed $v_{\mathrm{K}} = (GM/r)^{1/2}$ (where G is Newton's constant of gravity and M is the mass of the central star) so that any inner annulus of gas rotates faster than its neighbouring outer annulus. In the presence of viscosity, viscous stresses arising from the differential rotation will tend to accelerate the outer annulus of gas whereas the inner one will be decelerated. The result is therefore an outward transport of angular momentum, thereby allowing mass to be transported inward which constitutes the basis of an accretion disk. The viscous evolution of disks was first described by Lynden-Bell and Pringle (1974).

The first step in these simple models is to reduce the problem to only one (radial) dimension by assuming the disk is axi-symmetric and deriving a simple vertical structure of the disk. The most basic approximation can be derived assuming the disk is vertically isothermal and thin (i.e., the radial scale of the disk is much larger than its vertical scale). Then, the balance between the gravity of the central star and the pressure gradient force in the vertical direction yields

$$c_s^2 \frac{\mathrm{d}\rho_\mathrm{g}}{\mathrm{d}z} = -\rho_\mathrm{g} z \frac{GM}{r^3}, \tag{1.1}$$

where c_s is the isothermal sound speed of the gas and ρ_g its mass density. Integrating the above equation allows to derive the vertical distribution of gas

$$\rho_\mathrm{g} = \rho_0 \exp\left(-\frac{z^2}{2H_\mathrm{g}^2}\right), \tag{1.2}$$

where ρ_0 is the density at the midplane of the disk (i.e., at $z = 0$) and $H_\mathrm{g} \equiv c_s/\Omega_\mathrm{K}$ is the scale height of the disk, with $\Omega_\mathrm{K} = (GM/r^3)^{1/2}$ the Kepler frequency. With this vertical structure in hand, the global radial evolution of the disk can be followed, defining its surface density as the vertically integrated column density

$$\Sigma_\mathrm{g}(r) = \int_{-\infty}^{+\infty} \rho_\mathrm{g}(r, z)\,\mathrm{d}z. \tag{1.3}$$

From the equation of mass continuity

$$r\frac{\partial \Sigma_\mathrm{g}}{\partial t} + \frac{\partial}{\partial r}(r\Sigma_\mathrm{g} v_r) = 0, \tag{1.4}$$

and the equation of conservation of angular momentum

$$\Sigma_\mathrm{g} v_r \frac{\partial}{\partial r}(r^2\Omega_\mathrm{K}) = \frac{1}{r}\frac{\partial}{\partial r}(r^2 T_{r\phi}), \tag{1.5}$$

where $T_{r\phi} = \Sigma_\mathrm{g}\nu r(\partial\Omega_\mathrm{K}/\partial r)$ is the viscous shear stress and ν is the viscosity, the equation governing the evolution of the surface density of the disk is (Pringle 1981)

$$\frac{\partial \Sigma_\mathrm{g}}{\partial t} = \frac{3}{r}\frac{\partial}{\partial r}\left[r^{1/2}\frac{\partial}{\partial r}(\nu\Sigma_\mathrm{g} r^{1/2})\right]. \tag{1.6}$$

This equation can be solved numerically (given a viscosity and initial conditions) to follow the viscous evolution of the disk. The general picture is that the disk spreads both inward and outward on the viscous timescale $\tau_\mathrm{visc} \sim r^2/\nu$ and its surface density decreases with time as mass is accreted onto the central star.

At this point however, nothing was said about the viscosity of the disk. The molecular viscosity within protoplanetary disks is far too low to account for the observed accretion rates and typical lifetime of circumstellar disks (3–5 My). A possible solution is that turbulence within the disks provide an effective viscosity that could be much larger than the molecular viscosity. The source of turbulence is highly debated however (see e.g., Turner et al. 2014). A common approach, proposed by Shakura and Sunyaev (1973), is to assume that turbulent eddies that would provide the viscosity have a size and velocity that are a fraction of typical length scales and velocities within the disk, namely the sound speed c_s and scale height of the disk H_g. Therefore, the viscosity of the disk may be written as

$$\nu = \alpha c_s H_\mathrm{g}, \tag{1.7}$$

where the dimensionless α parameter is a measure of the turbulence level in the disk and its value would range 10^{-4}–10^{-2} within protoplanetary disks. We discuss the relevance of this parametrization at the end of this section.

In these viscous disks, the main source of energy comes from viscous dissipation. A balance between the energy provided by viscous dissipation and that radiated at the photosphere of the disk yields the following equation for the photospheric temperature (e.g., Armitage 2009),

$$\sigma_\mathrm{SB} T_\mathrm{e}^4 = \frac{9}{8}\nu \Sigma_\mathrm{g} \Omega_\mathrm{K}^2, \tag{1.8}$$

where $\sigma_\mathrm{SB} = 5.67 \times 10^{-8}\ \mathrm{W\,m^{-2}\,K^{-4}}$ is Stefan-Boltzmann's constant. To determine the temperature at the midplane of the disk (where the planets will form), its opacity should be considered and complicated radiative transfer calculations must in principle be performed. It is nevertheless convenient to consider some simpler analytic estimates, especially when the global evolution of disks on long timescales is of interest. Nakamoto and Nakagawa (1994) derived the following expression for the midplane temperature,

$$T_\mathrm{m}^4 = \left(\frac{3}{4}\tau_\mathrm{R} + \frac{1}{\tau_\mathrm{P}}\right) T_\mathrm{e}^4, \tag{1.9}$$

where τ_R and τ_P are the Rosseland and Planck mean optical depths, respectively. The optical depth from the midplane to the surface of the disk can be approximated by

$$\tau_\mathrm{R} = \frac{\kappa_\mathrm{R} \Sigma_\mathrm{g}}{2}, \tag{1.10}$$

with κ_R the Rosseland mean opacity of dust grains and assuming that it is constant

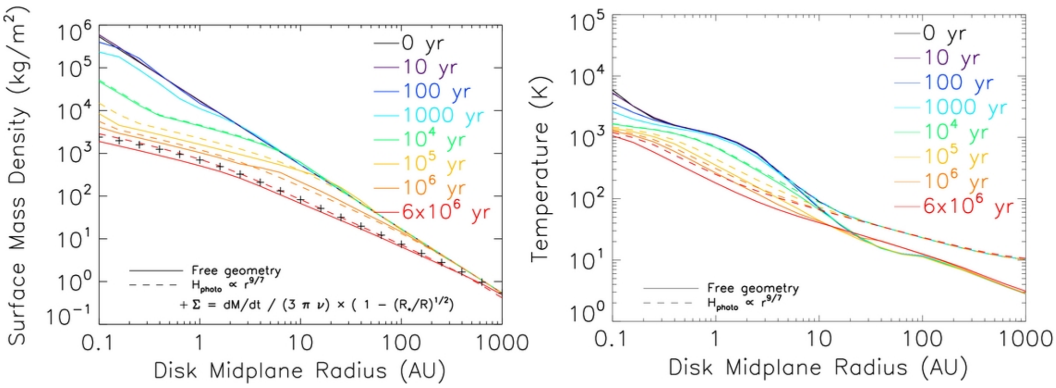

Figure 1.4: Surface density (left) and temperature (right) evolution of a viscous disk (extracted from Baillié and Charnoz (2014)).

in the vertical direction. The Rosseland mean opacity is generally given in the form of power laws which depend on both the temperature and density of the disk, $\kappa_{\rm R} = \kappa_0 \rho_{\rm g}^m T_{\rm m}^n$, and the slopes depend upon the composition of the dust (e.g., Pollack et al. 1985). The Planck mean optical depth is assumed to be $\tau_{\rm P} = 2.4\tau_{\rm R}$ (Nakamoto and Nakagawa 1994). Due to the fact that the temperature of the disk depends on the viscosity, which itself depends on the temperature in the α-model, the equations of the evolution of the surface density and temperature must be solved together in a self-consistent manner.

A good proxy for these kind of viscous disks models is the work by Hueso and Guillot (2005) and that by Baillié and Charnoz (2014), to name a few. Figure 1.4 shows the evolution of the surface density and midplane temperature as given by the viscous disk model of Baillié and Charnoz (2014). Both quantities are decreasing functions of the distance to the star and time. Such profiles have important implications for the evolution of the dust, in terms of dynamics as well as in terms of composition, and in turn on the formation of the planets. Obviously, the outwardly decreasing temperature implies that (at any time) more and more volatile species can be found in condensed form as one is moving away from the star, whereas the overall cooling of the disk over time suggests that the regions where given condensates can be found move inward. Of primordial importance is the limit where water ice is stable within the disk, the so-called snowline. Water is inferred to have been one of the most abundant species in the Solar System's protoplanetary disk (Lodders 2003) and hence constitutes a large reservoir of mass available in solid form beyond the snowline. Moreover, icy grains have different sticking properties as compared to silicate grains which could be important for the growth of objects as discussed in the next section.

Although such simple models are convenient to set the background of planetary formation theories and models, their relevance is questionable. The so-called

Magneto-Rotational Instability (MRI; Balbus and Hawley 1991), arising in differentially rotating weakly magnetized fluids, has been the most trendy mechanism for angular momentum transport in protoplanetary disks. 3D simulations of small portions of disks under the assumption of ideal magnetohydrodynamics (MHD) showed sustained turbulence and outward transport of angular momentum with effective viscosity consistent with that inferred for protoplanetary disks (Hawley et al. 1995). However, the MRI is only effective if the magnetic field in the disk can couple with the gas. Resistive (or Ohmic) dissipation can suppress MRI if the ionization level of the disk is too weak, which is expected in most parts of protoplanetary disks. This lead to the idea of layered disks (Gammie 1996) where turbulent transport of angular momentum would be efficient only in the most inner parts of the disk, where thermal ionization is effective, and in the upper layers, where cosmic rays ionization is effective. This already calls for a revision of the standard α-disk model, showing that a more realistic evolution of the disks should be described with a both radially and vertically varying α value. More critically though, the most recent numerical investigations of the structure of protoplanetary disks include full non-ideal MHD terms, notably the Hall drift which is the dominant non-ideal effect in the planetary formation regions (between 10–20 au), and show that the evolution of disks might be significantly different than previously thought (e.g., Béthune et al. 2016, 2017, Bai 2017). These studies reveal that the disks are in fact largely laminar, though exhibiting complicated flow structures, and that accretion is mainly driven by magnetic winds launched at the surface of the disks with mass loss rates comparable to mass accretion rates onto the star. The angular momentum is therefore transported vertically by the winds and the evolution of such disks cannot be described with viscous models where angular momentum is transported radially outward. This different picture of the evolution of disks might have profound implications for our understanding of planet formation but also for the formation of satellites around jovian planets as those are thought to originate from circum-planetary disks which are currently mostly described with α-disk models.

1.2.2 The evolution of dust

In the previous section we briefly described the structure of protoplanetary disks. Although their evolution remains uncertain, the radial decrease of density and temperature is a robust feature (see however Suzuki et al. 2016), and it is interesting to discuss how dust would evolve in protoplanetary disks as this is a main component of the formation of planets. For simplicity, it was assumed in the previous section that gas was rotating at Keplerian speed v_{K}, which is a good approximation to describe the global evolution of the gas but must be alleviated to understand the dynamics of dust grains. In fact, protoplanetary disks are pressure supported. The global pressure gradient within the disk results in an outwardly directed radial force that counteracts the gravitational pull from the central star. The orbital velocity of the gas is therefore

$$v_{\mathrm{g}} \equiv v_{\mathrm{K}} - \eta v_{\mathrm{K}} \approx v_{\mathrm{K}} + \frac{1}{2}\frac{c_s^2}{v_{\mathrm{K}}}\frac{\partial \ln P}{\partial \ln r}, \tag{1.11}$$

with the pressure $P = c_s^2 \rho_{\mathrm{g}}$. For reasonable disk parameters, the deviation from Keplerian speed is only of the order of a few 10^{-3}. But even this tiny deviation from Keplerian rotation has an important effect on the dynamics of the dust.

Dust grains embedded in a protoplanetary disk do not feel the pressure support and tend to rotate at the Keplerian speed, hence slightly faster than the gas. Therefore, dust grains feel a constant headwind and will tend to spiral in toward the star, which is known as the radial drift. The acceleration due to the drag force experienced by a particle might be expressed as

$$\mathbf{a}_{\mathrm{drag}} = -\frac{1}{t_{\mathrm{s}}}(\mathbf{v}_{\mathrm{d}} - \mathbf{v}_{\mathrm{g}}), \tag{1.12}$$

where $\mathbf{v}_{\mathrm{d}}$ is the velocity of the particle, $\mathbf{v}_{\mathrm{g}}$ that of the gas, and t_{s} is the stopping (or friction) time which expresses the time needed for the drag to bring the velocity of the particle to that of the gas.

In the case of small particles (relative to the mean free path of the gas), the stopping time is given by the simple relation known as the Epstein drag law (e.g., Weidenschilling 1977)

$$t_{\mathrm{s}} = \frac{\rho_{\mathrm{s}} a}{\rho_{\mathrm{g}} v_{\mathrm{th}}}, \tag{1.13}$$

with ρ_{s} the internal density of the dust grain, a its size and $v_{\mathrm{th}} = \sqrt{8/\pi} c_s$ the thermal velocity of the gas. It is convenient to describe the aerodynamic coupling of the dust with the gas through the dimensionless Stokes number, $\mathrm{St} = t_{\mathrm{s}}\Omega_{\mathrm{K}}$.

Particles with similar Stokes number will have similar dynamics. The radial velocity of a dust particle due to gas drag is (Weidenschilling 1977)

$$v_{\mathrm{r,d}} = -\frac{2\mathrm{St}}{\mathrm{St}^2 + 1}\eta v_{\mathrm{K}}, \tag{1.14}$$

where we have neglected the drag due to the radial velocity of the gas itself. The particles that will drift inward the most rapidly are those for which the Stokes number is close to unity. Recall that η is of the order of a few times 10^{-3}, the drift timescale, $\tau_{\mathrm{drift}} \equiv r/v_{\mathrm{r,d}}$, for the particles with $\mathrm{St} \sim 1$ is of the order of $\sim 10^2$–$10^3\,\Omega_{\mathrm{K}}^{-1}$. This is short ! At 1 au, the typical lifetime of a protoplanetary disk is of the order of $10^7\,\Omega_{\mathrm{K}}^{-1}$. Small ($\mathrm{St} \ll 1$) and large ($\mathrm{St} \gg 1$) particles do not experience substantial radial drift, although for different reasons. Small particles are very tightly coupled to the gas and will therefore rotate at the same subkeplerian velocity than the gas, it is their azimuthal motion that is mainly affected. Large objects on the other hand are hardly affected by gas drag and will mostly have their eccentricity and inclination damped by gas drag.

The friction with the gas also affects the vertical motion of the dust particles. Even assuming that the gas has no vertical velocity (i.e., perfect hydrostatic equilibrium), a dust particle experiences a vertical acceleration

$$\ddot{z} = -\frac{v_{\mathrm{z,d}}}{t_{\mathrm{s}}} - \Omega_{\mathrm{K}}^2 z \tag{1.15}$$

and will settle towards the midplane of the disk on a timescale (Chiang and Youdin 2010)

$$t_{\mathrm{sett}} \sim \left(\frac{2\mathrm{St}^2 + 1}{\mathrm{St}}\right) \Omega_{\mathrm{K}}^{-1}. \tag{1.16}$$

The particles with St ~ 1 are again those that will settle the most rapidly, on a timescale comparable with their orbital timescale which is shorter than the timescale for their radial drift. The dynamics are generally shorter (by a factor $\sim \eta^{-1}$) in the vertical direction than in the radial direction. However, turbulence can diffuse particles in both the radial and vertical direction, thus preventing dust particles to settle into an infinitely thin layer at the disk midplane (see Chapter 3 for more details on turbulent diffusion). By equating the vertical diffusion timescale of particles with their settling timescale, Youdin and Lithwick (2007) derive an expression for the scale height of the dust layer,

$$H_{\mathrm{p}} = \sqrt{\frac{\alpha}{\mathrm{St} + \alpha}} H_{\mathrm{g}}, \tag{1.17}$$

with α the turbulence parameter of the disk. Particles with St $\ll 1$ are prone to diffusion and settle on rather long timescales so that their vertical distribution is similar to that of the gas. As St becomes comparable or even larger than α, settling is efficient and particles reside close to the midplane, which has important implications for the formation of planetesimals and the growth of planets.

Now that we have established that the dynamics of dust largely depends on their aerodynamic properties, we need an estimate of the expected sizes of dust grains within protoplanetary disks. The initial size of the dust grains would likely be comparable to what is observed in the interstellar medium, grains with typical sizes of 0.1–1 μm. However, once embedded in the disk, the grains will grow by mutual collisions on timescales (e.g., Birnstiel et al. 2012)

$$\tau_{\mathrm{coag}} = \frac{a}{\dot{a}} \approx (\epsilon_{\mathrm{d}} \Omega_{\mathrm{K}})^{-1}, \tag{1.18}$$

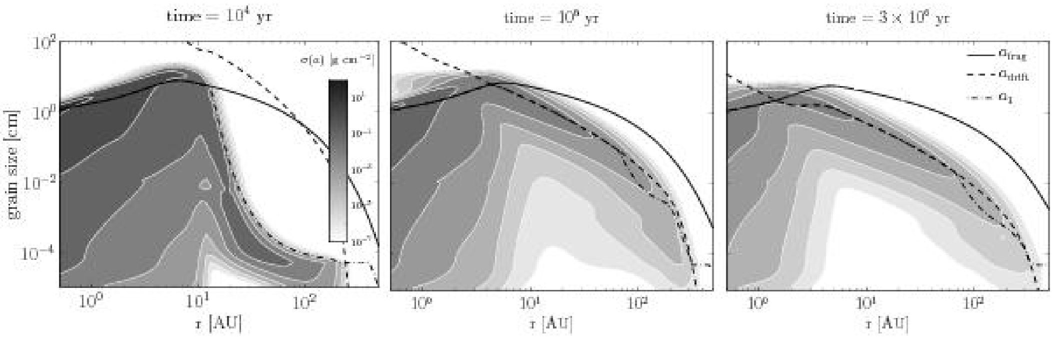

Figure 1.5: Snapshots of the dust surface density distributions as a function of radius and grain size from (Birnstiel et al. 2012). The solid and dashed lines show the maximum grain sizes inferred from the fragmentation and drift barriers, respectively. The dotted-dashed line shows the maximum size limited by the coagulation timescale of the grains. The simulated disk has a turbulent parameter $\alpha = 10^{-3}$ and the fragmentation velocity threshold was set to $u_f = 10\ \mathrm{m\,s^{-1}}$ everywhere.

where $\epsilon_{\rm d} = \Sigma_{\rm d}/\Sigma_{\rm g}$ is the vertically integrated dust-to-gas mass ratio of the disk (a typical value is $\epsilon_{\rm d} = 10^{-2}$). The collisional growth of dust grains cannot proceed indefinitely and suffers some important barriers.

First, if two dust grains encounter each other at a relative velocity above a certain threshold velocity u_f, they will fragment instead of sticking together. Ormel and Cuzzi (2007) derived the approximate relative velocities between similar-sized particles due to turbulent motion,

$$\Delta v = \sqrt{3\alpha \mathrm{St}}c_s, \tag{1.19}$$

where α is the turbulent parameter of the disk as defined in the previous section. The relative velocity among the dust grains hence depends on their Stokes number so that they cannot grow much above the point when $\Delta v = u_f$. This can be directly translated into a maximum Stokes number due to the fragmentation barrier

$$\mathrm{St}_{\rm frag} = \frac{1}{3}\frac{u_f^2}{\alpha c_s^2}. \tag{1.20}$$

The exact value of u_f would depend on the size and porosity of the dust particles as well as on their composition on a complicated way. Typically, a velocity threshold $u_f = 1\ \mathrm{m\,s^{-1}}$ for silicate dust and $u_f = 10\ \mathrm{m\,s^{-1}}$ for icy grains (which are stickier than silicate dust grains) is often assumed (e.g., Morbidelli et al. 2015a, Ida and Guillot 2016).

Another important limiting effect for dust growth is the radial drift. If the drift timescale of dust particles is shorter than their coagulation timescale they will move inward and be locally removed before having time to grow further. The maximum Stokes number particles can reach before being removed by radial drift

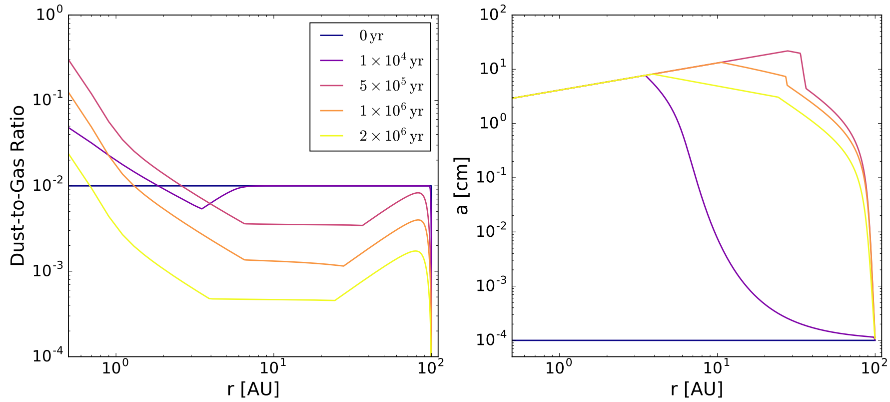

Figure 1.6: Evolution of the dust-to-gas mass ratio $\epsilon_{\rm d}$ (left) and grain representative size (right) as a function of radius at different epochs.

can be estimated by equating $\tau_{\rm drift}$ and $\tau_{\rm coag}$, which gives,

$$\mathrm{St}_{\rm drift} \approx \frac{1}{2}\epsilon_{\rm d}\eta^{-1}. \tag{1.21}$$

At a given distance from the star, the maximum size of the dust grains can therefore be inferred by considering the minimum value between $\mathrm{St}_{\rm frag}$ and $\mathrm{St}_{\rm drift}$ which translates into (e.g., Birnstiel et al. 2012)

$$a_{\rm max} = \min[\mathrm{St}_{\rm frag}, \mathrm{St}_{\rm drift}]\frac{2\Sigma_{\rm g}}{\pi\rho_{\rm s}}. \tag{1.22}$$

In principle, dust grains have a size distribution whose maximum is limited by either of these growth barriers. Figure 1.5 shows the resulting distributions obtained by Birnstiel et al. (2012) with a complete model of dust coagulation, fragmentation and drift along with the analytically inferred size limits provided by fragmentation and drift. Such models are computationally expensive but interestingly, Birnstiel et al. (2012) shows that the overall results can be well reproduced using a representative size approach. It consists in following the evolution of a single size dust population which traces well the evolution of the full size distribution. By comparing with the results of their full simulations, Birnstiel et al. (2012) find that the representative size is slightly below the maximum theoretical size and is approximately $0.37a_{\rm frag}$ and $0.55a_{\rm drift}$ in the fragmentation and drift limited regimes, respectively.

The evolution of the dust surface density follows from the same kind of equation as the gas surface density presented in the previous section. In the representative size approach it is given by a single advection-diffusion equation (e.g., Birnstiel et al.

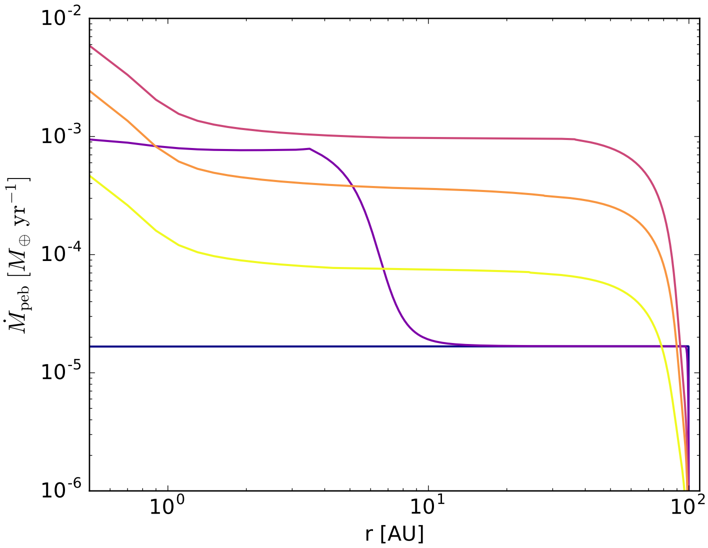

Figure 1.7: Evolution of the flux of dust grains through the disk, $\dot{M}_{\rm peb}$, at epochs corresponding to that shown on Figure 1.6.

2012)

$$\frac{\partial \Sigma_{\rm d}}{\partial t} + \frac{1}{r}\frac{\partial}{\partial r}\left[r\left(\Sigma_{\rm d} v_{\rm r,d} - D_{\rm g}\Sigma_{\rm g}\frac{\partial}{\partial r}\left(\frac{\Sigma_{\rm d}}{\Sigma_{\rm g}}\right)\right)\right] = 0. \tag{1.23}$$

In the above expression, $D_{\rm g}$ is the gas diffusivity generally approximated as $D_{\rm g} = \nu$ with ν the turbulent viscosity as defined in the previous section. In principle, the dust diffusivity is given by (Youdin and Lithwick 2007)

$$D_{\rm d} = \frac{D_{\rm g}}{1 + {\rm St}^2}. \tag{1.24}$$

However, for dust grains with Stokes number below unity, and also considering the fact that the smaller dust grains will dominate the diffusion term, using the gas diffusivity is a good approximation for the representative size approach (see Birnstiel et al. 2012, for a less hand-waving justification).

Figure 1.6 shows the result of numerical integration of equation 1.23 on a background steady-state gaseous disk where the size of the dust grains was determined at each radial bin and each timestep by considering the fragmentation and drift barriers and selecting the appropriate representative size. The evolution of the dust-to-gas mass ratio $\epsilon_{\rm d}$ is shown on the left panel whereas the right panel shows the evolution of the dust size, starting as μm dust grains growing on a timescale $\tau_{\rm coag}$ with $\epsilon_{\rm d} = 10^{-2}$ everywhere initially. Due to growth and subsequent rapid inward drift of the dust particles, the outer regions of the disk are depleted while the inner regions are substantially enriched in dust as shown by the evolution of $\epsilon_{\rm d}$.

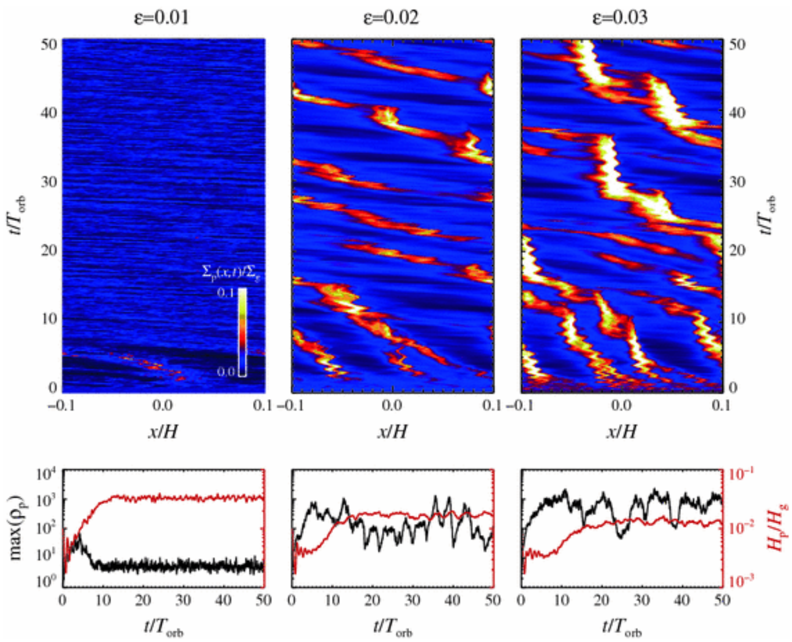

Figure 1.8: Evolution of the surface density of solids in 3D simulations for particles with Stokes number St $= 0.25, 0.50, 0.75, 1.00$ and three different initial dust-to-gas mass ratio $\varepsilon = 0.01, 0.02, 0.03$ (from left to right). Bottom panels show corresponding maximum particle densities attained in the simulations as a function of time and dust scale height. For an initial metallicity $\varepsilon = 0.01$ the drag exerted by the dust particles is too weak to allow for an efficient clumping. For the other cases, self-gravity of the dust would yield to the collapse of gravitationally bound clumps. Simulations were performed by Johansen and Klahr (2011).

Of primordial interest for the growth of planets is the overall dust mass flux through the disk, $\dot{M}_{\rm peb} = 2\pi r \Sigma_{\rm d} v_{\rm r,d}$, whose evolution is shown on Figure 1.7. Interestingly, this flux varies only weakly with distance to the star between 1–100 au. At 5 au, the flux varies from a few 10^{-3} down to $\sim 10^{-4}$ $M_\oplus\,{\rm yr}^{-1}$ for the simulation presented on Figure 1.6. In the next section, we present a channel of planetary accretion recently investigated which consists in accreting the drifting dust grains.

Finally, it is interesting to note that the existence of growth barriers for the dust grains is problematic for the formation of planetesimals (objects with sizes of a few km up to a few hundred kilometers such as asteroids located in the main belt and the Kuiper Belt beyond the orbit of Neptune) which are the seeds for the growth of massive embryos and giant planets' cores. It has been suggested that very porous dust aggregates can overcome the radial drift barrier and grow to planetesimal sizes if fragmentation is insignificant which could be the case for icy particles (Okuzumi et al. 2012). A more promising planetesimal formation mechanism is to overcome the growth barriers by direct gravitational collapse of dust swarms into large objects. This requires dust particles concentrations that are sufficiently high to allow the swarm being gravitationally unstable. Several mechanisms can lead to dust concentration in protoplanetary disks (see Johansen et al. 2014, for a review). The streaming instability (Youdin and Goodman 2005) is one such mechanism that received a lot of attention over the past decade. It arises from the back-reaction of the dust onto the gas (i.e., the dust grains drag the gas) which has been neglected in the above analysis of dust evolution. The principle is that an initially small overdensity of dust will locally increase the gas orbital motion through drag, thereby slowing down its radial drift which allows particles outside of the clump to catch up with it and increase its density. Figure 1.8 shows result of the evolution of dust surface density and maximum dust concentration in 3D box simulations by Johansen and Klahr (2011) including back-reaction of the dust. Streaming instability operates efficiently on particles with Stokes number close to unity for initial dust-to-gas mass ratio $\epsilon_{\rm d} \geqslant 0.02$, that is twice the expected metallicity of the Solar System's protoplanetary disk. Particles with smaller Stokes number are also prone to concentration via the streaming instability, although requiring higher initial metallicities (Yang et al. 2017, find efficient concentrations of particles with $\mathrm{St} = 10^{-3}$ for $\epsilon_{\rm d} \sim 0.04$). This suggests that planetesimals formation might not be efficient everywhere in protoplanetary disks and could be restricted to localized regions which would be sweet spots for the formation of planets (Drążkowska et al. 2016, Schoonenberg and Ormel 2017, Drążkowska and Alibert 2017).

1.2.3 Growth of planets : the new paradigm of pebble accretion

In this section the growth of planets, and particularly giant planets, is discussed in the framework of an emerging paradigm, the so-called pebble accretion (see e.g., Ormel 2017, Johansen and Lambrechts 2017, for recent reviews). This recently discovered mechanism involves the accretion of mm–cm sized dust grains that couple on approximately orbital timescales with the gaseous component of a protoplanetary disk (i.e., their Stokes number is close to unity; see previous section), designated as pebbles, as opposed to the planetesimal accretion involving much larger objects ($>$ km in size) that are aerodynamically decoupled from the gas. Although pebble accretion has been quite recently evidenced and investigated, it is an ingredient of the much older core-accretion scenario for the formation of the giant planets (e.g., Mizuno 1980, Pollack et al. 1996).

In the core-accretion model, which is the most commonly accepted scenario, a solid core builds up first, followed by accretion of a massive gaseous envelope. Although the precise core mass required to accrete a massive gaseous envelope depends on the accretion rate of solids onto the core, the molecular weight of the gas in the envelope and its opacity (e.g., Hori and Ikoma 2011), it is generally assumed that the core should be of the order of $\sim$10 $M_\oplus$ to trigger rapid envelope accretion. This is also supported by observations of a large fraction of super-Earths in extrasolar systems, and Uranus and Neptune in our Solar System, having gaseous envelopes limited to about 10% of their mass, suggesting that these bodies did not experience runaway gas accretion while still forming in a gaseous environment.

The building of this massive core is a critical phase of the core-accretion scenario as it should operate on a short enough timescale to allow for the accretion of the envelope before the dissipation of the protoplanetary disk in typically 3–5 Myr. This is very challenging if growth proceeds through planetesimal accretion (e.g., Pollack et al. 1996). It is especially difficult to explain the formation of Uranus and Neptune as the planetesimal accretion rate is $\propto \Omega_{\rm K}$ and therefore drops sharply with distance to the central star as $r^{-1.5}$. Moreover, the system must be kept dynamically cold to allow for an efficient accretion but realistic simulations including multiple cores show that this is unrealistic (Levison et al. 2010). Levison et al. (2010) find that multiple Earth-mass embryos embedded within a planetesimal disk generally grow very little, even when the effects of collisions, fragmentation and gas drag, which help in damping the inclination and eccentricity of the planetesimals, are taken into account. Morbidelli et al. (2015a) pointed out that planetesimal accretion is also unable to account for the fact that, during the lifetime of the protoplanetary disk, massive giant planets' cores should grow rapidly while the growth of embryos in the inner Solar System was stalled at approximately Mars' mass.

Pebble accretion, on the other hand, can overcome the hurdles of planetesimal accretion and allows for the rapid formation of massive cores even at large orbital distances. It takes advantage of the large flux of drifting particles (Fig. 1.7) expected from theoretical investigations of dust evolution in protoplanetary disks (e.g., Birnstiel et al. 2010, see previous section) and enhanced collisional cross-sections due to the fact that gas drag dissipates the energy of the pebbles during an encounter with a massive object. Observations of circumstellar disks also reveal that cm–mm sized dust grains dominate the dust mass budget of protoplanetary disks with larger sizes found in the inner parts of disks (e.g., Pérez et al. 2015, but note that inner parts here refers to tens of AU), in agreement with theoretical expectations (see Fig. 1.5). The physics behind pebble accretion can be understood intuitively from the different timescales involved during an encounter between an accreting seed (a large planetesimal or a protoplanet) and a dust grain. If the timescale of the encounter (that is, the time within which the dust particle passes the region of gravitational influence of the accreting seed) is comparable to the stopping time of the dust particle, gas drag will cause the particle to spiral into the seed.

The interaction radius of a seed of mass M_s with a particle approaching at relative velocity δv is (e.g., Johansen and Lambrechts 2017)

$$R_g = \frac{GM_s}{\delta v^2}. \tag{1.25}$$

The relative velocity between the seed moving on a keplerian orbit and a small pebble entrained with the sub-keplerian flow is $\delta v \approx \eta v_{\rm K}$ (i.e., the deviation from keplerian speed due to pressure support of the gas disk, see section 1.2.1). This defines the so-called Bondi radius (Lambrechts and Johansen 2012),

$$R_{\rm B} = \frac{GM_s}{(\eta v_{\rm K})^2}, \tag{1.26}$$

and the associated encounter timescale $t_{\rm B} = R_{\rm B}/(\eta v_{\rm K})$. All particles with $t_{\rm stop} \approx t_{\rm B}$ passing through the Bondi radius will settle towards the seed. Particles with $t_{\rm stop} < t_{\rm B}$ will be more strongly coupled with the gas flow and accreted from a region smaller than the Bondi radius, whereas particles with $t_{\rm stop} > t_{\rm B}$ will not lose sufficient energy to settle down to the seed and accretion would proceed similarly as the gas-free accretion (geometrical cross-section enhanced by gravitational focusing). Optimal accretion therefore occurs for particles with a size that depends on the mass of the seed. However, this regime (known as the Bondi or drift regime) is only relevant for low mass accreting seeds. At some point, the gravitational pull from the central star cannot be ignored so that the gravitational interaction region is limited to the Hill sphere of the seed with radius

$$R_{\rm H} = \left(\frac{GM_s}{3\Omega_K^2}\right)^{1/3}. \tag{1.27}$$

The mass at which the Bondi radius becomes equivalent to the Hill radius (equivalently, when $\Omega_{\rm K} R_{\rm H} = \eta v_{\rm K}$) marks a transition in the pebble accretion regime and is given by

$$M_{\rm t} = \sqrt{\frac{1}{3}}\frac{(\eta v_{\rm K})^3}{G\Omega_K}. \tag{1.28}$$

Typically, in the giant planets' region, the transition mass is a few $10^{-3}\ M_\oplus$ (Lambrechts and Johansen 2012), in between the mass of Ceres ($1.5 \times 10^{-4}\ M_\oplus$) and the Moon ($1.2 \times 10^{-2}\ M_\oplus$). Here we will thus focus on the Hill regime (also known as the shear regime) which is the most relevant for the growth of giant planets' cores.

Above the transition mass, the relative velocity between an approaching pebble and the accreting seed is given by the Hill speed, $v_{\rm H} \equiv \Omega_{\rm K} R_{\rm H}$. What it means is that the relative velocity due to the overall Keplerian motion of the objects ($v_{\rm K} \propto r^{-1/2}$), the Keplerian shear, dominates over the relative velocity arising from the slightly sub-keplerian rotation of pebbles entrained with the gas flow. The characteristic encounter timescale is then $t_{\rm H} = R_{\rm H}/v_{\rm H} = \Omega_{\rm K}^{-1}$, which is now independent of the mass of the seed. Therefore, optimal accretion occurs for particles with stopping times $t_{\rm stop} \approx \Omega_{\rm K}^{-1}$, that is in fact for particles with Stokes number ${\rm St} \approx 1$, which is also independent of the mass of the accreting seed. Particles with smaller stopping times need to approach closer to the seed to be deflected from the gas flow and eventually accreted. For these particles, the effective radius from which accretion is efficient will therefore be smaller than the Hill radius. It can be estimated by equating the deflection timescale $t_{\mathrm{d}} = \delta v/g$, where g is the seed's gravitational attraction, with the stopping time t_{stop} of the considered particle. Using $\delta v \approx r\Omega_{\mathrm{K}}$, this gives

$$\frac{R_{\mathrm{eff}}^3 \Omega_{\mathrm{K}}}{G M_s} = t_{\mathrm{stop}}, \tag{1.29}$$

and the effective accretion radius is therefore approximately

$$R_{\mathrm{eff}} \approx \mathrm{St}^{1/3} R_{\mathrm{H}}. \tag{1.30}$$

In fact, numerical integrations by Lambrechts and Johansen (2012) show that particles with $\mathrm{St} = 0.1$ are readily accreted from the entire Hill sphere of the accreting seed in the Hill regime so that $R_{\mathrm{eff}} = (\mathrm{St}/0.1)^{1/3} R_{\mathrm{H}}$.

It is now possible to determine the accretion rate onto the seed in the Hill regime. The most general expression for the accretion rate is

$$\dot{M}_s = \sigma n_{\mathrm{d}} m_{\mathrm{d}} \delta v, \tag{1.31}$$

where σ is the collisional cross-section, n_{d} is the number density of particles and m_{d} their mass. If the pebbles are vertically distributed on a thin layer with $H_{\mathrm{d}} \ll R_{\mathrm{eff}}$, where H_{d} is the scale height of the particles which can be related to the gas scale height through $H_{\mathrm{d}} = \sqrt{\alpha/(\mathrm{St}+\alpha)} H_{\mathrm{g}}$ (Youdin and Lithwick 2007), we can use the 2D planar approximation to express the accretion rate. In that case, the collisional cross-section is simply $\sigma_{\mathrm{2D}} = 2R_{\mathrm{eff}}$, $n_{\mathrm{d}} = \Sigma_{\mathrm{d}}/m_{\mathrm{d}}$ and in the Hill regime we have $\delta v = R_{\mathrm{eff}} \Omega_{\mathrm{K}}$, so that the accretion rate becomes

$$\dot{M}_{s,\mathrm{2D}} = 2 \left(\frac{\mathrm{St}}{0.1}\right)^{2/3} R_{\mathrm{H}} v_{\mathrm{H}} \Sigma_{\mathrm{d}}. \tag{1.32}$$

On the other hand, if the disk of particles is thick compared to R_{eff}, the planar approximation does not hold and the collisional cross-section is $\sigma_{\mathrm{3D}} = \pi R_{\mathrm{eff}}^2$, the particle number density is $n_{\mathrm{d}} = \rho_{\mathrm{d}}/m_{\mathrm{d}}$, and the accretion rate is

$$\dot{M}_{s,\mathrm{3D}} = \pi \left(\frac{\mathrm{St}}{0.1}\right) v_{\mathrm{H}} R_{\mathrm{H}}^2 \rho_{\mathrm{d}}. \tag{1.33}$$

Noting that $\rho_{\mathrm{d}} = \Sigma_{\mathrm{d}}/(\sqrt{2\pi} H_{\mathrm{d}})$, the 3D accretion rate can be written as a fraction of the 2D accretion rate (Morbidelli et al. 2015a),

$$\dot{M}_{s,\mathrm{3D}} = \dot{M}_{s,\mathrm{2D}} \left(\frac{\pi R_{\mathrm{eff}}}{2\sqrt{2\pi} H_{\mathrm{d}}}\right). \tag{1.34}$$

It is convenient to express the accretion rate as a function of dust mass flux through the disk $\dot{M}_{\rm d} = 2\pi r v_{\rm r,d}\Sigma_{\rm d}$ (see section 1.2.2). For particles with small Stokes number, $v_{\rm r,d} \approx 2{\rm St}\eta v_{\rm K}$. Inserting this into equation 1.32, we find the planar mass accretion rate might be expressed as

$$\dot{M}_{s,\rm 2D} = (2\pi 0.3^{2/3}\eta)^{-1}\left(\frac{\rm St}{0.1}\right)^{-1/3} q_{\rm seed}^{2/3}\dot{M}_{\rm d}, \tag{1.35}$$

where $q_{\rm seed} = M_{\rm s}/M_*$, with M_* the mass of the central star. Because η, $\dot{M}_{\rm d}$, and St depend generally only weakly with distance to the Star (see, e.g., sec. 1.2.2; Lambrechts and Johansen 2014, Morbidelli et al. 2015a), so does the mass accretion rate through pebble accretion. This is one of the strengths of pebble accretion as compared to classical planetesimal accretion.

Another interesting quantity to derive from the accretion rate is the accretion efficiency $\varepsilon_{\rm PA} = \dot{M}_s/\dot{M}_{\rm d}$, that is, the fraction of pebbles drifting past the seed that will be accreted. This quantity gives an idea of the total dust mass required to grow an object. In the 2D Hill regime, we can directly use the expression derived above to obtain

$$\varepsilon_{\rm PA} \sim 0.07\left(\frac{\rm St}{0.1}\right)^{-1/3}\left(\frac{\eta}{10^{-3}}\right)^{-1}\left(\frac{M_s}{M_\oplus}\right)^{2/3}, \tag{1.36}$$

where we have considered a Sun mass star. This illustrates well the weak point of pebble accretion, it is a quite inefficient mechanism requiring dust mass budgets that are generally an order of magnitude larger than the typical mass of giant planets' cores to allow their growth (see Lambrechts and Johansen 2014, for an estimate of the required dust mass). On the other hand, the low efficiency of pebble accretion implies that the dust mass flux would not be significantly reduced by an accreting core and therefore allows for the formation of multiple massive cores with basically the same mass budget as that required to grow a single core (although see Kretke and Levison 2014, Levison et al. 2015, for caveats). Moreover, the low efficiency of pebble accretion is compensated by the large mass flux provided by drifting grains. Considering a dust mass flux $\dot{M}_{\rm d} = 2\times10^{-4}\ M_\oplus\,{\rm yr}^{-1}$ (see section 1.2.2), the growth timescale of a giant planet's core, $\tau_{\rm growth} \equiv M_{\rm core}/\dot{M}_s$, would approximately be

$$\tau_{\rm growth} = \frac{M_{\rm core}}{\varepsilon_{\rm PA}\dot{M}_{\rm d}} \sim 2\times10^5\left(\frac{M_{\rm core}}{10\ M_\oplus}\right)^{1/3}\ \text{years}. \tag{1.37}$$

The growth of a giant planet's core should therefore be very fast in the 2D Hill regime of pebble accretion. The growth up to the mass when this regime applies might however be substantially longer, of the order of 1 My or so, and proceed initially through planetesimal accretion rather than pebble accretion (at least up to the mass of ~Ceres; Johansen et al. 2015, Johansen and Lambrechts 2017).

Pebble accretion does not proceed indefinitely, it is a self-limited process. Massive cores gravitationally perturb the gas disk in their surrounding and start carving a shallow gap in the gas distribution. At the outer edge of this gap, the pressure gradient is reversed so there exists a local pressure maximum (so-called pressure bumps) where the pressure gradient force vanishes and the gas therefore rotates at the Keplerian speed. This halts the radial drift of pebbles coming from the outer regions of the disk and put an end to the core growth. Following Johansen and Lambrechts (2017), the mass at which pebble accretion ends, the so-called isolation mass, can be estimated considering the first-order perturbation on the gas velocity induced by the gravitational pull of the core at a radial distance of H_g,

$$\Delta v_\mathrm{g} \sim \frac{GM_\mathrm{core}}{rH_\mathrm{g}\Omega_\mathrm{K}}. \tag{1.38}$$

Balancing this with the sub-Keplerian flow of the gas,

$$\eta v_\mathrm{K} \sim \left(\frac{H_\mathrm{g}}{r}\right)^2 \frac{\partial \ln P}{\partial \ln r} v_\mathrm{K}, \tag{1.39}$$

yields the isolation mass

$$M_\mathrm{iso} \sim \left(\frac{H_\mathrm{g}}{r}\right)^3 M_*. \tag{1.40}$$

Using 3D hydrodynamical simulations of a core embedded in a Keplerian disk, Lambrechts et al. (2014) actually find

$$M_\mathrm{iso} \approx 20 \left(\frac{h}{0.05}\right)^3 M_\oplus, \tag{1.41}$$

with $h \equiv H_\mathrm{g}/r$ and a solar mass central star was assumed. The cubic dependance on the aspect ratio h of the disc implies that in flared disks, where h is an increasing function of the orbital distance, isolation becomes harder to achieve in the outer parts of the disk. More recently, Bitsch et al. (2018) investigated the effect of disk's viscosity and pebble diffusion on the pebble isolation mass and showed that isolation would occur at masses 2–3 times larger than derived by Lambrechts et al. (2014) for high levels of turbulence. The dependence on the disk's aspect ratio nevertheless remains valid.

The first implication of the existence of a pebble isolation mass is the abrupt cut-off of the strong heating provided by the accretion of solids onto the core ($L_\mathrm{acc} = GM_\mathrm{core}\dot{M}_s/R_\mathrm{core}$). The pressure support of the envelope heated by the release of potential energy of the accreted material prevents its contraction onto the solid core and slows down the accretion of gas. Rapid gas accretion is triggered when the gravitational pull of the core overcomes the pressure support of the gaseous envelope which defines the critical core mass. If pebble accretion were to be a never ending process, Lambrechts et al. (2014) find that the critical core masses would be $\gtrsim 100\ M_\oplus$ between 5–30 au, which is an order of magnitude larger than the inferred core masses of the Solar System's planets (Guillot 2005). However, the abrupt termination of solid accretion, hence the quenching of the accretion luminosity, allows critical core masses to drop well below the pebble isolation mass. It results that when a core reaches the pebble isolation mass it will subsequently rapidly contract and accrete a massive gaseous envelope at a high pace. Lambrechts et al. (2014) argue this could be the origin of the divide between gas and ice giants. Due to the fact that isolation is harder to achieve at larger orbital distances, Uranus' and Neptune's core never reached the pebble isolation mass and could only attract a thin envelope of hydrogen and helium enriched in volatiles released by the sublimation of pebbles settling towards their core.

The second implication of the pebble isolation mass is that once a protoplanet reaches isolation, it cuts the flux of drifting pebbles and thus starves any protoplanet forming inward its orbit. Morbidelli et al. (2015a) proposed that Jupiter's core thereby starved the inner Solar System and prevented the terrestrial planets' embryos to grow beyond the mass of Mars. Further build-up of the terrestrial planets would therefore remain unchanged relative to traditional models and proceed through mutual embryos collisions after the dispersal of the protoplanetary gas disk.

As will be argued in the subsequent chapters of this thesis, *the cut-off in pebble accretion and their accumulation at the outer edge of the gap opened by a forming gas giant might have important implications for the formation of their satellites systems and challenges our current understanding of formation of moons.*

1.2.4 Dynamical evolution of the giant planets

An important aspect of the origin of planets and satellites and their architecture is their dynamical evolution, either as the objects are forming or at later times. It has been realized early on that gravitational interactions between a massive object such as a planet and a gaseous disk induce a torque that would modify the orbit of the former (Goldreich and Tremaine 1980). This process is known as planetary migration (it is more specifically known as type I migration, as opposed to type II which refers to migration of planets that have opened a gap in the disk) and within typical protoplanetary disks, where the density and the temperature are smooth functions of the orbital distance, the torque experienced by a planet is negative and the migration is radially inward (i.e., the semimajor axis of the planet shrinks; Tanaka et al. 2002). The migration timescale, $\tau_{\mathrm{I}} \equiv r/\dot{r}$, due to this effect was derived by Tanaka et al. (2002),

$$\tau_{\rm I} = \frac{1}{C_{\rm I}\Omega_{\rm p}}\left(\frac{M_\odot^2}{M_{\rm p}r^2\Sigma_{\rm g}}\right)h^2 \approx 5\times10^5\left(\frac{10\,M_\oplus}{M_{\rm p}}\right)\left(\frac{100\,{\rm g cm}^{-2}}{\Sigma_{\rm g}}\right)\left(\frac{h}{0.05}\right)^2\left(\frac{5\,{\rm au}}{r}\right)^{1/2}\ {\rm years}, \tag{1.42}$$

where $C_{\rm I} = 2.7 + 1.1{\rm q}$ in the case of isothermal disks with q the exponent of the radial dependence of the surface density of the disk, $\Sigma_{\rm g} \propto r^{-{\rm q}}$. The parameter $C_{\rm I}$ was nevertheless set to unity in deriving the above estimate of the migration timescale due to many uncertainties in the migration rates of planets. Paardekooper et al. (2010) find that the migration rates in adiabatic and optically thick disks are generally slower than in isothermal disks and also depend on the temperature profile of the disk. In any case, the above estimate shows that migration in the mass range of giant planets cores is fast and migration might therefore play a non-negligible role in the formation of the gas and ice giant planets.

As already pointed out in the previous section, more massive planets significantly perturb the gas distribution in their vicinity and this affects their migration rate. The common picture for migration of massive planets that have opened a gap in their disk (type II migration regime) is that they are locked in the gap and migrate as the disk viscously evolves on longer timescales than advocated in the case of type I migration (e.g., Lin and Papaloizou 1986). This might in fact be inaccurate as gas is still able to flow within the gap opened by a planet and the migration rate would decorrelate from the viscous evolution of the disk (Duffell et al. 2014, Dürmann and Kley 2015). In the case of low viscosity, particularly, the planet is likely to migrate faster than the viscous advection of the gas. This issue however remains controversial and type II migration rates might well be proportional to the disk's viscosity, although they should differ from the gas drift speed (e.g., Kanagawa et al. 2018, Robert et al. 2018).

Considering the currently inferred migration rates of planets, and even assuming type II migration proceeds at the viscous timescale, the cores of all four giant planets of the Solar System should have started their formation at radial distances of 15–25 au to account for their current masses and orbits (Bitsch et al. 2015b, Johansen and Lambrechts 2017). This would mean that they accreted in very different (chemical) environments throughout their history and that Jupiter and Saturn migrated over very wide orbital distances. However, as pointed out by Morbidelli and Raymond (2016), it is unclear in this case why massive planets would not have formed in the region between 5–10 au, where the building of core seeds would have probably been more efficient (as it procceeds through planetesimal accretion Johansen et al. 2015, Johansen and Lambrechts 2017), and migrated towards the inner Solar System. It should also be noted that the growth tracks of giant planets investigated in Bitsch et al. (2015b) consider isolated planets and the gravitational interactions among them are therefore not accounted for.

Another migration scenario has been proposed by Walsh et al. (2011), known as the Grand Tack. It is based on the fact that hydrodynamic simulations of Jupiter and Saturn mass planets together in a disk have shown that when the two planets are caught in their mutual 2:1 or 3:2 mean motion resonance (that is the configuration when the ratio of their orbital period is 2 and 1.5, respectively), they open a common gap in the disk and migrate together outwards (Masset and Snellgrove 2001, Morbidelli and Crida 2007, Pierens et al. 2014). Walsh et al. (2011) postulated that Jupiter could have migrated down to 1.5 au before being caught in resonance with Saturn and migrating outwards near its current position at the time the protoplanetary disk dispersed. The rationale for having Jupiter entering in the inner Solar System is that this would result in a depletion of planetesimals beyond 1 au from the Sun after Jupiter's tack, which seems a necessary condition to account for the fact that the mass of Mars is only 10 percent of that of the Earth and Venus (the mass and orbits of the terrestrial planets are best reproduced if they formed out of a narrow annulus at 0.7–1 au; Hansen 2009). Planetesimals initially residing from 1 to 13 au are scattered in all directions during the migration of the giant planets as shown in the simulations by Walsh et al. (2011). Therefore, during the outward motion of the planets, the asteroid belt region (between 1.8 and 3.2 au from the Sun) is populated with material originating from initially very different locations in the disk, thereby accounting for the presence of both anhydrous (the S-type spectral class asteroids, thought to originate from inside the orbit of Jupiter before its migration) and icy objects (the C-type asteroids, thought to originate from beyond Jupiter's orbit) in the main asteroid belt. Although this scenario is attractive because of the many features of the inner Solar System it can account for, it must however operate on a tight schedule as pointed out by Bromley and Kenyon (2017). Jacobson and Morbidelli (2014) showed that the timing of terrestrial planets accretion, and Mars particularly, is best reproduced if Jupiter tacks when the terrestrial embryos have grown to nearly Mars mass. Radio-isotope analysis suggest that Mars accreted half its mass in less than $\sim$2 Myr after the condensation of Calcium-Aluminum rich Inclusions (CAIs, typically assumed to be the birth-age of the Solar System) and neared completion $\sim$3–4 My after CAIs (Dauphas and Pourmand 2011), therefore constraining the timing of the tack at this same epoch. On the other hand, the outward migration of Jupiter and Saturn requires that the disk still contains substantial amount of gas. Wang et al. (2017) claim that the nebular gas (in the inner Solar System at least) had dispersed by $\sim$4 My after CAIs following from their analysis of paleomagnetism inside meteorites, which would leave a small window for the tack.

In a recent series of papers, Izidoro et al. (2016), Raymond and Izidoro (2017a,b),

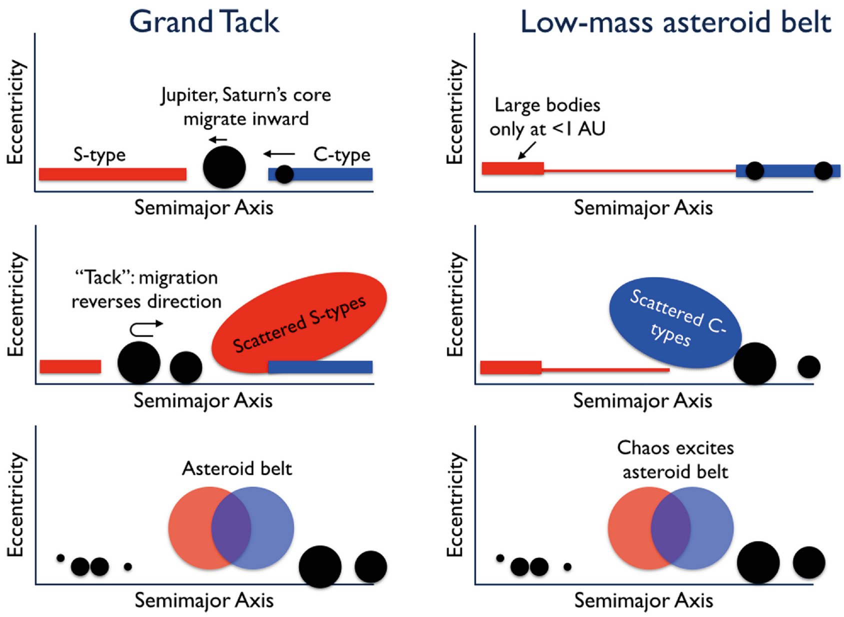

Figure 1.9: Sketch representation of possible architectures of the early Solar System and its dynamical evolution, from Morbidelli and Raymond (2016). *Left :* the Grand Tack hypothesis where the whole region inside of Jupiter's orbit is populated and the migration of the giant planets account for a later depletion beyond 1 au and mixing of objects in the asteroid belt. *Right :* the primordial depletion hypothesis where the asteroid belt region is populated by the mere growth of the terrestrial and giant planets.

showed that the structure of the asteroid belt could be reproduced without invoking the migration of Jupiter in the inner Solar System. The mere growth of the giant planets results in an efficient redistribution of the planetesimals located in their vicinity and the implantation of some of them in the asteroid belt region. The persistent inward migration of the planets (qualitatively consistent with the evolution of the giant planets proposed by Bitsch et al. 2015b) yields very similar results. The fact that the terrestrial planets grew from a narrow annulus of material could in fact reflect that planetesimals formation was not efficient throughout the inner Solar System (Drążkowska et al. 2016). The growth of terrestrial planets from such an annulus leads to the implantation of planetesimals in the asteroid belt. Therefore, the depletion of the asteroid belt might well have been primordial and this region was later populated with icy objects, due to the formation of the giant planets, and rocky objects, due to the formation of the terrestrial planets.

It therefore appears that the early dynamical evolution of the giant planets is largely unconstrained as their inward migration, inward then outward migration or no migration at all, could have resulted in roughly the same distribution of objects in the inner Solar System. To further discriminate among different scenarios, it will be necessary to consider the resulting distributions of more refined spectral classes of asteroids than just S- and C-type asteroids as those actually encompass a wide diversity of objects (DeMeo and Carry 2014, Vernazza et al. 2017). This would however require a better knowledge of the source regions of the different classes of asteroids. The regular and irregular satellites of the giant planets might help in providing additional constraints. In the subsequent chapters, we unveil a potential link between the regular satellites of Jupiter and some asteroids that would currently be located in the main belt but originated from just beyond Jupiter's orbit. Further analysis might allow one to better constrain the nature of these asteroids and the early history of the giant planets. Radio-isotopes and petrologic analysis of the meteorites collected on Earth, combined with thermal evolution models, also provide great constraints on the timing of accretion of different asteroids. Kruijer et al. (2017) recently inferred that Jupiter's core separated the reservoirs of inner, so called non-carbonaceous type objects, and outer carbonaceous type objects no later than ∼1 My after CAIs, thereby constraining the timing of formation of Jupiter's core and the source region of the parent bodies of carbonaceous meteorites (see the discussion in Chapter 4 for a potential link with the jovian satellites). Parent bodies of the most primitive meteorites collected on Earth are thought to have accreted ∼3 My after CAIs (e.g., Sugiura and Fujiya 2014) and large comets ∼4–5 My after CAIs to retain their volatiles (Mousis et al. 2017a) whereas some differentiated asteroids are likely to have accreted almost concurrently with CAIs. It results that, depending on their timing, early dynamical evolution of the giant planets could have affected some asteroids population but not others that would have formed later. Finally, the migration of planets in more realistic disk conditions, including the effects of non-ideal MHD terms, needs to be investigated as the picture could substantially depart from that found in viscous disks (McNally et al. 2017, 2018).

To end this section, we note that the current understanding of planetary migration predicts that the giant planets should have been in a more compact configuration right after their formation than what is observed today (due to the fact that more massive planets that are able to clear wide gaps migrate at slower rate than less massive planets). This does not constitute evidence against early migration of the giant planets however. Tsiganis et al. (2005), Gomes et al. (2005) and Morbidelli et al. (2005) presented a new framework for the dynamical evolution of the giant planets after the dispersal of the protoplanetary disk known as the Nice model. They showed that the gravitational interactions of the giant planets with a distant ring of planetesimals can spread the orbits of the giant planets–Uranus, Neptune and Saturn migrating outward as they scatter planetesimals whereas Jupiter migrates slightly inward. During this planetesimal driven migration, Jupiter and Saturn cross their mutual 2:1 mean motion resonance, increasing suddenly the eccentricity of Saturn, and the whole system becomes unstable for a short period of time. During this chaotic phase, the two ice giants are scattered outward following close encounters with Saturn and among themselves. In the end, starting from a compact configuration with nearly circular obits, the current semimajor axes, eccentricities and inclinations of the four giant planets are very well reproduced. This model has been subsequently revised to provide with better constraints on the initial configuration of the giant planets, including the existence of an additional ice giant (e.g., Nesvorný and Morbidelli 2012). Overall, this scenario can account for the capture of the trojan satellites of Jupiter (in co-orbital motion with their primary) and Neptune (Morbidelli et al. 2005, Nesvorný and Vokrouhlický 2009, Nesvorný et al. 2013), as well as the capture of the irregular satellites of the giant planets (Nesvorný et al. 2007), and the presence of very primitive objects (P- and D-type asteroids, that are very similar to the jovian trojans) in the main asteroid belt (Levison et al. 2009, Vokrouhlický et al. 2016). It is possible that trojan and irregular satellites populations have been captured prior to the Nice model instability but these would have been erased during the chaotic phase of evolution of the giant planets–which is unfortunate for better constraining the earlier evolution of the giant planets.

1.3 Organization of this manuscript

This thesis focuses on the investigation of the origin and conditions of formation of satellites systems that will be the targets of future space exploration missions, such as the JAXA MMX mission, aiming at returning a sample from one of the two martian moons, and the future ESA JUICE and NASA Europa Clipper missions that will both explore the Galilean moons orbiting around Jupiter.

Part of the work developed also has implications for our general understanding of moon formation around gas giant planets and the prospect of finding analogues to the Galilean moons outside of the Solar System.

Chapter 2 describes the main properties of the Galilean system of satellites orbiting around Jupiter, the main constraints available on their formation history and the prevailing theories for their origin.

Chapter 3 discusses pebble accretion in the Galilean system. A numerical code developed to follow the transport of particles embedded in a gaseous disk is presented and applied to a simple parametrization of a circum-jovian disk. We show that pebbles are able to reproduce the overall bulk composition of the Galilean moons in terms of their ice-to-rock mass ratio. This result is interesting because in an actively-supplied disk scenario for the origin of the moons, their growth is likely to proceed through pebble accretion. However, this raises some important questions. Given the low efficiency of pebble accretion, the mechanism of solids delivery to the circum-jovian disk must be efficient to allow for the formation of the massive Galilean moons. The origin of pebbles and initial seeds of the satellites also remains unclear in this framework.

Chapter 4 focuses on the important issue of the delivery of solid material to the circum-jovian disk. We revisit the delivery mechanism in the context of the pebble accretion scenario for the growth of giant planets as presented in the first chapter of this thesis. The dynamics of planetesimals that would originate from the accumulation of solids at the outer edge of the gap opened by Jupiter are investigated using N-body simulations. The decisive role of Saturn's formation nearby Jupiter on the delivery of planetesimals to the circum-jovian disk is evidenced. The overall redistribution of material induced by the two giant planets leads to the implantation of icy material in the asteroid belt located in between the current orbits of Mars and Jupiter, revealing a potential link between primitive asteroids and the Galilean moons. The implications for moon formation in extrasolar systems are also discussed.

Chapter 5 discusses the origin of the two martian moons, Phobos and Deimos. We show that the physical and spectral properties of the matian moons are consistent with their formation following a giant impact on Mars, similarly to the event that is believed to have given birth to the Moon. Overall, the giant impact scenario seems the only one able to account for both the observed spectra of the martian moons and their nearly circular and co-planar orbits in the equatorial plane of Mars.

Chapter 6 presents an application of the transport model described in Chapter 3 to the vertical transport of icy grains in the outer parts of the circumsolar disk and their irradiation by cosmic rays. The aim is to investigate the possible origin of molecular oxygen, detected at a high level in the coma of the comet 67P/Churyumov-Gerasimenko, from radiolysis of water ice. It is shown that the energy dose received by dust grains during the typical lifetime of a protoplanetary disk is too low to account for the high abundance of O_2 with respect to water detected in 67P/C-G. Radiolysis of water ice remains an interesting mechanism to account for the presence of molecular oxygen in comets but would have likely operated in the low density environment of the parent molecular cloud of the Solar System before its collapse.

Chapter 7 summarizes the results presented in the present manuscript and briefly discusses some open questions and possible future developments that might help in better understanding the history of the giant planets and the origin of their satellite systems.

Chapter 2

Conditions of formation of the Galilean satellites

2.1 Introduction

The Galilean moons constitute a remarkable system of satellites orbiting around Jupiter with nearly circular and coplanar orbits with respect to the planet's equatorial plane. The system also exhibits an outward decrease of satellite densities with inner rocky Io and outermost icy Callisto. These properties have long ago set the idea that the Galilean system is much like a miniature solar system, motivating the development of theories of giant planets' satellites formation within circumplanetary disks (hereafter, CPDs). We note that we refer here to CPDs as (mainly) gaseous accretion disks, as opposed to debris disks or planetary rings. Despite the early interest for the formation of satellites in CPDs, many uncertainties remain because of the wide range of processes involved, starting with the formation of the giant planets themselves. In this chapter, we review some of the early proposed models for the formation of satellites in CPDs as well as more recent developments.

2.2 Constraints on the formation of the Galilean system

A successful model for the origin of the Galilean moons must account for the basic properties of the system. One such of these is the fact that the four satellites have roughly similar masses (table 2.1). The most massive moon of the system, Ganymede, is about a factor of three more massive than Europa, the smallest of the four moons. The total mass of the system adds up to only a tiny fraction of the mass of Jupiter, that is $M_{\mathrm{T}} \approx 2.1 \times 10^{-4}\, M_{\mathrm{Jup}}$ (with $M_{\mathrm{Jup}} = 1,9 \times 10^{27}$ kg), which corresponds to approximately $6.7 \times 10^{-2}\, M_{\oplus}$. This is much smaller than the mass

	a (R_{Jup})	M_{sat} (M_{Jup})	R_{sat} (km)	ρ_{sat} (g cm^{-3})	$C/(MR^2)$
Io	5.9	4.7×10^{-5}	1822	3.53	0.378
Europa	9.4	2.5×10^{-5}	1565	2.99	0.346
Ganymede	15.0	7.8×10^{-5}	2631	1.94	0.312
Callisto	26.4	5.7×10^{-5}	2410	1.83	0.355

Table 2.1: data from Schubert et al. (2004)

ratio of the Earth-Moon system, the mass of the moon being $\sim 10^{-2}\,M_{\oplus}$. Assuming the Galilean satellites formed out of a material with solar composition (i.e., with a solid-to-gas mass ratio of 0.01), then a minimum mass of $\sim 0.02\,M_{\mathrm{Jup}}$ is required to build them. As described in the next section, all of this material might have been present at one time around Jupiter or it could have been processed through a longer timescale while Jupiter was still feeding from the circumsolar disk.

An important property of the Galilean system is its rather compact radial scale. Whereas the Hill sphere of Jupiter is approximately 744 R_{Jup} wide (where $R_{\mathrm{Jup}} \approx 7 \times 10^7$ m is the radius of Jupiter), the outermost Galilean satellite, Callisto, is orbiting at only 26 R_{Jup} from the planet. The radial extent of the system is also small compared with the typical size expected for the circum-planetary disk ($\sim 0.3\,R_{\mathrm{H}} \approx 220\,R_{\mathrm{Jup}}$; Tanigawa et al. 2012).

Another peculiarity of the Galilean system is the radially outward decreasing density of the moons (see Table 2.1). The density of Io, the innermost satellite, is compatible with that of an anhydrous body made of rock and metal. The somewhat lower density of Europa suggests that water makes up to ∼8% of its mass, whereas the low density of Ganymede and Callisto implies that these bodies are roughly half ice and half rock and metal. This is generally seen as a consequence of their formation in a CPD whose temperature decreased with distance to Jupiter. An implication is that the limit where water ice is stable (the so-called snowline) was located close to Ganymede's location during the formation of the satellites. The origin of Europa's low water content is however less clear (see next chapter). It could require a complicated interplay between its growth and migration and the cooling of the disk over time. Alternatively, Europa could have formed as ice rich as Ganymede and lost its water after its formation (with tidal heating being the main driver). If so, Io could also have formed with a non-negligible amount of water since subsequent loss should have been more efficient than in the case of Europa given that it dissipates even more tidal energy in its interior (see the discussion in Canup and Ward 2009).

Finally, an important constraint comes from the internal state of Callisto. The gravity data collected by the *galileo* spacecraft (orbiting around Jupiter from 1995 to 2003) allowed for the determination of the satellites' axial moments of inertia, C, as reported in table 2.1. This moment of inertia is related to the distribution of mass within a satellites (Hussmann et al. 2015),

$$C = \frac{8\pi}{3} \int_0^R \rho(r) r^4 dr, \tag{2.1}$$

with $\rho(r)$ the mass density as a function of the radial distance from the center of the body. The lower the value of the dimensionless moment C/MR, the more mass is concentrated toward the center of the body (i.e., the more the body is differentiated). The value for a perfectly uniform sphere is 0.4. In practice, due to compression effects, the value of the normalized moment of inertia for an undifferentiated body could be somewhat lower (≈0.38 for an object the mass of Callisto). The inferred moments of all three inner moons suggest that they are well differentiated, with an iron-rich core surrounded by a rocky mantle and an icy upper mantle in the case of Europa and Ganymede as well as a liquid water ocean underneath their icy crust (see Hussmann et al. 2015, for a review). Callisto, on the other hand, appears as largely undifferentiated (Anderson et al. 2001), although this interpretation might be erroneous if Callisto's interior is non-hydrostatic (e.g., Hussmann et al. 2015). This put constraints on its accretion history as ice melting due to energy deposited by the accreted material (and decay of short-lived radionuclides such as ^{26}Al) should be avoided. Barr and Canup (2008) find that Callisto's accretion timescale should be $\geqslant 5 \times 10^5$ years and must finish no earlier than $\sim$3 My after CAIs to satisfy this constraint. This timescale is very long compared with the orbital period at Callisto's radial distance which is approximately two weeks.

We describe in the next section the main theories for the origin of the Galilean moons which have been designed to fit the above mentioned constraints.

2.3 Formation in a circum-planetary disk

2.3.1 The Minimum Mass models

Early models for the formation of the satellites of giant planets considered Minimum Mass Subnebulae (MMSN) models, where the solid components of satellites are spread in a disk augmented by gas upon reaching a solar composition (e.g., Lunine and Stevenson 1982). These models therefore consider satellites' accretion in a closed system and rely upon the assumption that the appropriate initial conditions are matched at the termination of the parent planet's own accretion. Applied to a compact system such as the Galilean satellites, such models yield very dense, optically thick CPDs. To account for the icy composition of Ganymede and Callisto,

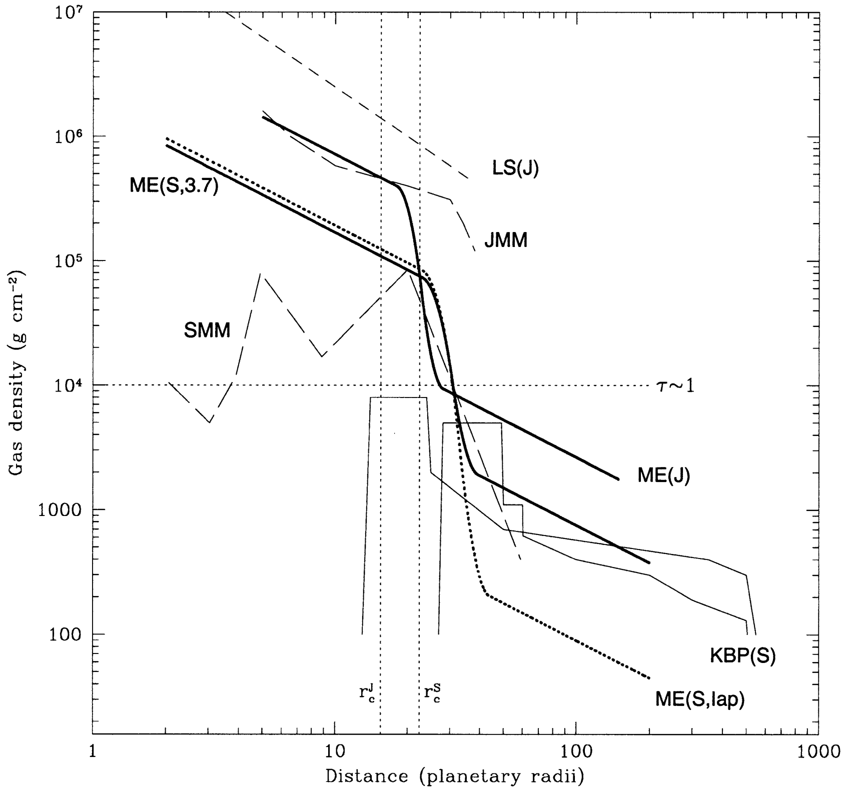

Figure 2.1: Figure extracted from Mosqueira and Estrada (2003a) showing the surface density profiles of their MMSN models for Jupiter, labelled ME(J), and Saturn, labelled ME(S) with two variations in the treatment of the outer disk, as well as the profiles used by several authors such as Lunine and Stevenson (1982), labelled LS(J), Korycansky et al. (1991), labelled KBP(S) and KBP(J) for their spin-out model of Saturn and Jupiter, respectively. Mosqueira and Estrada (2003a) indicate that the curves labelled JMM and SMM refer to minimum mass models of Pollack et al. (1994) for Jupiter and Saturn although no evidence for such models was found in the provided reference.

or that of Saturn's large satellite Titan, MMSN models hence require that the CPDs are almost inviscid and their opacity very low (e.g., grain-free opacity) to allow for the condensation of ices in the outer parts of the disk. Due to the short dynamical timescales found in CPDs, MMSN models generally yield a rapid assemblage of the satellites which might be difficult to reconcile with the observed only partially differentiated state of Callisto and Titan. The most recent MMSN model for the formation of the jovian and saturnian satellites was developed by Mosqueira and Estrada (2003a,b) and recently investigated with a population synthesis model by Miguel and Ida (2016). We present in the following the main aspects of their model and the results obtained by Miguel and Ida (2016).

One of the notable changes introduced by Mosqueira and Estrada is a two-component CPD characterized by an inner and dense disk, similar to that considered by Lunine and Stevenson (1982), and an extended and low density outer disk.

The motivation for such a two-component disk comes from an analysis of the angular momentum of the gas accreted by a forming giant planet. Before the opening of a deep gap in the circum-solar disk, it is assumed that the giant planet is accreting all of the material entering its Hill sphere (with radius $R_{\mathrm{H}} = a(M_{\mathrm{p}}/3M_{\odot})^{1/3}$, where a is the planet's semimajor axis, M_{p} its mass and $M_{\odot}$ the Sun's mass). The specific angular momentum of the accreted material relative to the planet is then approximately given by (Lissauer 1995)

$$j \approx -\Omega \frac{\int_0^{R_{\mathrm{H}}} 1.5x^3 dx}{\int_0^{R_{\mathrm{H}}} x dx} + \Omega R_{\mathrm{H}}^2 \approx \frac{1}{4}\Omega R_{\mathrm{H}}^2, \tag{2.2}$$

where $\Omega = (GM_{\odot}/a^3)^{1/2}$, and x is the difference in the semimajor axes of the planet and the accreted gas parcel. The first term of the above expression accounts for the specific angular momentum of the gas relative to the planet (Keplerian shear divided by the mass flux) and the second term arises from the consideration of a frame rotating with the planet. With conservation of angular momentum, the incoming material with specific angular momentum j will achieve centrifugal balance at a distance r_{c} of the planet defined by $r_{\mathrm{c}} = j^2/GM_{\mathrm{p}} \approx R_{\mathrm{H}}/48$. Considering a Jupiter mass planet at 5 au from the Sun, the above analysis gives $r_{\mathrm{c}} \sim 15\ R_{\mathrm{Jup}}$ (where R_{Jup} is Jupiter's current radius), which is a good match to Ganymede's current position. Mosqueira and Estrada (2003a,b) therefore argue for the existence of a dense inner disk out to the centrifugal radius and containing enough mass to build Io, Europa and Ganymede. On the other hand, Callisto, which is currently orbiting at a distance of $\sim$26 R_{Jup}, could not have formed within this disk. Hence, Mosqueira and Estrada (2003a) postulate the formation of an extended disk posterior to the opening of a gap by the giant planet. From this point, the authors assume that gas enter the Hill sphere of the planet at very small relative velocity so that the first term of eq. (2.2) becomes negligible and the specific angular momentum of the accreted material is then $j \sim \Omega R_{\mathrm{H}}^2$. This material would now attain centrifugal balance at a distance $r_{\mathrm{c}} \sim R_{\mathrm{H}}/3$ from the planet, which, applied to Jupiter, translates to a distance of $\sim$250 R_{Jup}. Because gas accretion may be substantially reduced after the opening of a wide gap by the giant planet, the outer disk would have a much lower surface density than the inner disk and contained just enough mass to build Callisto. Overall, Mosqueira and Estrada's MMSN model is thus characterized by a dense, optically thick (even considering gaseous opacity only) inner disk with gas surface densities typically exceeding 10^5 g cm^{-2} and an optically thin outer disk with surface densities in the range 10^2–10^3 g cm^{-2}. We note here that the use of gaseous opacity for the CPD was briefly justified in Mosqueira and Estrada (2003a,b) because of the potentially short coagulation timescales of dust grains resulting in very low grain opacity. The temperature was prescribed so that it allowed the condensation of ices (corresponding to $T \sim 250\,\mathrm{K}$ for the pressure ranges considered) at Ganymede's distance for the jovian CPD or Rhea's distance for the saturnian disk. The temperature profile is decreasing as $1/r$ in the optically thick disk while it is assumed constant and set to the surrounding nebular temperature in the optically thin outer disk. The surface density is also assumed to decrease as $1/r$ except for the so-called transitional region connecting the optically thick and thin regions of the CPD which exhibits a much steeper profile. The obtained surface density profiles are shown in Fig. (2.1).

Assuming that viscous dissipation is the dominant energy source term in the optically thick portion of the CPD, and knowing *a priori* the temperature and density profiles of the disk (as it is the case here), it is possible to determine the level of turbulence of the CPD (with the assumption that disk's viscosity is due to turbulence). In this case, the photospheric temperature of the disk would be given by

$$T_{\mathrm{e}}^4 = \frac{9\Omega^2}{8\sigma_{\mathrm{SB}}}\nu\Sigma_{\mathrm{g}} + T_{\mathrm{neb}}^4 \tag{2.3}$$

where Ω is the local Kepler frequency, σ_{SB} is Stefan-Boltzmann's constant, Σ_{g} is the gas surface density, T_{neb} the background nebular temperature and $\nu = \alpha c_s^2/\Omega$ is the disk's viscosity where α is a non-dimentional parameter measuring the level of turbulence of the disk (Shakura and Sunyaev 1973), and c_s is the (isothermal) sound speed. Using the temperature and density profiles prescribed for the CPDs and solving the above equation for α, Mosqueira and Estrada (2003a) find very weakly turbulent disks with $\alpha \sim 10^{-6}$–10^{-5}.

This very weak turbulent regime is a necessary ingredient to many aspects of the scenario proposed by Mosqueira and Estrada (2003a,b), such as the persistence of the steep surface density gradient between the inner and outer disks to stall Callisto's inward migration or the opening of a gap by the inner Galilean moons to allow their survival against rapid gas driven migration. Satellites' survival is indeed one of the main hurdles of MMSN models. Satellites embedded within gaseous disks will create spiral density waves at resonant locations known as the Lindblad resonances (e.g., Ward 1997, Goldreich and Tremaine 1980). Gravitational interactions with the density waves as well as with material located in the co-orbital region of the satellite will exert a generally negative torque on the satellite whose semimajor axis will therefore shrink. This process, known as type I migration, would act on very short timescales in dense environments such as that advocated by MMSN models. Canup and Ward (2002) estimate the type I migration timescale for Ganymede in a MMSN jovian CPD as

$$\tau_{\mathrm{I}} \approx \frac{1}{C_{\mathrm{I}}\Omega}\left(\frac{M_{\mathrm{p}}}{M_{\mathrm{s}}}\right)\left(\frac{M_{\mathrm{p}}}{r^2\Sigma_{\mathrm{g}}}\right)\left(\frac{c_s}{r\Omega}\right)^2$$
$$\sim 10^2 \text{ years}\left(\frac{3}{C_{\mathrm{I}}}\right)\left(\frac{2500\mathrm{km}}{R_{\mathrm{s}}}\right)^3\left(\frac{2\mathrm{gcm}^{-3}}{\rho_{\mathrm{s}}}\right)\left(\frac{c_s/r\Omega}{0.1}\right)^2$$
$$\left(\frac{3\times 10^5\mathrm{gcm}^{-2}}{\Sigma_{\mathrm{g}}}\right)\left(\frac{15R_{\mathrm{Jup}}}{r}\right)^{1/2},$$

where C_{I} is a factor of the order of unity (which depends on the disk's structure), M_{s} is the satellite's mass, R_{s} its radius and ρ_{s} its internal density. Such a short inward migration timescale implies that the satellites should form on even shorter timescales, but the satellites need also survive for the lifetime of the CPD. Clearly, to allow satellites' formation and survival in such environments require that either the CPD was quickly dissipated after satellites' formation or that the migration rate of the objects was substantially slowed down, if not completely stalled. At this point, it seems fair to note that planetary migration remains an uncertain mechanism (partly because of the lack of a clear picture on the structure and evolution of accretion disks) and the way it affected planetary formation still is an open question (e.g., Morbidelli and Raymond 2016). Nevertheless, a potential way to reduce the migration timescale of an object is the transition to the so-called type II migration regime which occurs if the planet (or satellite) is massive enough to open a gap in the disk (Lin and Papaloizou 1986). In this case, the object is in an equilibrium state at the center of the gap and its evolution is tied to that of the disk which takes place on the viscous timescale (see however Duffell et al. 2014, for a challenge of this picture). Here, the turbulence level, and hence viscosity of the disk, plays a central role because 1) gaps are more easily opened in low viscosity disks and 2) the viscous timescales are longer for lower viscosity. For the very low values of α derived by Mosqueira and Estrada (2003a), Io and Ganymede might have been massive enough to open a gap in the CPD (Mosqueira and Estrada 2003b). However, even in a very low viscosity environment, another criterion for gap opening is that a satellite's Hill radius should be larger than the disk scale height. Otherwise, large quantities of gas will enter the gap in the vertical direction and type II regime of migration would not apply. The latter criterion translates to

$$q_{\mathrm{s}} > 3\times 10^{-3}\left(\frac{h}{0.1}\right)^3, \tag{2.4}$$

where $q_{\mathrm{s}} = M_{\mathrm{s}}/M_{\mathrm{p}}$, and $h = H/r$ is the aspect ratio of the disk. This value is almost two orders of magnitude larger than that of the Galilean satellites, $q_{\mathrm{Gan}} \sim 8\times 10^{-5}$ and $q_{\mathrm{Io}} \sim 5\times 10^{-5}$. Even for a lower aspect ratio of 5%, which is more

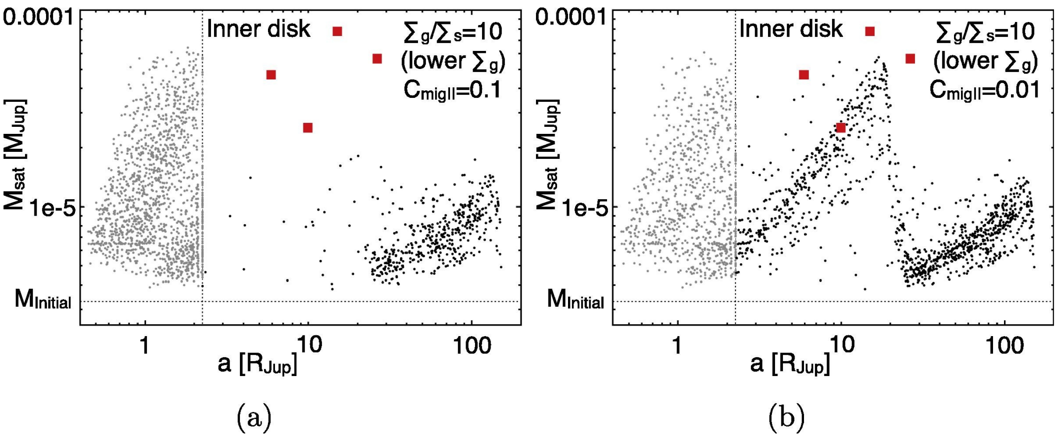

Figure 2.2: Figure extracted from Miguel and Ida (2016) showing the results of their population synthesis model using an MMSN disk with a heavy element composition that is enhanced by a factor of 10 over solar and a type II migration rate that is reduced by a factor of 10 (a) and 100 (b). Red squares indicate the position and mass of the current Galilean satellites. Black dots show the surviving satellites resulting from 100 simulations whereas gray dots are satellites that migrated to the inner boundary of the disk and are lost to Jupiter. A reduction of the migration rate allows for the survival of larger satellites in the region of the Galilean satellites but their architecture is not well reproduced. No satellites as massive as Ganymede or Callisto are formed while satellites with a mass comparable to Io's hardly survive in the inner disk.

appropriate for protoplanetary disks, the satellites would be almost an order of magnitude less massive than required to open a proper gap in the CPD. It should also be noted that even in the case where satellites would migrate in the type II regime, a non-viscous mechanism is still required to rapidly (as compared to the viscous timescale) dissipate the CPD to allow for the survival of the satellites. Perhaps a more promising mechanism to prevent satellites from falling onto Jupiter is the existence of an inner magnetic cavity that truncated the CPD (e.g., Sasaki et al. 2010). This possibility is further discussed in the following sections. As regards Callisto's migration history, Mosqueira and Estrada (2003a,b) envision a different picture motivated mainly by the fact that Callisto is not currently part of the resonant Laplace system characterizing Io, Europa and Ganymede. Mosqueira and Estrada (2003b) show that the type I torque experienced by a satellite would vanish at the transitional region of the CPD, therefore acting as a satellite trap. The persistence of the steep surface density gradient in this region hence would have prevented Callisto from entering the inner disk and would explain the current architecture of the Galilean system.

We now turn to the accretion of the satellites in an MMSN environment as envisioned by Mosqueira and Estrada (2003a) and investigated by Miguel and Ida (2016). Mosqueira and Estrada argue for the accretion of satellites by the combination of two mechanisms, the sweep-up of dust and rubble piles entrained with the gas flow followed by the accretion of larger satellitesimals drifting inward through gas drag. They find that the sweep-up timescale is shorter than the drift timescale for any particle size located within a distance of $\sim$38 R_{Jup} from Jupiter, thus promoting the formation of large seeds ($\sim$1000 km in size). Growth up to satellite size is then determined by the rate at which gas drag can bring larger satellitesimals to the feeding zone of the seed. Under such circumstances, Ganymede would form on a 10^3–10^4 year timescale, while Callisto, which feeds from the more extended reservoir provided by the outer disk, would form on a 10^5–10^6 year timescale. The study of Mosqueira and Estrada (2003a,b) remains qualitative and though a lot of processes are discussed in their papers, they did not perform an explicit integration of satellites' accretion and their orbital evolution. It is therefore not clear that the initial conditions advocated by their MMSN model would actually result in a system of Galilean like satellites. The first investigation of satellites formation in the Mosqueira and Estrada MMSN model has been recently undertaken by Miguel and Ida (2016).

These authors used a population synthesis model to study the influence of various parameters on the architecture of the formed systems. Their model assumes that satellites' seeds have already formed and are randomly injected in the disk to follow their growth and orbital evolution as they feed from the satellitesimals' disk and migrate. Miguel and Ida (2016) varied the dissipation timescale of the CPD from 10^4 to 10^6 years, the size of the satellitesimals from 1 to 30 km, the rate of type II migration (by artificially slowing down migration by a factor 0.1–0.01), as well as considering solids enhancement over solar composition by either adding solids or removing gas. The surface density of the satellitesimals' disk evolves due to accretion by the seeds and gas drag. They find that the lifetime of the satellitesimals' disk range from 10^2 to 10^3 years for sizes of 1 and 30 km, respectively. Therefore, larger satellitesimals are preferred as they give more time to the satellites to grow. However, the competition between the CPD's dispersal and the satellites' migration does not favor the formation of Galilean like satellites. Satellites formed in the inner regions of the disk rapidly migrate inward so that both a reduction of their migration rate and a rapid dispersal of the CPD are required to allow for their survival. On the other hand, such requirements do not allow for the formation of massive satellites in the outer disk such as Ganymede and Callisto (generally requiring long dispersion timescales of the CPD). Overall, Miguel and Ida (2016) find that migration rate 100-times lower than the nominal value and enhancement of the solid budget of the disk favor the formation and survival of Galilean like satellites but allowing for both the survival of the inner satellites and the formation of massive outer satellites is complicated (see Figure 2.2). It results that even with tuned initial conditions and artificial reduction of the satellites' orbital migration, accounting for the architecture of the current Galilean system is not straightforward in a MMSN model.

2.3.2 The Gas Starved model

Considering that the short migration and accretion timescales of satellites in MMSN models are difficult to reconcile with the properties of the Galilean moons, Canup and Ward (2002) proposed a new framework for satellites' accretion in a low density environment known as the gas-starved model. Contrary to MMSN models which consider that the CPD is a closed system, Canup and Ward (2002) investigate the conditions of accretion of satellites in an actively supplied CPD where Jupiter is still accreting material from the circumsolar disk. Because fresh material is constantly supplied to the CPD over time, it needs not contain all the necessary material to form the Galilean satellites at one time. The satellites could therefore form in lower density (and low temperature) environments where they would migrate on much longer timescales than in the MMSN models. Another argument put forward by Canup and Ward (2002) in favor of satellites' formation while Jupiter is still accreting is that given the short collision timescale among objects in the CPD (due to the short orbital periods), it would be difficult to explain that satellite accretion would "wait" until gas inflow to Jupiter had completely stopped. It should also be noted that the opening of a gap by a Jupiter mass planet does not necessarily shut down its accretion as material would still be able to enter its Hill sphere in the vertical direction (e.g., Morbidelli et al. 2014), contrary to what Mosqueira and Estrada (2003a,b) postulate. The approach of Canup and Ward (2002) also differs from MMSN studies in the sense that instead of trying to define the best initial conditions for the formation of the Galilean moons, they try to define the CPD's structure according to some important quantities that are regarded as free parameters and investigate the implications for the formation of satellites.

Canup and Ward (2002) derive a steady-state solution for the surface density of a CPD with a size r_d where material is uniformly deposited from the inner boundary of the CPD out to the centrifugal radius r_c (see Figure 2.3 for an illustration) :

$$\Sigma_g(r) = \frac{\dot{M}_\mathrm{p}}{3\pi\nu} \begin{cases} 1 - \frac{4}{5}\sqrt{\frac{r_\mathrm{c}}{r_\mathrm{d}}} - \frac{1}{5}\left(\frac{r}{r_\mathrm{c}}\right)^2 & \text{for } r \leqslant r_\mathrm{c} \\ \\ \frac{4}{5}\sqrt{\frac{r_\mathrm{c}}{r}} - \frac{4}{5}\sqrt{\frac{r_\mathrm{c}}{r_\mathrm{d}}} & \text{for } r > r_\mathrm{c}, \end{cases} \tag{2.5}$$

where $\dot{M}_\mathrm{p}$ is the mass accretion rate onto the planet and ν is the viscosity of the disk parameterized using the α turbulent model. The photospheric temperature of the disk is calculated using an equation similar to equation (3.18) and is related to

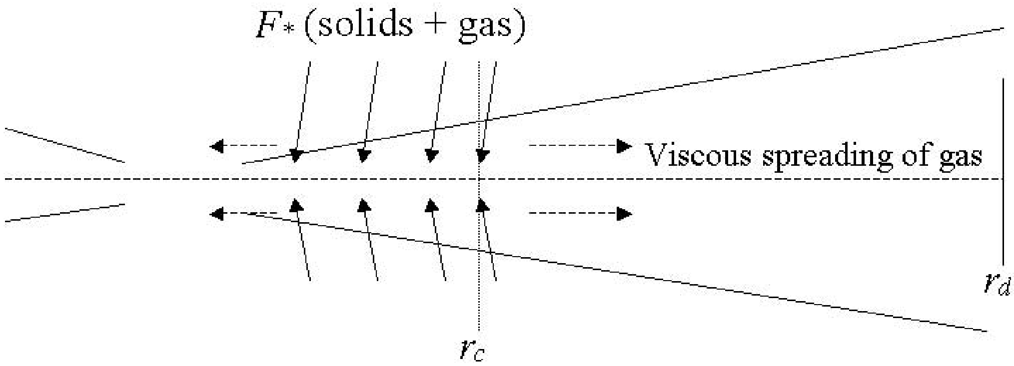

Figure 2.3: Sketch of the CPD model considered in Canup and Ward (2002). A mixture of gas and solids with some characteristic specific angular momentum is delivered to the CPD within a region extending from the surface of the planet out to the centrifugal radius $r_{\rm c}$. The solids are envisioned to rapidly grow up to decoupling sizes such that they mainly remain in the region inside the centrifugal radius. Gas, on the other hand, viscously spread both onto the planet and out to the outer edge of the disk at some distance $r_{\rm d}$.

the midplane temperature $T_{\rm m}$ through

$$T_{\rm m} \cong \left\{1 + \frac{3}{2}\left[1 - \left(\frac{T_{\rm neb}}{T_{\rm e}}\right)^4\right]\tau\right\}^{1/4} T_{\rm e}, \tag{2.6}$$

where $\tau \equiv \kappa\Sigma_{\rm g}$ is the disk's vertical optical depth and κ is the opacity which is assumed to be constant throughout the disk. It is interesting to note that in the case of an actively supplied CPD in steady-state, the photospheric temperature is independent of the gas surface density and the disk's viscosity and hence on the choice of the α parameter. This is due to the fact that in a steady state, the product of the surface density by the viscosity is directly related to the mass accretion rate $\dot{M}_{\rm p}$, as can be inferred from equation (2.5). Thus, for an optically thin disk, the temperature profile is determined by the mass accretion rate. For optically thick disks, however, the choice of α and κ would affect the midplane temperature through the optical depth τ.

Figure (2.4) shows surface density and temperature profiles of the CPD for a mass accretion rate $\dot{M}_{\rm p} = 2 \times 10^{-7}\ M_{\rm Jup}\,{\rm yr}^{-1}$, $\alpha = 5 \times 10^{-3}$ and $\kappa = 10^{-4}\ {\rm cm}^2\,{\rm g}^{-1}$, and a disk size $r_{\rm d} = 150\ R_{\rm Jup}$ and centrifugal radius $r_{\rm c} = 30\ R_{\rm Jup}$. For the parameters adopted, the surface density peaks at $\sim\!10^3\ {\rm g\,cm}^{-2}$, orders of magnitude lower than in MMSN models. For the adopted accretion rate, considering that the system of Galilean satellites possesses a total mass of $\sim 2 \times 10^{-4}\ M_{\rm Jup}$ and if the inflowing material was of solar composition (i.e., the dust-to-gas mass ratio was 10^{-2}), a mass of solids equivalent to that of the satellites would have been brought to the CPD in $\sim\!10^5$ years. Similarly to the MMSN models however, the use of the low gaseous opacity is necessary to allow for water ice to be stable in the region of

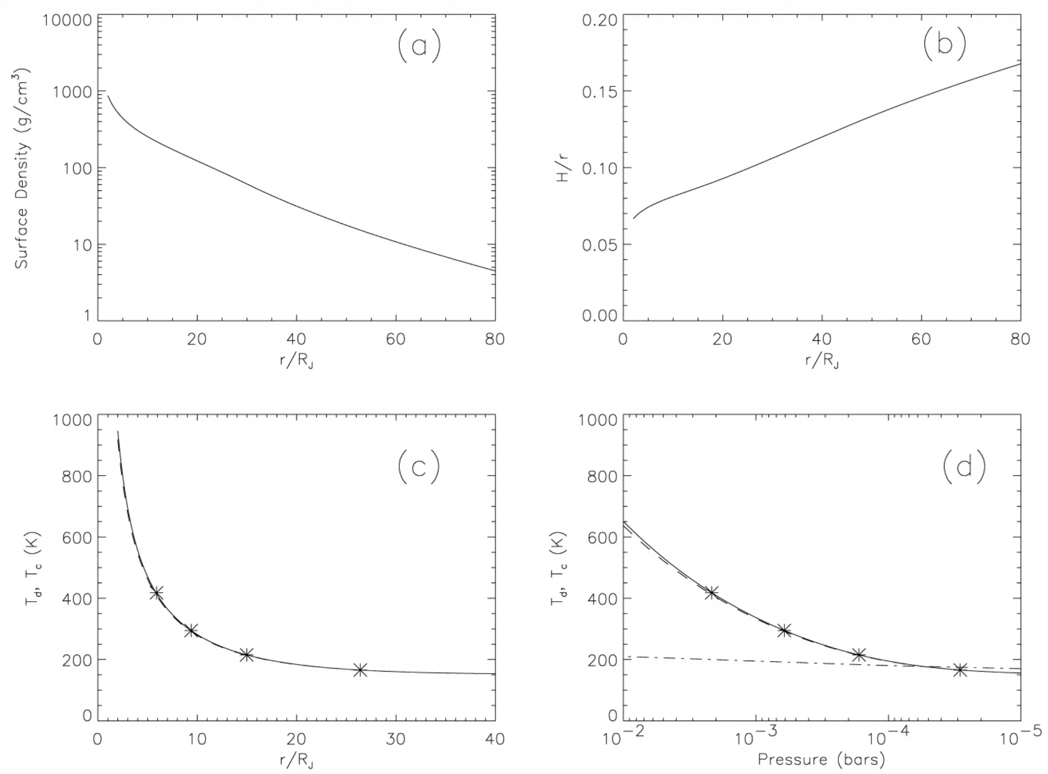

Figure 2.4: Figure extracted from Canup and Ward (2002) showing (a) the surface density, (b) aspect ratio, (c) temperature and (d) temperature vs. pressure profiles of a CPD obtained with $\dot{M}_\mathrm{p} = 2 \times 10^{-7}\ M_\mathrm{Jup}\,\mathrm{yr}^{-1}$, $\alpha = 5 \times 10^{-3}$ and $\kappa = 10^{-4}\ \mathrm{cm}^2\,\mathrm{g}^{-1}$. Disk midplane and photospheric temperatures are shown by the solid and dashed lines, respectively. Stars show the current position of the Galilean satellites. The dot-dashed line in (d) shows the water ice stability curve. For the adopted parameters, the disk is optically thin even in the region of the regular satellites so that the midplane and effective temperatures are similar and independent of α.

the outer satellites. If the absorption by micron and submicron sized grains were to be important, the opacity of the disk would have been substantially higher with $\kappa \sim 10^{-1}$–$1\ \mathrm{cm}^2\,\mathrm{g}^{-1}$. In this case, the CPD would be optically thick in the region of the regular satellites and its midplane temperature $\gtrsim 200$ K even for substantially lower accretion rates.

In the gas-starved model, the radial extent of the Galilean system is accounted for by assuming that solids are delivered to the CPD as they are entrained with the inflowing gas. Therefore, the initial solids should be brought in the form of small dust grains that couple with the gas in the circumsolar disk and then rapidly grow up to decoupling sizes within the CPD to prevent their viscous spreading, resulting in satellitesimals remaining in the region enclosed by the centrifugal radius. Canup and Ward (2002) argue that any solids with sizes $\lesssim 1$ m would effectively couple with the gas and be delivered to the CPD. However, their criterion is more appropriate to marginal coupling and perfect coupling with the gas flow would rather imply solids with sizes $\lesssim 0.1$ mm. This more restrictive size range could have severe implications for the proposed scenario that will be further discussed in the subsequent chapters.

Based on the above framework, Canup and Ward (2006) investigated the growth of Galilean satellites in an evolving CPD where $\dot{M}_\mathrm{p}$ decreases over time. In a gas-starved CPD, the growth timescale of a satellite would be regulated by the time necessary to deliver an amount of solids M_s to a satellite's feeding zone. Canup and Ward (2006) find this timescale can be approximated as

$$\tau_\mathrm{acc} \approx \left(\frac{\Sigma_\mathrm{g}\pi r_\mathrm{c}^2}{f\dot{M}_\mathrm{p}}\right)\left(\frac{M_\mathrm{s}}{4\pi r H \Sigma_\mathrm{g}}\right)^{4/5}, \tag{2.7}$$

where f is the dust-to-gas mass ratio of the inflowing material. The accretion timescale depends inversely on the distance from Jupiter (contrary to accretion in a system with a fixed mass where the orbital timescale regulates growth), with $\tau_\mathrm{acc} \propto r^{-4/5}$, because outer satellites have a larger surface area to collect material. A satellite will effectively grow up to a mass m_crit for which $\tau_\mathrm{acc} \sim \tau_\mathrm{I}$, i.e., the timescale for further growth is comparable to the type I migration timescale. From Canup and Ward (2006), this critical mass corresponds to

$$\frac{m_\mathrm{crit}}{M_\mathrm{Jup}} \approx 5.4\left(\frac{\pi}{C_\mathrm{I}}\right)^{5/9}\left(\frac{H}{r}\right)^{26/9}(\alpha f)^{2/3}\,(\Omega\tau_\mathrm{G} f)^{1/9} \tag{2.8}$$

$$\approx 5.6\times10^{-5}\chi\left(\frac{3.5}{C_\mathrm{I}}\right)^{5/9}\left(\frac{h}{0.1}\right)^{26/9}\left(\frac{r/r_\mathrm{c}}{0.5}\right)^{10/9}\left(\frac{\alpha f}{3\times10^{-5}}\right), \tag{2.9}$$

where $\chi = [(1\ \mathrm{week}/(2\pi/\Omega))(\tau_\mathrm{G}/10^7\ \mathrm{years})]^{1/9}$ and $\tau_\mathrm{G} = M_\mathrm{Jup}/\dot{M}_\mathrm{p}$ is Jupiter's growth timescale, and m_crit is comparable to the masses of the Galilean satellites for reasonable choices of parameters. The type I migration timescale is generally shorter than τ_G, especially in the early stages when the CPD is denser, so that many satellites would form and be lost to Jupiter. Canup and Ward (2006) argue that the competition between formation of satellites and their loss through inward migration set the mass ratio between the satellites systems and their primary, which is $\sim 10^{-4}$ for Jupiter, Saturn and Uranus. As accretion onto Jupiter wanes, the surface density of the CPD decreases and the type I migration timescale lengthens. The Galilean satellites we see today would therefore be the last surviving satellites that formed around Jupiter. Earlier generations would mainly consist of rocky moons due to the higher temperature of the CPD, whereas in the waning disk, ice could have been stable beyond Ganymede's current orbit.

There exist some variations of the Canup and Ward (2002, 2006) scenario, and notably the work by Sasaki et al. (2010) which introduces two important changes with respect to the original gas-starved model. Firstly, Sasaki et al. (2010) argue that the opening of a gap by Jupiter, combined with the short viscous timescale of the CPD (for values of $\alpha \sim 10^{-2}$–10^{-3}), abruptly depleted the CPD and the subsequent evolution of the satellites was "frozen" at that time. Such an assumption provides a connection with MMSN models since after Jupiter opened up a gap in the circum-solar disk, the satellites evolved in a closed system in their scenario. Secondly, Sasaki et al. (2010) argue for the existence of a magnetic cavity that truncated the CPD. The truncation of the disk can act to halt the migration of the satellites at the edge of the cavity (e.g., Ogihara et al. 2010, Liu et al. 2017), preventing them from falling onto Jupiter and favoring the formation of resonant chains (Ogihara and Ida 2012). The existence of a magnetic cavity around Jupiter is uncertain and has been postulated as an analogy with young T Tauri stars around which such cavities are inferred. Jupiter could have opened up a magnetic cavity if the magnetic coupling with its CPD was strong enough to allow for efficient transfer of angular momentum. The existence of the cavity therefore relies upon the strength of young Jupiter's magnetic field and the ionization level of the inner CPD. Nevertheless, the magnetic cavity might well be needed (at some point) to account for the subcritical rotation rate of Jupiter and giant planets in general (Takata and Stevenson 1996, Batygin 2018). If Jupiter could sustain a magnetic cavity at the time of accretion of its satellites but Saturn couldn't (because of e.g., a colder environment and a weaker magnetic field), it might explain the different architectures of their satellites system according to Sasaki et al. (2010).

2.4 Concluding remarks

The proposed scenarios for the formation of the Galilean satellites in a circum-planetary disk are mainly constrained by the observed properties of the moons. The presence of water ice as a main constituent of Ganymede and Callisto (and their survival against inward migration) constrains the structure of the gaseous disk at the time of accretion of the moons. The inferred only partially differentiated state of Callisto, on the other hand, constrains the accretion timescale of the moons and thus the structure of the satellitesimal disk out of which they accreted.

The gas-starved model developed by Canup and Ward (2002, 2006) has received more attention than MMSN models and has been well accepted as a plausible scenario for the formation of the Galilean satellites. Both semi-analytical (Alibert et al. 2005, Sasaki et al. 2010) and N-body (Canup and Ward 2006, Ogihara and Ida 2012) investigations of the accretion of satellites in this framework showed the ability of the model to produce Galilean like systems for reasonable choices of the mass accretion rate onto Jupiter and turbulence level of the disk.

However, these investigations suffer from important limitations. Whereas it is envisioned that the CPD is fed with small dust grains entrained with the gas flow, all the investigations performed so far assume that satellites' growth proceed through the accretion of large satellitesimals aerodynamically decoupled from the gas. In the N-body simulations of Canup and Ward (2006) and Ogihara and Ida (2012), the inflow of solid material is mimicked by adding particles with masses 10^{-8}–10^{-6} $M_{\rm Jup}$ to the CPD. For objects with densities of 2 $\rm g\,cm^{-3}$, this corresponds to sizes of $\sim$100–600 km. In the study by Sasaki et al. (2010), the size of the satellitesimals is not specified but they are considered as fully decoupled from the gas and are only removed due to accretion by simulated satellites' seeds while constantly replenished with the gas inflow. This results in a pile-up of the solid components in the CPD whose solid-to-gas mass ratio is increased by one to two orders of magnitude over the simulated timescales. Given our current understanding of dust evolution in gaseous disks (see section 1.2.2), we can reasonably consider that these are in fact poor descriptions of the evolution of the system in an actively-supplied CPD. The fragmentation and drift of dust grains limit their growth to Stokes number that are generally below unity which implies a rapid depletion of solids through radial drift. The growth of satellites is therefore most likely to proceed through pebble accretion in a gas-starved framework (section 1.2.3). This will be discussed in the next chapter.

Another questionable point of the gas-starved model is the assumption that the inflowing material has a solar dust-to-gas mass ratio. The current picture of the formation of giant planets implies a cut-off in the accretion of solids after the completion of its core, much earlier than the late stages when the satellites would accrete. The flow structure around an accreting gas giant found in hydrodynamical simulations is also hinting towards the accretion of dust depleted material in the late stages of its growth (e.g., Tanigawa et al. 2012). This could have dramatic implications for the global picture of satellites formation around jovian planets. This is discussed more thoroughly in Chapter 4 where a new scenario for the delivery of solid material to the circum-jovian disk is presented.

Chapter 3

Pebble accretion in the Galilean System

3.1 Introduction

One of the peculiar characteristics of the Galilean system is the radial gradient in the mean density of the satellites which suggests an increasing water mass fraction of the moons with increasing orbital distance. The inferred bulk composition of the innermost satellite, Io, and that of the two outer satellites, Ganymede and Callisto, is consistent with their formation inward and outward of the snowline, respectively (e.g., Lunine and Stevenson 1982, Mosqueira and Estrada 2003a, Canup and Ward 2002, Mousis and Gautier 2004). However, the origin of the low water content of Europa (∼8% by mass) remains more elusive. An intriguing possibility is that the overall compositional gradient is due to post-formation processes such as outgassing driven by dissipation of tidal energy in the interiors of the satellites. In this case, both Io and Europa could have started from a composition similar to that of Ganymede and Callisto and lost their volatiles over time. However, given the inferred values of tidal energy dissipated within Europa, efficient loss of water would require that all the available heat goes into the vaporization of water in localized "hot spots", which seems rather unlikely (Canup and Ward 2009) although detailed studies are currently lacking.

Therefore, Europa's water content is generally seen as the result of the accretion of the satellite both inward and outward of the snowline, in proportions averaging out to its current composition (e.g., Canup and Ward 2009). This could be due to i) the migration of Europa inward of the snowline during its growth, ii) the progressive cooling of the CPD and hence inward migration of the snowline during the satellite's formation or iii) an interplay between the two mechanisms (Alibert et al. 2005, Sasaki et al. 2010, Ogihara and Ida 2012). Detailed investigations of these hypotheses remain limited by the current understanding of the structure of disks and their evolution as well as that of migration of the satellites.

Dwyer et al. (2013) investigated the evolution of the ice/rock ratio of accreting satellites using N-body simulations in a gas-starved framework (Canup and Ward 2002, 2006, Sasaki et al. 2010). They find that reproducing the steep compositional gradient among the Galilean satellites is very difficult and that their Io and Europa analogues accrete substantial amounts of ice during their growth. However, N-body simulations are limited to the investigation of large satellitesimals although it is envisioned that the CPD is replenished by inflowing material carrying small and aerodynamically coupled dust grains during satellites growth. The whole picture of the accretion of the satellites might in fact be different in an actively-supplied disk.

In the following, the evolution of solid particles of different sizes embedded in a circum-jovian disk is presented. The dynamical evolution of the solids take into account the effects of aerodynamic drag and turbulent transport. The evolution of the surface temperature is also tracked along with the sublimation of water ice, thereby allowing to follow the ice/rock ratio of the objects which is compared to the corresponding values inferred for the satellites. We show that pebbles could provide a good match to the overall composition of the satellites and can account for the low water content of Europa. We argue that satellites growth in a gas-starved scenario would in fact proceed through pebble accretion (rather than satellitesimal accretion) and derive the expected grain sizes, pebble accretion efficiencies and accretion timescales of the satellites in the CPD.

3.2 Methods

The details of the particle transport model are presented below. The CPD's surface density is given by equation 2.5 and the temperature profile is given by

$$T_{\rm d} \approx 225 \left(\frac{r}{10\,R_{\rm Jup}}\right)^{-3/4} \left(\frac{\dot{M}_{\rm p}}{10^{-7}\,M_{\rm Jup}\,{\rm yr}^{-1}}\right)^{1/4}\,{\rm K}, \tag{3.1}$$

which was derived assuming an optically thin disk to avoid complications due to the uncertain opacity of the CPD (Sasaki et al. 2010). The derivation of the gas radial and azimuthal velocities, based on the study by Takeuchi and Lin (2002), is described as well as the particle tracking model which is based on the work by Ciesla (2010, 2011).

3.2.1 Gas dynamics

As we are interested in the transport of solids within a gaseous disk, it is important to consider the velocity field of the gas. For simplicity, we assume that the gas is in hydrostatic equilibrium in the vertical direction and the gas has no vertical velocity. In the radial direction however, the generally outward pressure gradient force causes the gas to rotate at a slightly subkeplerian velocity. The equation of motion of a gas parcel in the radial direction is given by

$$r\Omega_g^2 = \frac{GMr}{R^3} + \frac{1}{\rho_g}\frac{\partial P}{\partial r}\,, \tag{3.2}$$

where Ω_g is the rotation frequency of the gas, M is the mass of the central object and R is the distance of the gas parcel from this object. Assuming $P = c_s^2\rho_g$, this gives the well known relation for the gas orbital velocity $v_{\phi,g}$ (see e.g., Weidenschilling 1977)

$$v_{\phi,g} \equiv v_{\mathrm{K}} - \eta v_{\mathrm{K}} \approx v_{\mathrm{K}} + \frac{1}{2}\frac{c_s^2}{v_{\mathrm{K}}}\frac{\partial \ln P}{\partial \ln r}\,, \tag{3.3}$$

where v_{K} is the keplerian orbital velocity and η is a measure of the gas pressure support.

The radial velocity of the gas can be inferred from the azimuthal momentum equation of the viscous gas,

$$\rho_g v_{r,g}\frac{\partial}{\partial r}(r v_{\phi,g}) = \frac{1}{r}\frac{\partial}{\partial r}(r^2 T_{r\phi}) + \frac{\partial}{\partial z}(r T_{\phi z})\,. \tag{3.4}$$

where $T_{r\phi}$ and $T_{\phi z}$ are the shear stresses expressed as (e.g., Takeuchi and Lin 2002)

$$T_{r\phi} = r\nu\rho_g\tfrac{\partial\Omega_g}{\partial r} \quad \text{and} \quad T_{\phi z} = r\nu\rho_g\tfrac{\partial\Omega_g}{\partial z}\,. \tag{3.5}$$

Equation 3.4 directly yields the expression for the radial velocity of the gas :

$$v_{r,g}(z) = \left[\frac{\partial}{\partial r}(r^2\Omega_g)\right]^{-1}\left[\frac{1}{r\rho_g}\frac{\partial}{\partial r}\left(r^3\nu\rho_g\frac{\partial\Omega_g}{\partial r}\right) + \frac{r^2\nu}{\rho_g}\frac{\partial}{\partial z}\left(\rho_g\frac{\partial\Omega_g}{\partial z}\right)\right], \tag{3.6}$$

where we used the fact that $v_{\phi,g} = r\Omega_g$ and replace the shear stresses by their expressions.

The gas density in the vertical direction assuming hydrostatic equilibrium is given by

$$\rho_g(r,z) = \rho_0(r)e^{-\frac{z^2}{2H_g^2}}\,, \tag{3.7}$$

with

$$\rho_0(r) = \frac{\Sigma_g}{\sqrt{2\pi}H_g}\,. \tag{3.8}$$

This set of equations allows to determine the radial velocity of the gas flow as a function of the distance to the planet and height above the disk midplane. Note that the density-weighted average of equation 3.6 over z results in the mean

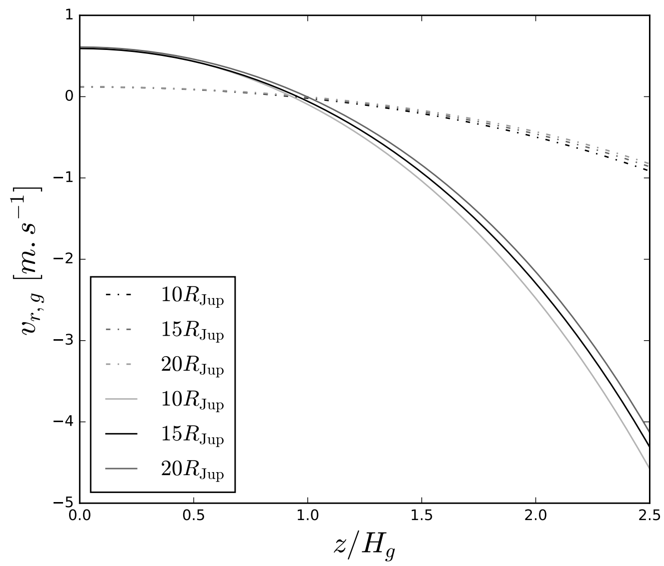

Figure 3.1: Radial velocity profiles of the gas as a function of the height above the midplane at different distances from Jupiter. Solid and dashed lines correspond to profiles calculated with $\alpha = 1 \times 10^{-4}$ and 5×10^{-4}, respectively.

accretion flow velocity $v_{\rm acc}$ derived by Lynden-Bell and Pringle (1974),

$$v_{\rm acc} = -\frac{3}{\Sigma_g r^{1/2}} \frac{\partial}{\partial r} (\nu \Sigma_g r^{1/2}) \,. \tag{3.9}$$

Figure 3.1 represents the radial velocity vertical profiles calculated at different distances from Jupiter and for different values of α. The velocity profiles are poorly influenced by the distance from the central planet. Instead, they strongly depend on the disk's viscosity where higher levels of turbulence result in larger velocities (both inward and outward) and consequently faster evolution of the disk. The velocities are small and slightly positive (outward) close to the midplane while at greater heights, namely in the less dense parts of the disk, they become larger and negative (inward). Such profiles have already been detailed in several studies of protoplanetary disks (PPDs) (e.g., Takeuchi and Lin 2002, Keller and Gail 2004, Ciesla 2009). It should be noted that such velocity profiles have not been found in turbulent simulations of disks (Fromang et al. 2011) because the Magneto-Rotational Instability (MRI), which is the source of turbulence in these simulations, results in non-uniform effective viscosity in the vertical direction. Also, the turbulence driven evolution of disks has been highly questioned in the recent years and PPDs as well as CPDs might in fact not be viscously evolving (see Turner et al. 2014, for a review on angular momentum transport processes). However, the outward radial velocity in the midplane of CPDs has been evidenced in several 3D hydrodynamic simulations (Tanigawa et al. 2012, Klahr and Kley 2006) as well as in MHD simulations (Gressel et al. 2013) and Batygin (2018) even describes CPDs as de-cretion disks. It is therefore unclear, given the current knowledge of the structure of CPDs and PPDs, whether or not the radial velocity profiles derived here are realistic.

3.2.2 Particles dynamics and thermodynamics

The lagrangian integrator developed to investigate the transport of solids in disks is described in the following. The model includes the effect of gas drag and turbulent diffusion on the evolution of solid particles. Because solids are not pressure supported, they rotate at keplerian velocities and feel a headwind due to the slightly sub-keplerian motion of the gas. Solids therefore transfer angular momentum to the gas via friction forces on a timescale called the stopping time of the particle t_s. This quantity generally depends on the size of the particle R_s, the gas density and the relative velocity $v_{\rm rel}$ between the particle and the gas. Assuming that solids are spherical particles, the stopping time can be expressed as (Perets and Murray-Clay 2011, Guillot et al. 2014)

$$t_s = \left(\frac{\rho_g v_{\rm th}}{\rho_s R_s}\min\left[1, \frac{3}{8}\frac{v_{\rm rel}}{v_{\rm th}}C_D({\rm Re})\right]\right)^{-1}, \tag{3.10}$$

where $v_{\rm th} = \sqrt{8/\pi}c_s$ is the gas thermal velocity, ρ_s the density of the solid particle, assumed to be 1 g cm^{-3} regardless of its size. The dimensionless drag coefficient C_D is a function of the Reynolds number Re of the flow around the particle (Perets and Murray-Clay 2011):

$$C_D = \frac{24}{\rm Re}(1+0.27{\rm Re})^{0.43} + 0.47\left(1 - e^{-0.04{\rm Re}^{0.38}}\right). \tag{3.11}$$

The Reynolds number is given by (Supulver and Lin 2000) as

$${\rm Re} = \frac{4R_s v_{\rm rel}}{c_s l_g}, \tag{3.12}$$

where $l_g \simeq 5\times10^{-9}/\rho_g$ (g cm^{-3}) is the mean free path of the gas.

The stopping time is divided into two regimes. The Epstein regime is valid when the particle size is smaller than the mean free path of the gas. In this case, the stopping time does not depend upon the relative velocity between the particle and the gas. When the particles are larger than the mean free path of the gas, the gas should be considered as a fluid. In such a case, the stopping time depends upon the relative velocity and the Reynolds number of the flow.

The equation of motion of the particles within the CPD is then given by

$$\frac{d\boldsymbol{v}_s}{dt} = -\frac{GM_p}{R^3}\boldsymbol{R} - \frac{1}{t_s}(\boldsymbol{v}_s - \boldsymbol{v}_g), \tag{3.13}$$

where M_p is the mass of the central planet (here Jupiter), $\boldsymbol{R}$ the position vector of the particle, $\boldsymbol{v}_s$ its velocity vector and $\boldsymbol{v}_g$ is the velocity of the gas. The equation is integrated with an adaptive time step ODE solver[1] (Brown et al. 1989), using Adams methods for particles with sizes down to 10^{-3} m and the implicit backward differentiation formula scheme to integrate the motion of lower size particles whose small stopping times imply a too restrictive time step for an explicit scheme (the time step should be smaller than the stopping times of the particles). The use of the implicit scheme ensures the stability of the method regardless of the timestep used but limits its order to 5, whereas the order of the classical integration scheme might be up to 12. In either case, step sizes and method order are automatically selected by the solver to satisfy the supplied error tolerances. Here we have applied error tolerances of 10^{-6} when the implicit backward differentiation formula method was used and 10^{-8} otherwise.

Small dust grains ($\sim\mu$m) have very short stopping times (e.g., $t_s \ll \Omega_\mathrm{K}^{-1}$), meaning that they quickly become coupled with the gas. On the other hand, large planetesimals (tens or hundreds of kilometers in radius) have long stopping times ($t_s \gg \Omega_\mathrm{K}^{-1}$) and their motion is hardly affected by the friction with the gas. Intermediate planetesimals, with sizes in the $\sim$cm–m range, efficiently loose angular momentum but on timescales that are too long to allow them to become coupled with the gas. These bodies thus always feel a headwind and they continue loosing angular momentum, causing them to rapidly drift inward towards the central planet. The solids that experience the most rapid inward drift are those whose Stokes number St, namely the stopping time multiplied by the local keplerian frequency ($\Omega_\mathrm{K} t_s$), is of order unity.

Figure 3.2 represents the mid plane radial velocity of particles as a function of their Stokes number (left panel) as well as the size associated with the Stokes number (right panel) for solids at a distance of 15 R_Jup from Jupiter. The left panel of Figure 3.2 shows a comparison of the velocity of particles in the simulation (black dots) with that derived from the analytical formula (see e.g. Birnstiel et al. 2012) :

$$v_{r,s} = -\frac{2\mathrm{St}}{1+\mathrm{St}^2}\eta v_\mathrm{K} + \frac{1}{1+\mathrm{St}^2}v_{r,g}. \tag{3.14}$$

Almost all solids are steady in the disk compared to the very rapid dynamics of the pebbles (particles with St $\sim$ 1) that drift inward at high velocities. The other

[1] The ODE solver is available at the following webpage: https://computation.llnl.gov/casc/odepack/

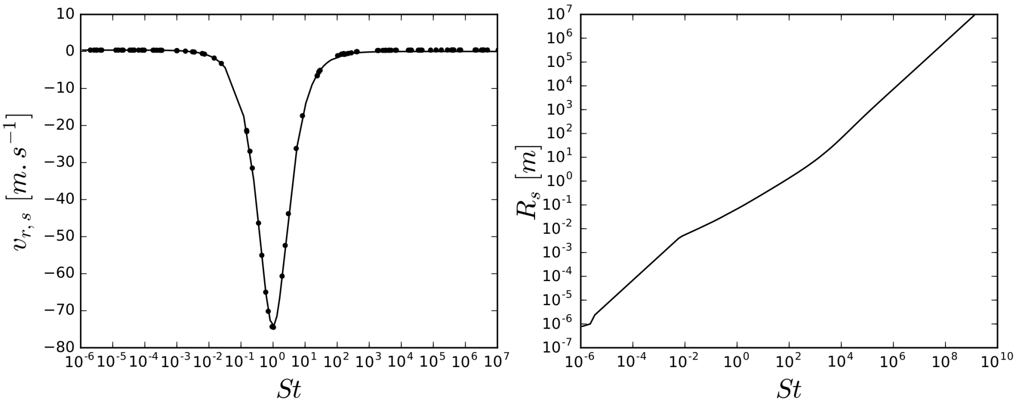

Figure 3.2: *Left*: particles radial velocity as a function of their Stokes number (black dots) at 15 $R_{\rm Jup}$ from a Jupiter mass planet in the midplane of a CPD with $\dot{M}_{\rm p} = 10^{-7}\,M_{\rm Jup\,yr}^{-1}$ and $\alpha = 10^{-3}$. The solid line shows the solution of the analytical formula given by Equation 3.14 which fits well the results of our integration. Small dust grains with sizes smaller than $\sim 10^{-3}$ m have a slightly positive velocity which is that of the gas at the midplane ($v_{r,g} \simeq 0.15\,{\rm m\,s^{-1}}$). Overall, there is more than one order of magnitude difference between the velocity of pebbles (solids with St $\sim$ 1) and those of the larger (St $\gg$ 1) and smaller (St $\ll$ 1) particles. *Right:* correspondence between the Stokes number and the size of the particles.

mechanism affecting the motion of solids is turbulent diffusion. Turbulent eddies can entrain particles during their cohesion timescale and would efficiently mix radially and vertically small dust grains that couple well with the gas. The motion of solids due to turbulence is modeled following Ciesla (2010, 2011) with a stochastic kick in the position of the particle (see also Charnoz et al. 2011). Additional advection terms are also added to account for the non uniform background gas density and diffusivity of solids (see eq. 3.17). Accounting for all transport mechanisms, the new position of a solid particle along any axis of a cartesian coordinate system after a timestep dt can be expressed as (Ciesla 2010, 2011, Charnoz et al. 2011)

$$x(t+dt) = x(t) + v_{\rm adv}dt + R_1 \left[\frac{2}{\sigma^2} D_p dt\right]^{\frac{1}{2}}, \tag{3.15}$$

where x stands for any cartesian coordinate, $R_1 \in [-1;1]$ is a random number, σ^2 the variance of the random number distribution, D_p the diffusivity of the solid particles and $v_{\rm adv}$ is the term accounting for the non uniform density of the gas in which the particles diffuse as well as the non uniform diffusivity of the particles, and the forces experienced by the particle, namely the gravitational attraction from the central planet and the gas drag (see eq. 3.17). D_p is related to the gas diffusivity through the Schmidt number Sc as (Youdin and Lithwick 2007)

$$\mathrm{Sc} \equiv \frac{\nu}{D_p} \sim 1 + \mathrm{St}^2, \tag{3.16}$$

implying that solids with large Stokes number are not significantly affected by turbulence. The advective velocity v_{adv} is given by (Ciesla 2010, 2011, Charnoz et al. 2011)

$$v_{\text{adv}} = \frac{D_p}{\rho_g}\frac{\partial \rho_g}{\partial x} + \frac{\partial D_p}{\partial x} + v_{s,x}, \tag{3.17}$$

where the two first terms account for the gradients in gas density and solid diffusivity and the last term is the velocity of the particle determined from its equation of motion (eq. 3.13).

The sublimation of water ice is also included in our model to track the evolution of the ice fraction of the solids during their transport within the CPD. This ice fraction is compared with the present water content of the Galilean satellites. The surface temperature of the solids is calculated following the prescription of D'Angelo and Podolak (2015), in which several heating and cooling mechanisms are considered. The main heat source is the radiation from the ambiant gas at the local temperature T_{d}. Friction with the gas also heats up the surface of the body. Water ice sublimation on the other hand is an endothermic process that substantially lowers the surface temperature. Finally, energy is radiated away from the surface at the surface temperature of the body. Taking into account all the heating and cooling sources, and considering that these processes only affect an isothermal upper layer of thickness δ_s, the evolution of the surface temperature T_s of the solid is given by (D'Angelo and Podolak 2015)

$$\begin{aligned} \frac{4}{3}\pi\left[R_s^3 - (R_s-\delta_s)^3\right]\rho_s C_s \frac{dT_s}{dt} &= \frac{\pi}{8} C_D \rho_g R_s^2 v_{rel}^3 \\ &+ 4\pi R_s^2 \epsilon_s \sigma_{SB}\left(T_d^4 - T_s^4\right) + L_s \frac{dM_s}{dt}, \end{aligned} \tag{3.18}$$

where R_s is the radius of the particle, C_s is the specific heat of the material set to $1.6 \times 10^3\,\text{J}\,\text{kg}^{-1}\,\text{K}^{-1}$ (specific heat of water ice at $\sim$200 K), ϵ_s is the emissivity of the material, σ_{SB} is the Stefan-Boltzmann constant and L_s is the latent heat of sublimation of water ice ($L_s = 2.83 \times 10^6\,\text{J}\,\text{kg}^{-1}$). Usually, the heating due to gas friction has a negligible effect so that the surface temperature of the bodies tends to equal that of the disk when water ice sublimation is not significant. On the other hand, when sublimation is important, the surface temperature can be significantly lowered (see Section 3.3 and Figure 3.5 for more details). The resulting mass loss rate due to water ice sublimation is then given by

$$\frac{dM_s}{dt} = -4\pi R_s^2 P_v(T_s)\sqrt{\frac{\mu_s}{2\pi R_g T_s}}, \tag{3.19}$$

i	e_i
0	20.9969665107897
1	3.72437478271362
2	−13.9205483215524
3	29.6988765013566
4	−40.1972392635944
5	29.7880481050215
6	−9.13050963547721

Table 3.1: Coefficients for the polynomial relation giving the equilibrium vapor pressure of water at a given temperature.

where $P_v(T_s)$ is the equilibrium vapor pressure of water over water ice at the temperature T_s, μ_s the molecular weight of water and R_g the ideal gas constant. The above expression is neglecting the effect of the partial pressure of water and holds in vacuum. In practice, P_v should be replaced by $(P_v(T_s) - P_{\mathrm{H_2O}}(r))$ in Equation 3.19, with $P_{\mathrm{H_2O}}(r)$ the partial pressure of water vapor in the disk. However, we do not follow the evolution of the water vapor in this study and the initial composition of the CPD is uncertain as water was most likely in condensed form at Jupiter's orbit. Our expression therefore yields to "colder" snowlines as the sublimation of water ice should be inhibited whenever $P_{\mathrm{H_2O}} > P_v$ in more realistic conditions. The equilibrium vapor pressure $P_v(T_s)$ is computed from Fray and Schmitt (2009) :

$$\ln\left(\frac{P_v(T)}{P_t}\right) = \frac{3}{2}\ln\left(\frac{T}{T_t}\right) + \left(1 - \frac{T_t}{T}\right)\gamma\left(\frac{T}{T_t}\right) \tag{3.20}$$

$$\gamma\left(\frac{T}{T_t}\right) = \sum_{i=0}^{6} e_i \left(\frac{T}{T_t}\right)^i \tag{3.21}$$

where $P_t = 6.11657 \times 10^{-3}$ bar and $T_t = 273.16$ K are the pressure and temperature of the triple point of water respectively. The coefficients e_i are given in Table 3.1. The thickness of the isothermal layer is given by D'Angelo and Podolak (2015) as

$$\delta_s = \min\left[R_s, 0.3\frac{K_s}{\sigma_{SB} T_s^3}\right] \tag{3.22}$$

where K_s is the thermal conductivity of ice ($\sim 3\ \mathrm{W\,m^{-1}\,K^{-1}}$ at 200 K). At a surface temperature of 150 K the thickness of the isothermal layer is $\delta_s \sim 4.7$ m while at

200 K it is reduced to ∼2 m. For the sake of simplicity, we do not consider here a mixture of ice and rock that would primarily have a slightly lower specific heat and a slightly higher thermal conductivity. The impact on the sublimation of water ice would nevertheless be minor as D'Angelo and Podolak (2015) demonstrated that the differences in the ablation rates among completely icy and mixed composition bodies are no more than ∼10%.

The equations depicting the surface temperature evolution and mass ablation rate are integrated together with the equation of motion of the particle. The change in radius caused by ice ablation is taken into account during the determination of the stopping time and consequently in the motion equation of the particle. For the sake of simplicity, we assume that the density of the solids is not modified during ice ablation and the radius of the particle is therefore always given by $Rs = (3M_s/4\pi\rho_s)^{1/3}$. This is equivalent to considering that the porosity of the body increases when ice sublimates.

In the next section, we apply the model to a steady-state circum-jovian disk and investigate the evolution of solids with different sizes.

3.3 Results

Figure 3.3 presents the results of simulations with initial sizes of 10^{-6}, 10^{-1}, 1, 10^3 and 10^4 m, to illustrate their very different behavior in terms of dynamics and thermodynamics. We applied our model to particles of different initial sizes (10^{-6}, 10^{-1}, 1, 10^3 and 10^4 m) and tracked the dynamical and compositional evolution over a short timespan (although the simulations actually span $\sim 4 \times 10^5\, \Omega^{-1}_{\mathrm{K},25 R_{\mathrm{Jup}}}$, which is orders of magnitude larger than the expected collisional timescale within the CPD). Specifically, one thousand particles per size bin were initially released in the midplane of the CPD at distances ranging between 20 and 35 R_{Jup}. At the beginning of the simulation, all particles have an ice mass fraction $f_{\mathrm{ice}} = m_{\mathrm{ice}}/m_{\mathrm{tot}} = 0.5$. The CPD is assumed to be in steady-state with $\dot{M}_{\mathrm{p}} = 10^{-7}\, M_{\mathrm{Jup}\,\mathrm{yr}}^{-1}$ and $\alpha = 10^{-3}$ which gives the surface density and temperature profiles drawn on Figure 3.4, allowing to focus the results on solids' evolution. The inner edge of the disk is set equal to $3.5\, R_{\mathrm{Jup}}$. Solids crossing this distance are considered lost to the planet, implying that their motion is no longer integrated. In Figure 3.3, we display the rock mass fraction ($f_{\mathrm{rock}} = 1 - f_{\mathrm{ice}}$), height and distance to Jupiter of the solids as a function of time.

The different dynamical behavior as a function of particle size is well illustrated in Figure 3.3. A common feature for all particle sizes is the much faster vertical than radial diffusion timescale. The first column of the figure, showing the radial and vertical position of the solids after ∼2.7 years of evolution, illustrates the fact that

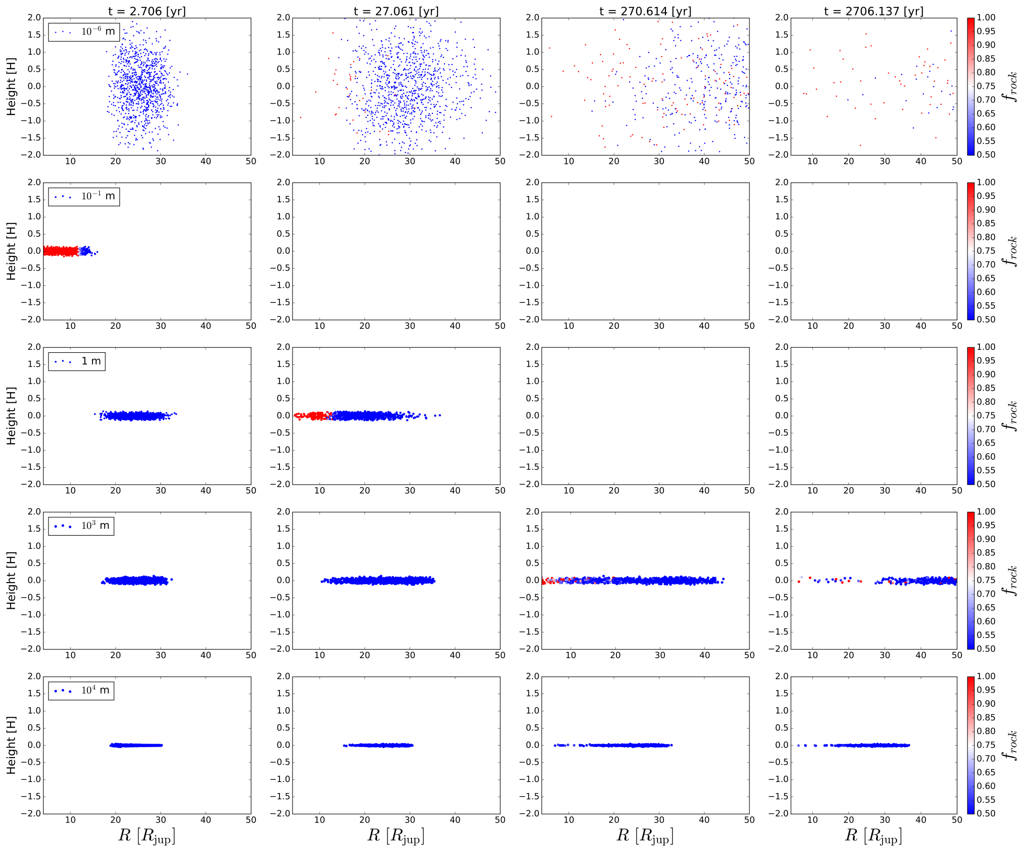

Figure 3.3: From left to right: snapshots of the evolution of particles at different times within a Jovian CPD with parameters $\dot{M}_p = 10^{-7}\ M_{\rm Jup}\, yr^{-1}$ and $\alpha = 10^{-3}$. From top to bottom, each row displays the evolution of solids of different initial sizes with radii of 10^{-6}, 10^{-1}, 1, 10^{3} and 10^{4} m. The radial and vertical positions of the solids are expressed in $R_{\rm Jup}$ and local gas scale height respectively. The color of each particle illustrates its composition with bluer particles having a higher water ice mass fraction.

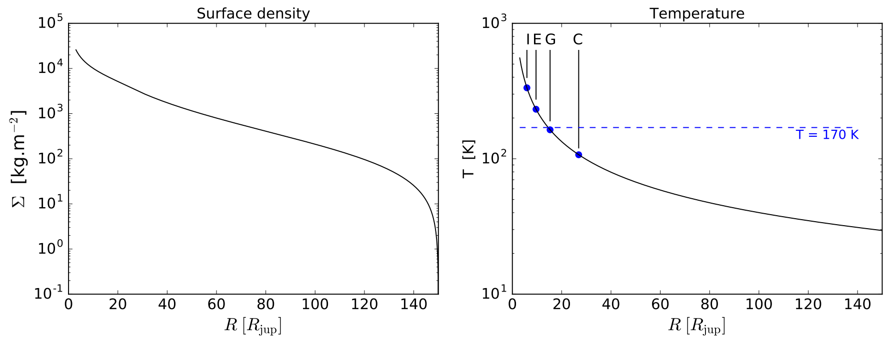

Figure 3.4: Surface density and temperature profiles of the CPD, with the distance from Jupiter expressed in units of Jovian radii ($R_{\rm Jup}$) calculated for $\dot{M}_{\rm p} = 1 \times 10^{-7}\, M_{\rm Jup\,yr}^{-1}$ and $\alpha = 10^{-3}$. The vertical bars designated by the letters I, E, G and C correspond to the current orbits of Io, Europe, Ganymede and Callisto, respectively.

solids are already distributed vertically and this distribution does not significantly change further in time. As expected, larger solids concentrate more in the midplane of the disk whereas micron sized dust particles are efficiently entrained by turbulence and follow the distribution of the gas. It is important to note that the vertical position of the solids (Figure 3.3) is represented in units of the gas scale height $H_g(r)$ at the radial position of the particle. The radial drift of the particles also follows a well-known trend with very small particles (micron-sized) being well coupled with the gas, intermediate-sized particles (1cm-1m) drifting inward at a high pace, and large particles ($\geq$1 km) drifting inward and diffusing outward at a very low pace.

Regarding the compositional evolution of the particles, some clear trends emerge (see Figure 3.3). It appears that size strongly influences the ability of a given particle to retain water while drifting inward. In short, larger bodies are able to retain significantly more water than the smaller ones. For example, meter-sized bodies located inside of $\sim$12 $R_{\rm Jup}$ have lost all their water after 27 years of evolution whereas kilometer-sized bodies (fourth row of Figure 3.3) have retained most of their water at the same location. The same applies for 10^3 and 10^4 m solids after 270 and 2700 years of evolution. It is also interesting to note that due to their limited inward drift and rather long sublimation timescales, water-free and water-rich kilometer-sized bodies can coexist at the same location, a feature that is not observed among the smaller particles.

The origin of such compositional evolution as a function of particle size is twofold. First, from Eq. 3.19, one can derive that the ablation timescale at a given location of a particle is $M_s(dM_s/dt)^{-1} \propto R_s$, implying that larger particles retain more water than smaller ones. Second, because water ice sublimation is an endothermic process, it cools down the surface temperature of large particles efficiently for longer time. Considering negligible the heating due to friction with the

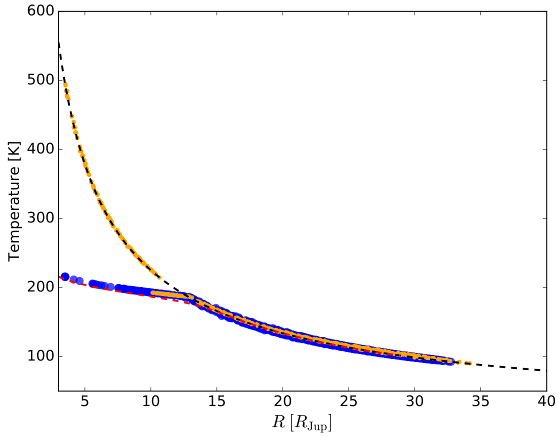

Figure 3.5: Surface temperature of 10 km (blue dots) and 10 cm (yellow dots) bodies as a function of the distance from Jupiter within a CPD with $\dot{M}_p = 10^{-7}\,M_{\mathrm{jup}}\,\mathrm{yr}^{-1}$ and $\alpha = 10^{-3}$. The black dashed line represents the temperature profile of the CPD while the red dashed line is the solution of Equation 3.23. The high water ice ablation rates suffered by these bodies efficiently cools down their surface temperatures in the inner part of the disk, making them substantially depart from the ambient gas temperature. However, 10 cm bodies cannot retain water ice below $\sim 10\,R_{\mathrm{Jup}}$ so that their surface temperature is that of the ambient gas interior to this distance.

gas and that an equilibrium is rapidly attained, Equation 3.18 reduces to

$$\epsilon_s \sigma_{SB}(T_d^4 - T_s^4) = L_s P_v(T_s)\sqrt{\frac{\mu_s}{2\pi R_g T_s}}. \tag{3.23}$$

When the release of sublimation heat is important (right-hand side of the equation), the surface temperature of the bodies departs from that of the surrounding gas.

This process is well illustrated in Figure 3.5 where the surface temperature of 10 km and 10 cm-sized planetesimals is shown (blue and yellow dots, respectively) along with the temperature of the surrounding gas (black dashed line) and the solution of Equation 3.23 (red dashed line). Closer to Jupiter, where the CPD is hotter, the temperature of these bodies departs from that of the gas because a significant amount of water sublimates at their surfaces. The surface temperature given by Equation 3.23 slightly underestimates the temperature but is a good approximation. In spite of that, the ablation timescale of 10 cm particles remains short and their water ice is entirely sublimated when they approach at distances $\lesssim 10\,R_{\mathrm{Jup}}$. Interior to this distance, the surface temperature of the 10 cm bodies abruptly catches up with the disk temperature. The efficient cooling during water ice sublimation and the fact that the sublimation timescale scales with the size of the object allows larger bodies to retain water over much longer timescales than their smaller siblings.

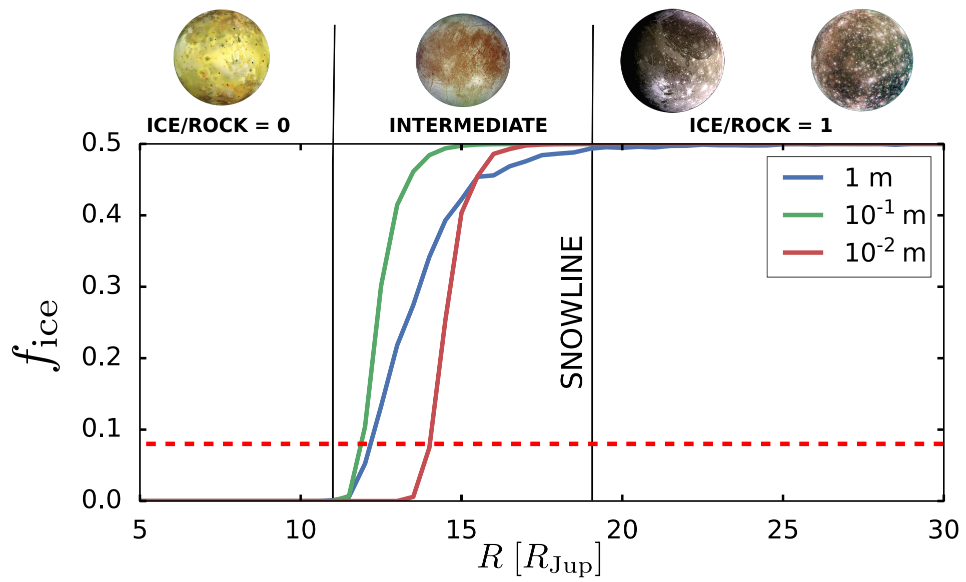

Figure 3.6: Average water ice mass fraction of solids as a function of radial distance from Jupiter. 10^4 particles of each size have been released in the 25–35 R_{Jup} region. The horizontal dashed line corresponds to Europa's estimated water mass fraction.

Due to the very short lifetime of the solids with sizes in the 10^{-1}– 1 m range, we ran an other set of simulations to study in more detail their evolution within the CPD. We also extended the size range down to 10^{-2} m particles.We ran simulations using 10,000 particles, released between 25 and 35 R_{Jup} and we opted to randomly re-inject in this region the particles that cross the inner boundary of the CPD set at 3.5 R_{Jup}. In a way, we mimic a flux of pebbles that would originate from farther locations within the CPD. The parameters of the CPD are those used in the previous simulations and the size of the particles evolve due to the effect of ice ablation only (no coagulation nor fragmentation was modeled–we discuss the expected grain size within the CPD in section 3.4.2).

Figure 3.6 shows the average water ice mass fraction f_{ice} of solids with sizes of 10^{-2}, 10^{-1} and 1 m as a function of the distance to Jupiter. Due to the rapid dynamics of these solids and the fact that we re-inject them, an equilibrium is rapidly attained, meaning that the curves shown on Figure 3.6 are steady in time for a stationary CPD. These curves would however shift towards Jupiter as the disk slowly cools down compared to the drift timescale of the pebbles. During their inward migration, solids gradually loose water ice and therefore exhibit a gradient in their water mass fraction as a function of the radial distance. The solids able to transport water the farthest inside the disk are the 10^{-1}m pebbles because of their very rapid inward motion. The solids with a size of 10^{-2}m display a very similar behavior although their water mass fraction is shifted in the outer radial direction. This shift is due to the shorter ablation timescale of 10^{-2}m pebbles compared to that of the larger ones although their velocity is comparable (see Figure 3.2). Larger meter sized bodies exhibit a less steep gradient in their water mass fraction because of their much slower inward velocities. They spend a greater amount of time in a given environment than smaller pebbles causing them to be more ablated and therefore they are not able to carry as much water as 10^{-1} m pebbles.

Overall, we find that the pebbles define three distinct compositional regions. In the outer region, the solids mostly retain their primordial water content because they do not suffer from substantial sublimation. In the innermost region, the solids have already lost all of their water ice and are essentially rocky. In between these two regions, the particles exhibit a gradient in their water content over an area that is $\sim 3\ R_{\rm Jup}$ wide due to the combined effect of inward drift and sublimation.

3.4 Discussion

Here we put in perspective the results presented in the previous section with the current composition of the Galilean system. We try to provide some constraints on the size of the building blocks of the Jovian moons and discuss the implications on different mechanisms, such as the delivery of solids to the CPD or the migration of the satellites, which were not studied here.

3.4.1 Constraints on the size of the building blocks of the Galilean satellites

We presented in Section 3.3 the dynamical and compositional evolution of particles with a wide range of sizes. We find that larger objects are able to retain more water ice than smaller ones, and that the ablation timescale of planetesimals with sizes $\gtrsim 10^4$ m is significantly enhanced in hot environments due to an efficient cooling of their surfaces. While it is common to assume that solids inside the snowline are rocky whereas the ones residing outward are icy (e.g., Alibert et al. 2005, Sasaki et al. 2010), our results show that the solids embedded within Jupiter's CPD should have been (at least initially) relatively smaller than 10^3 m to ensure this. If the initial building blocks of the satellites were large (D$\geq 10^3$ m) icy objects ($f_{\rm ice}$=1), Io and Europa would probably have formed with substantially more water than they possess today. This finding is also supported by the study of Dwyer et al. (2013) which demonstrated that water loss during collisions of large planetesimals is not a sufficient mechanism to account for the formation of a water free Io and Europa with less than 10% water by mass. Conversely, if the initial building blocks of the satellites were small (D$\leq 10^{-6}$ m) icy particles (ice/rock=1), Io and Europa would have formed without water and Europa should be dry today.

There is only one size range that allows the direct formation of a dry Io, of a

Europa with a low water content and of two icy moons (Ganymede, Callisto) in the outer region of the CPD, namely 10^{-2} m $\leqslant$ D $\leqslant$ 1 m. More precisely, those are the only solids for which the ice-to-rock ratio could directly reflect that of the moons. Close inspection of the row of figure 3.3 representing the evolution of solids with a size of 10^3 m reveals that dry and hydrated material can coexist over a wide orbital range. It could therefore be possible to reproduce the observed gradient among the moons' composition from ∼km sized satellitesimals although it would rely on a more or less stochastic scenario of the accretion of the moons. If indeed the composition of the Galilean satellites directly reflects that of the solids they accreted, it implies that Europa could have had any water content between 0 and 50% while forming in the intermediate region (see Figure 3.6). In summary, the growth of Europa could have been restricted to this "intermediate" region, where the protosatellite would have accreted partially dehydrated, drifting material. We discuss in more details pebble accretion in the Galilean system in the following.

It should be noted that the positions of the different regions defined on Figure 3.6 do not match the current location of the Galilean satellites. Whereas it would be easy to adjust the mass accretion rate $\dot{M}_p$ to shift the position of the different regions, we do not want to suggest that these bodies formed in a steady disk or that they necessarily formed at the position we observe them today by doing so. These issues are further discussed in the following.

3.4.2 Growing the Galilean satellites through pebble accretion

In the scenario depicted in Canup and Ward (2006), the formation of satellites competes with their loss through migration so that there exists an equilibrium mass of the satellite system and many satellite generations would have formed around Jupiter, the Galilean moons we see today being the last survivors. This was supported by their N-body simulations of the accretion of the satellites. However, an important limitation of their investigation is that the solids added to the CPD to mimick the replenishment from circumsolar material were large. Although it is expected that the solids brought with the gas inflow were in the form of small dust grains, Canup and Ward (2006) added objects with a size ∼100–600 km to the CPD to keep their simulations tractable. This could be accurate if the small grains brought to the CPD rapidly grew into such large satellitesimals before being accreted by the protosatellites. However, forming large satellitesimals from dust grains would be very difficult in the CPD (see Shibaike et al. 2017, and discussion below). It is much more likely that the dust grains grew to pebble sizes and rapidly drifted inward until being either lost to Jupiter or accreted by a forming satellite. Pebble accretion hence seems a more accurate description of the growth of the satellites in a gas-starved scenario than the investigation conducted by Canup and

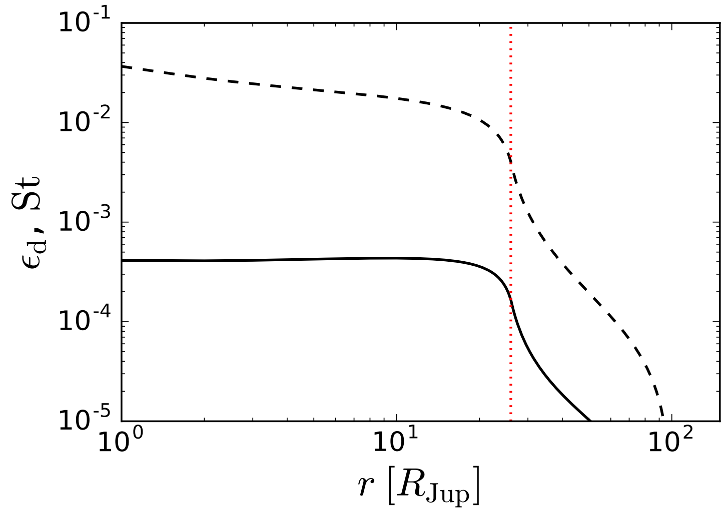

Figure 3.7: Steady-state values of the dust-to-gas mass ratio $\epsilon_{\rm d}$ (solid line) and Stokes number of the dust grains (dashed line) within a CPD with parameters similar to that shown on Figure 3.4. The vertical red dotted line marks the position of the centrifugal radius inside of which dust is replenished by the inflow of material.

Ward (2006) (although the question of how to form the seeds that would accrete the pebbles remains; see next chapter for more details).

The growth of planetary bodies through pebble accretion is a new paradigm that has been described recently (e.g., Ormel and Klahr 2010, Lambrechts and Johansen 2012) and quite successfully applied to the Solar System's planets (e.g., Lambrechts and Johansen 2014, Lambrechts et al. 2014, Morbidelli et al. 2015a, Levison et al. 2015), population synthesis models (e.g., Bitsch et al. 2015b) and the formation of compact systems around dwarf stars (Ormel et al. 2017). However, its application to the growth of giant planets' moons remains to be investigated. The closest analogues to the Galilean moons would be compact systems such as the TRAPPIST-1 planets (the architecture of this system in fact resembles more that of the Galilean system than the architecture of Saturn's moons do), although an important difference resides in the fact that the jovian CPD could have been constantly replenished with circumsolar material throughout satellites' formation (Canup and Ward 2002, 2006).

Due to the short orbital timescales within the CPD, the small dust grains brought with the inflowing material would rapidly coagulate and drift inward which would limit their growth (see section 1.2.2). In a steady-state CPD where dust grains are constantly replenished by circumsolar material and cannot grow up to decoupling sizes, the flux of pebbles through the disk would be controlled by the rate at which material is brought to the CPD. In this case, $\dot{M}_{\rm peb} \approx f \dot{M}_{\rm p}$ inside of the centrifugal radius of the disk (where f is the dust-to-gas mass ratio of the inflowing material). Noting that the fluxes of pebbles and gas through the CPD are $\dot{M}_{\rm peb/gas} = 2\pi r v_{\rm r,d/g}\Sigma_{\rm d/g}$, the dust-to-gas mass ratio within the CPD, $\epsilon_{\rm d} = \Sigma_{\rm d}/\Sigma_{\rm g}$, would approximately be

$$\epsilon_{\rm d} \sim \frac{3}{4} f\alpha h^2\eta^{-1}{\rm St}^{-1} = 3\times 10^{-4}\left(\frac{f}{10^{-2}}\right)\left(\frac{\alpha}{10^{-3}}\right)\left(\frac{h}{0.1}\right)^2\left(\frac{\eta}{0.005}\right)^{-1}\left(\frac{\rm St}{0.05}\right)^{-1} \tag{3.24}$$

where we have used $v_{\rm r,d} \sim 2{\rm St}\eta v_{\rm K}$ and $v_{\rm r,g} = (3/2)\nu/r$. We assumed a value of the Stokes number which is typical for a drift limited size of the grains (e.g., Lambrechts and Johansen 2014). Inserting back the inferred value of $\epsilon_{\rm d}$ in the expression of the maximum Stokes number in the drift regime (section 1.2.2) yields ${\rm St}_{\rm drift} = 0.5\epsilon_{\rm d}\eta^{-1} = 0.03$, in good agreement with our assumption.

We confirm this simple estimate through numerical integration of the advection-diffusion equation of the surface density of the dust (eq. 1.23), computing the drift limited size of the grains at each timestep and radial distance until a steady-state was reached. A source term $S = f\dot{M}_{\rm p}/(\pi r_{\rm c}^2)$ was added interior to the centrifugal radius to mimick the inflow of material. Figure 3.7 shows the steady-state dust-to-gas ratio and Stokes number of the dust grains as a function of the radial distance from Jupiter for $f = 10^{-2}$, $\dot{M}_{\rm p} = 10^{-7}\, M_{\rm Jup}\,{\rm yr}^{-1}$ and $\alpha = 10^{-3}$. The results are in very good agreement with the estimations above. The Stokes number of the dust grains ranges from several 10^{-3} to a few 10^{-2}, corresponding to sizes between a few centimeters up to a few meters, comparable with those shown on figure 3.6. The dust-to-gas mass ratio is almost constant inside of the centrifugal radius and is $\epsilon_{\rm d} \approx 4\times 10^{-4}$. Outside of the centrifugal radius (marked by the vertical dotted line on figure 3.7), the dust-to-gas ratio drops rapidly due to the lack of a replenishment which further limits the growth of the dust.

Clearly, forming large satellitesimals from the dust inflow, as often assumed in investigations of satellites growth in the gas-starved framework, would be very difficult. Direct coagulation, as in the case of protoplanetary disks in general (e.g., Johansen et al. 2014), seems unable to grow particles that would decouple from the gas. Local enhancements of $\epsilon_{\rm d}$ due to, e.g., water vapor diffusion at the snowline (Stevenson and Lunine 1988, Schoonenberg and Ormel 2017, Drążkowska and Alibert 2017), could provide suitable conditions for the streaming instability and result in the localized formation of large satellitesimals. The streaming instability requires $\epsilon_{\rm d} \gtrsim 0.02$ to operate (Carrera et al. 2015, Yang et al. 2017) which is two orders of magnitude higher than the expected value in the CPD. Schoonenberg and Ormel (2017) and Drążkowska and Alibert (2017) find enhancements of the dust-to-gas mass ratio of factors ~2–5 near the snowline which would be insufficient to trigger the streaming instability in the CPD based on our results. We also note that the gravitational collapse of an overdense dust filament would occur if the particle density crosses the Roche density (Johansen et al. 2012),

$$\rho_{\mathrm{R}} = \frac{9}{4\pi}\frac{\Omega^2}{G}. \tag{3.25}$$

At a distance of $20\,R_{\mathrm{Jup}}$, the Roche density is $\gtrsim 10^3$ the corresponding value at 1 au from the Sun. The formation of satellitesimals in the CPD via gravitational collapse thus requires particles concentrations that are much higher than those needed for planetesimals formation around the Sun. This hints toward the fact that the capture of already formed planetesimals on heliocentric orbits might well be a necessary ingredient of the growth of the satellites. This issue is further investigated in the next Chapter dedicated to the delivery of material to the circum-jovian disk.

Leaving aside the issue of the origin of the satellites seeds for now, the growth timescale of a satellite through pebble accretion might be expressed as (e.g., Ormel et al. 2017)

$$\tau_{\mathrm{growth}} = \frac{M_{\mathrm{sat}}}{\varepsilon_{\mathrm{PA}}\dot{M}_{\mathrm{peb}}}, \tag{3.26}$$

where M_{sat} is the satellite's mass and $\varepsilon_{\mathrm{PA}}$ is the pebble accretion efficiency. In the 2D accretion limit, valid when the scale height of the pebbles $H_{\mathrm{peb}} \ll R_{\mathrm{Hill,sat}}$, an estimate of the pebble accretion efficiency is (see section 1.2.3)

$$\varepsilon_{\mathrm{PA}} \sim 0.2\left(\frac{\mathrm{St}}{0.05}\right)^{-1/3}\left(\frac{0.005}{\eta}\right)\left(\frac{q_{\mathrm{sat}}}{8\times10^{-5}}\right)^{2/3}, \tag{3.27}$$

and $q_{\mathrm{sat}} = M_{\mathrm{sat}}/M_{\mathrm{Jup}} \simeq 8\times10^{-5}$ for Ganymede. The Hill sphere of a satellite would be larger than the scale height of the pebbles for

$$q_{\mathrm{sat}} \gtrsim 8\times10^{-6}\left(\frac{0.05}{\mathrm{St}}\right)^{3/2}\left(\frac{\alpha}{10^{-3}}\right)^{3/2}\left(\frac{h}{0.1}\right)^{3}, \tag{3.28}$$

so that most of the growth of a Galilean sized satellite would indeed proceed in the 2D Hill regime of pebble accretion. The above estimates imply a growth timescale

$$\tau_{\mathrm{growth}} \sim 4\times10^{5}\left(\frac{q_{\mathrm{sat}}}{8\times10^{-5}}\right)^{1/3}\left(\frac{f}{0.01}\right)^{-1}\left(\frac{\dot{M}_{\mathrm{p}}}{10^{-7}\,M_{\mathrm{Jup}}\,\mathrm{yr}^{-1}}\right)^{-1}\ \text{years}. \tag{3.29}$$

Similarly to the scenario proposed by Canup and Ward (2002, 2006), the growth timescale is regulated by the inflow of material accreted by Jupiter and could therefore be long enough to account for Callisto's partially differentiated state. It is also interesting to note that the small sizes of the pebbles are favorable to the formation of partially differentiated objects as accretional heating would be mostly deposited at the surface of the accreting body and more readily radiated away (e.g., Barr and Canup 2008). The growth timescale derived above is very long but would apply in the very late stages of Jupiter's accretion only. The accretion rate onto Jupiter during satellites' formation could have been as high as a few $10^{-6}\,M_{\rm Jup}\,{\rm yr}^{-1}$ in the early stages of their growth, implying satellites growth timescales that are an order of magnitude shorter initially.

Pebble accretion ends when the accreting body becomes massive enough to perturb the gas velocity in its vicinity and halt the drift of pebbles (Morbidelli and Nesvorny 2012, Lambrechts et al. 2014). This occurs at the so-called pebble isolation mass which is of the order of $q_{\rm iso} \sim (1/2)h^3$ (Ormel et al. 2017, Johansen and Lambrechts 2017), where $h = H_g/r$ is the aspect ratio of the disk. For values of h between 0.05–0.1, this gives maximum satellites masses of $q_{\rm sat,iso} \sim 6.25 \times 10^{-5}$–$5 \times 10^{-4}$. This is an interesting alternative to the critical satellite mass defined by Canup and Ward (2006) which is a migration limited mass.

The type I migration timescale of the satellites in the CPD would be

$$\tau_{\rm I} \sim 7 \times 10^5 \left(\frac{8 \times 10^{-5}}{q_{\rm sat}}\right) \left(\frac{10^2\,{\rm g\,cm^{-2}}}{\Sigma_{\rm g}}\right) \left(\frac{h}{0.1}\right)^2 \left(\frac{r}{15\,R_{\rm Jup}}\right)^{-1/2} \text{ years,} \tag{3.30}$$

which is comparable to the satellites growth timescale derived above but could be slow enough to allow for their survival. Migration and loss of the satellites could be critical in the pebble accretion scenario because of the rather low efficiency of the pebble accretion. The total mass (gas and solids) required to build a Ganymede mass satellite through pebble accretion is $0.05\,M_{\rm Jup}$ considering an inflow with solar composition so that it could be difficult to form several generations of satellites as proposed by Canup and Ward (2006).

Also, directly reproducing the composition of the Galilean moons through pebble accretion, and particularly that of Europa, requires that each satellite accreted in a well defined region of the CPD with respect to the snowline (see Figure 3.6). This would imply that either i) the formation of the satellites was short compared to both their migration timescale and the time evolution of the CPD which was ignored here, or ii) their migration timescale was comparable to the time evolution of the CPD so that Europa moved together with the snowline as the disk cooled down over time.

Regarding i), this could be the case if the satellites were trapped into a resonant chain early on due to the existence of an inner magnetic cavity that truncated the CPD as proposed by Sasaki et al. (2010). In this scenario, the migration of the satellites would be halted and if the CPD evolved on long enough timescales (e.g., $\gg \tau_{\rm growth}$), the temperature would not have significantly varied during the accretion of the moons. On the other hand, the migration of the satellites (Ganymede particularly) could have been tied to the evolution of the snowline due to the existence of a so-called migration trap (e.g., Bitsch et al. 2015a). Migration traps are regions in the disk where the torques acting on an object vanish and the migration is therefore stalled. These traps arise when the temperature and entropy gradient becomes large in a given region. Such gradients could be associated with the water ice line due to the sharp opacity transition when the composition of the dust is taken into account. As the disk is cooling and the snowline is moving inward, so does the migration trap and trapped satellites, making ii) an interesting possibility. However, due to the short coagulation and drift timescales of the dust grains, it is possible that the opacity provided by the dust within the CPD was minor (Ormel 2014). In this case, no steep temperature gradient would be expected at the snowline, hence no migration trap either.

3.4.3 Model assumptions and limitations

We discuss here some of the assumptions upon which the results presented in this chapter rely and how they might affect the conclusions drawn.

Temperature of the CPD—Here we have used a low mass accretion rate onto Jupiter, within the range of values assumed in gas-starved models, resulting in a cold CPD. This is typically done to allow water ice to be stable at the current location of Ganymede and lengthen Callisto's accretion timescale, as presented in the preceding chapter. Hydrodynamic simulations suggest that the mass accretion rate onto Jupiter would have been at least one order of magnitude higher (i.e., a few $10^{-6}\,M_{\rm Jup}\,{\rm yr}^{-1}$), resulting in a denser and hotter CPD than assumed in our simulations (Szulágyi et al. 2014). Lower accretion rate onto the planet would imply very low accretion rates onto the young Sun, which cannot be sustained very long against the rapid photoevaporation of the PPD (e.g., Koepferl et al. 2013). The accretion rates typically used in gas-starved models might therefore be irrelevant. As regards pebble sized particles, the main implication would be that the ice rich and intermediate regions defined on figure 3.7 are shifted outward. As for larger satellitesimals, the implications are more difficult to assess. If icy objects are exposed to temperatures above the critical temperature for water, $T_{\rm crit} \approx 650\,{\rm K}$, the evaporation is energy limited (e.g., Podolak et al. 1988), and their ablation timescale, $\tau_{\rm abl} \equiv M_{\rm s}({\rm d}M_{\rm s}/{\rm d}t)^{-1}$, might be expressed as

$$\tau_{\rm abl} = \frac{R_{\rm s}\rho_{\rm s}L_{\rm s}}{3\sigma_{\rm SB}(T_{\rm d}^4 - T_{\rm crit}^4)}. \tag{3.31}$$

Applying the above expression to a 10 km sized satellitesimal embedded in a hot disk with $T_{\rm d} = 1000\,{\rm K}$ yields $\tau_{\rm abl} \approx 6\,{\rm yr}$, that we might divide by a factor of 2 to account for the fact that water ice represents only half of the initial mass of the object. Although this ablation timescale appears to be very short, so are the dynamical timescales in the region of formation of the satellites (the orbital period of Io is ∼2 days and that of Callisto is ∼2 weeks). Even this short ablation timescale might in fact be too long to allow for the complete loss of water from the satellitesimal before it is accreted by a forming satellite. From the expression of the mass accretion rate of an embryo embedded in a planetesimal swarm (see, e.g., Lissauer 1993), we can estimate the collision timescale $\tau_{\rm col}$ of satellitesimals with an accreting satellite seed in the CPD,

$$\begin{aligned}\tau_{\rm col} \approx \frac{M_{\rm s}}{\Sigma_{\rm s}\pi R_{\rm seed}^2 \Omega_{\rm K} F_g} \sim 10^{-1}\,{\rm yr}\left(\frac{10\,{\rm g\,cm^{-2}}}{\Sigma_{\rm s}}\right)\left(\frac{500\,{\rm km}}{R_{\rm seed}}\right)^2 \\ \times\left(\frac{R_{\rm s}}{10\,{\rm km}}\right)^3\left(\frac{1}{F_g}\right)\left(\frac{r}{10\,R_{\rm Jup}}\right)^{3/2},\end{aligned} \tag{3.32}$$

where $\Sigma_{\rm s}$ is the surface density of satellitesimals and $F_g = 1 + (v_{\rm esc}/v_{\rm rel})^2$ is the gravitational focusing factor for objects with a mutual escape velocity $v_{\rm esc}$ and relative velocity at infinity $v_{\rm rel}$. The collision timescale is therefore about one order of magnitude shorter than the ablation timescale for the 10 km satellitesimals which means that even a satellite forming in such hot regions as those considered here ($T_{\rm d} = 1000\,{\rm K}$) could accrete substantial amounts of water. Applying the same analysis to 100 km sized satellitesimals, we find $\tau_{\rm col} \sim \tau_{\rm abl} \sim 10^2\,{\rm yr}$, so that these objects could be dried up before they are accreted. However, as the seed grow larger, it would accrete mass at a higher rate, hence collision timescales would shorten as the satellite is growing. For a satellite near completion, with $R_{\rm seed} = 2500\,{\rm km}$ and $F_g = 10$ (Canup and Ward 2002), the collisional timescale for 100 km sized satellitesimals drops to $\sim 10^{-1}{\rm yr} \ll \tau_{\rm abl}$. From these order of magnitude estimates, it appears that avoiding accretion of non negligible amounts of water would be difficult if the satellites fed from large satellitesimals, even when considering a hotter CPD.

Condensation of water—The model presented in this chapter neglects the possibility that water condenses on the surface of the particles, only water sublimation has been modeled. As condensation primarily occurs on small dust grains (e.g., Ros and Johansen 2013, Krijt et al. 2016), the compositional evolution of the 10^{-6}m sized particles presented on the top row of figure 3.3 is not representative. A lot of dry particles are found at large orbital distances in our simulations. These particles were exposed to sufficiently high temperature to have their water ice sublimated and subsequently diffused outward. Rapid condensation of water vapor onto their surface in the colder regions of the CPD would in fact revert their composition to ice rich (Krijt et al. 2016). The effect of condensation on pebbles or larger satellitesimals would however be moderate. As already mentioned, the condensation of water vapor could allow water ice to be stable at higher temperatures than given in our model due to the fact that sublimation rates depend upon the partial pressure of water in the disk. Finally, we also miss effects such as enhancements of the dust-to-gas ratio in the vicinity of the snowline due to water vapor diffusion and subsequent condensation (e.g., Stevenson and Lunine 1988, Schoonenberg and Ormel 2017, Drążkowska and Alibert 2017). However, as argued in the above subsection, this latter effect likely had minimal effect in the CPD due to the expected low dust-to-gas ratio.

Ablation during capture—Here we have investigated the compositional evolution of satellitesimals on circular orbits within the CPD. Since it is unlikely that large satellitesimals (with sizes $\gtrsim$ a few meters) were formed in the CPD, such objects should have been captured from heliocentric orbits when passing close to Jupiter and dragged onto orbits closer and closer from the planet (see, e.g., Fujita et al. 2013, D'Angelo and Podolak 2015, and the Chapter 4 for a detailed investigation). During this capture phase, the objects are initially on very eccentric orbits and exposed to hot and cold environments during orbital timescales before they are eventually circularized. Moreover, their high eccentricities imply large relative velocities with respect to the gas and thus an efficient frictional heating. Therefore, satellitesimals captured from initially heliocentric orbits could have lost substantial amounts of ice before their orbits are circularized in the region of formation of the Galilean moons. Although Fujita et al. (2013) and D'Angelo and Podolak (2015) included the ablation of ice during capture, they do not provide evolutionary tracks of the composition of the objects so that it is difficult to assess the significance of this effect. Material ablated from satellitesimals/planetesimals during CPD crossing orbits is a potential source of small grains (that would eventually grow to pebble sizes) in the disk. The effects of ice ablation during the capture of large satellitesimals, either in terms of the induced compositional change or delivery of small grains, should therefore be further examined and quantified.

3.5 Conclusions

In this chapter, the evolution of solids with a wide range of sizes embedded within a jovian CPD was investigated using a particle tracking model. Pebbles, that drift inward at high pace, define three distinct regions in terms of their water ice content that can match the gradient in water mass fraction currently observed among the Galilean satellites. This finding is interesting because in the framework of the gas-starved scenario for the origin of the moons (Canup and Ward 2002, 2006), where solids are supposedly brought to the CPD in the form of small dust grains, pebble accretion would likely be the main growth channel of the satellites. Interestingly, the existence of a pebble isolation mass might explain the roughly similar masses of the four Galilean satellites. Similarly to the original scenario envisioned by Canup and Ward (2002, 2006), the growth timescale of the satellites would be regulated by the inflow of circumsolar material onto the CPD (contrary to protoplanetary disks where it is regulated by the inward drift of pebbles) and could be long enough to account for Callisto's partially differentiated state.

However, we also note some important caveats of the proposed scenario, some of which are further discussed and investigated in the next chapter.

- The gradient observed in the water ice mass fraction of pebbles in our model was found assuming that pebbles do not disrupt when crossing the snowline. In fact, it is possible that when icy pebbles cross the snowline they release much smaller silicate grains (Saito and Sirono 2011, Morbidelli et al. 2015a, Ida and Guillot 2016) and the picture would be more complicated than that presented here.

- Considering the efficiency of pebble accretion in the CPD (eq. 3.27), it seems unlikely that multiple generations of satellites have formed around Jupiter, as proposed by Canup and Ward (2006). Instead, the loss of satellites to Jupiter through inward migration must be prevented. This conclusion supports the idea that the CPD was truncated by an inner magnetic cavity (Takata and Stevenson 1996, Batygin 2018) that stalled the migration of the inner moon (Sasaki et al. 2010, Ogihara and Ida 2012). It is however unclear in this context why Callisto avoided to be part of the resonant chain of satellites.

- Finally, the actual dust-to-gas mass ratio of the material accreted by Jupiter is largely unknown and, as is shown in the next chapter, would very likely be subsolar. In this case (and again considering the pebble accretion efficiency) not enough material would be processed through the disk in the final stages of Jupiter's formation to build the Galilean moons.

This final point is a weak point of the gas-starved scenario in general but is exacerbated when considering pebble accretion because several times the mass of the Galilean system should be brought to the CPD to actually build the moons. This and related issues are further discussed in the next chapter where we investigate the delivery of solid material to the circum-jovian disk.

Chapter 4

Delivery of solids to the circum-jovian disk

4.1 Introduction

The origin and delivery mechanism of the solid material necessary to build the moons is a crucial issue for the formation of the Galilean system. The spatial and size distributions of satellitesimals in the circum-jovian disk are a main component of models of satellites' growth. The starved and minimum mass models for the formation of the Galilean moons mainly differ in their assumptions regarding the distribution of solids within the CPD. Whereas the starved-disk models rely upon the fact that solid material is constantly deposited within the CPD throughout the satellites' growth, MMSN models assume that enough material to build the whole Galilean system is available at once. Therefore, a better understanding of the delivery of solids to the jovian CPD can put strong constraints on the proposed scenarios of satellites' formation.

The way solid material is delivered to the circum-jovian disk largely depends on its distribution in Jupiter's vicinity at the epoch of formation of the moons. In recent years, new ideas have emerge regarding the growth of giant planets and specifically the formation of planetesimals and subsequent accretion of solids (e.g., Ormel and Klahr 2010, Lambrechts and Johansen 2012, Johansen et al. 2014). These new theories take advantage of the aerodynamic properties of dust grains in protoplanetary disks. Dust particles whose frictional timescale due to interaction with the gas is comparable to their orbital timescale can concentrate into dense filaments in turbulent protoplanetary disks, a process known as the streaming instability. The densest parts of these filaments gravitationally collapse into large planetesimals. These planetesimals would grow by mutual collisions up to the size of Ceres or the Moon, but then it is the accretion of drifting dust grains that will account for most of their growth (Johansen et al. 2015). The collisional cross section of an embryo with a drifting particle is substantially enlarged (as compared to the geometrical cross section) due to the fact that the dust grains lose angular momentum through friction with the gas and can thus spiral into the embryo. This drag assisted accretion is known as pebble accretion and can promote the growth of giant planets' cores ($\sim$10–20 $M_\oplus$) on a timescale much shorter than the typical lifetime of a protoplanetary disk (1–10 My). These theories are attractive because similar particles, the pebbles, are involved in the formation of planetesimals and their further growth. An implication, which seems supported by the observation of young circumstellar disks (see e.g., Testi et al. 2014), is that mm–cm sized dust grains should be the main carriers of the solid mass budget in protoplanetary disks. This new paradigm of giant planets' formation has been intensively studied recently but its implications for the formation of the satellites around giant planets have not been investigated.

Another important point is that the models of formation of the Galilean satellites generally consider the formation and evolution of Jupiter only (although Mosqueira et al. 2010, studied the influence of both Jupiter and Saturn on circumsolar planetesimals in the context of satellites formation). While this approach is interesting to investigate some general mechanisms applicable to any giant planet, it might be inaccurate regarding the delivery of solids to the circum-jovian disk. The other giant planets of the Solar System could have had a great influence on the distribution of solids in Jupiter's vicinity, especially at the epoch of formation of the Galilean satellites.

In this chapter, the issue of the delivery of solid material to the circum-jovian disk in light of the recent theories of giant planets formation is addressed. We begin by discussing the complications introduced by the pebble accretion scenario for the so far proposed mechanisms of solids delivery. Based on our current understanding of giant planets' growth and the evolution of dust in protoplanetary disks, we propose a framework for the delivery of material to Jupiter's CPD which rely on the existence of a massive reservoir of planetesimals at the outer edge of the gap opened by Jupiter in the circumsolar disk and investigate it through N-body simulations.

4.2 Sources of solid material

We discuss in the following the mechanisms of solids delivery proposed by Canup and Ward (2002, 2006) and Mosqueira and Estrada (2003a,b), Mosqueira et al. (2010), generally associated with the gas-starved and MMSN models, respectively. Our framework for the delivery of material to the circum-jovian disk is then introduced.

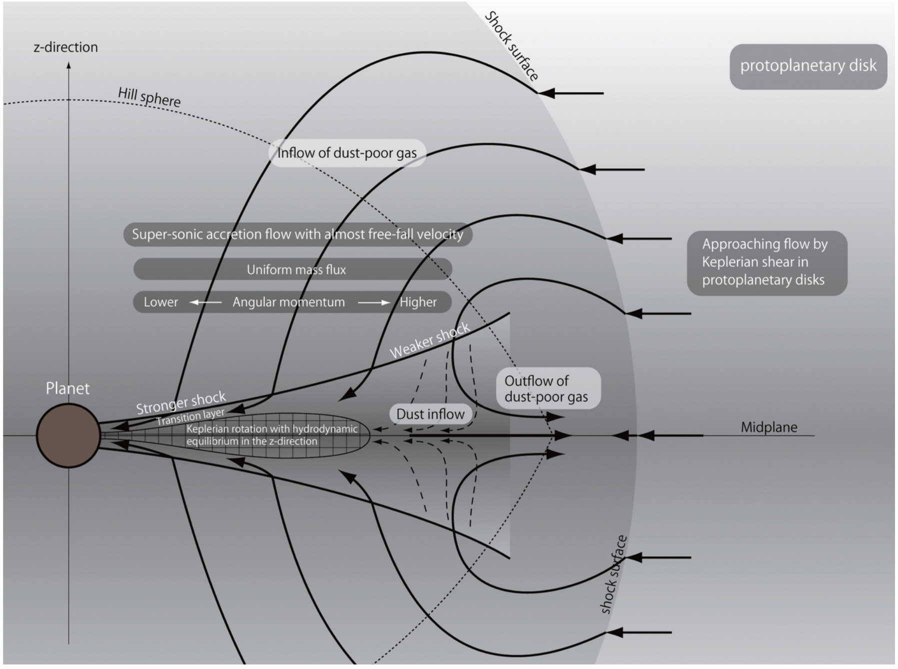

Figure 4.1: Sketch of the late stage accretion of Jupiter and gas flow around the planet and its CPD (from Tanigawa et al. 2012).

4.2.1 Inflow of small dust grains

In the gas-starved model proposed by Canup and Ward (2002, 2006), Jupiter is still accreting material from the circumsolar disk at the time its satellites formed. Therefore, Canup and Ward assume that the CPD is constantly replenished with a mixture of solar composition having a dust-to-gas mass ratio $f = 0.01$. With this assumption, as Jupiter accretes the last ten percents of its current mass, $\sim 3 \times 10^{-1}\ M_{\oplus}$ of solid material would be processed through its CPD which is an order of magnitude larger than the mass of the current Galilean system.

However, the dust-to-gas mass ratio of the material accreted by Jupiter is quite uncertain. Only dust grains that are small enough to couple with the gas flow would be entrained and deposited onto the CPD. Moreover, 3D hydrodynamics simulations of a Jupiter mass planet in a protoplanetary disk show that the gas actually falling onto the CPD mostly originate from heights $\gtrsim H_{\rm g}$ (e.g. Tanigawa et al. 2012, Szulágyi et al. 2014, 2016), where $H_{\rm g}$ is the scale height of the protoplanetary disk's gas. A sketch of the flow pattern is shown on figure (4.1). This finding, combined with the fact that the pressure bump located at the outer edge of Jupiter's gap in the circumsolar disk act as a dust trap for partially decoupled solids (i.e., pebbles, Lambrechts et al. 2014), further constrains the size of the particles that could reach the CPD by following the gas inflow.

The vertical distribution of the dust grains in the circumsolar disk depends on their aerodynamic properties (larger particles will settle towards the midplane of the disk) and the turbulence level of the disk (higher level of turbulence favors the vertical transport of grains). The ratio of the dust scale height H_p to the gas scale height is given by Youdin and Lithwick (2007) as

$$\frac{H_\mathrm{p}}{H_\mathrm{g}} = \sqrt{\frac{\alpha}{\mathrm{St} + \alpha}}. \tag{4.1}$$

Only particles for which the scale height is comparable to that of the gas would be efficiently entrained with the gas accreted onto the CPD, requiring that St $\ll \alpha$. Since it is believed that $\alpha \sim 10^{-4}$–10^{-2} in protoplanetary disks, the criterion for accretion of dust grains is actually more restrictive than St $\ll 1$ advocated by Canup and Ward (2002, 2006). Assuming that the dust size distribution follows a power-law such that $n(a) \propto a^{-\beta}$, where a is the size of a dust grain, the ratio of the mass contained in grains smaller than a given size a_l to the total dust mass is

$$\frac{m(a < a_l)}{m_\mathrm{tot}} = \frac{a_l^{4-\beta} - a_\mathrm{min}^{4-\beta}}{a_\mathrm{max}^{4-\beta} - a_\mathrm{min}^{4-\beta}} \simeq \left(\frac{a_l}{a_\mathrm{max}}\right)^{4-\beta}, \tag{4.2}$$

where the third expression is valid for $a_\mathrm{max}, a_l \gg a_\mathrm{min}$, with a_min and a_max the minimum and maximum grain sizes of the dust size distribution, respectively. In the Epstein drag regime, valid for small grains, the Stokes number is proportional to the grain size so that equation (4.2) can be translated into

$$\frac{m(\mathrm{St} \ll \alpha)}{m_\mathrm{tot}} \ll \left(\frac{\alpha}{\mathrm{St}_\mathrm{max}}\right)^{4-\beta}. \tag{4.3}$$

The dust-to-gas mass ratio of the accreted gas would then be

$$f \ll \epsilon_\mathrm{d}\left(\frac{\alpha}{\mathrm{St}_\mathrm{max}}\right)^{4-\beta} = 2 \times 10^{-2}\left(\frac{\epsilon_\mathrm{d}}{10^{-2}}\right)\left(\frac{\alpha}{10^{-3}} \cdot \frac{0.05}{\mathrm{St}_\mathrm{max}}\right) f_\odot, \tag{4.4}$$

where ϵ_d is the dust-to-gas mass ratio of the circumsolar disk at the location where Jupiter accretes material and we assumed $\beta = 3$. Even if ϵ_d is enhanced locally as compared to the solar value $f_\odot$ due to, e.g., trapping and accumulation of dust at the outer edge of Jupiter's gap, solar metallicity of the gas accreted by Jupiter would be very difficult to achieve.

This issue is very problematic for the scenario proposed by Canup and Ward (2002, 2006). In the previous chapter, we showed that if the main source of solids in the CPD was the inflow of small dust grains, the satellites would grow through pebble accretion as large satellitesimals would not be able to form. Considering the above estimate for the dust-to-gas mass ratio of the material accreted by Jupiter, the total mass of material needed to grow Ganymede would be

$$M_{\rm tot} = \frac{M_{\rm Gan}}{\varepsilon_{\rm PA} f} = 2 \left(\frac{0.2}{\varepsilon_{\rm PA}}\right) \left(\frac{2 \times 10^{-4}}{f}\right) M_{\rm Jup}, \tag{4.5}$$

where $\varepsilon_{\rm PA}$ is the pebble accretion efficiency as derived in equation 3.27 of the previous chapter. It would be impossible to grow the Galilean moons with such an inflow. Even if the inflow was depleted in solids by an order of magnitude as compared to solar, half the mass of Jupiter should be processed through the CPD to build its moons which would render the whole scenario very complicated.

Although dust grains brought with the gas inflow onto the CPD might well have participated in the growth of the Galilean moons, the fact that it was the only, or even the main, source of solid material seems implausible due to the difficulty to form large satellitesimals within the circum-jovian disk (see previous chapter and Shibaike et al. 2017) and the total mass required to build the moons through pebble accretion.

4.2.2 Capture of large planetesimals

A potential mechanism to deliver solid material to the CPD is the capture/ablation of already formed planetesimals located in the vicinity of Jupiter due to either collisions in a gas poor environment (Estrada and Mosqueira 2006) or gas drag within a gas rich CPD (Mosqueira et al. 2010). The latter mechanism is discussed here.

Planetesimals might be captured by Jupiter if they lose sufficient energy while passing close to the planet to become planet-bound. Dissipation due to gas drag as a planetesimal crosses the CPD is the most likely source of energy dissipation. This process has been numerically investigated by several authors (Fujita et al. 2013, D'Angelo and Podolak 2015, Suetsugu et al. 2016, Suetsugu and Ohtsuki 2017). Basically, these studies show that capture of large planetesimals is a viable mechanism that might have provided enough material to build the Galilean satellites. D'Angelo and Podolak (2015) find that most of the solids' mass within the CPD is carried by the largest captured objects with radii ∼100 km in their simulations.

However, all the above mentioned investigations mainly focused on planetesimals initially located in the close vicinity of Jupiter. In the study by D'Angelo and Podolak (2015), where both the circumsolar and circum-jovian gas disks distributions were included, all the planetesimals were initially located in regions that are within the gap opened by Jupiter in the circumsolar disk. The existence of planetesimals in these regions is in fact questionable, especially at the epoch of formation of the Galilean moons. Levison et al. (2010) performed a thorough investigation of embryos' growth in the giant planets region through planetesimals accretion. Their study included many physical processes besides gravitational interactions, such as collisional damping, gas drag and fragmentation. They find that none of these processes can prevent an embryo from efficiently scattering planetesimals in its vicinity, creating a gap in the planetesimal distribution and isolating itself rather than accreting material. Since it is not expected that new generations of planetesimals could form in the direct vicinity of a growing embryo, it results that the feeding zone of a growing giant planet would actually be devoid of large planetesimals.

Suetsugu and Ohtsuki (2017) considered the effect of a gap in the distribution of planetesimals around a fully-formed Jupiter and find that for planetesimals on initially circular orbits (as would be expected following their formation), the capture within the jovian CPD is suppressed. This is problematic considering that the Galilean moons should have formed in the latest stages of Jupiter's formation, when a gap in the planetesimal distribution around Jupiter is expected. It is also important to note that in the current paradigm, specific conditions are needed to trigger planetesimal formation. A probable outcome is that planetesimals could have formed in localized regions of the disk only (e.g., Drążkowska et al. 2016, Drążkowska and Alibert 2017, Schoonenberg and Ormel 2017). The existence of a sea of planetesimals in the giant planets region to feed Jupiter's CPD (Mosqueira et al. 2010) therefore remains hypothetical.

Overall, it seems that a giant planet efficiently isolates itself from the main sources of solid material, dust grains/pebbles and planetesimals, in the late stages of its formation. A consistent picture for the delivery of solids to the circum-jovian disk is hence needed to account for the presence of the massive jovian moons.

4.2.3 Existence of a reservoir of planetesimals close to Jupiter

In the pebble accretion paradigm, the core of Jupiter would have accreted from the radial flux of pebbles drifting toward the Sun (e.g., Lambrechts and Johansen 2012, 2014). Such a growth mechanism would have continued up to the so-called pebble isolation mass. At this point, the core becomes massive enough so as to create a pressure bump outside of its orbit (i.e., it opens a shallow gap) that stalls the inward drift of pebbles and thus terminates efficient accretion of solids (Lambrechts et al. 2014). Once Jupiter's core reached the pebble isolation mass, estimated to be $\sim 20\ M_\oplus$ (Lambrechts et al. 2014) or a factor of a few larger if viscous diffusion of pebbles was important (Bitsch et al. 2018), pebbles remained trapped at the outer edge of its gap and accumulated over time. Lambrechts and Johansen (2014) provides with a simple estimate of the flux of pebbles in the circumsolar disk over time,

$$\dot{M}_{\rm peb} \approx 9.5 \times 10^{-5} \left(\frac{t}{10^6\ \rm yr}\right)^{-1/3} M_\oplus\, \rm yr^{-1}, \tag{4.6}$$

where we only show the dependence with respect to time and assume standard values for the other parameters on which this expression depends. If Jupiter reached the pebble isolation mass at 1 Myr (Kruijer et al. 2017), the above expression implies that as much as $\sim$84 $M_\oplus$ of solids would have accumulated at the outer edge of its gap 1 Myr later. The accumulation of solids at the pressure bump would have provided suitable conditions for the formation of planetesimals (Auffinger and Laibe 2018). Therefore, a (potentially massive) reservoir of planetesimals should have built up over time outside of Jupiter's orbit, whereas the close vicinity of the planet was devoid of material.

It would be surprising were such a reservoir of material to have existed and not play any role in the formation of the jovian moons, the origin of whose building blocks remains elusive. Yet, as demonstrated by Suetsugu and Ohtsuki (2017), if the planetesimals located at the outer edge of Jupiter's gap were on initially circular and coplanar orbits, they would have mainly remained out of the giant planet's reach. However, Jupiter is not the sole giant planet of our Solar System. There is now little doubt that Saturn (and also Uranus and Neptune) was once orbiting closer to Jupiter than it is today (see e.g., Tsiganis et al. 2005, Deienno et al. 2017). Whether the giant planets formed closer together or migrated into a compact configuration remains unclear. In either case however, Saturn could have had a great influence on the dynamics of the planetesimals residing at the outer edge of Jupiter's gap, exciting their orbits and potentially allowing their delivery to the circum-jovian disk. It is this idea that is investigated in the following.

4.3 Delivering planetesimals from the reservoir

Here we present the investigation of the orbital evolution of planetesimals initially located at the outer edge of Jupiter's gap and under the influence of both Jupiter and Saturn. In every scenario investigated, that are presented below, we assumed that Jupiter had acquired its current mass and was located at a fixed heliocentric distance of 5.4 au with initially zero eccentricity and inclination. The heliocentric distance was chosen so as to agree with the later dynamical evolution of the giant planet, suggesting Jupiter was orbiting at 5.4 au from the Sun before migrating inward to its current location at 5.25 au after the dispersal of the circumsolar gas disk (Tsiganis et al. 2005). Assuming a fixed orbit for Jupiter does not imply that the giant planet never suffered from any migration within the gaseous disk. Nevertheless, given the many uncertainties on planetary migration and the detailed history of Jupiter's formation, it seems that such an assumption is reasonable for the purpose of investigating Saturn's influence on the delivery of material to the circum-jovian disk.

Regarding Saturn, we explored two different cases. In the first case, we consider the possibility that Saturn formed at the outer edge of Jupiter's gap, as first proposed by Kobayashi et al. (2012). As mentioned in the previous section, the radial flux of pebbles expected within a typical protoplanetary disk imply that as much as $\sim$84 $M_\oplus$ of material drifted towards the pressure bump within $\sim$1 My after the formation of Jupiter's core. This is potentially more than enough material to build the core of Saturn and the Galilean moons. In the second case, we consider a scenario where Saturn would have formed further from Jupiter and migrated inward until both planets were caught on a mutual mean motion resonance (MMR).

The orbital integrations were performed using the hybrid `HERMES` integrator available with the open source `REBOUND` package[1]. Each simulation included 5,000 planetesimals as test particles spread between 7 and 7.5 au, and their orbits were integrated with a timestep of $10^{-2}/2\pi$ yr[2].

The following acceleration terms were added to the equation of motion of the planets to mimic eccentricity and semimajor axis damping (in the case where Saturn is migrating) due to interaction with the gas disk on prescribed timescales τ_e and τ_mig (e.g., Cresswell and Nelson 2008),

$$\mathbf{a}_\mathrm{mig} = -\frac{\mathbf{v}}{\tau_\mathrm{mig}}, \tag{4.7}$$

$$\mathbf{a}_\mathrm{e} = -2\frac{(\mathbf{v}\cdot\mathbf{r})\mathbf{r}}{r^2\tau_\mathrm{e}}. \tag{4.8}$$

In the above expressions, $\mathbf{v}$ is the velocity vector of the planet, $\mathbf{r}$ its position vector and r the distance to the star. In the case where Saturn is migrating, the eccentricity damping timescale τ_e was taken to be $0.01\,\tau_\mathrm{mig}$ (e.g., Lee and Peale 2002). In other cases, we used $\tau_\mathrm{e} = 5\times10^3$ years for both planets.

We used disk profiles including a Jupiter mass planet and associated gap obtained from 2D hydrodynamic simulations performed with FARGO (Masset 2000). Figure 4.2 shows the gas distribution obtained after 300 orbits of Jupiter. We normalized the disk profiles so that the surface density at 1 AU is $\sim$300 g cm^{-2}, which corresponds to a moderately evolved disk (Bitsch et al. 2015a). We included the effect of aerodynamic drag in the equation of motion of the planetesimals, considering they have a radius of 100 km and a density of 1 g cm^{-3}. The acceleration term due to gas drag is

$$\mathbf{a}_\mathrm{drag} = -\frac{1}{t_s}(\mathbf{v}-\mathbf{v}_g). \tag{4.9}$$

[1] The `REBOUND` code is available at http://github.com/hannorein/rebound

[2] We note that this is the timestep for the simplectic integrator only. Close encounters with the massive planets are handled with the high order adaptive timesteping `IAS15` integrator (Rein and Tamayo 2015, Rein and Spiegel 2015)

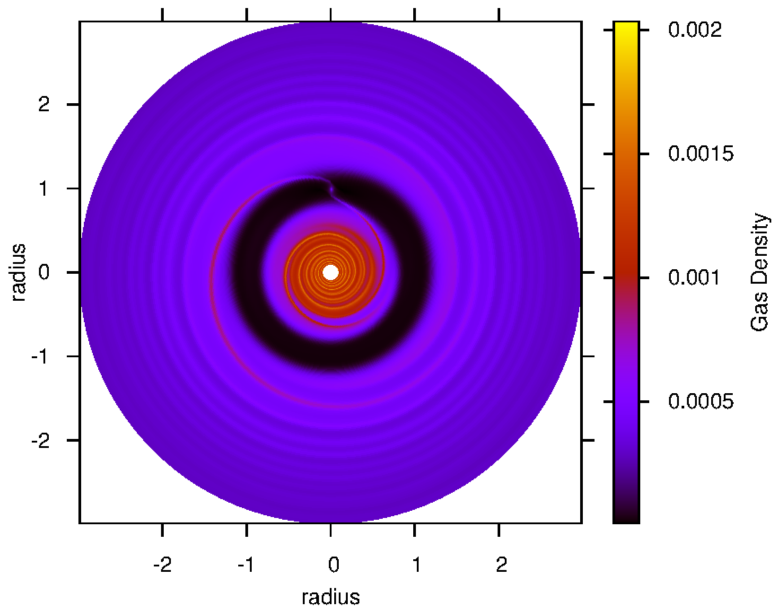

Figure 4.2: Fargo simulation of a Jupiter mass planet in a viscous disk with a constant aspect ratio of 0.05 (i.e., the scale height of the disk normalized by the orbital distance). The turbulent viscosity was accounted for following the prescription of Shakura and Sunyaev (1973) with $\alpha = 2 \times 10^{-3}$. The radius is expressed in terms of the giant planet's semi-major axis and the gas density is in arbitrary units. This gas distribution is obtained after 300 orbits of the planet. The Fargo simulations were run by A. Crida who also kindly provided us with the above figure.

In the above expression, $\mathbf{v}_g$ is the velocity of the gas given by the hydrodynamic simulation when planetesimals are far from Jupiter. When planetesimals are at a distance of 150 $R_{\rm Jup}$ from Jupiter or closer, the gas velocity is found assuming a keplerian velocity around the giant planet to model the interaction with the CPD. The stopping time t_s is computed using the following expression (Perets and Murray-Clay 2011, Guillot et al. 2014),

$$t_s = \left(\frac{\rho_g v_{th}}{\rho_s R_s}\min\left[1, \frac{3}{8}\frac{v_{rel}}{v_{th}}C_D(Re)\right]\right)^{-1}. \tag{4.10}$$

In this expression, R_s is the size of the planetesimal and ρ_s its internal density. The gas density ρ_g is obtained by assuming hydrostatic equilibrium in the vertical direction with an aspect ratio of the disk $h = 0.05$ in the case of the PPD or it is given by the CPD prescription described below when planetesimals are close to Jupiter. The gas thermal velocity is $v_{th} = \sqrt{8/\pi}c_g$, c_g is the isothermal sound speed and v_{rel} is the relative velocity between the gas and the planetesimal, either in the CPD or the PPD. The dimensionless drag coefficient C_D is computed as a function of the Reynolds number Re of the flow around the planetesimal (Perets and Murray-Clay 2011),

$$C_D = \frac{24}{Re}(1+0.27Re)^{0.43} + 0.47\left(1 - e^{-0.04Re^{0.38}}\right), \tag{4.11}$$

$$Re = \frac{4R_s v_{rel}}{c_g l_g}. \tag{4.12}$$

The mean free path of the gas l_g is taken from the prescription of Supulver and Lin (2000).

The CPD density and temperature profiles are taken from the work by Sasaki et al. (2010). The surface density is expressed similarly to Canup and Ward (2002) (see equation 2.5) and the temperature is given by

$$T_d \simeq 225\left(\frac{r}{10\,R_{\rm Jup}}\right)^{-3/4}\left(\frac{\dot{M}_{\rm p}}{10^{-7}\,M_{\rm Jup}\,{\rm yr}^{-1}}\right)^{1/4}\ {\rm K}. \tag{4.13}$$

Sasaki et al. (2010) assumed a nominal value of $\dot{M}_{\rm p} = 2\times10^{-7}\ M_{\rm Jup}\,{\rm yr}^{-1}$ at the time of accretion of the Galilean satellites but here we assume a larger value of $10^{-6}\ M_{\rm Jup}\,{\rm yr}^{-1}$. The CPD thus has a surface density peaking at a few 10^4 g cm^{-2} instead of a few 10^3 g cm^{-2} as in Sasaki et al. (2010). The larger surface density facilitates the capture of large planetesimals and might be representative of the earlier stages of evolution of the CPD. A comparison between the surface density and temperature profiles obtained for the different values of $\dot{M}_{\rm p}$ is shown on Figure (4.3).

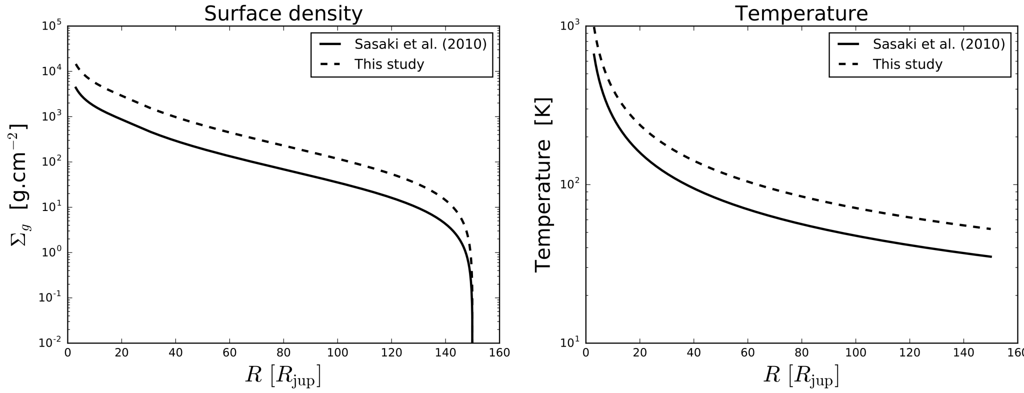

Figure 4.3: *Left.* Comparison between the surface density profile used by Sasaki et al. (2010) (solid line), obtained with $\dot{M}_p = 2 \times 10^{-7}\ M_{\rm Jup}\,{\rm yr}^{-1}$, and the profile used in this study (dashed line) obtained with $\dot{M}_p = 1 \times 10^{-6}\ M_{\rm Jup}\,{\rm yr}^{-1}$. *Right.* Comparison between the temperature profile assumed in this study (dashed line) and that assumed by Sasaki et al. (2010).

We consider that planetesimals are captured within the circum-jovian disk when they are found on a bound orbit with a semi-major axis with respect to Jupiter that is less than 0.2 $R_{\rm Hill}$, where $R_{\rm Hill} = a_{\rm Jup}(M_{\rm Jup}/3M_\odot)^{1/3}$ is the Hill's radius of Jupiter. This quite arbitrary threshold was chosen because it corresponds roughly to the extension of the circum-jovian disk and is plausibly deep enough in Jupiter's potential to consider the objects as permanently captured within the CPD. The orbital parameters of the planetesimals with respect to the Sun or Jupiter are computed using the dedicated tools provided in the `REBOUND` package. Captured planetesimals are removed from the simulation to save computing power and their orbital parameters with respect to Jupiter are stored. In the present study, we have not investigated ablation of planetesimals as they cross the CPD (see, e.g., Mosqueira et al. 2010, D'Angelo and Podolak 2015) and assumed that the captured objects remained intact.

4.3.1 Case 1 : Growth of Saturn at the edge of Jupiter's gap

Here we present the results of simulations considering the growth of a body from a mass of ~1 $M_\oplus$ up to the mass of Saturn and located at a heliocentric distance of 7 au (with Jupiter placed at 5.4 au). The mass of the protoplanet, $M_{\rm Sat}$, is increased on a timescale $\tau_{\rm growth}$ ranging between 10^5–10^6 years following

$$M_{\rm Sat}(t) = M_i + \Delta M\,[1 - \exp(-t/\tau_{\rm growth})]\,, \tag{4.14}$$

where M_i is the initial mass of the core and ΔM is the difference between the initial core mass and the final mass of Saturn. This evolution pathway is very simplified compared to the core accretion model where an envelope is slowly contracted until

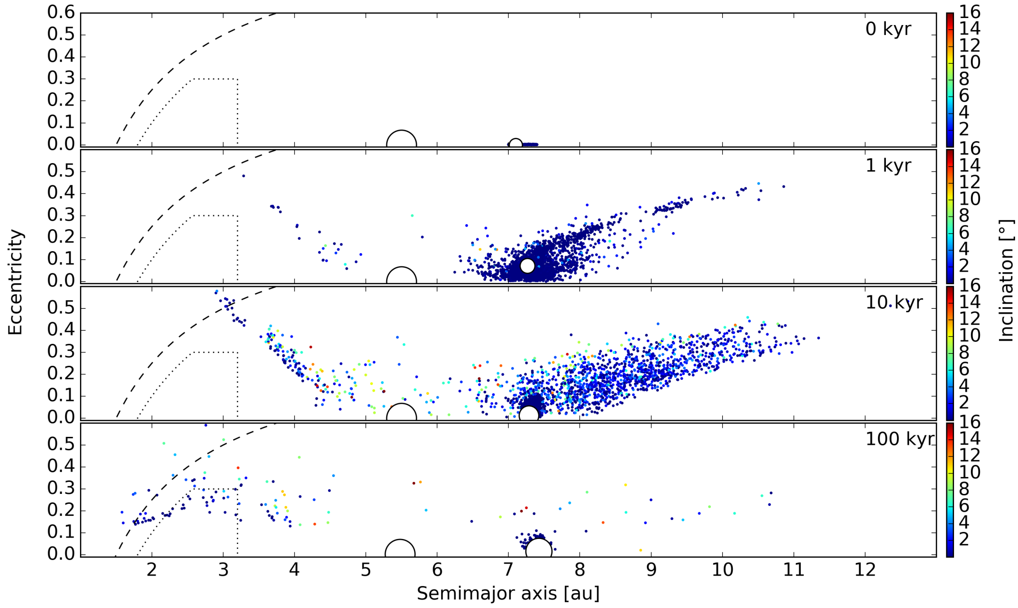

Figure 4.4: Orbital evolution of the planetesimals with Saturn growing at the outer edge of the gap over a timescale $\tau_{\text{growth}} = 5\times10^5$ yr. The orbits of the planetesimals, initially nearly circular, are excited by the growing planet and scattered both inwards and outwards. The excitation of the eccentricity of the planetesimals allows their capture within the circum-jovian disk and injection in the inner Solar System. The dotted box roughly represents the extension of the asteroid belt while the dashed line marks the orbits with $q = 1.5$ au. Planetesimals with a perihelion $q \leqslant 1.5$ au would interact with the embryos of the terrestrial planets, and potentially deliver water to them.

a rapid runaway gas accretion is triggered and then followed by a slower accretion phase when the planet carves a gap in the disk (e.g., Pollack et al. 1996). However, the classical picture of core accretion might be inaccurate due to the fact that the gas and solids distributions are significantly perturbed in the particular case considered here. Detailed investigations would be needed to obtain a more realistic growth pattern but we do not aim here at studying the precise evolution of Saturn. We nevertheless varied the growth timescale to see whether some trends stand out in the final planetesimals distribution.

Figure (4.4) shows the orbital evolution in the semimajor axis-eccentricity plane obtained from a simulation with Saturn growing over a timescale $\tau_{\text{growth}} = 5 \times 10^5$ years. The eccentricity of the planetesimals is excited by Jupiter and the growing core, allowing them to cross Jupiter's orbit and be redistributed inwards or outwards. Some of the planetesimals are implanted in the main asteroid belt, whose boundaries are illustrated by the dotted box in Figure (4.4), and others have orbits that cross the region of terrestrial planets embryos (which were not included in the simulation) marked by the dashed line (see figure legend for details). Issues regarding the implantation of objects in the inner Solar System are further discussed in

$\tau_{\rm growth}$ (year)	Capture	Implantation
1×10^5	8.7%	0.9%
5×10^5	14.8%	1.3%
1×10^6	11.8%	1.8%

Table 4.1: CPD capture (in both prograde and retrograde orbits) and main belt implantation efficiencies for case 1 scenario

the next sections. Here, we are more concerned with the capture of planetesimals within the circum-jovian disk.

A matter of critical importance is the relative number of objects captured by Jupiter with respect to that of objects implanted in the Main Belt. Currently, the mass of the asteroid belt is estimated to be $\sim 5 \times 10^{-4}$ $M_\oplus$ (Krasinsky et al. 2002) whereas the mass of the Galilean system is approximately $\sim 6 \times 10^{-2}$ $M_\oplus$. Although it is expected that the asteroid belt has been depleted in mass throughout its history (Morbidelli et al. 2015b), a scenario where more mass is implanted in the asteroid belt than in the CPD would be hardly reconcilable with the two orders of magnitude more massive Galilean system observed today. Moreover, it is very likely that the accretion of the jovian moons was far from being perfectly efficient, implying that more than the current mass of the Galilean system should have been embedded within the CPD.

The results of the simulations with different growth timescales are summarized in Table 4.1. The CPD capture and Main Belt implantation efficiencies are expressed as a percentage of the total number of objects initially located at the outer edge of Jupiter's gap. In all the cases investigated, we find that approximately one order of magnitude more objects end up captured within the CPD rather than being implanted in the Main Belt. We also note that some planetesimals directly collide with Jupiter in our simulations (and would be subsequently ablated in its envelope) in proportions similar to that of the captured objects. The higher capture efficiency was obtained for Saturn growing on a 5×10^5 years timescale. In this case, considering that a mass equivalent to that of the Galilean system ($\sim 6 \times 10^{-2}\, M_\oplus$) was captured by Jupiter implies an initial mass of planetesimals of $\sim 0.41\, M_\oplus$ in the reservoir and $\sim 5.3 \times 10^{-3}\, M_\oplus$ of material implanted in the main asteroid belt. Considering the efficiencies obtained from different growth timescales yield very similar results with an initial reservoir mass varying from ~ 0.41 to $0.69\, M_\oplus$ and a mass implanted in the asteroid belt varying from $\sim 5.3 \times 10^{-3}$ to $\sim 9.2 \times 10^{-3}\, M_\oplus$. These values are crude order of magnitude estimates as the mass captured within the CPD should be higher than that of the Galilean satellites, unless the accretion was perfectly efficient. The mass implanted in the asteroid belt nevertheless compares

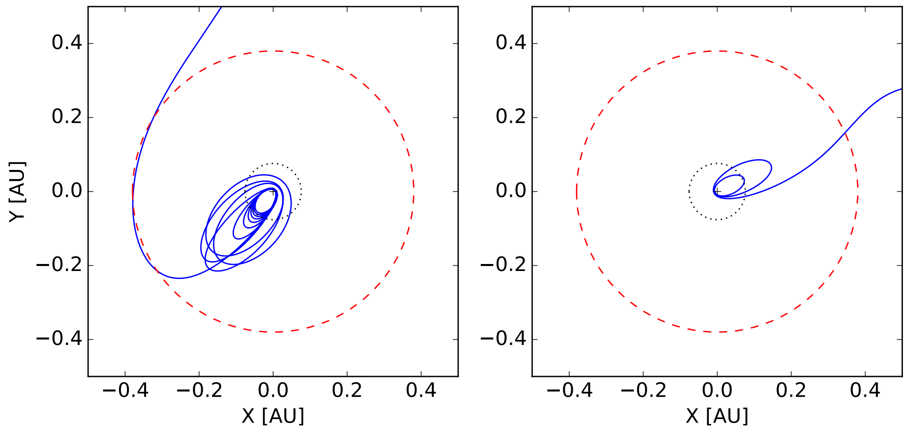

Figure 4.5: Orbits of captured planetesimals in a cartesian plane centered on Jupiter. The dashed red circle is Jupiter's Hill sphere whereas the dotted black circle shows the extension of the CPD. *Left :* Orbit of a planetesimal captured in the prograde direction with respect to Jupiter. *Right :* Orbit of a planetesimal captured in the retrograde direction.

well with that estimated in the Grand Tack scenario of Walsh et al. (2011). These authors find a primordial asteroid belt containing $\sim 4 \times 10^{-3}\, M_{\oplus}$ of planetesimals originating from beyond Jupiter's orbit.

We present here further details about the capture process of planetesimals within the circum-jovian disk. More detailed investigations on the capture process can be found in the studies by Fujita et al. (2013), Suetsugu et al. (2016) and Suetsugu and Ohtsuki (2017), as well as analytical estimates in the Hill's approximation. Gas drag is not efficient enough to allow for the direct capture within the circum-jovian disk of large planetesimals, such as those investigated in the present study, over a single passage through the CPD. Therefore, planetesimals experience a phase where they are captured on large orbits with respect to the extension of the CPD. During this phase, they cross the circum-jovian disk multiple times and their orbit gradually shrinks. Because the drag experienced by a planetesimal having a retrograde orbit with respect to Jupiter is much more efficient than that experienced in the case of prograde orbits (due to the lower relative velocity between the gas and the planetesimal in the latter case), planetesimals on retrograde orbits are more rapidly captured inside the CPD. They are however subsequently rapidly lost to Jupiter due to their fast orbital decay (see next section).

This is illustrated in Figure 4.5 where the orbits of planetesimals captured in the prograde (left panel) and retrograde (right panel) directions are showed. The orbits of these objects were integrated until they were found on bound orbits with a semi-major axis with respect to Jupiter that is smaller than 0.1 R_{Hill}. The orbits were taken from a Case 1 simulation with Saturn growing on a 5.5×10^{5} year timescale.

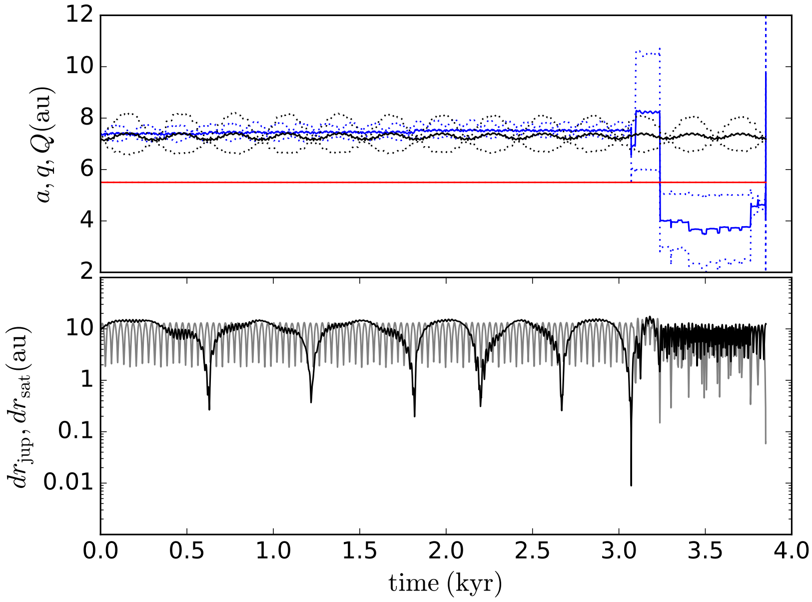

Figure 4.6: *Top :* Evolution of the semimajor axis (a), perihelion distance (q) and aphelion distance (Q) of Jupiter (red), Saturn's core (black) and a planetesimal (blue) finally captured by Jupiter. *Bottom :* Evolution of the radial distance of the planetesimal relative to Jupiter (gray) and Saturn (black).

The planetesimal captured in the prograde direction clearly experienced many more CPD-crossing orbits before reaching our capture threshold than its sibling captured on a retrograde orbit. We note that the capture of large planetesimals, although dependant on their initial energy, generally requires that the objects approach Jupiter at a distance $\lesssim 10^{-2}\, R_{\rm Hill}$ for the CPD's parameters adopted here. To test the sensitivity of the capture efficiencies on the capture threshold imposed, we ran a full Case 1 simulation with a 0.1 $R_{\rm Hill}$ capture threshold. We obtained a capture efficiency of 14.6%, in very good agreement with the results obtained using the less restrictive threshold.

Figure 4.6 shows an example of the heliocentric orbital evolution of a planetesimal before it is captured within the jovian CPD. The top panel shows the evolution of the semimajor axis (solid lines), perihelion and aphelion distances (dotted lines) of Jupiter (red), Saturn's core (black) and the planetesimal (blue). The bottom panel shows the corresponding evolution of the radial distance of the planetesimal relative to Jupiter (gray line) and Saturn's core (black line). Initially, the semimajor axis and the eccentricity of both Saturn's core and the planetesimal oscillate due to their proximity with the outer 3:2 MMR with Jupiter located at ~7.2 AU. The planetesimal experiences a close encounter with Saturn's core after ~3.05 kyr, which can be identified in the bottom panel of Figure 4.6. This interaction yields an abrupt change of the semimajor axis of the planetesimal, from ~7.5 to ~6.9 AU, and an increase of the eccentricity, originally varying around a value of ~0.03, up to a value of ~0.13. This event triggers a more chaotic evolution of the planetesimal which interacts with Jupiter several times, further increasing its eccentricity to values close to 0.4 after it is scattered inward of Jupiter's orbit at 3.24 kyr. Interestingly, the planetesimal experiences two encounters with Jupiter soon before it is captured, at 3.76 and 3.81 kyr, both bringing its semimajor axis closer to that of Jupiter and reducing its eccentricity down to a value of ~0.04. Due to the chaotic evolution of the planetesimals before their capture, a typical evolution is not easy to define but we find that captured planetesimals generally experience a close encounter with Saturn's core, triggering a chaotic phase of evolution during which their eccentricity is high and they interact several times with Jupiter. We find that the eccentricity of a planetesimal is often reduced following a close encounter with Jupiter right before the object is captured and is generally $\lesssim 0.2$ then.

4.3.2 Case 2 : Migration of Saturn toward Jupiter

Another plausible scenario is that Saturn formed further from Jupiter and migrated inwards rapidly (before possibly opening its own gap), thereby catching up with Jupiter until the giants were caught in a mean motion resonance (MMR). Contrary to Case 1, this scenario does not constrain a precise location for the formation of Saturn. The formation of Saturn in the more distant regions of the disk could be the mere result of the initial distribution of material in the disk and the stochastic nature of accretion (e.g., Levison et al. 2015), or, it could be the result of self-organization in the disk when Hall effect is considered. The self-organization results in zonal flows which naturally creates axisymmetric dust traps at different radial distances whose number and locations depends on the magnetic flux and intensity of the Hall effect (Béthune et al. 2016).

To investigate such a scenario, we conducted simulations where Saturn started at 12 AU and then migrated on different timescales towards Jupiter. We considered a fully formed Saturn to highlight the effect of the migration timescale on the final distribution of planetesimals. For the sake of simplicity, we turned off the semimajor axis damping when Saturn is caught in the 2:1 MMR with Jupiter to avoid unphysical crossing of the resonance. Whether Jupiter and Saturn end up in their mutual 2:1 or 3:2 MMR is nevertheless not critical for the delivery of planetesimals. Also, given the many uncertainties in the formation history of the giant planets and considering our very simplified model, we do not aim here at exploring the full range of possible parameters.

Figure 4.7 shows snapshots of the evolution of the system with Saturn migrating on a timescale $\tau_{\mathrm{mig}} = 10^5$ years. The sweeping of the reservoir of planetesimals by

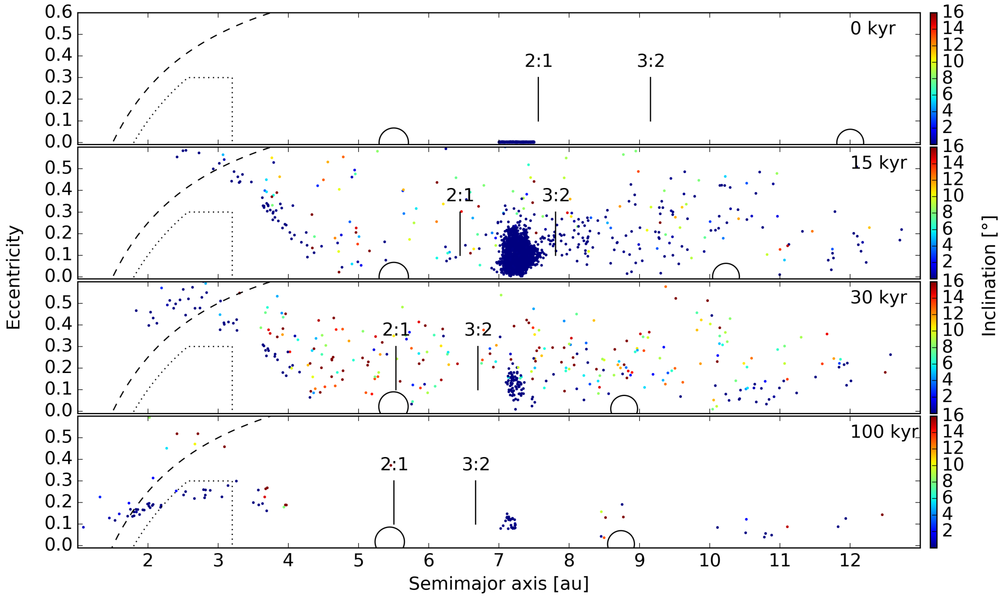

Figure 4.7: Orbital evolution of planetesimals with Saturn migrating towards Jupiter over a timescale $\tau_{\mathrm{mig}} = 10^5$ years. The small vertical lines, labelled 2:1 and 3:2, show the positions of the corresponding MMRs with Saturn. The dashed line and the dotted box are equivalent to those of Figure 4.4. The planetesimals are excited when the reservoir is swept out by the 2:1 and 3:2 MMRs with Saturn after 15 and 30 kyr, respectively.

τ_{mig} (year)	Capture	Implantation
5×10^4	12.9%	0.6%
1×10^5	14.4%	0.4%
5×10^5	9.0%	0.5%

Table 4.2: CPD capture and main belt implantation efficiencies for case 2 scenario

the 2:1 and 3:2 MMRs with Saturn excites the planetesimals' orbits and allows their delivery to the jovian CPD and the inner Solar System. The vast majority of planetesimals have been redistributed after the passage of the 3:2 MMR with Saturn across the reservoir.

The percentage of objects captured within the CPD and implanted in the main asteroid belt at the end of the simulations for different migration timescales of Saturn are summarized in Table 4.2. The capture efficiencies differ from case to case due to the fact that the excitation of the eccentricity of the planetesimals in MMR with Saturn depends on the velocity of the giant planet. In the case where Saturn migrates on a 5×10^5 years timescale, the planetesimals are efficiently captured in the 2:1 MMR and reach very high eccentricities.

In the other cases, the planetesimals are only excited by the 2:1 MMR, they are not captured, and reach lower eccentricities. Therefore, more objects with lower eccentricities remain when the 3:2 MMR with Saturn sweeps the reservoir and this yields slightly higher capture efficiencies. Nevertheless, the differences are not dramatic. The percentage of captured objects varies from ∼14.4% in the most favorable case down to ∼9% for the slow migration case, assessing the robustness of the mechanism against the range of plausible migration rates of Saturn. The implantation of objects in the Main Belt is also comparable for each investigated migration rate with efficiencies that are more than one order of magnitude lower than the CPD capture efficiencies. Similarly to the Case 1 scenario, we find that a number of objects equivalent to that of the captured planetesimals directly collide with Jupiter.

We find that a migration rate $\tau_{\text{mig}} = 10^5$ years yields the highest capture efficiency within the circum-jovian disk with ∼14.4% of planetesimals from the reservoir captured. Considering the captured objects represent the mass of the Galilean system ($\sim 6\times10^{-2}\,M_\oplus$), the initial reservoir should have had a mass of $\sim 0.42\ M_\oplus$ and the mass implanted in the asteroid belt would be $\sim 1.7\times10^{-3}\,M_\oplus$. With the different efficiencies derived, we find that the intial mass of the reservoir would vary from ~ 0.42 to $0.67\ M_\oplus$ and the mass implanted in the asteroid belt from $\sim 1.7\times10^{-3}$ to $3.3\times10^{-3}\,M_\oplus$. These results are very similar to those obtained in the Case 1 scenario with the notable difference that the implantation of objects in the asteroid belt is less efficient.

4.4 Evolution of captured planetesimals

We now investigate the evolution of the planetesimals captured in orbits around Jupiter. For all cases considered, the planetesimals captured within the CPD have initially very eccentric and inclined orbits at large distances from Jupiter. Slightly less than half of the objects captured are actually found in retrograde orbits. Figure 4.8 shows that the distributions of orbital parameters of the objects at the time of their capture are quite similar in the most favorable scenarios of cases 1 and 2. Similar trends were obtained by Suetsugu and Ohtsuki (2017) although they considered that planetesimals initially populate the close vicinity of Jupiter (i.e., the region inside of Jupiter's gap in our configuration) and no other massive object but Jupiter perturbed their orbits. It should be noted that the distribution of objects in Figure 4.8 is not representative of the system at a particular time because the planetesimals were not all captured concurrently. The delivery of planetesimals actually spans $\sim 10^4$–10^5 years depending on the adopted parameters (see Figure 4.9).

To illustrate the subsequent evolution of the captured planetesimals, we conducted simulations centered on Jupiter as the only massive object and integrated

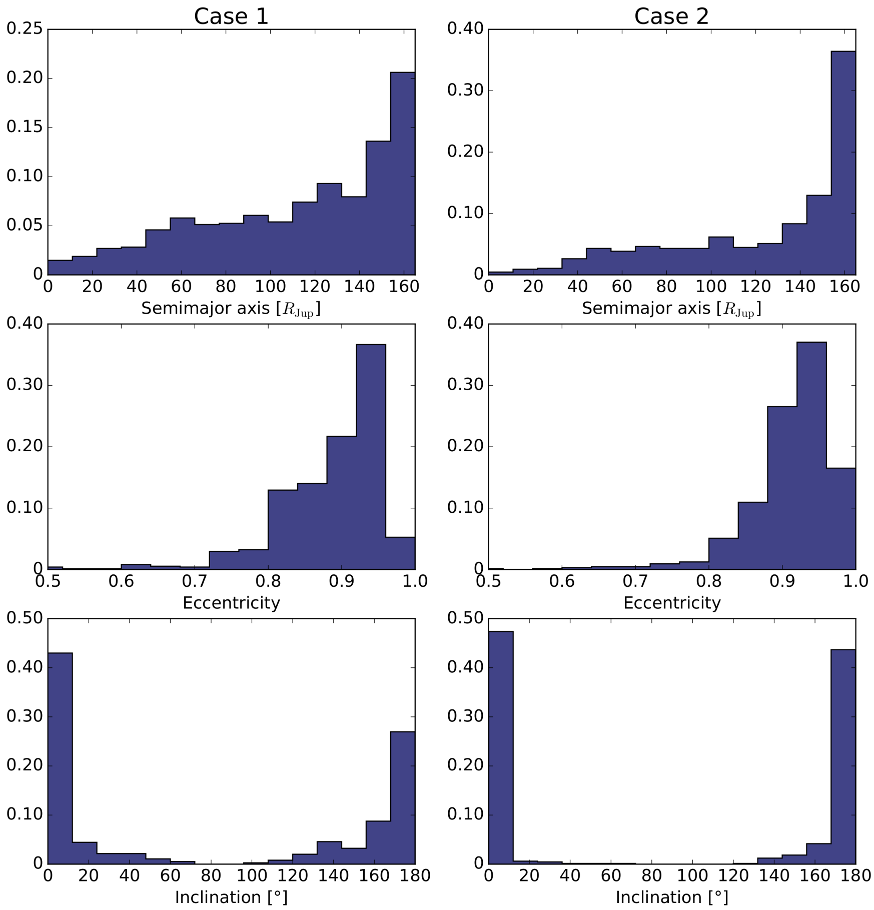

Figure 4.8: Comparison of the orbital parameters of the captured objects in case 1 with $\tau_{\rm growth} = 5 \times 10^5$ years (left) and in case 2 with $\tau_{\rm mig} = 10^5$ years (right). The histograms are normalized according to the total number of captured objects. Both cases exhibit very similar trends with planetesimals initially captured on large, very eccentric and inclined orbits.

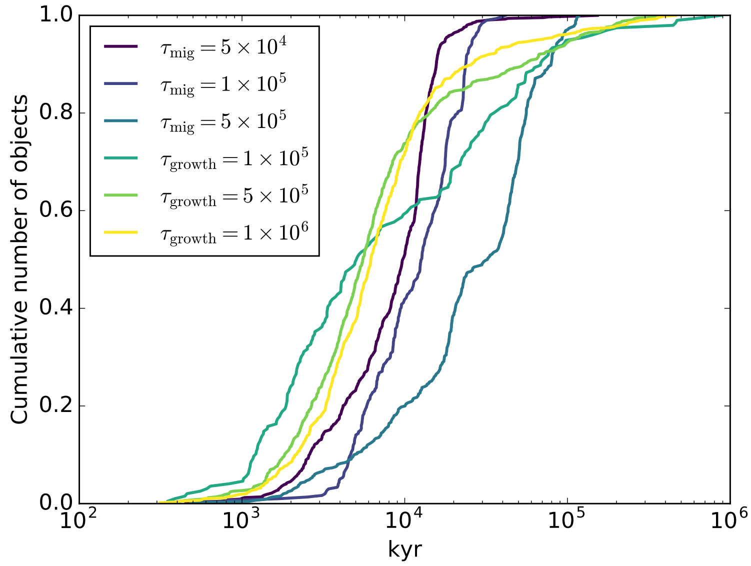

Figure 4.9: Time evolution of the cumulative number of objects captured within Jupiter's CPD in case 1 (formation of Saturn at the gap) and in case 2 (migration of Saturn towards Jupiter), for different parameters investigated. In each scenario, the delivery of planetesimals to the circum-jovian disk spans a few 10^5 years.

the orbits of the planetesimals within the CPD for the most favorable scenario of case 1. The simulation started at the time of capture of the first planetesimal and objects were subsequently added at their corresponding capture time as the simulation evolves. We also assumed a slightly subkeplerian velocity of the gas around Jupiter ($v_{\rm orb} = (1-\eta)v_{\rm kep}$, where η is a measure of the pressure support of the disk and we used $\eta = 0.005$, typical for keplerian disks, Johansen et al. 2014) to account for the potential loss of objects through inward drift due to gas drag. Figure 4.10 shows the distribution of the planetesimals as a function of their distance from Jupiter at different epochs of the CPD's evolution. Objects that are captured on initially retrograde orbits are rapidly lost to Jupiter due to gas drag. On the other hand, the planetesimals initially captured on prograde orbits with large eccentricities and inclinations rapidly circularize and pile up in the inner part of the CPD (c.f., the histogram drawing the distribution of captured objects after 5 kyr of evolution). The hatched region of Figure 4.10 illustrates the current extension of the Galilean system with the inner and outer radial boundaries being the position of Io and Callisto, respectively. Interestingly, the region where planetesimals pile-up matches well that where the Galilean satellites orbit.

After having rapidly reached a maximum at $\sim$5 kyr, the number of objects in the CPD slowly decreases as the planetesimals drift inward due to gas drag faster than the replenishment due to the capture of new objects. The decay is nevertheless

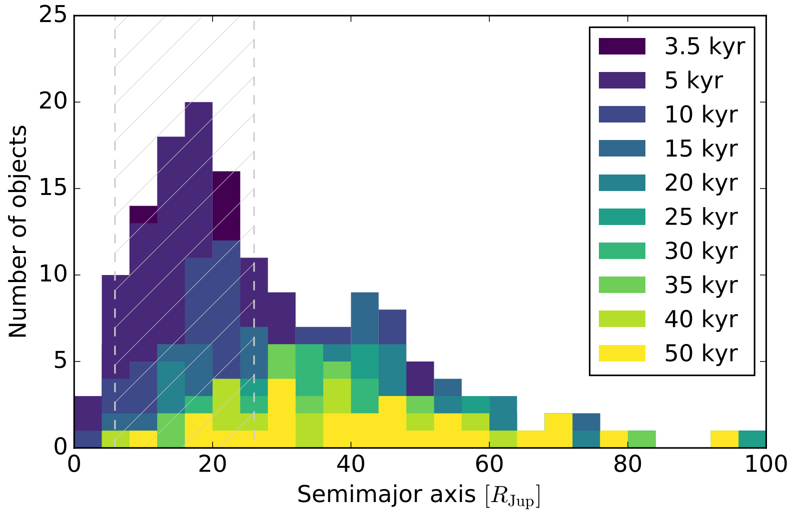

Figure 4.10: Distribution of planetesimals at different epochs in case 1 with $\tau_{\rm growth} = 5 \times 10^5$ years. Each bin is 4 $R_{\rm Jup}$ wide. The hatched region indicates the present day extension of the Galilean system, with the inner and outer edges being the radial positions of Io ($\sim$5.9 $R_{\rm Jup}$) and Callisto ($\sim$26 $R_{\rm Jup}$).

slow compared to the orbital period of the objects which is $\sim$2 days at Io's orbit and $\sim$17 days at Callisto's orbit. The timescale of orbital decay due to gas drag can be estimated as $\tau_{\rm drag} = r\frac{\rm dt}{{\rm d}r}$ with $\frac{{\rm d}r}{\rm dt} = \frac{2{\rm St}}{1+{\rm St}^2}\eta v_{\rm kep}$ (e.g., Weidenschilling 1977), with St the Stokes number of the planetesimal. Considering that St $\gg 1$, relevant for large planetesimals, the decay timescale can be expressed as :

$$\tau_{\rm drag} \sim \frac{1}{2}{\rm St}\frac{T_{\rm orb}}{2\pi\eta} \sim 1.6 \times 10^6 \left(\frac{\rm St}{10^5}\right)\left(\frac{0.005}{\eta}\right) T_{\rm orb} \tag{4.15}$$

In the above expression $T_{\rm orb}$ is the orbital period of the object. On the other hand, Canup and Ward (2002) approximate a satellite's growth timescale as

$$\tau_{\rm acc} \sim 8 \times 10^6 \left(\frac{\rho_s}{2\,{\rm g\,cm^{-3}}}\right)\left(\frac{R_{\rm sat}}{2500\,{\rm km}}\right)\left(\frac{1\,{\rm g\,cm^{-2}}}{\Sigma_s}\right)\left(\frac{10}{F_g}\right) T_{\rm orb}. \tag{4.16}$$

In the latter expression, ρ_s is the mass density of the satellite, $R_{\rm sat}$ its radius, Σ_s is the surface density of solids within the CPD and $F_g = 1 + (v_{\rm esc}/v_{\rm rel})^2$ is the gravitational focusing factor with $v_{\rm rel}$ the relative velocity between satellitesimals and $v_{\rm esc}$ their mutual escape velocity. Therefore, the collisional growth of the objects should have been efficient (i.e., $\tau_{\rm acc} \ll \tau_{\rm drag}$) provided that the surface density of solids was $\gg$ 1 g cm^{-2} which is a rather low value appropriate for starved-disk formation models. Even in the case where each test particle of the simulation would represent a single planetesimal (with mass $\sim 4 \times 10^{18}$ kg), the surface density of

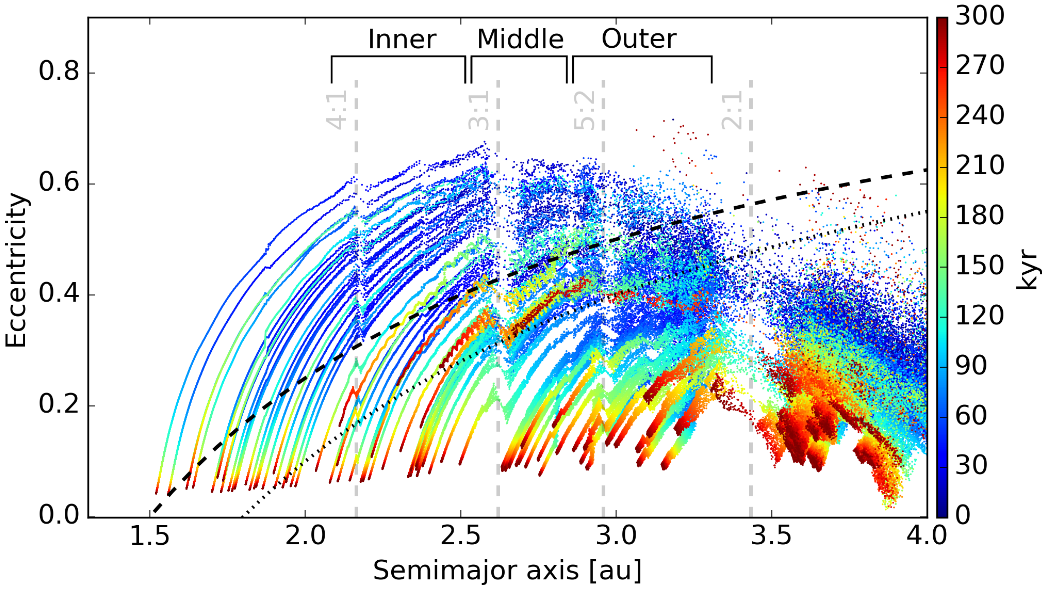

Figure 4.11: Trajectories of planetesimals in the semimajor axis-eccentricity plane of the asteroid belt region. The colors of the dots give an indication of the time. The dotted and dashed lines mark the limit where the periapsis of the orbit is $q = 1.8$ au (roughly the edge of the asteroid belt) and $q = 1.5$ au (region of the terrestrial planets' embryos), respectively. The positions of major mean motion resonances with Jupiter are represented by the vertical dashed lines. These are the resonances that define today's asteroid belt regions, labelled Inner, Middle and Outer in the figure. The different regions are shifted inward as compared to the position of the MMRs because Jupiter is orbiting at $\sim$5.4 au at the end of the simulation, consistently with models of later dynamical evolution of the outer Solar System.

planetesimals between 5–30 $R_{\rm Jup}$ would range between $\sim$10–2 $\mathrm{g\,cm^{-2}}$.

4.5 Discussion

4.5.1 Implantation of planetesimals in the asteroid belt

In Section 4.3, we have shown that for both the formation of Saturn at the outer edge of Jupiter's gap and at further distances, planetesimals from the reservoir are redistributed accross the inner Solar System. Recently Raymond and Izidoro (2017a) proposed that the redistribution of planetesimals by the gas giants is a natural outcome of their formation, providing an explanation for the delivery of water to the terrestrial planets and the presence of primitive C-type asteroids in the outer asteroid belt. The authors demonstrated that some planetesimals were always scattered inward of Jupiter's orbit regardless of the precise growth timescale or migration rates of Jupiter and Saturn in their simulations. However, the planetesimals were initially spread between 2–20 au in their simulations , which is quite different from the distribution we consider in this work. Our results therefore support the findings of Raymond and Izidoro (2017a), showing them to be robust against more specific initial conditions and accounting for the fact that objects might be captured by Jupiter instead of being scattered inward of its orbit.

Figure 4.11 represents the trajectories of planetesimals in the semimajor axis-eccentricity plane in the 1.2–4.0 au region, along with important MMRs with Jupiter and the different regions of the main asteroid belt (inner, middle and outer belt). Our simulations show that planetesimals are not preferentially implanted in the outer region of the Main Belt, where the majority of C-type asteroids are found today. This result should nevertheless be considered with caution for several reasons. First, planetary embryos were not included in our simulations. The planetesimals ending up in the inner parts of the asteroid belt have trajectories that cross the embryos' region, marked by the dashed line in Figure 4.11. The final distribution of objects in the inner belt might be inaccurate due to the fact that the influence of embryos was not accounted for in this work. Second, the C-type spectral group embraces a great diversity of objects with potentially very different origins or formation times (e.g., Vernazza et al. 2017). If the diversity among C-type asteroids indeed traces different origins, it is likely that the different populations were not implanted at the same time, or that some C-type asteroids have formed *in situ* so that not all of the objects from this group were actually implanted in the belt. Finally, we have not implemented the decay of the gas density due to the viscous evolution of the PPD and/or the photoevaporation of the disk. As the density decays, the damping due to gas drag is less efficient and planetesimals can reach more distant regions in the inner solar system (Raymond and Izidoro 2017a). As we used a constant surface density, the planetesimals were implanted quite homogeneously from 1.5 to 3.5 au in our simulations. Along these lines, we note that a decreasing surface density in the inner disk would have the effect of reducing the fraction of objects implanted in the main belt as they would instead reach terrestrial planet crossing orbits. The ratio of objects captured within the jovian CPD to that of objects implanted in the asteroid belt would therefore be higher than found in our simulations in more realistic conditions.

Instead of reasoning in terms of spectral types, Kruijer et al. (2017) proposed that the observed dichotomy in the isotopic ratios of carbonaceous and non carbonaceous meteorites is due to the separation of the formation regions of the parent bodies of these meteorites by Jupiter's core. This way, the two reservoirs of objects could not mix and their isotopic differences were preserved. The authors were able to put new constraints on the formation timescales of the carbonaceous chondrites that would have formed beyond Jupiter's orbit. They showed that the formation of the parent bodies of the carbonaceous meteorites started ∼1 My after the condensation of the CAIs (Carbon and Aluminium rich Inclusions) and ended ∼4 My after CAIs, implying that the reservoir of carbonaceous material has been separated from that of non carbonaceous material for ∼3 My. These constraints can be matched in the framework of our scenario, suggesting that the formation of the parent bodies of carbonaceous chondrites was triggered by the end of the accretion of solid material onto Jupiter's core. From this moment, solids (in the form of pebbles) accumulated at the pressure perturbation induced by the forming planet and eventually collapsed into larger objects. Their injection in the inner solar system was then triggered by either the formation of Saturn's core or its migration in the vicinity of Jupiter. This would naturally account for the delay between the formation of the carbonaceous meteorites parent bodies and their mixing with the non carbonaceous meteorites parent bodies, which formed and remained inside of Jupiter's orbit and were not included in our simulations.

4.5.2 Effect of the surface density of the CPD

Our nominal set of simulations was performed using a CPD with a surface density that is approximately one order of magnitude higher than that of the gas-starved disk proposed by Canup and Ward (2002, 2006), with a peak surface density at $\sim 10^4\ \mathrm{g\,cm^{-2}}$. Such surface densities are still lower than that adopted in the minimum mass model (surface density peak at $\sim 10^6\ \mathrm{g\,cm^{-2}}$, Mosqueira and Estrada 2003a,b). The disk profile we used is likely representative of the stage when Jupiter is still feeding from the surrounding nebula (e.g., Fujii et al. 2017). However, as the PPD's density is supposedly decaying and Jupiter's gap deepening over time, the surface density of the CPD would also decay, leading to a less efficient capture of planetesimals through gas drag. Therefore, the capture efficiencies may be lower than obtained here.

To investigate whether our results are realistic, we ran the case 1 and case 2 scenarios with the optimal parameters, namely $\tau_{\mathrm{growth}} = 5 \times 10^5$ years for case 1 and $\tau_{\mathrm{mig}} = 10^5$ years for case 2, with a CPD profile identical to that of Sasaki et al. (2010). These authors investigated the growth of the Galilean satellites with a semi-analytical model in the context of a slightly modified starved disk scenario. In both simulations, the CPD capture efficiencies dropped to ∼8%. Such efficiencies are still in the range of values obtained by varying Saturn's growth or migration timescale.

In Section 4.4 we showed that planetesimals are delivered over a $\sim 10^5$ years timescale. The capture of large planetesimals would therefore remain efficient if the CPD's surface density does not decay significantly during this timescale (i.e., Jupiter is still accreting gas from the PPD and/or the viscous evolution of the CPD is slow). A more subtle effect that has been ignored in the present study is that planetesimals with different sizes would have different capture efficiencies due to a more or less efficient gas drag braking within the circum-jovian disk. The evolution of the CPD's surface density would likely result in an evolution of the size distribution of captured objects which could affect the subsequent growth of the satellites. More detailed studies, including plausible planetesimal size distributions at the outer edge of Jupiter's gap and evolution of the circum-jovian disk, are needed to determine more realistic conditions of accretion of the Galilean satellites.

4.5.3 Influence of Saturn's growth track

Although we varied Saturn's growth timescale by an order of magnitude when investigating the dynamical evolution of planetesimals, the use of equation (4.14) always implies that the mass doubling timescale of the planet is shorter in the early phases of its growth. As demonstrated by Shiraishi and Ida (2008), a growing planet generally experiences more close encounters with nearby planetesimals if its mass doubling timescale is shorter because the expansion of its Hill sphere is then fast compared to the gap opening timescale in the planetesimals' disk. If the growth of Saturn was initially slow enough, the protoplanet might have carved a gap in the planetesimal's distribution which would have prevented an efficient scattering and delivery of the planetesimals towards Jupiter. Hence, the use of equation (4.14) might overestimate the ability of Saturn's core to scatter nearby planetesimals in the early phases of its growth. We note however that if Saturn's core had grown through pebble accretion, its mass doubling timescale would have indeed been shorter in the early phases of its growth (due to the sublinear dependance of the pebbles accretion rate on the mass of the core, Lambrechts and Johansen 2012) and certainly shorter than the gap opening timescale in the planetesimals' disk.

To assess the robustness of the redistribution of planetesimals against Saturn's growth track, we ran an additional simulation with a qualitatively different growth rate for Saturn. In this simulation, we let Saturn grow according to $M_{\text{sat}}/\dot{M}_{\text{sat}} = 10^6$ years, which yields a very slow initial growth (the mass of the protoplanet is $\sim 2\,M_\oplus$ after $\sim 5\times10^5$ years) and a rapid final assemblage of the planet. The capture efficiency within the CPD obtained was ∼11%, which compares well with the results obtained using equation (4.14). This is due to the fact that the opening of a gap within the planetesimals' disk by the growing core is prevented by nearby Jupiter which stirs the orbits of the objects in the reservoir, maintaining high eccentricities. It is therefore the combined influence of Jupiter and growing Saturn, and not uniquely Saturn's growth, which allows for an efficient redistribution of the planetesimals. The precise growth of Saturn hence has little effect on its ability to scatter nearby planetesimals. We note that an effect which might damp the eccentricities of the planetesimals and was not included in our simulations is collisions among the objects. Taking collisions into account would however require the assumption of an initial mass of the reservoir, considered as unknown in the present study. We leave such a different approach to the problem, and the investigation of the effects of collisions, to future work.

4.5.4 Formation of Saturn's satellite system

Saturn possesses a unique assemblage of regular satellites with a possible dual origin. The small satellites orbiting close to Saturn are thought to have formed from the spreading of ring material across the Roche radius while Titan and Iapetus could have formed via a mechanism similar to those invoked for the formation of the Galilean satellites (Charnoz et al. 2010, Crida and Charnoz 2012, Salmon and Canup 2017). When the two gas giants were close together within the PPD (in their mutual 2:1 or 3:2 MMR), they would have opened a unique and large gap in the disk (Morbidelli and Crida 2007, Pierens et al. 2014). The solids would then be trapped outside of Saturn's orbit, at the outer edge of the common gap opened by Jupiter and Saturn. If enough material remained in the form of pebbles at this time in the PPD, a new reservoir of planetesimals could have built up there. Either the formation of the cores of Uranus and Neptune at the gap, or their migration towards Saturn, could have allowed the delivery of planetesimals from this new reservoir to Saturn's CPD to build Titan and Iapetus.

4.5.5 Implications for the formation of extrasolar moons

In this study, we have pointed out that the gap opened by a giant planet in a PPD efficiently isolates it from the main sources of solid material. In our proposed scenario, the delivery of solids to the giant planet's CPD results from the interaction of a massive object with a reservoir of planetesimals. From this perspective, it is to be expected that the formation of massive moons is not ubiquitous, especially in systems with single or isolated giant planets. Moreover, if a giant planet is orbiting close to its host star, its Hill sphere is reduced and the capture rate of planetesimals could be lowered due to larger orbital velocities, therefore acting against the formation of a massive satellite system.

4.6 Summary

An important step in understanding the formation of the giant planet's satellite systems is to elucidate the origin and delivery mechanism of the solid material needed to build the moons. Here we attempted to revisit the origin and delivery of the building blocks of the Galilean satellites, based on our current understanding of giant planet formation. Our findings can be summarized as follows:

- In Section 4.2, we concluded that the gap opened by Jupiter efficiently isolated the giant planet and its circumplanetary disk from sources of solid material such as pebbles or planetesimals. However, the accumulation of solids at the outer edge of the gap likely translated into a planetesimals reservoir there.

- The planetesimals' orbits were then excited by the formation of Saturn at Jupiter's gap or during its migration towards Jupiter.

- This triggered the redistribution of planetesimals from the reservoir to the circum-jovian disk and the inner Solar System, with a moderate dependency on the input parameters of our model such as the growth timescale of Saturn or its migration rate. Therefore, we find there exists a link between primitive asteroids of the Main Belt and the Galilean satellites, as they shared a common reservoir. This link could be a testable constraint of our scenario by future missions to the jovian system, such as the ESA Juice mission, as some isotopic correspondences (e.g., the D/H ratio in water) should exist between the satellites and the asteroids.

- We find that the planetesimals are initially captured on very eccentric, both prograde and retrograde orbits within the circum-jovian disk. The subsequent gas drag damping of the orbits results in an accumulation of objects in the region where the Galilean satellites are found today.

- The decisive role of Saturn in the delivery of material to the jovian disk has severe implications for the occurence of massive moons around extrasolar giant planets. If our proposed scenario is correct, massive satellites would preferentially form around giant planets in multiple planet systems.

Finally, it appears difficult to disentangle the formation of Saturn at the outer edge of the gap opened by Jupiter from its formation further from Jupiter and subsequent migration considering only the implications for the formation of the Galilean moons. Both scenarios provide quite similar results, although we believe that the case 1 scenario provides a more consistent model for Saturn's formation. Additional constraints should come from more detailed studies of Saturn's growth and the implications of the different formation scenarios on its final composition. In the present study, we left aside some important issues such as the size distribution of planetesimals, the evolution of the circum-jovian disk or the accretion of the satellites. More detailed simulations are needed to assess realistic conditions for the accretion of Jupiter's massive moons.

Chapter 5

Origin of the two martian moons Phobos and Deimos

5.1 A controversial origin

Phobos and Deimos are two small moons (with radii $13.0 \times 11.4 \times 9.1$ km and $7.5 \times 6.0 \times 5.2$ km, respectively) orbiting about Mars on prograde and nearly circular and co-planar orbits lying in Mars' equatorial plane at $\sim$2.8 and $\sim$6.9 Mars radii from their parent planet, respectively. Data collected by the Mariner 9 (1971) and Viking (1976-77) spacecraft seemed to confirm previous suspicions that the physical properties and surfaces of the martian moons resemble that of primitive carbonaceous asteroids (Veverka 1978), hence the idea that both objects originated from the outer asteroid belt and were once captured by Mars. From the perspective of the orbital evolution of the satellites however, the capture scenario is very problematic. Szeto (1983) thoroughly discuss the dynamical issues inherent to the capture hypothesis. The evolution of Deimos' orbit (currently at 6.9 martian radii) due to martian tides over the age of the Solar System is negligible (Goldreich 1965) implying that, were it a captured object, Deimos must have been captured with its current low inclination with respect to Mars' equatorial plane and very low eccentricity ($e \sim 10^{-4}$) which is completely at odd with the expected outcome of gravitational capture (e.g., the irregular satellites of the giants planets are believed to be captured objects and all have eccentricities of at least a few 10^{-1} and large inclinations–with both prograde and retrograde objects). The inclination of Phobos (currently orbiting at 2.8 martian radii) is not expected to have varied much either (Goldreich 1965), making the hypothesis of the capture of the two objects very improbable. Cazenave et al. (1980) show that the inclination of the martian moons must in fact have remained small compared to their Laplacian plane which is close to the ecliptic plane for moons orbiting farther from Mars (due to the important effect of stellar tides) and close to the equatorial plane of Mars for moons orbiting closer to the planet. Therefore, Phobos and Deimos could have been captured from initially heliocentric orbits in the ecliptic plane rather than in the equatorial plane of Mars. This appears as slightly less improbable although the objects of the asteroid belt exhibit a wide distribution of inclinations with respect to the ecliptic. Nevertheless, this does not resolve the issue of Deimos' very low eccentricity. Moreover, Szeto (1983) shows that backward integration of the orbits of Phobos and Deimos under the effect of martian tides result in an unavoidable collision of the two objects in the past which is not reconcilable with Deimos' eccentricity. The only capture scenario that might be reconciled with the present orbits of the martian moons is their drag assisted capture within an extented proto-martian atmosphere (Hunten 1979) or gaseous circum-martian disk (Pollack et al. 1979), similarly to some proposed scenario for the capture of the jovian irregulars (Ćuk and Burns 2004). The formation of a massive gaseous disk around Mars is however not expected and the orbital evolution of Phobos and Deimos following their capture in a martian proto-atmosphere is so fast that this envelope should be removed in a few years to allow for the survival of the satellites (Hunten 1979). Despite such early robust evidence against a capture scenario, the fact that the moons share similar physical properties (low albedo, red and featureless VNIR reflectance, low density) with outer main belt D-type asteroids has kept the capture scenario alive (Fraeman et al. 2012, 2014, Pajola et al. 2013).

Whereas the present orbits of the moons are hardly compatible with a capture scenario, they correspond to the expected outcome of an in situ formation scenario (Goldreich 1965) either as the result of co-accretion or of a large impact. Co-accretion with Mars appears unlikely because Phobos and Deimos would consist of the same building block materials from which Mars once accreted. Those building blocks would most likely comprise water-poor chondritic meteorites (enstatite chondrites, ordinary chondrites) and/or achondrites (e.g., angrites), which are all suspected to have formed in the inner ($\leq$2.5 AU) solar system, namely interior to the snowline. This assumption is supported by the fact that the bulk composition of Mars can be well reproduced assuming ordinary chondrites (OCs), enstatie chondrites and/or angrites as the main building blocks (Sanloup et al. 1999, Burbine and O'Brien 2004, Fitoussi et al. 2016). Yet, OCs as well as the remaining candidate building blocks (enstatite chondrites, angrites) are spectrally incompatible with the martian moons, even if space weathering effects are taken into account (see panel b in Figure 5.1).

It thus appears from above that accretion from an impact-generated accretion disk remains as the only plausible mechanism at the origin of the martian moons. As a matter of fact, the large impact theory has received growing attention in recent years (Craddock 2011, Rosenblatt and Charnoz 2012, Citron et al. 2015, Rosenblatt et al. 2016, Canup and Salmon 2018). This hypothesis is attractive because it could explain the orbital parameters of the satellites as well as some features observed on Mars such as (i) its excess of prograde angular momentum possibly caused by a large impact (Craddock 2011), and (ii) the existence of a large population of oblique impact craters at its surface that may record the slow orbital decay of ancient moonlets formed from the impact-generated accretion disk (Schultz and Lutz-Garihan 1982). Along these lines, Citron et al. (2015) have recently shown that a large impact (impactor with 0.01–0.02 Mars masses) would generate a circum-Mars debris disk comprising ∼1–4% of the impactor mass, thus containing enough mass to form both Phobos and Deimos. Although the impact scenario has become really attractive, it has not yet been demonstrated that it can explain the physical properties and spectral characteristics of the martian moons.

Here, we present the results of an investigation of the mineralogical composition and texture of the dust that would have crystallized in an impact-generated accretion disk. Since there are no firm constraints regarding the thermodynamic properties of the disk, we perform our investigation for various thermodynamic conditions and impactor compositions. We show that under specific disk's pressure and temperature conditions, Phobos and Deimos' physical and orbital properties can be finally reconciled. Several studies on the impact origin of Phobos and Deimos postdate the investigation presented in the following (Rosenblatt et al. 2016, Hyodo et al. 2017a,b, Hyodo and Genda 2018, Hyodo et al. 2018, Canup and Salmon 2018) and their results are discussed at the end of this chapter.

5.2 Formation from a cooling magma

Investigations of the structure of the protolunar disk by Thompson and Stevenson (1988) and Ward (2012, 2014) show that it consists in a melted midplane layer surrounded by a silicate vapor atmosphere. Beyond the Roche limit, gravitational instabilities develop and large clumps can form directly from the melt (e.g. Kokubo et al. 2000, Salmon and Canup 2012). Those clumps then agglomerated to form the Moon. By analogy, we consider that the martian moons might have originated from a melted disk following the impact, in a process similar to that of the Moon's formation. In the case of the Moon, because of internal evolutionary processes (differentiation, convection in the internal magma ocean, etc.), the mineralogical composition and thus the spectral properties of the lunar mantle and crust would differ from that of the clumps formed at the Roche radius. In the Martian case, the situation is different in the sense that the clumps would possess right away a mass/size comparable to that of Phobos and Deimos (Rosenblatt and Charnoz

2012). This implies that the final composition and spectral properties of the Martian moons would directly reflect those of the minerals that crystallized from the magma disk.

5.2.1 Methods

We considered three different compositions for the impactor (see Table 5.1), namely a Mars-like composition (1), a Moon-like composition (2) and an outer solar system composition (3) (i.e., TNO). The latter case would be coherent with an inward migration of a large planetesimal as a consequence of the possible late migration of the giant planets (e.g., Gomes et al. 2005). By analogy with the Earth-Moon system, it has been suggested, however, that the impactor most probably formed near the proto-Mars (Hartmann and Davis 1975, see cases (1) and (2)) but one cannot exclude that the impactor formed elsewhere (3).

In addition, since the relative proportions of the impactor and martian materials are poorly constrained in the resulting disk (Rosenblatt et al. 2016), we considered various proportions between these two materials. We considered two cases, namely a disk exclusively made of the impactor mantle and a half–half fraction. Case (1) complements this sequence by illustrating the case for a 100% fraction of the martian mantle.

To estimate the composition of the solids crystallized from the magma and thus of the moons, we performed a CIPW normative mineralogy calculation (González-Guzmán 2016). This method allows determining the nature of the most abundant minerals that crystallize from an anhydrous melt at low pressure while providing at the same time a good estimate of their final proportions. The CIPW norm calculation is well adapted to our case given that the disk supposedly cooled down slowly through radiation (Ward 2012, 2014), allowing complete crystallization of the minerals. It should be noted that the aim here is not to determine the exact composition of the moons. Considering the few constraints on the system, the purpose is rather to discriminate between plausible and implausible scenarios and thus provide new constraints for future studies.

5.2.2 Results

In this section, we present the inferred mineralogical composition of the moons for the three aforementioned impactor compositions (see Table 5.2) and for the different relative abundances of the impactor and martian mantle.

- *Case 1 (Mars-like impactor)* : Since the impactor has a composition similar to that of Mars, we performed the calculation using a Bulk Silicate Mars (BSM) magma composition (taken from Lodders 2000). The BSM is an estimate of

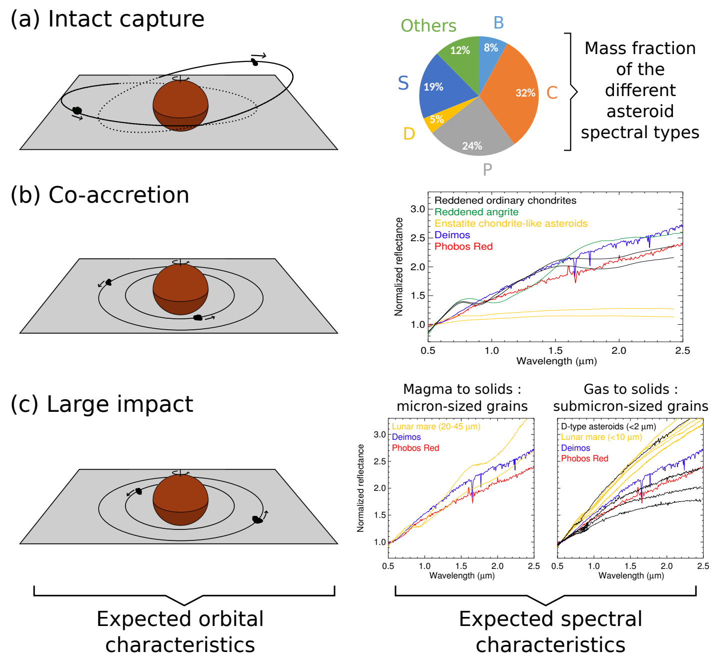

Figure 5.1: Schematic representation of the expected orbital (left) and spectral (right) characteristics of the martian moons for each of the three different scenarios currently invoked for their origin. Note that in the case of Phobos, we display the average spectrum of the red region. The Phobos and Deimos spectra are CRISM/MRO data that were retrieved from PDS: http://pds-geosciences.wustl.edu/. The lunar mare spectra were retrieved from: http://pgi.utk.edu/. The meteorite spectra were retrieved from RELAB: www.planetary.brown.edu/relab/. The asteroid spectra were retrieved from: http://smass.mit.edu/. (a) The intact capture scenario would likely produce retrograde, large, eccentric and inclined orbits. The nearby asteroid belt being a good proxy for the asteroid types that could have been captured, we display the spectral diversity of the latter (DeMeo and Carry 2013). Both D-type asteroids (which are the closest spectral analogs to Phobos and Deimos) and P-types are thought to have formed in the primordial trans-Neptunian disk and to have been injected in the inner solar system during the late migration of the giant planets (e.g., the Nice model; Levison et al. 2009). Such event could have potentially led to a few of these objects being captured as moons by Mars. The problem with this scenario is that P-types are twice as abundant as D-types; the capture of two D-types around Mars rather than two P-types or even one P-type and one D-type is thus not statistically favored. Along these lines, an additional caveat of the capture scenario is that the density of the largest (D $\geq$ 200km) P- and D-type asteroids lies in the 0.8-1.5 g/cm^3 range (Carry 2012). Density decreasing with asteroid size for a given composition (Carry 2012), we would expect the density of Phobos and Deimos to be somewhere in between the density of the comet 67P ($\sim$0.5 g cm^3; Sierks et al. 2015) and the one of the largest P and D-types (Carry 2012), thus clearly below the one of the Martian moons. (b) In the co-accretion scenario, circular and co-planar orbits would be expected and the spectral characteristics of the martian moons would likely resemble those of either reddened ordinary chondrites, reddened angrites or enstatite chondrite-like asteroids (note: enstatite chondrites barely redden via space weathering effects - see Vernazza et al. (2009)). Yet, this is not the case. (c) Within the impact scenario, a condensation directly from a magma (left) would lead to the martian moons having typical lunar mare like spectral properties resulting from the coexistence of fine ($\leq$10 microns; spectrally featureless) and of large ($\geq$10 microns; spectrally feature-rich) olivine and pyroxene grains at their surfaces. Alternatively, gas-to-solid condensation in the external part of the disk (right) would lead to the formation of small grains ($\leq$2 microns) and thus naturally explain the similarity in spectral properties between the moons and both D-type asteroids and fine grained ($\leq$10 microns) lunar soils.

Oxide wt%	BSM[1]	Dep. BSM[2]	Moon[3]	IDP[4]
SiO_2	45.39	17.4	44.60	47.00
MgO	29.71	20.5	35.10	16.8
MnO	–	–	–	0.1
NiO	–	–	–	1.1
Al_2O_3	2.89	2.19	3.90	1.3
TiO_2	0.14	0.09	0.17	–
FeO	17.21	10.55	12.40	24.4
CaO	2.36	1.81	3.30	0.9
Cr_2O_3	–	–	–	0.2
Na_2O	0.98	0.01	0.05	–
K_2O	0.11	0.01	0.004	–
S	–	–	–	7.3
Total	98.79	52.54	99.5	99.09

Table 5.1: [1]Bulk Silicate Mars (Lodders 2000). [2]Depleted BSM estimated for a 50% vaporized disk (Canup et al. 2015). [3]Bulk Silicate Moon (O'Neill 1991). [4]Interplanetary Dust Particle (Rietmeijer 2009).

Minerals wt%	BSM	Dep. BSM	Moon	Moon/BSM	IDP	IDP/BSM
Quartz	–	–	–	–	9.83	–
Plagioclase	11.59	10.45	10.88	11.24	3.62	9.57
Orthoclase	0.66	–	0.02	0.34	–	0.33
Diopside	6.97	–	4.78	5.87	0.76	5.69
Hypersthene	21.29	–	23.24	22.24	66.00	48.86
Olivine	59.22	84.65	60.76	60.01	–	27.58
Magnetite	–	2.97	–	–	4.01	–
Pyrite	–	–	–	–	15.78	7.84
Total	99.73	98.07	99.68	99.70	100	99.87

Table 5.2: Bulk mineral composition resulting from the CIPW norm calculation

the chemical composition of Mars' mantle. By calculating the CIPW norm, we found that both olivine and orthopyroxene (hypersthene) are the main minerals to crystallize (∼59% and ∼21% respectively). Both diopside and feldspar (plagioclase) are also formed although in significantly lower proportions (∼7% and ∼12% respectively).

Note, however, that the above results do not account for a partial vaporization of the disk. The fraction of vaporized material is speculative although theoretical considerations advocate that it should be more than 10% in the case of the protolunar disk (Ward 2012, 2014). To emphasize the role of vaporization on the resulting composition of the building blocks of the moons, we considered the case of a half vaporized disk (see Table 5.1). Its magma composition was derived following the results of Canup et al. (2015) for a Bulk Silicate Earth (BSE) disk's composition. This first order approximation is quantitatively valid as the BSE and a BSM compositions are very similar Visscher and Fegley (2013). By applying the CIPW norm to this new magma composition, we found that significantly more olivine is crystallized (∼85%), whereas both orthopyroxene and diopside do not form. The proportion of feldspar remains, however, the same (∼10%).

- *Case 2 (Moon-like impactor)* : Here, we used the Bulk Silicate Moon composition as a proxy for the impactor composition. For both a 50-50% Moon-Mars mixing ratio and a pure lunar-like composition, we found that both olivine and orthopyroxene (hypersthene) are the main crystallizing minerals (∼60% and ∼22% respectively). In both cases, it thus appears that the derived bulk composition of the moons is very close to the one obtained for a Bulk Silicate Mars disk's composition. Taking into account a partial vaporization of the magma would also lead to results similar to those obtained for *case 1*.

- *Case 3 (TNO-like impactor)* : Here we used the composition of interplanetary dust particles (IDPs; Rietmeijer 2009) as a proxy for the composition of the TNO-like impactor. IDPs which are the likely building blocks of comets may also be the ones of TNOs if one follows the basic and currently accepted assumption that both population formed in the outer solar system. However, by using directly the composition of IDP grains, we neglect the effect of differentiation that has likely occurred on a Moon-sized TNO. This implies that we certainly overestimate the amount of iron in the disk.

  When considering a pure IDP-like composition, quartz crystallizes because of an excess of silica. Indeed, the amount of Mg and Fe does not allow to form enough olivine and pyroxene to account for all the available Si. Moreover, quartz and Mg-rich olivine being mutually exclusive minerals, the absence of one of the two is the norm if the other is formed. In this case, the resulting composition is pyroxene-rich instead of olivine-rich. A substantial amount of pyrite is also formed due to the high proportion of sulfur in IDPs. When considering a 50-50% TNO-Mars mixing ratio, there is no longer an excess of silica. Orthopyroxene remains the most abundant mineral but olivine is formed instead of quartz and in a larger amount.

In summary, we find that for every tested scenario the inferred mineralogical composition of the building blocks of the moons (and thus of the moons) is either olivine-rich or pyroxene-rich. Since minerals that solidify from a slow cooling magma are usually coarse grained (grain size usually in the 10μm-1mm range; see Supplementary Notes; Cashman 1993, Solomatov 2015), our findings imply that if Phobos and Deimos actually formed from a disk of magma, then their spectra –similarly to those of either S-type asteroids or lunar mares– should display detectable 1 and 2 micron bands (see Fig. 1, panel c - left) that are characteristic of the presence of olivine (1 micron) and pyroxene (1 and 2 microns).

Yet, this is not the case. It is very unlikely that space weathering effects –which are more significant at 1 AU than at 1.5 AU– could suppress the olivine and pyroxene absorption bands in the martian moons spectra considering that those effects are not able to suppress them in the lunar ones (Pieters et al. 2000, Yamamoto et al. 2012). We thus conclude that it is highly unlikely that Phobos and Deimos actually formed from a disk of magma. Another argument in disfavor of this scenario is given by the fact that the magma resides inside the Roche limit (at $\sim 3R_{\mathrm{Mars}}$) which in the martian case is located inside the synchronous orbit (at $\sim 6R_{\mathrm{Mars}}$). Thus, the bodies that formed directly from the magma must have impacted Mars a long time ago as a consequence of their orbital decay due to tidal forces (Rosenblatt and Charnoz 2012).

5.3 Formation in an extended gaseous disk

A different formation mechanism is thus required to explain both the current orbits of the moons as well as their spectral characteristics. Of great interest, Rosenblatt and Charnoz (2012) suggested that the moons could have formed in an extended gaseous disk farther from Mars than in the two-phase disk case. Such a disk should be initially hot so that it would thermally expand under pressure gradients and be gravitationally stable beyond the Roche limit. As the disk would thermally expand, it would cool down rapidly. The extended disk would also have a lower pressure and a larger radiative surface allowing, again, a faster cooling than a compact disk residing inside the Roche limit.

In this scenario, the (thermodynamic) conditions under which Phobos and

Deimos formed could have been similar to those that occurred in the protosolar nebula in the sense that small solid grains could have condensed directly from the gas without passing through a liquid (magma) phase (see Supplementary Notes). In this case, Phobos and Deimos would consist of material that has the same texture –not necessarily the same composition– as the one that has been incorporated into comets and D-type asteroids, namely fine grained dust (grain size $\leq$ 2 microns; see Supplementary Notes; Vernazza et al. (2015)). It would therefore not be surprising that these objects share similar physical properties, including i) a low albedo (pv$\sim$0.06) and ii) featureless and red spectral properties in the visible and near-infrared range (see Fig. 5.1 panel c -right, Vernazza et al. (2015)). It is important to stress here that there are currently no available laboratory reflectance spectra in the visible and near-infrared range for sub-micron sized particles. The spectral behavior in this wavelength range can be reproduced via the Mie theory as implemented by Vernazza et al. (2015). These authors showed that a space weathered mixture of sub-micron sized olivine and pyroxene grains would possess spectral properties similar to those of P- and D-type asteroids. Future laboratory measurements will be necessary in order to characterize the reflectance properties of all kinds of minerals (silicates, phyllosilicates, iron oxides, etc..) in order to provide more accurate constraints on the composition of the moons. Note that a further comparison of the Phobos and Deimos spectra with those of fine grained lunar mare soils (grain size $\leq$ 10 microns) reinforces the idea that the moons may effectively be aggregates of sub-micron sized grains. Indeed, although the average grain size of the lunar soils is small ($\leq$ 10 microns), absorption bands at 1 micron are still visible, suggesting that the grains at the surface of the martian moons must be even smaller than these already fine grained lunar samples.

Finally, accretion from such poorly consolidated sub-micron sized material would also naturally explain the low densities ($\sim$1.86 g/cm^3 for Phobos and $\sim$1.48 g/cm^3 for Deimos) and high internal porosities ($\sim$40-50% assuming an anhydrous silicate composition) of the moons (Andert et al. 2010, Rosenblatt 2011, Willner et al. 2014). Importantly, such high porosity is not observed in the case of S-type asteroids with diameters in the 10-30 km size range (a $\sim$20-30% porosity is observed for these objects; Carry 2012), reinforcing the idea that the building blocks of the martian moons must be drastically different in texture from those of S-type asteroids (i.e., OCs).

The fact that the building blocks of the moons should avoid a magma phase provides interesting constraints on the thermodynamic conditions that prevailed inside the disk. Whereas a magma layer inside the Roche limit is not inconsistent with our findings (the moon or moons that would have formed from this layer would have impacted Mars a long time ago), future modeling of the disk should account

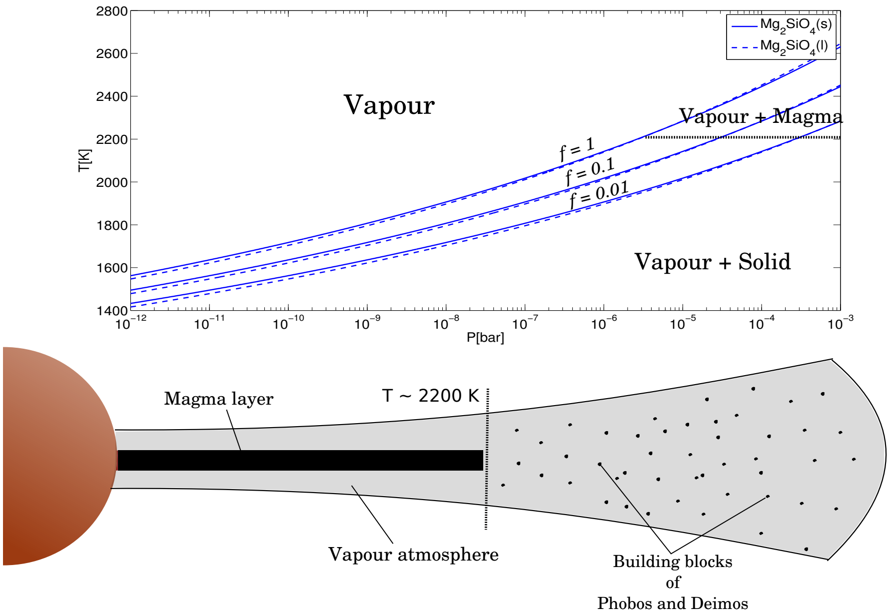

Figure 5.2: Schematic representation of the plausible structure of the accretion disk around Mars. The external part of the disk where Phobos and Deimos may have formed is defined as the region on the right side of the vertical line where the temperature drops below ∼2200 K and solids start to condense. The location of the synchronous orbit shall lie in this extended part of the disk to prevent rapid orbital decay of the moons towards Mars.The equilibrium curves of solid (solid line) and liquid (dotted line) forsterite are shown for different fractions (f) of Mg and Si bound into MgO and SiO_2.

for an extended disk where the pressure and the temperature allow for a direct condensation of the vapor into solid grains.

In order to provide constraints for future models of the martian disk, we determined the pressure-temperature ranges where the gas would directly condense into solid grains assuming a BSM composition of the gas. We restricted our analysis to the condensation of olivine only. Gail (1998) found that olivine would first condense as nearly pure forsterite and iron might be included later on in the solution. We consequently considered the condensation of pure forsterite. The pressure up to which solid or liquid forsterite is stable for a given temperature can be calculated with the following formula:

$$P(T)^3 = \frac{1}{x_{\mathrm{MgO}}^2 x_{\mathrm{SiO_2}} e^{-\Delta G_{s,l}/RT}} \tag{5.1}$$

where $\Delta G_{s,l}$ is the Gibbs free energy of formation of solid or liquid forsterite from gaseous MgO and SiO_2 (it can be calculated with the JANAF online tables), and x_{MgO} and $x_{\mathrm{SiO_2}}$ are the molar fraction of the gases. An extensive chemical model would thus be required in order to infer these molar fraction. As such detailed modeling is beyond the scope of the present work, we simply assumed that different fractions (f) of Mg and Si were bound into MgO and SiO_2 molecules in the gas phase and thus $x_{\mathrm{MgO,SiO_2}} = f\epsilon_{\mathrm{Mg,Si}}$, ϵ being the fraction of the element.

The stability curves are shown in Figure 5.2 for $f = 1$, $f = 0.1$ and $f = 0.01$. The last two cases are more realistic given that Mg is usually found as a free atom whereas Si is mainly found in SiO molecules (Visscher and Fegley 2013). We find that the solid phase of forsterite becomes more stable than the liquid one below a temperature of $\sim 2200\,\mathrm{K}$. At this temperature, the condensation of forsterite occurs at a pressure lower than 10^{-6} to 10^{-3} bar depending on the partial pressures of MgO and SiO_2. P-T profiles of the cooling outer disk must therefore intersect the equilibrium curves shown on Figure 5.2 in this low pressure range to allow for vapor to solid condensation.

5.4 Discussion

Here, we have opened the possibility that gas-to-solid condensation in the external part of an extended gaseous disk is a likely formation mechanism for the martian moons building blocks as it would lead to the formation of small (≤ 2 microns) dust particles. Accretion from such tiny grains would naturally explain the similarity in spectral properties between D-type asteroids (or comets) and the martian moons as well as their low densities. It therefore appears that accretion in the external part of an impact-generated gaseous disk is a likely formation mechanism for the martian moons that would allow reconciling their orbital and physical properties.

Rosenblatt et al. (2016) performed a set of simulations including the impact of Mars with an object with a mass of $0.028\,M_{\mathrm{Mars}}$ and formation of the debris disk, subsequent tidal evolution of the debris disk and formation of large moons at the Roche limit (following the approach developed in Rosenblatt and Charnoz 2012), and accretion of small debris in the outer parts of the disk. They find that the debris disk has a total mass of 5×10^{20} kg, mostly residing inside of the Roche limit, but some material is also found further from Mars and even beyond the synchronous orbit (at $\sim 6R_{\mathrm{Mars}}$). As already pointed out by Rosenblatt and Charnoz (2012), the moon(s) formed from the spreading of material at the Roche limit has a mass of about 10^{19} kg, which is three orders of magnitude larger than the mass of Phobos ($\sim 10^{16}$ kg), and falls back to Mars after about 5 My due to tidal interactions with the planet. This is clearly not a good analogue to the observed martian moons, which is also confirmed by the expected mineralogical and textural properties of such an object which would provide a poor match to Phobos' and Deimos' spectra (fig. 5.1). However, before receding back to Mars, tidal interactions of this massive transient moon with the remaining disk of debris would result in an initially outward migration (Rosenblatt and Charnoz 2012, Rosenblatt et al. 2016). Outer mean motion resonances with this massive object would therefore sweep the outer parts of the disk and promote the accretion of smaller moons at the 2:1 and 3:2 resonances (Rosenblatt et al. 2016). The masses of these smaller moons formed in the outer debris disk and their subsequent evolution under the effects of martian tides are consistent with the observed martian system. These results therefore support our findings that Phobos' and Deimos' properties are likely the consequences of their accretion in the low density and low pressure of the outer debris disk.

Hyodo et al. (2017a) investigated the thermodynamics of the debris disk following the impact as simulated by Rosenblatt et al. (2016). They find that the energy released during the impact may allow for the vaporization of about 5% of the total mass of the debris disk only. The subsequent condensation of this vapor into small submicron grains would nevertheless be sufficient to entirely cover the surface of larger grains (0.1–1 mm) that were not vaporized during the impact (Hyodo et al. 2017a).

Future work should attempt modeling the mineralogy resulting from the gas-to-solid condensation sequence and verify that a space weathered version of the derived composition sieved to sub-micron sized grains is compatible with the spectral properties of the moons. Such investigation would greatly benefit form detailed numerical models that would constrain the thermodynamic properties of a circum-Mars impact generated disk as a function of radial distance.

Finally, it is interesting to note that the proposed scenario is not incompatible with the presence of weak hydration features in the spectra of Phobos and Deimos (Giuranna et al. 2011, Fraeman et al. 2012, 2014). Water has been delivered to the surfaces of most if not all bodies of the inner solar system, including the Moon (Sunshine et al. 2009), Mercury (Lawrence et al. 2013) and Vesta (Scully et al. 2015). It has thus become clear over the recent years, that space weathering processes operating at the surfaces of atmosphere-less inner solar system bodies do not only comprise the impact of solar wind ions and micrometeorites, which tend to redden and darken the spectra of silicate-rich surfaces, but they also comprise contamination and mixing with foreign materials including water-rich ones (Pieters et al. 2014).

Supplementary Notes

Grain size resulting from magma solidification

The grain size of a crystal resulting from magma solidification has been extensively studied and appears closely related to its cooling history. Rapid cooling ($\gtrsim 10^2$ $\mathrm{K\,hr^{-1}}$) will lead to the formation of smaller grains ($\sim 10^{-2}$ mm) whereas slow cooling ($\lesssim 1$ $\mathrm{K\,hr^{-1}}$) will lead to the formation of larger grains (~ 1 mm) as is observed in experimental studies and Earth's samples (Flemings et al. 1976, Cashman and Marsh 1988, Cashman 1993). This is well illustrated in the case of Earth's rocks via basalts and gabbros. These rocks possess the same composition but a very different texture. Basalts are extrusive igneous rocks that experienced rapid cooling either within Earth's atmosphere or oceans and possess a fine-grained structure. On the other end, gabbros are intrusive igneous rocks that crystallized below Earth's surface on much longer timescales and thus exhibit coarse grains.

In the present case, assuming that the temperature of the magma layer is regulated by the disk radiative cooling only, an order of magnitude of the disk cooling rate is :

$$\frac{dT}{dt} = -\frac{2\pi R_{\text{disk}}^2 \sigma_{SB} T_{ph}^4}{M_{\text{disk}} C_v} \sim -1\ \mathrm{K\,hr^{-1}} \tag{5.2}$$

where $R_{\text{disk}} = 3R_{\text{Mars}}$ which is approximately the Roche limit, $\sigma_{SB} = 5.67 \times 10^{-8}\ \mathrm{J\,m^{-2}\,K^{-1}}$ is the Stefan-Boltzmann constant, $T_{ph} = 2000$ K is the temperature of the disk at the photosphere that is maintained at ~ 2000 K throughout its lifetime (Ward 2012), $M_{\text{disk}} = 5 \times 10^{20}$ kg following the results of Citron et al. (2015) and $C_v = 4 \times 10^3\ \mathrm{J\,kg^{-1}\,K^{-1}}$ is the heat capacity of the vapor.

One may also consider that the clumps formed still molten at the Roche limit. In this case, assuming a density $\rho = 3300\ \mathrm{kg\,m^{-3}}$ and heat capacity $C_m = 1200\ \mathrm{J\,kg^{-1}\,K^{-1}}$ for the melt and clumps with typical sizes in the 1-10 km range, an order of mag-

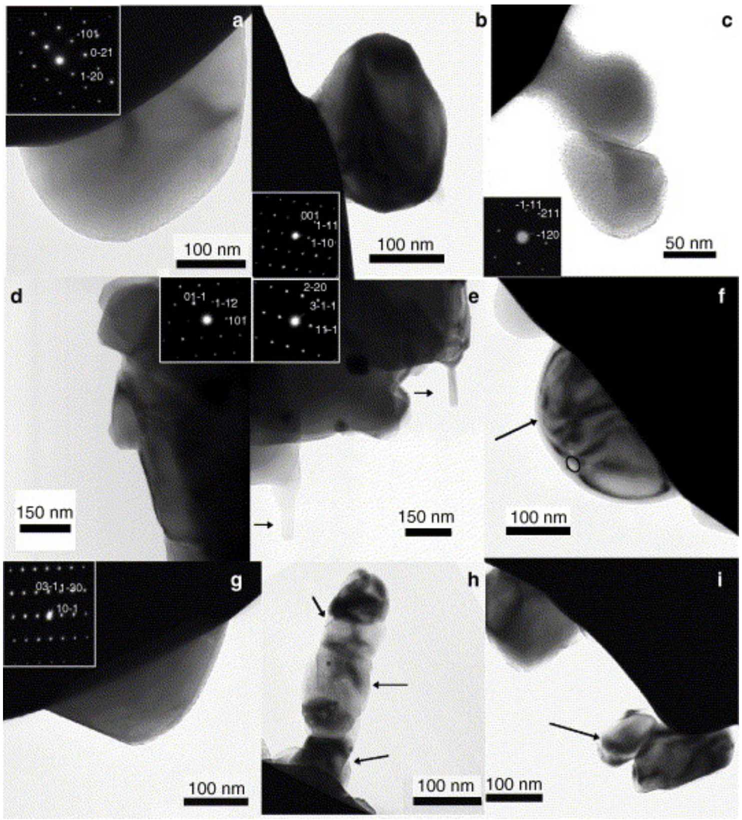

Figure 5.3: Results of condensation experiments of Si-Mg rich vapor near equilibrium performed by Toppani et al. (2006). Each panel corresponds to a different mineral that condensed into a small crystal with typical sizes of a few hundreds nanometers.

nitude of the clump cooling rate would be :

$$\frac{dT}{dt} = -\frac{3\sigma_{SB}T_s^4}{R_{\mathrm{clump}}\rho C_m} \sim -0.2\!-\!2\ \mathrm{K\,hr^{-1}} \tag{5.3}$$

where the largest clumps would possess the slowest cooling rates and vice versa. In either case, the cooling timescales are comparable to those derived from laboratory experiments and the rocks that would have crystallized from the magma should typically exhibit the same grain sizes as those found in magmatic rocks on Earth.

Grain size resulting from vapor condensation

The texture and size of the grains condensing directly from the vapor is, similarly to the solidification from a magma, closely related to the cooling rate of the vapor. Fast cooling will be associated with a high nucleation rate. As such, a rapid decrease of the temperature will imply the condensation of a large number of small grains. On the contrary, if the cooling rate is slow, fewer nuclei will condense but these will grow by continuous condensation of vapor onto their surface which will result, on average, in the development of larger grains. This process has been investigated via both theory (Gail et al. 1984, Gail and Sedlmayr 1988), and laboratory experiments (Rietmeijer et al. 1999a,b, Rietmeijer and Karner 1999, Toppani et al. 2006, De Sio et al. 2016). The theoretical investigations of grain growth in stellar outflows was applied to carbon growth and resulted in grains with sizes in the 10^{-3}–1 μm range (Gail et al. 1984). Concerning the laboratory experiments, two cases have been investigated, a rapid and a slow condensation of silicate rich vapor into solid grains. In the case of rapid condensation which occurs in non-equilibrium, the formation of very small amorphous grains with typical sizes of a few tens to a few hundred nanometers was observed, in agreement with theoretical calculations by Gail et al. (1984). In the case of slow condensation which occurs near equilibrium, the formation of small crystalline grains with typical sizes of a few hundred nanometers was observed (Toppani et al. 2006, fig. 5.3). It therefore appears that - in either case (slow and fast cooling) - small dust grains with typical sizes of $\sim$0.1 microns are the natural outcome of gas to solid condensation. This is also very consistent with the typical grain sizes observed among interplanetary dust particles (Rietmeijer 2009).

Chapter 6

Other contributions. Investigation of the origin of molecular oxygen in cometary ices

6.1 Context

The *Rosetta* spacecraft, managed by the European Space Agency, visited the Jupiter Family Comet (JFC) 67P/Churyumov-Gerasimenko and followed its path around the Sun from August 2014 until September 2016. The unique data collected during the course of the mission confirmed the very primitive nature of comets and their high content in very volatile compounds. The mission also revealed some surprising results. The deuterium-to-hydrogen (D/H) ratio measured in the water released from the nucleus of the comet was found to be about three times higher than the known ratios of other JFCs and generally in the higher range of values inferred for all comets (Altwegg et al. 2015). This D/H ratio is much higher than that of the terrestrial oceans, hence suggesting a limited contribution of comets to the water budget of the Earth. Another surprise came with the detection of molecular oxygen at a high level with respect to water despite the fact that this molecule has never been detected on a comet before (Bieler et al. 2015). The elusive origin of 67P/C-G's oxygen has been first investigated in Mousis et al. (2016) and a subsequent analysis which made use of the particle transport model presented in Chapter 3 is briefly described in the following.

Molecular oxygen (O_2) has been detected in the coma of comet 67P/Churyumov–Gerasimenko (67P/C-G) with abundances in the 1–10% range and a mean value of 3.80 ± 0.85% by the Rosetta Orbiter Spectrometer for Ion and Neutral Analysis-

Double Focusing Mass Spectrometer (ROSINA) instrument on board the Rosetta spacecraft (Bieler et al. 2015). Moreover, the production rate of O_2 has been found remarkably correlated with that of H_2O in 67P/C-G's coma, suggesting that both molecules come from the same icy phase (Bieler et al. 2015). A subsequent reanalysis of the Giotto mass spectrometry data shows that O_2 was also present in the coma of comet 1P/Halley with an abundance of 3.7 ± 1.7% with respect to water at the time of its encounter with the ESA spacecraft, suggesting that this species could be a common parent species in comets (Rubin et al. 2015).

The strong correlation of O_2 with H_2O allows to readily preclude some scenarios for its origin in comets. Pure O_2 ice and O_2 clathrate hydrates, which are two possible icy phases of molecular oxygen (the latter consisting in a cage of water ice within which the molecule is trapped) have sublimation temperatures that are much lower than water ice and are therefore incompatible with an O_2–H_2O correlation (Mousis et al. 2016). A good candidate for the origin of the molecular oxygen detected on comets 67P/C-G and 1P/H is the radiolysis of water ice, i.e., the formation of O_2 following the destruction of water ice molecules by deposition of energy from particles (such as cosmic rays particles). Such an O_2 production mechanism is observed at the surface of the icy Galilean moons (Spencer and Calvin 2002). When produced by radiolysis in water ice, O_2 can be trapped in the voids of the water ice structure whereas hydrogen would rapidly diffuse out, thus preventing further hydrogenation of O_2 and allowing its abundance relative to water to increase over time (Mousis et al. 2016, Bieler et al. 2015). Cosmic rays particles are however unable to deposit energy at depths below a few meters within icy objects such as comets. Bieler et al. (2015) pointed out that a few meters of surface material is lost during each orbit of a comet around the Sun so that radiolysis of cometary ice cannot account for the observed molecular oxygen.

A remaining possibility is that radiolysis occurred on ice grains prior to the accretion of the comets in the protoplanetary disk. The main issue with this scenario is that the cosmic ray flux (CRF) of particles is attenuated by the presence of the disk. It is then questionable whether or not the embedded dust grains would receive enough energy for substantial radiolysis of water ice to occur before the formation of comets. To test this hypothesis, the model of particle transport presented in Chapter 3 has been used to infer the energy dose received by small dust grains as they are lifted above the disk midplane by turbulent motion of the gas.

6.2 Irradiation of grains

To study the irradiation of grain precursors to comets by cosmic rays, we employ a simple protoplanetary disk model where the surface density and temperature

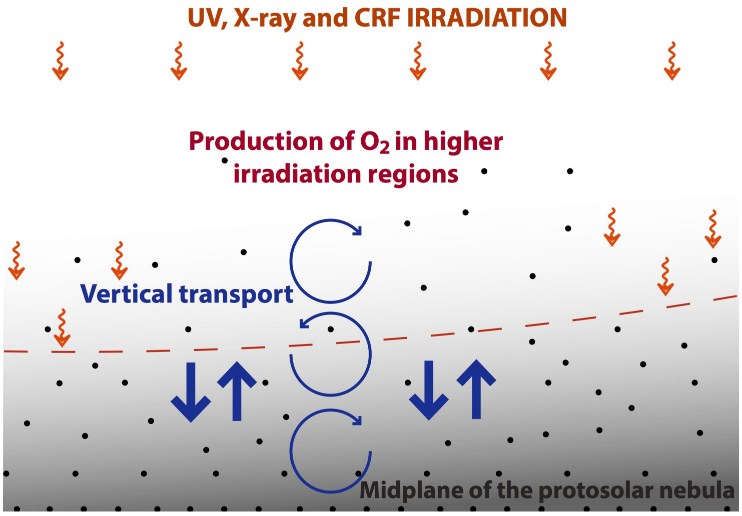

Figure 6.1: Illustration of the mechanism envisioned for the production of O_2 in the precursor grains of comets. Turbulent eddies in the gaseous disk lift the grains above the midplane towards low density regions where the CRF is less attenuated and radiolysis of water ice is more efficient.

profiles are given by power-laws :

$$\Sigma_{\rm g}(r) = 2000 \left(\frac{r}{1\,{\rm au}}\right)^{-1} {\rm g\,cm^{-2}}, \tag{6.1}$$

and

$$T_{\rm d}(r) = 280 \left(\frac{r}{1\,{\rm au}}\right)^{-1/2} {\rm K}. \tag{6.2}$$

The vertical distribution of the gas is inferred from hydrostatic equilibrium,

$$\rho_{\rm g}(r,z) = \frac{\Sigma_{\rm g}}{\sqrt{2\pi}H} \exp\left(-\frac{z^2}{2H^2}\right), \tag{6.3}$$

where $H = c_s/\Omega_{\rm K}$ is the gas scale height and c_s is the isothermal sound speed derived assuming a mean molecular weight of the gas $\mu = 2.4\,{\rm g\,mol^{-1}}$.

Here we are mainly interested in the vertical motion of the dust particles. If particles would remain at the midplane of the disk, they would receive negligible irradiation dose from cosmic rays. Sustained turbulence would however stir the dust grains above the midplane towards regions where the gas density is lower and the CRF is less attenuated, potentially allowing more efficient radiolysis of the water ice (fig. 6.1). We therefore applied equation 3.15 in the z-direction by solving the equation of motion of the particles in the vertical direction :

$$\frac{dv_z}{dt} = -\frac{GMz}{r^3} - \frac{v_z}{t_s}, \tag{6.4}$$

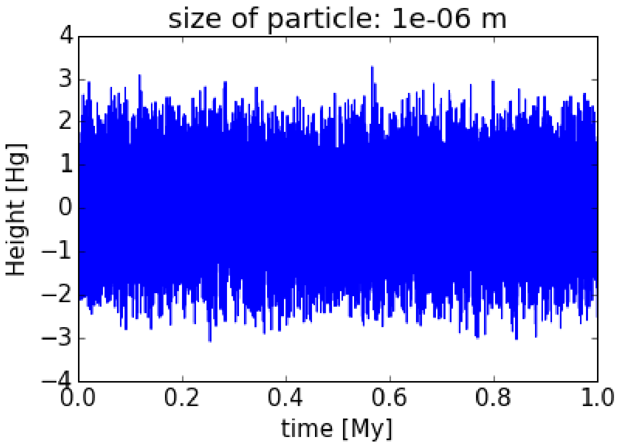

Figure 6.2: Random vertical path of a single micron sized grain located at an orbital distance of 30 au for a turbulent parameter $\alpha = 10^{-2}$. The dust particle is randomly lifted above the midplane of the disk throughout its evolution, reaching heights up to three times the scale height of the disk.

where v_z is the vertical velocity of the dust particle, t_s its stopping time, and M is the mass of the Sun (see chapter 3 for further details). Figure 6.2 shows the example of the vertical trajectory of a single micron sized particle initially released at the midplane of the disk, illustrating the effect of the turbulent stirring.

The energy received by water molecules by million years due to cosmic rays irradiation as a function of the column density of gas σ above the particle is taken from Yeghikyan (2011) and is denoted as $W_{\rm irr}(\sigma)$. At each timestep, the column density of gas above a given particle located at height z' can be calculated as

$$\sigma = \frac{N_A}{\mu} \int_{z'}^{+\infty} \rho_{\rm g}(z) dz, \tag{6.5}$$

where N_A is Avogadro's number. The energy deposited per water molecules during the timestep dt is simply $E_{\rm dep} = W_{\rm irr}(\sigma)dt$. The energy required to alter one water ice molecules is $E_w = 235$eV. Assuming that radiolysis is perfectly efficient at producing O_2, which is unrealistic, the fraction of O_2 produced by the alteration of two water molecules would be

$$\frac{\rm O_2}{\rm H_2O} = \frac{E_{\rm dep(t)}}{2E_w}. \tag{6.6}$$

Figure 6.3 shows the mean abundance of O_2 relative to that of H_2O produced by radiolysis of icy grains with different sizes as a function of time at a fixed orbital distance of 30 au and for turbulent parameters $\alpha = 10^{-2}$–10^{-3}. After 10 My of integration, even the smallest particles reach an O_2/H_2O ratio of $\sim 10^{-4}$ which is two orders of magnitude lower than the value observed in 67P/C-G although a

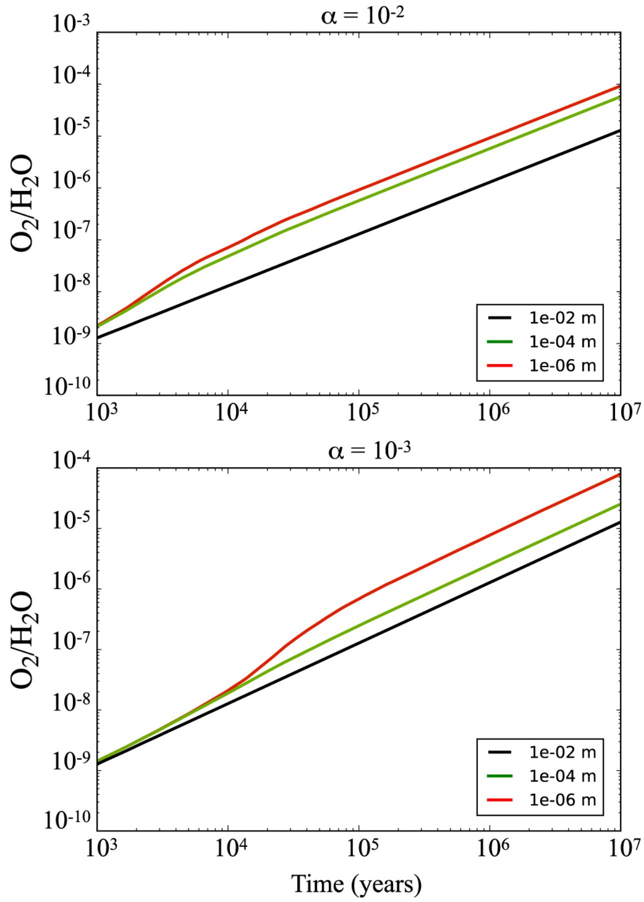

Figure 6.3: Mean abundance of O_2 relative to H_2O in 10^{-6}, 10^{-4}, and 10^{-2} m particles as a function of time in the protoplanetary disk and at an orbital distance of 30 au for α values equal to 10^{-2} (top panel) and 10^{-3} (bottom panel).

perfect efficiency of O_2 production was assumed. Differences in the level of molecular oxygen produced mainly arise from the different efficiencies of turbulent transport of the grains. In the case of the highly turbulent disk with $\alpha = 10^{-2}$, the scale height H_d of the 10^{-6} and 10^{-4} m particles (calculated as the standard deviation of the dust vertical distribution) are almost equivalent and $\sim H$, the gas scale height. For the centimeter sized particles however, $H_\mathrm{d} \sim 0.03H$. In the case of the lower turbulence level, the scale height of the micron sized particles remains equivalent to that of the gas whereas the scale height of 10^{-4} m particles drops to $\sim 0.7H$ which is why the green curve on Figure 6.3 departs more from the red curve in this case. The scale height of centimeter grains is slightly smaller than in the higher level of turbulence case, $H_\mathrm{d} \sim 0.01H$, but those particles basically remain exposed to the same environment close to the midplane in each case. Since the expected lifetime of a protoplanetary disk is 1–10 My, it is very unlikely that radiolysis in the protosolar nebula accounts for the measured level of molecular oxygen in 67P/C-G or 1P/H.

6.3 Discussion

It seems that radiolysis of water ice in the precursor grains of comets within their natal protoplanetary disk is unable to account for the high O_2/H_2O measured in the coma of 67P/C-G and 1P/H. The incorporation of molecular oxygen as pure ice or clathrate hydrate is on the other hand precluded by the strong correlation observed between the release of O_2 and H_2O in the coma of 67P/C-G. Bouquet et al. (2018) explored the possibility of endogenic radiolysis due to the particles emitted by the decay of short- and long-lived radionuclides present in the dust component of the comet. Such a process could at most account for O_2 production at the $\sim$1 percent level relative to water ice over the age of the Solar System.

The remaining possibility is that radiolysis of water ice occurred in the low density environment of the parent molecular cloud of the Solar System before its collapse. This in turn implies that the precursor grains of comets "survived" the collapse of the molecular cloud and remained pristine. Since O_2 is efficiently trapped within the radiation cavities of water ice (Mousis et al. 2016), this pristine nature of grains relative to the presence of molecular oxygen would have been preserved as long as the grains have never been exposed to temperature above that of sublimation of water ice ($\sim$150–160 K). An alternative means of production of O_2 is ice grains surface chemistry within the molecular cloud. This would however require a cloud temperature and density higher than typically expected to account for the observed level of O_2 in comets (Taquet et al. 2016). Either case yields similar conclusions regarding the primordial nature of the molecular oxygen detected and the preservation of the icy grains during the collapse of the parent molecular cloud of the Solar System.

Similarly to O_2, sulphur dimers (S_2) which have been detected in the comae of several comets, including 67P/C-G, might have been produced by radiolysis or photolysis of ice grains in the interstellar medium (Mousis et al. 2017b). Mousis et al. (2017b) showed that S_2 may be stabilized in the voids of either water ice or H_2S ice. Since sulphur dimers might quickly react with other gaseous compounds or be photo-dissociated (in a few hundred seconds; Reylé and Boice 2003), it is important that they remain trapped in the ice to allow for their long-term survival. This reinforces the idea of the pristine nature of the cometary grains, which is also supported by the high deuterium-to-hydrogen ratio measured in the coma of 67P which appears consistent with the expected ratio within interstellar medium water ice.

Chapter 7

Conclusions and perspectives

In the present work, the origin of the regular satellites of Mars and Jupiter was discussed and investigated. In the case of the martian moons, Phobos and Deimos, their confused origin stems from the fact that their orbits are characteristic of an in-situ formation around Mars whereas their physical properties and observed spectra resemble closely that of primitive asteroids, suggesting a capture origin. To alleviate this apparent discrepancy, we propose that their spectra are in fact merely reflecting the abundance of micron sized grains at their surfaces. Such small grains could be produced following a giant impact on Mars provided that enough material was vaporized and subsequently recondensed at low pressure in the outer parts of the debris disk. These conclusions seem to be supported by recent dynamical studies of the formation of Phobos and Deimos in a giant impact scenario, showing that the moons must have accreted in the outer debris disk to account for their current orbits.

The case of the Galilean satellites orbiting around Jupiter is different in the sense that the theories developed in the early 2000s by Canup and Ward (2002, 2006) have been recognized as a plausible and reasonable framework for the formation of satellites around giant planets. Nevertheless, the origin of the satellites of Jupiter are deeply linked with the formation of the giant planet itself and the distribution of gas and solids in its vicinity. New theories have emerged over the past decade regarding the formation of planetesimals and the accretion of planets. Our understanding of the evolution of dust grains in protoplanetary disks and of the gas flow around a Jupiter mass planet have also greatly expanded. As we have shown in Chapter 3, the accretion process of the satellites as investigated by Canup and Ward (2006) is inconsistent with their proposed scenario where the circum-jovian disk is constantly replenished with small dust grains. Pebble accretion provides a better description of satellites growth in the gas-starved scenario due to the fact that the small grains brought in to the CPD with the gas inflow would be unable to grow above pebble sizes (even if the fragmentation of the grains is ignored). We also pointed out that the formation of satellitesimals (which are necessary at some point to provide at least the satellites' seeds) through the streaming instability within the CPD would be very difficult for two reasons. Firstly, in an inflow-regulated disk, the expected dust-to-gas mass ratio is very low (of the order of a few 10^{-4}). This nominal value should be enhanced by two orders of magnitude to meet the conditions where the streaming instability can operate. It is interesting to note that the situation is different from protoplanetary disks where the flux of pebbles is controlled by their growth and drift timescales. Secondly, the gravitational collapse of an overdense dust filament requires densities that are typically three orders of magnitude larger in the CPD than in the asteroid belt region around the Sun. Finally, the efficiency of pebble accretion within the jovian CPD has been estimated and it was shown that at most 20% of the pebble flux would be accreted by a Ganymede mass satellite. This in turn implies that at least 5% of Jupiter's mass in gas and solids should have been processed through the CPD to build the Galilean system if the material accreted by Jupiter had a solar dust-to-gas mass ratio.

In Chapter 4, the delivery of small dust grains to the CPD as proposed by Canup and Ward (2002, 2006) have been questioned and it was shown that it is unlikely that such a mechanism was solely responsible for the formation of the massive Galilean moons. Since the gas inflowing toward the circum-jovian disk mostly originate from the surface of the circumsolar disk (Tanigawa et al. 2012, Morbidelli et al. 2014, Szulágyi et al. 2014), dust growth and settling near the midplane of the disk act against its efficient delivery to the jovian CPD. Instead, we propose a new framework for the delivery of the building blocks of the jovian moons which seems consistent with the recent developments of the theory of giant planets accretion. We postulate that the opening of a gap in the circumsolar disk by Jupiter allowed for the build up of a potentially massive reservoir of planetesimals. In this scenario, the formation of Saturn nearby Jupiter plays a central role in pushing or scattering some of the planetesimals towards Jupiter, a fraction of which are captured within the CPD with the help of gas drag. The drag assisted capture of planetesimals yields orbits with initially large semimajor axes (especially as compared to the current extension of the Galilean system) and eccentricities. Subsequent interactions with the gaseous CPD lead to the circularization of the orbits of the prograde planetesimals closer to Jupiter. This could naturally account for the compactness of the Galilean system with respect to Jupiter's Hill sphere. Reproducing the observed gradient in the composition of the Galilean satellites might be difficult if their building blocks were large icy planetesimals, as discussed in Chapter 3. Either large planetesimals only provided the seeds of the satellites which then accreted smaller objects, or the gradient was established after the formation of the satellites (due to, e.g., tidal heating). This latter possibility has not been quantitatively explored but probably requires stronger heating in Europa's interior in the past to allow for an efficient loss of water from this satellite (Canup and Ward 2009).

It is interesting to note that the architecture of the satellites systems of the other giant planets are very different from that of Jupiter and could be more consistent with their formation from the tidal spreading of ancient and massive rings (Crida and Charnoz 2012). This would make the Galilean system of satellites a unique one in the Solar System as regards their formation mechanism and as reflected by their quite unique architecture. However, the case of Saturn's satellite system appears complicated. Saturn's moon Titan has a mass comparable to that of Ganymede and Callisto and an estimated ice-to-rock mass ratio which is also comparable with that of the outer Galilean moons, suggesting a common formation mechanism. Moreover, forming Titan from the spreading of rings would require initially very massive rings (the origin of which remains elusive) around Saturn and a subsequent tidal evolution of the satellite which is faster than currently expected. On the other hand, the architecture and composition of the inner mid-sized moons of Saturn are very difficult to explain if these latter formed in a gaseous CPD. A possible conclusion is that Saturn's moons formed from both tidal spreading of rings and accretion in a CPD (Crida and Charnoz 2012, Salmon and Canup 2017). In fact, Jupiter also possesses four inner small moons with regular orbits. The origin of these objects does not really fit in the picture envisioned for the Galilean satellites as the larger of those moons, Amalthea, seems to be very icy whereas it orbits well inside the rocky Io (Anderson et al. 2005). Could it be that, similarly to Saturn's system, these inner moons formed from the tidal spreading of ancient icy rings ? This possibility was discarded by Crida and Charnoz (2012) because their semimajor axis-mass distribution does not follow the expected trend resulting from tidal spreading of ring material. However, no detailed long term orbital evolution of these moons was investigated so far. This scenario probably deserves better scrutiny. The differences in the satellites systems of Jupiter and Saturn likely reflect the differences in the evolution of their parent planets and a better understanding of both systems might therefore help in reconstructing the formation history of Jupiter and Saturn. On a similar topic, it is not clear whether or not Uranus and Neptune were once surrounded by a disk that allowed for the formation of satellites. In the scenario depicted by Lambrechts et al. (2014) for their formation, both ice giants would have never reached the pebble isolation mass before the dissipation of the circumsolar disk. The accretional heat would have prevented their contraction and these planets were therefore likely surrounded by an extended envelope rather than a disk. This supports the idea of a different origin of their satellite systems as compared to the Galilean moons.

Future exploration missions towards the martian and Galilean systems of satellites will likely shed light on their origins. The link between primitive asteroids and the Galilean satellites, as we postulated, might be revealed by specific isotopic signatures, such as the ratio of deuterium-to-hydrogen of the satellites' water. Such in-situ measurements could be made possible if Europa exhibits water vapor plumes, as claimed by Jia et al. (2018), allowing to probe its interior. For this purpose, the MASPEX and SUDA instruments on board the NASA Europa Clipper mission (launching planned on 2025) and the PEP instrument on board the ESA Juice mission (launching planned on 2025–2030) will be key instruments. Both missions will explore the Galilean system, the NASA Europa Clipper will be a flyby mission focusing on the moon Europa whereas the Juice mission will aim at characterizing the two outer moons, Ganymede and Callisto. Their mass spectrometers will allow to probe the composition of the exosphere of the moons with a great precision, providing key measurements for assessing the habitability of the moons and better understanding their origin.

Finally, the scenario proposed in Chapter 4 for the delivery of solid material to the circum-jovian disk has important implications for the occurence of analogues to the Galilean moons in extrasolar systems. The presence of massive satellites might not be ubiquitous around giant planets, especially if these latter are isolated. Future surveys dedicated to the detection of massive satellites of extrasolar giant planets might provide important insights on this particular point. Recently, Teachey et al. (2018) estimated an upper limit to the occurrence rate of Galilean analogues around planets orbiting within $\sim$1 au to their host star and find it to be surprisingly low (<0.38 with a 95% confidence and probably closer to 0.16). This could be the first hint that the Galilean satellites are the result of the peculiar architecture of the outer Solar system.

Bibliography

Y. Alibert, O. Mousis, and W. Benz. Modeling the Jovian subnebula. I. Thermodynamic conditions and migration of proto-satellites. *Astronomy&Astrophysics*, 439:1205–1213, September 2005. doi: 10.1051/0004-6361:20052841.

K. Altwegg, H. Balsiger, A. Bar-Nun, J. J. Berthelier, A. Bieler, P. Bochsler, C. Briois, U. Calmonte, M. Combi, J. De Keyser, P. Eberhardt, B. Fiethe, S. Fuselier, S. Gasc, T. I. Gombosi, K. C. Hansen, M. Hässig, A. Jäckel, E. Kopp, A. Korth, L. LeRoy, U. Mall, B. Marty, O. Mousis, E. Neefs, T. Owen, H. Rème, M. Rubin, T. Sémon, C. Y. Tzou, H. Waite, and P. Wurz. 67P/Churyumov-Gerasimenko, a Jupiter family comet with a high D/H ratio. *Science*, 347: 1261952, January 2015. doi: 10.1126/science.1261952.

J. D. Anderson, R. A. Jacobson, T. P. McElrath, W. B. Moore, G. Schubert, and P. C. Thomas. Shape, Mean Radius, Gravity Field, and Interior Structure of Callisto. *Icarus*, 153:157–161, September 2001. doi: 10.1006/icar.2001.6664.

John D. Anderson, Torrence V. Johnson, Gerald Schubert, Sami Asmar, Robert A. Jacobson, Douglas Johnston, Eunice L. Lau, George Lewis, William B. Moore, Anthony Taylor, Peter C. Thomas, and Gudrun Weinwurm. Amalthea's Density Is Less Than That of Water. *Science*, 308:1291–1293, May 2005. doi: 10.1126/science.1110422.

T. P. Andert, P. Rosenblatt, M. Pätzold, B. Häusler, V. Dehant, G. L. Tyler, and J. C. Marty. Precise mass determination and the nature of Phobos. *Geophysical Research Letters*, 37:L09202, May 2010. doi: 10.1029/2009GL041829.

Philip J. Armitage. *Astrophysics of Planet Formation*. Cambridge University Press, 2009. doi: 10.1017/CBO9780511802225.

J. Auffinger and G. Laibe. Linear growth of streaming instability in pressure bumps. *Monthly Notices of the Royal Astronomical Society*, 473:796–805, January 2018. doi: 10.1093/mnras/stx2395.

Xue-Ning Bai. Global Simulations of the Inner Regions of Protoplanetary Disks with Comprehensive Disk Microphysics. *The Astrophysical Journal*, 845:75, August 2017. doi: 10.3847/1538-4357/aa7dda.

Kévin Baillié and Sébastien Charnoz. Time Evolution of a Viscous Protoplanetary Disk with a Free Geometry: Toward a More Self-consistent Picture. *The Astrophysical Journal*, 786:35, May 2014. doi: 10.1088/0004-637X/786/1/35.

Steven A. Balbus and John F. Hawley. A Powerful Local Shear Instability in Weakly Magnetized Disks. I. Linear Analysis. *The Astrophysical Journal*, 376:214, July 1991. doi: 10.1086/170270.

Amy C. Barr and Robin M. Canup. Constraints on gas giant satellite formation from the interior states of partially differentiated satellites. *Icarus*, 198:163–177, November 2008. doi: 10.1016/j.icarus.2008.07.004.

K. Batygin. On the Terminal Rotation Rates of Giant Planets. *The Astronomical Journal*, 155:178, April 2018. doi: 10.3847/1538-3881/aab54e.

W. Béthune, G. Lesur, and J. Ferreira. Self-organisation in protoplanetary discs. Global, non-stratified Hall-MHD simulations. *Astronomy & Astrophysics*, 589: A87, May 2016. doi: 10.1051/0004-6361/201527874.

William Béthune, Geoffroy Lesur, and Jonathan Ferreira. Global simulations of protoplanetary disks with net magnetic flux. I. Non-ideal MHD case. *Astronomy&Astrophysics*, 600:A75, April 2017. doi: 10.1051/0004-6361/201630056.

A. Bieler, K. Altwegg, H. Balsiger, A. Bar-Nun, J. J. Berthelier, P. Bochsler, C. Briois, U. Calmonte, M. Combi, J. de Keyser, E. F. van Dishoeck, B. Fiethe, S. A. Fuselier, S. Gasc, T. I. Gombosi, K. C. Hansen, M. Hässig, A. Jäckel, E. Kopp, A. Korth, L. Le Roy, U. Mall, R. Maggiolo, B. Marty, O. Mousis, T. Owen, H. Rème, M. Rubin, T. Sémon, C. Y. Tzou, J. H. Waite, C. Walsh, and P. Wurz. Abundant molecular oxygen in the coma of comet 67P/Churyumov-Gerasimenko. *Nature*, 526:678–681, October 2015. doi: 10.1038/nature15707.

T. Birnstiel, C. P. Dullemond, and F. Brauer. Gas- and dust evolution in protoplanetary disks. *Astronomy&Astrophysics*, 513:A79, April 2010. doi: 10.1051/0004-6361/200913731.

T. Birnstiel, H. Klahr, and B. Ercolano. A simple model for the evolution of the dust population in protoplanetary disks. *Astronomy&Astrophysics*, 539:A148, March 2012. doi: 10.1051/0004-6361/201118136.

B. Bitsch, A. Johansen, M. Lambrechts, and A. Morbidelli. The structure of protoplanetary discs around evolving young stars. *Astronomy & Astrophysics*, 575: A28, March 2015a. doi: 10.1051/0004-6361/201424964.

B. Bitsch, A. Morbidelli, A. Johansen, E. Lega, M. Lambrechts, and A. Crida. Pebble-isolation mass: Scaling law and implications for the formation of super-Earths and gas giants. *Astronomy&Astrophysics*, 612:A30, April 2018. doi: 10.1051/0004-6361/201731931.

Bertram Bitsch, Michiel Lambrechts, and Anders Johansen. The growth of planets by pebble accretion in evolving protoplanetary discs. *Astronomy&Astrophysics*, 582:A112, October 2015b. doi: 10.1051/0004-6361/201526463.

A. Bouquet, O. Mousis, B. Teolis, G. Nicolaou, O. Ozgurel, F. Pauzat, Y. Ellinger, T. Ronnet, and J. H. Waite. Limits on the contribution of endogenic radiolysis to the presence of molecular oxygen in comet 67P/Churyumov-Gerasimenko. *The Astrophysical Journal*, accepted, 2018.

Benjamin C. Bromley and Scott J. Kenyon. Terrestrial Planet Formation: Dynamical Shake-up and the Low Mass of Mars. *The Astronomical Journal*, 153:216, May 2017. doi: 10.3847/1538-3881/aa6aaa.

Peter N. Brown, G. D. Byrne, and A. C. Hindmarsh. Vode: A variable-coefficient ode solver. *SIAM J. Sci. Stat. Comput.*, 10(5):1038–1051, September 1989. ISSN 0196-5204. doi: 10.1137/0910062. URL http://dx.doi.org/10.1137/0910062.

Thomas H. Burbine and Kevin M. O'Brien. Determining the possible building blocks of the Earth and Mars. *Meteoritics and Planetary Science*, 39:667–681, May 2004. doi: 10.1111/j.1945-5100.2004.tb00110.x.

Joseph A. Burns. Where are the Satellites of the Inner Planets? *Nature Physical Science*, 242:23–25, March 1973. doi: 10.1038/physci242023a0.

R. M. Canup and W. R. Ward. Formation of the Galilean Satellites: Conditions of Accretion. *The Astronomical Journal*, 124:3404–3423, December 2002. doi: 10.1086/344684.

R. M. Canup and W. R. Ward. A common mass scaling for satellite systems of gaseous planets. *Nature*, 441:834–839, June 2006. doi: 10.1038/nature04860.

R. M. Canup and W. R. Ward. *Origin of Europa and the Galilean Satellites*, page 59. 2009.

Robin Canup and Julien Salmon. Origin of Phobos and Deimos by the impact of a Vesta-to-Ceres sized body with Mars. *Science Advances*, 4:eaar6887, April 2018. doi: 10.1126/sciadv.aar6887.

Robin M. Canup, Channon Visscher, Julien Salmon, and Jr. Fegley, Bruce. Lunar volatile depletion due to incomplete accretion within an impact- generated disk. *Nature Geoscience*, 8:918–921, December 2015. doi: 10.1038/ngeo2574.

Daniel Carrera, Anders Johansen, and Melvyn B. Davies. How to form planetesimals from mm-sized chondrules and chondrule aggregates. *Astronomy&Astrophysics*, 579:A43, July 2015. doi: 10.1051/0004-6361/201425120.

B. Carry. Density of asteroids. *Planetary and Space Science*, 73:98–118, December 2012. doi: 10.1016/j.pss.2012.03.009.

Katharine V. Cashman. Relationship between plagioclase crystallization and cooling rate in basaltic melts. *Contributions to Mineralogy and Petrology*, 113:126–142, January 1993. doi: 10.1007/BF00320836.

Katharine V. Cashman and Bruce D. Marsh. Crystal size distribution (CSD) in rocks and the kinetics and dynamics of crystallization II: Makaopuhi lava lake. *Contributions to Mineralogy and Petrology*, 99:292–305, July 1988. doi: 10.1007/BF00375363.

A. Cazenave, A. Dobrovolskis, and B. Lago. Orbital history of the Martian satellites with inferences on their origin. *Icarus*, 44:730–744, December 1980. doi: 10.1016/0019-1035(80)90140-2.

S. Charnoz, J. Salmon, and A. Crida. The recent formation of Saturn's moonlets from viscous spreading of the main rings. *Nature*, 465:752–754, June 2010. doi: 10.1038/nature09096.

Sébastien Charnoz, Laure Fouchet, Jérôme Aleon, and Manuel Moreira. Three-dimensional Lagrangian Turbulent Diffusion of Dust Grains in a Protoplanetary Disk: Method and First Applications. *The Astrophysical Journal*, 737:33, August 2011. doi: 10.1088/0004-637X/737/1/33.

E. Chiang and A. N. Youdin. Forming Planetesimals in Solar and Extrasolar Nebulae. *Annual Review of Earth and Planetary Sciences*, 38:493–522, May 2010. doi: 10.1146/annurev-earth-040809-152513.

F. J. Ciesla. Two-dimensional transport of solids in viscous protoplanetary disks. *Icarus*, 200:655–671, April 2009. doi: 10.1016/j.icarus.2008.12.009.

F. J. Ciesla. Residence Times of Particles in Diffusive Protoplanetary Disk Environments. I. Vertical Motions. *The Astrophysical Journal*, 723:514–529, November 2010. doi: 10.1088/0004-637X/723/1/514.

F. J. Ciesla. Residence Times of Particles in Diffusive Protoplanetary Disk Environments. II. Radial Motions and Applications to Dust Annealing. *The Astrophysical Journal*, 740:9, October 2011. doi: 10.1088/0004-637X/740/1/9.

Robert I. Citron, Hidenori Genda, and Shigeru Ida. Formation of Phobos and Deimos via a giant impact. *Icarus*, 252:334–338, May 2015. doi: 10.1016/j.icarus.2015.02.011.

Robert A. Craddock. Are Phobos and Deimos the result of a giant impact? *Icarus*, 211:1150–1161, February 2011. doi: 10.1016/j.icarus.2010.10.023.

P. Cresswell and R. P. Nelson. Three-dimensional simulations of multiple protoplanets embedded in a protostellar disc. *Astronomy & Astrophysics*, 482:677–690, May 2008. doi: 10.1051/0004-6361:20079178.

A. Crida and S. Charnoz. Formation of Regular Satellites from Ancient Massive Rings in the Solar System. *Science*, 338:1196, November 2012. doi: 10.1126/science.1226477.

Matija Ćuk and Joseph A. Burns. Gas-drag-assisted capture of Himalia's family. *Icarus*, 167:369–381, February 2004. doi: 10.1016/j.icarus.2003.09.026.

G. D'Angelo and M. Podolak. Capture and Evolution of Planetesimals in Circumjovian Disks. *The Astrophysical Journal*, 806:203, June 2015. doi: 10.1088/0004-637X/806/2/203.

N. Dauphas and A. Pourmand. Hf-W-Th evidence for rapid growth of Mars and its status as a planetary embryo. *Nature*, 473:489–492, May 2011. doi: 10.1038/nature10077.

A. De Sio, L. Tozzetti, Ziyu Wu, A. Marcelli, M. Cestelli Guidi, G. Della Ventura, Haifeng Zhao, Zhiyun Pan, Wenjie Li, Yong Guan, and E. Pace. Physical vapor deposition synthesis of amorphous silicate layers and nanostructures as cosmic dust analogs. *Astronomy&Astrophysics*, 589:A4, May 2016. doi: 10.1051/0004-6361/201527222.

R. Deienno, A. Morbidelli, R. S. Gomes, and D. Nesvorný. Constraining the Giant Planets Initial Configuration from Their Evolution: Implications for the Timing of the Planetary Instability. *The Astronomical Journal*, 153:153, April 2017. doi: 10.3847/1538-3881/aa5eaa.

F. E. DeMeo and B. Carry. The taxonomic distribution of asteroids from multi-filter all-sky photometric surveys. *Icarus*, 226:723–741, September 2013. doi: 10.1016/j.icarus.2013.06.027.

F. E. DeMeo and B. Carry. Solar System evolution from compositional mapping of the asteroid belt. *Nature*, 505:629–634, January 2014. doi: 10.1038/nature12908.

J. Drążkowska and Y. Alibert. Planetesimal formation starts at the snow line. *Astronomy&Astrophysics*, 608:A92, December 2017. doi: 10.1051/0004-6361/201731491.

J. Drążkowska, Y. Alibert, and B. Moore. Close-in planetesimal formation by pile-up of drifting pebbles. *Astronomy&Astrophysics*, 594:A105, October 2016. doi: 10.1051/0004-6361/201628983.

P. C. Duffell, Z. Haiman, A. I. MacFadyen, D. J. D'Orazio, and B. D. Farris. The Migration of Gap-opening Planets is Not Locked to Viscous Disk Evolution. *The Astrophysical Journal Letters*, 792:L10, September 2014. doi: 10.1088/2041-8205/792/1/L10.

C. Dürmann and W. Kley. Migration of massive planets in accreting disks. *Astronomy&Astrophysics*, 574:A52, February 2015. doi: 10.1051/0004-6361/201424837.

A. Dutrey, D. Semenov, E. Chapillon, U. Gorti, S. Guilloteau, F. Hersant, M. Hogerheijde, M. Hughes, G. Meeus, H. Nomura, V. Piétu, C. Qi, and V. Wakelam. Physical and Chemical Structure of Planet-Forming Disks Probed by Millimeter Observations and Modeling. In *Protostars and Planets VI*, page 317, January 2014. doi: 10.2458/azu_uapress_9780816531240-ch014.

C. A. Dwyer, F. Nimmo, M. Ogihara, and S. Ida. The influence of imperfect accretion and radial mixing on ice:rock ratios in the Galilean satellites. *Icarus*, 225:390–402, July 2013. doi: 10.1016/j.icarus.2013.03.025.

P. R. Estrada and I. Mosqueira. A gas-poor planetesimal capture model for the formation of giant planet satellite systems. *Icarus*, 181:486–509, April 2006. doi: 10.1016/j.icarus.2005.11.006.

Caroline Fitoussi, Bernard Bourdon, and Xueying Wang. The building blocks of Earth and Mars: A close genetic link. *Earth and Planetary Science Letters*, 434:151–160, January 2016. doi: 10.1016/j.epsl.2015.11.036.

M.C. Flemings, R.G. Riek, and K.P. Young. Rheocasting. *Materials Science and Engineering*, 25:103 – 117, 1976. ISSN 0025-5416. doi: https://doi.org/10.1016/0025-5416(76)90057-4. URL http://www.sciencedirect.com/science/article/pii/0025541676900574.

A. A. Fraeman, R. E. Arvidson, S. L. Murchie, A. Rivkin, J. P. Bibring, T. H. Choo, B. Gondet, D. Humm, R. O. Kuzmin, N. Manaud, and E. V. Zabalueva. Analysis of disk-resolved OMEGA and CRISM spectral observations of Phobos and Deimos. *Journal of Geophysical Research (Planets)*, 117:E00J15, October 2012. doi: 10.1029/2012JE004137.

A. A. Fraeman, S. L. Murchie, R. E. Arvidson, R. N. Clark, R. V. Morris, A. S. Rivkin, and F. Vilas. Spectral absorptions on Phobos and Deimos in the visible/near infrared wavelengths and their compositional constraints. *Icarus*, 229: 196–205, February 2014. doi: 10.1016/j.icarus.2013.11.021.

N. Fray and B. Schmitt. Sublimation of ices of astrophysical interest: A bibliographic review. *Planetary and Space Science*, 57:2053–2080, December 2009. doi: 10.1016/j.pss.2009.09.011.

S. Fromang, W. Lyra, and F. Masset. Meridional circulation in turbulent protoplanetary disks. *Astronomy&Astrophysics*, 534:A107, October 2011. doi: 10.1051/0004-6361/201016068.

Y. I. Fujii, H. Kobayashi, S. Z. Takahashi, and O. Gressel. Orbital Evolution of Moons in Weakly Accreting Circumplanetary Disks. *The Astronomical Journal*, 153:194, April 2017. doi: 10.3847/1538-3881/aa647d.

T. Fujita, K. Ohtsuki, T. Tanigawa, and R. Suetsugu. Capture of Planetesimals by Gas Drag from Circumplanetary Disks. *The Astronomical Journal*, 146:140, December 2013. doi: 10.1088/0004-6256/146/6/140.

H. P. Gail. Chemical reactions in protoplanetary accretion disks. IV. Multicomponent dust mixture. *Astronomy&Astrophysics*, 332:1099–1122, April 1998.

H. P. Gail and E. Sedlmayr. Dust formation in stellar winds. IV. Heteromolecular carbon grain formation and growth. *Astronomy&Astrophysics*, 206:153–168, November 1988.

H. P. Gail, R. Keller, and E. Sedlmayr. Dust formation in stellar winds. I - A rapid computational method and application to graphite condensation. *Astronomy&Astrophysics*, 133:320–332, April 1984.

Charles F. Gammie. Layered Accretion in T Tauri Disks. *The Astrophysical Journal*, 457:355, January 1996. doi: 10.1086/176735.

M. Giuranna, T. L. Roush, T. Duxbury, R. C. Hogan, C. Carli, A. Geminale, and V. Formisano. Compositional interpretation of PFS/MEx and TES/MGS thermal infrared spectra of Phobos. *Planetary and Space Science*, 59:1308–1325, October 2011. doi: 10.1016/j.pss.2011.01.019.

P. Goldreich and S. Tremaine. Disk-satellite interactions. *The Astrophysical Journal*, 241:425–441, October 1980. doi: 10.1086/158356.

Peter Goldreich. Inclination of satellite orbits about an oblate precessing planet. *The Astronomical Journal*, 70:5, February 1965. doi: 10.1086/109673.

R. Gomes, H. F. Levison, K. Tsiganis, and A. Morbidelli. Origin of the cataclysmic Late Heavy Bombardment period of the terrestrial planets. *Nature*, 435:466–469, May 2005. doi: 10.1038/nature03676.

Renée González-Guzmán. NORRRM: A Free Software to Calculate the CIPW Norm. *Open Journal of Geology*, 6:30–38, 2016. doi: 10.4236/ojg.2016.61004.

O. Gressel, R. P. Nelson, N. J. Turner, and U. Ziegler. Global Hydromagnetic Simulations of a Planet Embedded in a Dead Zone: Gap Opening, Gas Accretion, and Formation of a Protoplanetary Jet. *The Astrophysical Journal*, 779:59, December 2013. doi: 10.1088/0004-637X/779/1/59.

T. Guillot, S. Ida, and C. W. Ormel. On the filtering and processing of dust by planetesimals. I. Derivation of collision probabilities for non-drifting planetesimals. *Astronomy & Astrophysics*, 572:A72, December 2014. doi: 10.1051/0004-6361/201323021.

Tristan Guillot. THE INTERIORS OF GIANT PLANETS: Models and Outstanding Questions. *Annual Review of Earth and Planetary Sciences*, 33:493–530, January 2005. doi: 10.1146/annurev.earth.32.101802.120325.

Brad M. S. Hansen. Formation of the Terrestrial Planets from a Narrow Annulus. *The Astrophysical Journal*, 703:1131–1140, September 2009. doi: 10.1088/0004-637X/703/1/1131.

Lee Hartmann, Gregory Herczeg, and Nuria Calvet. Accretion onto Pre-Main-Sequence Stars. *Annual Review of Astronomy and Astrophysics*, 54:135–180, September 2016. doi: 10.1146/annurev-astro-081915-023347.

William K. Hartmann and Donald R. Davis. Satellite-Sized Planetesimals and Lunar Origin. *Icarus*, 24:504–515, April 1975. doi: 10.1016/0019-1035(75)90070-6.

John F. Hawley, Charles F. Gammie, and Steven A. Balbus. Local Three-dimensional Magnetohydrodynamic Simulations of Accretion Disks. *The Astrophysical Journal*, 440:742, February 1995. doi: 10.1086/175311.

Y. Hori and M. Ikoma. Gas giant formation with small cores triggered by envelope pollution by icy planetesimals. *Monthly Notices of the Royal Astronomical Society*, 416:1419–1429, September 2011. doi: 10.1111/j.1365-2966.2011.19140.x.

R. Hueso and T. Guillot. Evolution of protoplanetary disks: constraints from DM Tauri and GM Aurigae. *Astronomy&Astrophysics*, 442:703–725, November 2005. doi: 10.1051/0004-6361:20041905.

Donald M. Hunten. Capture of Phobos and Deimos by photoatmospheric drag. *Icarus*, 37:113–123, January 1979. doi: 10.1016/0019-1035(79)90119-2.

H. Hussmann, C. Sotin, and J.I. Lunine. 10.18 - interiors and evolution of icy satellites. In Gerald Schubert, editor, *Treatise on Geophysics (Second Edition)*, pages 605 – 635. Elsevier, Oxford, second edition edition, 2015. ISBN 978-0-444-53803-1. doi: https://doi.org/10.1016/B978-0-444-53802-4.00178-0. URL https://www.sciencedirect.com/science/article/pii/B9780444538024001780.

Ryuki Hyodo and Hidenori Genda. Implantation of Martian Materials in the Inner Solar System by a Mega Impact on Mars. *The Astrophysical Journal*, 856:L36, April 2018. doi: 10.3847/2041-8213/aab7f0.

Ryuki Hyodo, Hidenori Genda, Sébastien Charnoz, and Pascal Rosenblatt. On the Impact Origin of Phobos and Deimos. I. Thermodynamic and Physical Aspects. *The Astrophysical Journal*, 845:125, August 2017a. doi: 10.3847/1538-4357/aa81c4.

Ryuki Hyodo, Pascal Rosenblatt, Hidenori Genda, and Sébastien Charnoz. On the Impact Origin of Phobos and Deimos. II. True Polar Wander and Disk Evolution. *The Astrophysical Journal*, 851:122, December 2017b. doi: 10.3847/1538-4357/aa9984.

Ryuki Hyodo, Hidenori Genda, Sébastien Charnoz, Francesco C. F. Pignatale, and Pascal Rosenblatt. On the Impact Origin of Phobos and Deimos. IV. Volatile Depletion. *The Astrophysical Journal*, 860:150, June 2018. doi: 10.3847/1538-4357/aac024.

S. Ida and T. Guillot. Formation of dust-rich planetesimals from sublimated pebbles inside of the snow line. *Astronomy&Astrophysics*, 596:L3, November 2016. doi: 10.1051/0004-6361/201629680.

André Izidoro, Sean N. Raymond, Arnaud Pierens, Alessandro Morbidelli, Othon C. Winter, and David Nesvorny'. The Asteroid Belt as a Relic from a Chaotic Early Solar System. *The Astrophysical Journal*, 833:40, December 2016. doi: 10.3847/1538-4357/833/1/40.

S. A. Jacobson and A. Morbidelli. Lunar and terrestrial planet formation in the Grand Tack scenario. *Philosophical Transactions of the Royal Society of London Series A*, 372:0174, September 2014. doi: 10.1098/rsta.2013.0174.

Xianzhe Jia, Margaret G. Kivelson, Krishan K. Khurana, and William S. Kurth. Evidence of a plume on Europa from Galileo magnetic and plasma wave signatures. *Nature Astronomy*, 2:459–464, June 2018. doi: 10.1038/s41550-018-0450-z.

A. Johansen, A. N. Youdin, and Y. Lithwick. Adding particle collisions to the formation of asteroids and Kuiper belt objects via streaming instabilities. *Astronomy&Astrophysics*, 537:A125, January 2012. doi: 10.1051/0004-6361/201117701.

A. Johansen, J. Blum, H. Tanaka, C. Ormel, M. Bizzarro, and H. Rickman. The Multifaceted Planetesimal Formation Process. *Protostars and Planets VI*, pages 547–570, 2014. doi: 10.2458/azu_uapress_9780816531240-ch024.

A. Johansen, M.-M. Mac Low, P. Lacerda, and M. Bizzarro. Growth of asteroids, planetary embryos, and Kuiper belt objects by chondrule accretion. *Science Advances*, 1:1500109, April 2015. doi: 10.1126/sciadv.1500109.

Anders Johansen and Hubert Klahr. Planetesimal Formation Through Streaming and Gravitational Instabilities. *Earth Moon and Planets*, 108:39–43, May 2011. doi: 10.1007/s11038-010-9370-3.

Anders Johansen and Michiel Lambrechts. Forming Planets via Pebble Accretion. *Annual Review of Earth and Planetary Sciences*, 45:359–387, August 2017. doi: 10.1146/annurev-earth-063016-020226.

Kazuhiro D. Kanagawa, Hidekazu Tanaka, and Ewa Szuszkiewicz. Radial Migration of Gap-opening Planets in Protoplanetary Disks. I. The Case of a Single Planet. *The Astrophysical Journal*, 861:140, July 2018. doi: 10.3847/1538-4357/aac8d9.

Ch. Keller and H. P. Gail. Radial mixing in protoplanetary accretion disks. VI. Mixing by large- scale radial flows. *Astronomy&Astrophysics*, 415:1177–1185, March 2004. doi: 10.1051/0004-6361:20034629.

H. Klahr and W. Kley. 3D-radiation hydro simulations of disk-planet interactions. I. Numerical algorithm and test cases. *Astronomy&Astrophysics*, 445:747–758, January 2006. doi: 10.1051/0004-6361:20053238.

H. Kobayashi, C. W. Ormel, and S. Ida. Rapid Formation of Saturn after Jupiter Completion. *The Astrophysical Journal*, 756:70, September 2012. doi: 10.1088/0004-637X/756/1/70.

C. M. Koepferl, B. Ercolano, J. Dale, P. S. Teixeira, T. Ratzka, and L. Spezzi. Disc clearing of young stellar objects: evidence for fast inside-out dispersal. *Monthly Notices of the Royal Astronomical Society*, 428:3327–3354, February 2013. doi: 10.1093/mnras/sts276.

Eiichiro Kokubo, Shigeru Ida, and Junichiro Makino. Evolution of a Circumterrestrial Disk and Formation of a Single Moon. *Icarus*, 148:419–436, December 2000. doi: 10.1006/icar.2000.6496.

D. G. Korycansky, P. Bodenheimer, and J. B. Pollack. Numerical models of giant planet formation with rotation. *Icarus*, 92:234–251, August 1991. doi: 10.1016/0019-1035(91)90048-X.

G. A. Krasinsky, E. V. Pitjeva, M. V. Vasilyev, and E. I. Yagudina. Hidden Mass in the Asteroid Belt. *Icarus*, 158:98–105, July 2002. doi: 10.1006/icar.2002.6837.

K. A. Kretke and H. F. Levison. Challenges in Forming the Solar System's Giant Planet Cores via Pebble Accretion. *The Astronomical Journal*, 148:109, December 2014. doi: 10.1088/0004-6256/148/6/109.

Sebastiaan Krijt, Fred J. Ciesla, and Edwin A. Bergin. Tracing Water Vapor and Ice During Dust Growth. *The Astrophysical Journal*, 833:285, December 2016. doi: 10.3847/1538-4357/833/2/285.

T. S. Kruijer, C. Burkhardt, G. Budde, and T. Kleine. Age of Jupiter inferred from the distinct genetics and formation times of meteorites. *Proceedings of the National Academy of Science*, 114:6712–6716, June 2017. doi: 10.1073/pnas.1704461114.

M. Lambrechts and A. Johansen. Rapid growth of gas-giant cores by pebble accretion. *Astronomy&Astrophysics*, 544:A32, August 2012. doi: 10.1051/0004-6361/201219127.

M. Lambrechts and A. Johansen. Forming the cores of giant planets from the radial pebble flux in protoplanetary discs. *Astronomy&Astrophysics*, 572:A107, December 2014. doi: 10.1051/0004-6361/201424343.

M. Lambrechts, A. Johansen, and A. Morbidelli. Separating gas-giant and ice-giant planets by halting pebble accretion. *Astronomy&Astrophysics*, 572:A35, December 2014. doi: 10.1051/0004-6361/201423814.

David J. Lawrence, William C. Feldman, John O. Goldsten, Sylvestre Maurice, Patrick N. Peplowski, Brian J. Anderson, David Bazell, Ralph L. McNutt, Larry R. Nittler, Thomas H. Prettyman, Douglas J. Rodgers, Sean C. Solomon, and Shoshana Z. Weider. Evidence for Water Ice Near Mercury's North Pole from MESSENGER Neutron Spectrometer Measurements. *Science*, 339:292, January 2013. doi: 10.1126/science.1229953.

M. H. Lee and S. J. Peale. Dynamics and Origin of the 2:1 Orbital Resonances of the GJ 876 Planets. *The Astrophysical Journal*, 567:596–609, March 2002. doi: 10.1086/338504.

H. F. Levison, E. Thommes, and M. J. Duncan. Modeling the Formation of Giant Planet Cores. I. Evaluating Key Processes. *The Astronomical Journal*, 139:1297–1314, April 2010. doi: 10.1088/0004-6256/139/4/1297.

H. F. Levison, K. A. Kretke, and M. J. Duncan. Growing the gas-giant planets by the gradual accumulation of pebbles. *Nature*, 524:322–324, August 2015. doi: 10.1038/nature14675.

Harold F. Levison, William F. Bottke, Matthieu Gounelle, Alessandro Morbidelli, David Nesvorný, and Kleomenis Tsiganis. Contamination of the asteroid belt by primordial trans-Neptunian objects. *Nature*, 460:364–366, July 2009. doi: 10.1038/nature08094.

D. N. C. Lin and J. Papaloizou. On the tidal interaction between protoplanets and the protoplanetary disk. III - Orbital migration of protoplanets. *The Astrophysical Journal*, 309:846–857, October 1986. doi: 10.1086/164653.

J. J. Lissauer. Urey prize lecture: On the diversity of plausible planetary systems. *Icarus*, 114:217–236, April 1995. doi: 10.1006/icar.1995.1057.

Jack J. Lissauer. Planet formation. *Annual Review of Astronomy and Astrophysics*, 31:129–174, January 1993. doi: 10.1146/annurev.aa.31.090193.001021.

B. Liu, C. W. Ormel, and D. N. C. Lin. Dynamical rearrangement of super-Earths during disk dispersal. I. Outline of the magnetospheric rebound model. *Astronomy&Astrophysics*, 601:A15, May 2017. doi: 10.1051/0004-6361/201630017.

Katharina Lodders. An Oxygen Isotope Mixing Model for the Accretion and Composition of Rocky Planets. *Space Science Reviews*, 92:341–354, April 2000. doi: 10.1023/A:1005220003004.

Katharina Lodders. Solar System Abundances and Condensation Temperatures of the Elements. *The Astrophysical Journal*, 591:1220–1247, July 2003. doi: 10.1086/375492.

J. I. Lunine and D. J. Stevenson. Formation of the Galilean satellites in a gaseous nebula. *Icarus*, 52:14–39, October 1982. doi: 10.1016/0019-1035(82)90166-X.

D. Lynden-Bell and J. E. Pringle. The evolution of viscous discs and the origin of the nebular variables. *Monthly Notices of the Royal Astronomical Society*, 168: 603–637, September 1974. doi: 10.1093/mnras/168.3.603.

F. Masset. FARGO: A fast eulerian transport algorithm for differentially rotating disks. *Astronomy & Astrophysics*, 141:165–173, January 2000. doi: 10.1051/aas:2000116.

F. Masset and M. Snellgrove. Reversing type II migration: resonance trapping of a lighter giant protoplanet. *Monthly Notices of the Royal Astronomical Society*, 320:L55–L59, February 2001. doi: 10.1046/j.1365-8711.2001.04159.x.

Colin P. McNally, Richard P. Nelson, Sijme-Jan Paardekooper, Oliver Gressel, and Wladimir Lyra. Low mass planet migration in magnetically torqued dead zones - I. Static migration torque. *Monthly Notices of the Royal Astronomical Society*, 472:1565–1575, December 2017. doi: 10.1093/mnras/stx2136.

Colin P. McNally, Richard P. Nelson, and Sijme-Jan Paardekooper. Low-mass planet migration in magnetically torqued dead zones - II. Flow- locked and runaway migration, and a torque prescription. *Monthly Notices of the Royal Astronomical Society*, 477:4596–4614, July 2018. doi: 10.1093/mnras/sty905.

Y. Miguel and S. Ida. A semi-analytical model for exploring Galilean satellites formation from a massive disk. *Icarus*, 266:1–14, March 2016. doi: 10.1016/j.icarus.2015.10.030.

H. Mizuno. Formation of the Giant Planets. *Progress of Theoretical Physics*, 64:544–557, August 1980. doi: 10.1143/PTP.64.544.

A. Morbidelli and D. Nesvorny. Dynamics of pebbles in the vicinity of a growing planetary embryo: hydro-dynamical simulations. *Astronomy&Astrophysics*, 546:A18, October 2012. doi: 10.1051/0004-6361/201219824.

A. Morbidelli and S. N. Raymond. Challenges in planet formation. *Journal of Geophysical Research (Planets)*, 121:1962–1980, October 2016. doi: 10.1002/2016JE005088.

A. Morbidelli, H. F. Levison, K. Tsiganis, and R. Gomes. Chaotic capture of Jupiter's Trojan asteroids in the early Solar System. *Nature*, 435:462–465, May 2005. doi: 10.1038/nature03540.

A. Morbidelli, J. Szulágyi, A. Crida, E. Lega, B. Bitsch, T. Tanigawa, and K. Kanagawa. Meridional circulation of gas into gaps opened by giant planets in three-dimensional low-viscosity disks. *Icarus*, 232:266–270, April 2014. doi: 10.1016/j.icarus.2014.01.010.

A. Morbidelli, M. Lambrechts, S. Jacobson, and B. Bitsch. The great dichotomy of the Solar System: Small terrestrial embryos and massive giant planet cores. *Icarus*, 258:418–429, September 2015a. doi: 10.1016/j.icarus.2015.06.003.

A. Morbidelli, K. J. Walsh, D. P. O'Brien, D. A. Minton, and W. F. Bottke. *The Dynamical Evolution of the Asteroid Belt*, pages 493–507. 2015b. doi: 10.2458/azu_uapress_9780816532131-ch026.

Alessandro Morbidelli and Aurélien Crida. The dynamics of Jupiter and Saturn in the gaseous protoplanetary disk. *Icarus*, 191:158–171, November 2007. doi: 10.1016/j.icarus.2007.04.001.

I. Mosqueira and P. R. Estrada. Formation of the regular satellites of giant planets in an extended gaseous nebula I: subnebula model and accretion of satellites. *Icarus*, 163:198–231, May 2003a. doi: 10.1016/S0019-1035(03)00076-9.

I. Mosqueira and P. R. Estrada. Formation of the regular satellites of giant planets in an extended gaseous nebula II: satellite migration and survival. *Icarus*, 163: 232–255, May 2003b. doi: 10.1016/S0019-1035(03)00077-0.

I. Mosqueira, P. R. Estrada, and S. Charnoz. Deciphering the origin of the regular satellites of gaseous giants - Iapetus: The Rosetta ice-moon. *Icarus*, 207:448–460, May 2010. doi: 10.1016/j.icarus.2009.10.018.

O. Mousis, T. Ronnet, B. Brugger, O. Ozgurel, F. Pauzat, Y. Ellinger, R. Maggiolo, P. Wurz, P. Vernazza, J. I. Lunine, A. Luspay-Kuti, K. E. Mandt, K. Altwegg, A. Bieler, A. Markovits, and M. Rubin. Origin of Molecular Oxygen in Comet 67P/Churyumov-Gerasimenko. *The Astrophysical Journal Letters*, 823:L41, June 2016. doi: 10.3847/2041-8205/823/2/L41.

O. Mousis, A. Drouard, P. Vernazza, J. I. Lunine, M. Monnereau, R. Maggiolo, K. Altwegg, H. Balsiger, J. J. Berthelier, G. Cessateur, J. De Keyser, S. A. Fuselier, S. Gasc, A. Korth, T. Le Deun, U. Mall, B. Marty, H. Rème, M. Rubin, C. Y. Tzou, J. H. Waite, and P. Wurz. Impact of Radiogenic Heating on the Formation Conditions of Comet 67P /Churyumov-Gerasimenko. *The Astrophysical Journal Letters*, 839:L4, April 2017a. doi: 10.3847/2041-8213/aa6839.

O. Mousis, O. Ozgurel, J. I. Lunine, A. Luspay-Kuti, T. Ronnet, F. Pauzat, A. Markovits, and Y. Ellinger. Stability of Sulphur Dimers (S₂) in Cometary Ices. *The Astrophysical Journal*, 835:134, February 2017b. doi: 10.3847/1538-4357/aa5279.

Olivier Mousis and Daniel Gautier. Constraints on the presence of volatiles in Ganymede and Callisto from an evolutionary turbulent model of the Jovian subnebula. *Planetary and Space Science*, 52:361–370, April 2004. doi: 10.1016/j.pss.2003.06.004.

Taishi Nakamoto and Yoshitsugu Nakagawa. Formation, Early Evolution, and Gravitational Stability of Protoplanetary Disks. *The Astrophysical Journal*, 421: 640, February 1994. doi: 10.1086/173678.

David Nesvorný and Alessandro Morbidelli. Statistical Study of the Early Solar System's Instability with Four, Five, and Six Giant Planets. *The Astronomical Journal*, 144:117, October 2012. doi: 10.1088/0004-6256/144/4/117.

David Nesvorný and David Vokrouhlický. Chaotic Capture of Neptune Trojans. *The Astronomical Journal*, 137:5003–5011, June 2009. doi: 10.1088/0004-6256/137/6/5003.

David Nesvorný, David Vokrouhlický, and Alessandro Morbidelli. Capture of Irregular Satellites during Planetary Encounters. *The Astronomical Journal*, 133: 1962–1976, May 2007. doi: 10.1086/512850.

David Nesvorný, David Vokrouhlický, and Alessandro Morbidelli. Capture of Trojans by Jumping Jupiter. *The Astrophysical Journal*, 768:45, May 2013. doi: 10.1088/0004-637X/768/1/45.

M. Ogihara and S. Ida. N-body Simulations of Satellite Formation around Giant Planets: Origin of Orbital Configuration of the Galilean Moons. *The Astrophysical Journal*, 753:60, July 2012. doi: 10.1088/0004-637X/753/1/60.

M. Ogihara, M. J. Duncan, and S. Ida. Eccentricity Trap: Trapping of Resonantly Interacting Planets Near the Disk Inner Edge. *The Astrophysical Journal*, 721: 1184–1192, October 2010. doi: 10.1088/0004-637X/721/2/1184.

Satoshi Okuzumi, Hidekazu Tanaka, Hiroshi Kobayashi, and Koji Wada. Rapid Coagulation of Porous Dust Aggregates outside the Snow Line: A Pathway to Successful Icy Planetesimal Formation. *The Astrophysical Journal*, 752:106, June 2012. doi: 10.1088/0004-637X/752/2/106.

H. St. C. O'Neill. The origin of the moon and the early history of the earth - A chemical model. Part 1: The moon. *Geochimica et Cosmochimica Acta*, 55: 1135–1157, April 1991. doi: 10.1016/0016-7037(91)90168-5.

C. W. Ormel. An Atmospheric Structure Equation for Grain Growth. *The Astrophysical Journal*, 789:L18, July 2014. doi: 10.1088/2041-8205/789/1/L18.

C. W. Ormel and J. N. Cuzzi. Closed-form expressions for particle relative velocities induced by turbulence. *Astronomy&Astrophysics*, 466:413–420, May 2007. doi: 10.1051/0004-6361:20066899.

C. W. Ormel and H. H. Klahr. The effect of gas drag on the growth of protoplanets. Analytical expressions for the accretion of small bodies in laminar disks. *Astronomy&Astrophysics*, 520:A43, September 2010. doi: 10.1051/0004-6361/201014903.

Chris W. Ormel. The Emerging Paradigm of Pebble Accretion. In *Astrophysics and Space Science Library*, volume 445, page 197, January 2017. doi: 10.1007/978-3-319-60609-5_7.

Chris W. Ormel, Beibei Liu, and Djoeke Schoonenberg. Formation of TRAPPIST-1 and other compact systems. *Astronomy&Astrophysics*, 604:A1, July 2017. doi: 10.1051/0004-6361/201730826.

S. J. Paardekooper, C. Baruteau, A. Crida, and W. Kley. A torque formula for non-isothermal type I planetary migration - I. Unsaturated horseshoe drag. *Monthly Notices of the Royal Astronomical Society*, 401:1950–1964, January 2010. doi: 10.1111/j.1365-2966.2009.15782.x.

M. Pajola, M. Lazzarin, C. M. Dalle Ore, D. P. Cruikshank, T. L. Roush, S. Magrin, I. Bertini, F. La Forgia, and C. Barbieri. Phobos as a D-type Captured Asteroid, Spectral Modeling from 0.25 to 4.0 μm. *The Astrophysical Journal*, 777:127, November 2013. doi: 10.1088/0004-637X/777/2/127.

H. B. Perets and R. A. Murray-Clay. Wind-shearing in Gaseous Protoplanetary Disks and the Evolution of Binary Planetesimals. *The Astrophysical Journal*, 733:56, May 2011. doi: 10.1088/0004-637X/733/1/56.

Laura M. Pérez, Claire J. Chandler, Andrea Isella, John M. Carpenter, Sean M. Andrews, Nuria Calvet, Stuartt A. Corder, Adam T. Deller, Cornelis P. Dullemond, Jane S. Greaves, Robert J. Harris, Thomas Henning, Woojin Kwon, Joseph Lazio, Hendrik Linz, Lee G. Mundy, Luca Ricci, Anneila I. Sargent, Shaye Storm, Marco Tazzari, Leonardo Testi, and David J. Wilner. Grain Growth in the Circumstellar Disks of the Young Stars CY Tau and DoAr 25. *The Astrophysical Journal*, 813:41, November 2015. doi: 10.1088/0004-637X/813/1/41.

A. Pierens, S. N. Raymond, D. Nesvorny, and A. Morbidelli. Outward Migration of Jupiter and Saturn in 3:2 or 2:1 Resonance in Radiative Disks: Implications for the Grand Tack and Nice models. *The Astrophysical Journal Letters*, 795:L11, November 2014. doi: 10.1088/2041-8205/795/1/L11.

Carlé M. Pieters, Larry A. Taylor, Sarah K. Noble, Lindsay P. Keller, Bruce Hapke, Richard V. Morris, Carl C. Allen, David S. McKay, and Susan Wentworth. Space weathering on airless bodies: Resolving a mystery with lunar samples. *Meteoritics* *and Planetary Science*, 35:1101–1107, September 2000. doi: 10.1111/j.1945-5100.2000.tb01496.x.

Carle M. Pieters, Scott Murchie, Nicolas Thomas, and Daniel Britt. Composition of Surface Materials on the Moons of Mars. *Planetary and Space Science*, 102: 144–151, November 2014. doi: 10.1016/j.pss.2014.02.008.

M. Podolak, J. B. Pollack, and R. T. Reynolds. Interactions of planetesimals with protoplanetary atmospheres. *Icarus*, 73:163–179, January 1988. doi: 10.1016/0019-1035(88)90090-5.

J. B. Pollack, O. Hubickyj, P. Bodenheimer, J. J. Lissauer, M. Podolak, and Y. Greenzweig. Formation of the Giant Planets by Concurrent Accretion of Solids and Gas. *Icarus*, 124:62–85, November 1996. doi: 10.1006/icar.1996.0190.

James B. Pollack, Joseph A. Burns, and Michael E. Tauber. Gas drag in primordial circumplanetary envelopes: A mechanism for satellite capture. *Icarus*, 37:587–611, March 1979. doi: 10.1016/0019-1035(79)90016-2.

James B. Pollack, Christopher P. McKay, and Bruce M. Christofferson. A calculation of the Rosseland mean opacity of dust grains in primordial solar system nebulae. *Icarus*, 64:471–492, December 1985. doi: 10.1016/0019-1035(85)90069-7.

James B. Pollack, David Hollenbach, Steven Beckwith, Damon P. Simonelli, Ted Roush, and Wesley Fong. Composition and Radiative Properties of Grains in Molecular Clouds and Accretion Disks. *The Astrophysical Journal*, 421:615, February 1994. doi: 10.1086/173677.

J. E. Pringle. Accretion discs in astrophysics. *Annual Review of Astronomy and Astrophysics*, 19:137–162, January 1981. doi: 10.1146/annurev.aa.19.090181.001033.

S. N. Raymond and A. Izidoro. Origin of water in the inner Solar System: Planetesimals scattered inward during Jupiter and Saturn's rapid gas accretion. *Icarus*, 297:134–148, November 2017a. doi: 10.1016/j.icarus.2017.06.030.

S. N. Raymond and A. Izidoro. The empty primordial asteroid belt. *Science Advances*, 3(9), 2017b. doi: 10.1126/sciadv.1701138.

H. Rein and D. S. Spiegel. IAS15: a fast, adaptive, high-order integrator for gravitational dynamics, accurate to machine precision over a billion orbits. *Monthly Notices of the Royal Astronomical Society*, 446:1424–1437, January 2015. doi: 10.1093/mnras/stu2164.

H. Rein and D. Tamayo. WHFAST: a fast and unbiased implementation of a symplectic Wisdom-Holman integrator for long-term gravitational simulations.

Monthly Notices of the Royal Astronomical Society, 452:376–388, September 2015. doi: 10.1093/mnras/stv1257.

Céline Reylé and D. C. Boice. An S₂ Fluorescence Model for Interpreting High-Resolution Cometary Spectra. I. Model Description and Initial Results. *The Astrophysical Journal*, 587:464–471, April 2003. doi: 10.1086/346147.

F. Rietmeijer. A cometary aggregate interplanetary dust particle as an analog for comet Wild 2 grain chemistry preserved in silica-rich Stardust glass. *Meteoritics and Planetary Science*, 44:1589–1609, November 2009. doi: 10.1111/j.1945-5100.2009.tb01193.x.

Frans J. M. Rietmeijer and James M. Karner. Metastable eutectic gas to solid condensation in the Al₂O₃-SiO₂ system. *Journal of Chemical Physics*, 110:4554–4558, March 1999. doi: 10.1063/1.478336.

Frans J. M. Rietmeijer, III Nuth, Joseph A., and James M. Karner. Metastable Eutectic Condensation in a Mg-Fe- SiO-H₂-O₂ Vapor: Analogs to Circumstellar Dust. *The Astrophysical Journal*, 527:395–404, December 1999a. doi: 10.1086/308080.

Frans J. M. Rietmeijer, III Nuth, Joseph A., and Jim M. Karner. Metastable eutectic, gas to solid, condensation in the FeO Fe2O3 SiO2 system. *Physical Chemistry Chemical Physics (Incorporating Faraday Transactions)*, 1:1511–1516, January 1999b. doi: 10.1039/A900053D.

C. M. T Robert, A. Crida, E. Lega, H. Méheut, and A. Morbidelli. Toward a new paradigm for Type II migration. *ArXiv e-prints*, art. arXiv:1808.00381, August 2018.

K. Ros and A. Johansen. Ice condensation as a planet formation mechanism. *Astronomy&Astrophysics*, 552:A137, April 2013. doi: 10.1051/0004-6361/201220536.

Pascal Rosenblatt. The origin of the Martian moons revisited. *Astronomy and Astrophysics Review*, 19:44, August 2011. doi: 10.1007/s00159-011-0044-6.

Pascal Rosenblatt and Sébastien Charnoz. On the formation of the martian moons from a circum-martian accretion disk. *Icarus*, 221:806–815, November 2012. doi: 10.1016/j.icarus.2012.09.009.

Pascal Rosenblatt, Sebastien Charnoz, Kevin M. Dunseath, Mariko Terao-Dunseath, Antony Trinh, Ryuki Hyodo, Hidenori Genda, and Stéven Toupin.

Accretion of Phobos and Deimos in an extended debris disc stirred by transient moons. *Nature Geoscience*, 9:581–583, August 2016. doi: 10.1038/ngeo2742.

M. Rubin, K. Altwegg, E. F. van Dishoeck, and G. Schwehm. Molecular Oxygen in Oort Cloud Comet 1P/Halley. *The Astrophysical Journal*, 815:L11, December 2015. doi: 10.1088/2041-8205/815/1/L11.

Etsuko Saito and Sin-iti Sirono. Planetesimal Formation by Sublimation. *The Astrophysical Journal*, 728:20, February 2011. doi: 10.1088/0004-637X/728/1/20.

J. Salmon and R. M. Canup. Accretion of Saturns Inner Mid-sized Moons from a Massive Primordial Ice Ring. *The Astrophysical Journal*, 836:109, February 2017. doi: 10.3847/1538-4357/836/1/109.

Julien Salmon and Robin M. Canup. Lunar Accretion from a Roche-interior Fluid Disk. *The Astrophysical Journal*, 760:83, November 2012. doi: 10.1088/0004-637X/760/1/83.

C. Sanloup, A. Jambon, and P. Gillet. A simple chondritic model of Mars. *Physics of the Earth and Planetary Interiors*, 112:43–54, March 1999. doi: 10.1016/S0031-9201(98)00175-7.

T. Sasaki, G. R. Stewart, and S. Ida. Origin of the Different Architectures of the Jovian and Saturnian Satellite Systems. *The Astrophysical Journal*, 714:1052–1064, May 2010. doi: 10.1088/0004-637X/714/2/1052.

D. Schoonenberg and C. W. Ormel. Planetesimal formation near the snowline: in or out? *Astronomy&Astrophysics*, 602:A21, June 2017. doi: 10.1051/0004-6361/201630013.

G. Schubert, J. D. Anderson, T. Spohn, and W. B. McKinnon. *Interior composition, structure and dynamics of the Galilean satellites*, pages 281–306. 2004.

P. H. Schultz and A. B. Lutz-Garihan. Grazing Impacts on Mars: a Record of Lost Satellites. *Lunar and Planetary Science Conference Proceedings*, 87:84–A96, January 1982. doi: 10.1029/JB087iS01p00A84.

Jennifer E. C. Scully, Christopher T. Russell, An Yin, Ralf Jaumann, Elizabeth Carey, Julie Castillo-Rogez, Harry Y. McSween, Carol A. Raymond, Vishnu Reddy, and Lucille Le Corre. Geomorphological evidence for transient water flow on Vesta. *Earth and Planetary Science Letters*, 411:151–163, February 2015. doi: 10.1016/j.epsl.2014.12.004.

N. I. Shakura and R. A. Sunyaev. Black holes in binary systems. Observational appearance. *Astronomy&Astrophysics*, 24:337–355, 1973.

Y. Shibaike, S. Okuzumi, T. Sasaki, and S. Ida. Satellitesimal Formation via Collisional Dust Growth in Steady Circumplanetary Disks. *The Astrophysical Journal*, 846:81, September 2017. doi: 10.3847/1538-4357/aa8454.

Masakazu Shiraishi and Shigeru Ida. Infall of Planetesimals onto Growing Giant Planets: Onset of Runaway Gas Accretion and Metallicity of Their Gas Envelopes. *The Astrophysical Journal*, 684:1416–1426, September 2008. doi: 10.1086/590226.

Holger Sierks, Cesare Barbieri, Philippe L. Lamy, Rafael Rodrigo, Detlef Koschny, Hans Rickman, Horst Uwe Keller, Jessica Agarwal, Michael F. A'Hearn, Francesco Angrilli, Anne-Therese Auger, M. Antonella Barucci, Jean-Loup Bertaux, Ivano Bertini, Sebastien Besse, Dennis Bodewits, Claire Capanna, Gabriele Cremonese, Vania Da Deppo, Björn Davidsson, Stefano Debei, Mariolino De Cecco, Francesca Ferri, Sonia Fornasier, Marco Fulle, Robert Gaskell, Lorenza Giacomini, Olivier Groussin, Pablo Gutierrez-Marques, Pedro J. Gutiérrez, Carsten Güttler, Nick Hoekzema, Stubbe F. Hviid, Wing-Huen Ip, Laurent Jorda, Jörg Knollenberg, Gabor Kovacs, J. Rainer Kramm, Ekkehard Kührt, Michael Küppers, Fiorangela La Forgia, Luisa M. Lara, Monica Lazzarin, Cédric Leyrat, Josè J. Lopez Moreno, Sara Magrin, Simone Marchi, Francesco Marzari, Matteo Massironi, Harald Michalik, Richard Moissl, Stefano Mottola, Giampiero Naletto, Nilda Oklay, Maurizio Pajola, Marco Pertile, Frank Preusker, Lola Sabau, Frank Scholten, Colin Snodgrass, Nicolas Thomas, Cecilia Tubiana, Jean-Baptiste Vincent, Klaus-Peter Wenzel, Mirco Zaccariotto, and Martin Pätzold. On the nucleus structure and activity of comet 67P/Churyumov-Gerasimenko. *Science*, 347:aaa1044, January 2015. doi: 10.1126/science.aaa1044.

V. Solomatov. Magma oceans and primordial mantle differentiation. In Gerald Schubert, editor, *Treatise on Geophysics (Second Edition)*, pages 81 – 104. Elsevier, Oxford, second edition edition, 2015. ISBN 978-0-444-53803-1. doi: https://doi.org/10.1016/B978-0-444-53802-4.00155-X. URL http://www.sciencedirect.com/science/article/pii/B978044453802400155X.

John R. Spencer and Wendy M. Calvin. Condensed O₂ on Europa and Callisto. *The Astronomical Journal*, 124:3400–3403, December 2002. doi: 10.1086/344307.

David J. Stevenson and Jonathan I. Lunine. Rapid formation of Jupiter by diffusive redistribution of water vapor in the solar nebula. *Icarus*, 75:146–155, July 1988. doi: 10.1016/0019-1035(88)90133-9.

R. Suetsugu and K. Ohtsuki. Distribution of Captured Planetesimals in Circumplanetary Gas Disks and Implications for Accretion of Regular Satellites. *The Astrophysical Journal*, 839:66, April 2017. doi: 10.3847/1538-4357/aa692e.

R. Suetsugu, K. Ohtsuki, and T. Fujita. Orbital Characteristics of Planetesimals Captured by Circumplanetary Gas Disks. *The astronomical Journal*, 151:140, June 2016. doi: 10.3847/0004-6256/151/6/140.

Naoji Sugiura and Wataru Fujiya. Correlated accretion ages and ∈⁵⁴Cr of meteorite parent bodies and the evolution of the solar nebula. *Meteoritics and Planetary Science*, 49:772–787, May 2014. doi: 10.1111/maps.12292.

Jessica M. Sunshine, Tony L. Farnham, Lori M. Feaga, Olivier Groussin, Frédéric Merlin, Ralph E. Milliken, and Michael F. A'Hearn. Temporal and Spatial Variability of Lunar Hydration As Observed by the Deep Impact Spacecraft. *Science*, 326:565, October 2009. doi: 10.1126/science.1179788.

K. D. Supulver and D. N. C. Lin. Formation of Icy Planetesimals in a Turbulent Solar Nebula. *Icarus*, 146:525–540, August 2000. doi: 10.1006/icar.2000.6418.

Takeru K. Suzuki, Masahiro Ogihara, Alessandro Morbidelli, Aurélien Crida, and Tristan Guillot. Evolution of protoplanetary discs with magnetically driven disc winds. *Astronomy&Astrophysics*, 596:A74, December 2016. doi: 10.1051/0004-6361/201628955.

Anthony M. K. Szeto. Orbital evolution and origin of the Martian satellites. *Icarus*, 55:133–168, July 1983. doi: 10.1016/0019-1035(83)90056-8.

J. Szulágyi, A. Morbidelli, A. Crida, and F. Masset. Accretion of Jupiter-mass Planets in the Limit of Vanishing Viscosity. *The Astrophysical Journal*, 782:65, February 2014. doi: 10.1088/0004-637X/782/2/65.

J. Szulágyi, F. Masset, E. Lega, A. Crida, A. Morbidelli, and T. Guillot. Circumplanetary disc or circumplanetary envelope? *Monthly Notices of the Royal Astronomical Society*, 460:2853–2861, August 2016. doi: 10.1093/mnras/stw1160.

T. Takata and D. J. Stevenson. Despin Mechanism for Protogiant Planets and Ionization State of Protogiant Planetary Disks. *Icarus*, 123:404–421, October 1996. doi: 10.1006/icar.1996.0167.

Taku Takeuchi and D. N. C. Lin. Radial Flow of Dust Particles in Accretion Disks. *The Astrophysical Journal*, 581:1344–1355, December 2002. doi: 10.1086/344437.

Hidekazu Tanaka, Taku Takeuchi, and William R. Ward. Three-Dimensional Interaction between a Planet and an Isothermal Gaseous Disk. I. Corotation and

Lindblad Torques and Planet Migration. *The Astrophysical Journal*, 565:1257–1274, February 2002. doi: 10.1086/324713.

T. Tanigawa, K. Ohtsuki, and M. N. Machida. Distribution of Accreting Gas and Angular Momentum onto Circumplanetary Disks. *The Astrophysical Journal*, 747:47, March 2012. doi: 10.1088/0004-637X/747/1/47.

V. Taquet, K. Furuya, C. Walsh, and E. F. van Dishoeck. A primordial origin for molecular oxygen in comets: a chemical kinetics study of the formation and survival of O₂ ice from clouds to discs. *Monthly Notices of the Royal Astronomical Society*, 462:S99–S115, November 2016. doi: 10.1093/mnras/stw2176.

A. Teachey, D. M. Kipping, and A. R. Schmitt. HEK. VI. On the Dearth of Galilean Analogs in Kepler, and the Exomoon Candidate Kepler-1625b I. *The Astronomical Journal*, 155:36, January 2018. doi: 10.3847/1538-3881/aa93f2.

L. Testi, T. Birnstiel, L. Ricci, S. Andrews, J. Blum, J. Carpenter, C. Dominik, A. Isella, A. Natta, J. P. Williams, and D. J. Wilner. Dust Evolution in Protoplanetary Disks. *Protostars and Planets VI*, pages 339–361, 2014. doi: 10.2458/azu_uapress_9780816531240-ch015.

Christopher Thompson and David J. Stevenson. Gravitational Instability in Two-Phase Disks and the Origin of the Moon. *The Astrophysical Journal*, 333:452, October 1988. doi: 10.1086/166760.

Alice Toppani, Guy Libourel, François Robert, and Jaafar Ghanbaja. Laboratory condensation of refractory dust in protosolar and circumstellar conditions. *Geochimica et Cosmochimica Acta*, 70:5035–5060, October 2006. doi: 10.1016/j.gca.2006.05.020.

K. Tsiganis, R. Gomes, A. Morbidelli, and H. F. Levison. Origin of the orbital architecture of the giant planets of the Solar System. *Nature*, 435:459–461, May 2005. doi: 10.1038/nature03539.

N. J. Turner, S. Fromang, C. Gammie, H. Klahr, G. Lesur, M. Wardle, and X. N. Bai. Transport and Accretion in Planet-Forming Disks. In *Protostars and Planets VI*, page 411, January 2014. doi: 10.2458/azu_uapress_9780816531240-ch018.

P. Vernazza, R. Brunetto, R. P. Binzel, C. Perron, D. Fulvio, G. Strazzulla, and M. Fulchignoni. Plausible parent bodies for enstatite chondrites and mesosiderites: Implications for Lutetia's fly-by. *Icarus*, 202:477–486, August 2009. doi: 10.1016/j.icarus.2009.03.016.

P. Vernazza, M. Marsset, P. Beck, R. P. Binzel, M. Birlan, R. Brunetto, F. E. Demeo, Z. Djouadi, C. Dumas, S. Merouane, O. Mousis, and B. Zanda. Interplanetary Dust Particles as Samples of Icy Asteroids. *The Astrophysical Journal*, 806:204, June 2015. doi: 10.1088/0004-637X/806/2/204.

P. Vernazza, J. Castillo-Rogez, P. Beck, J. Emery, R. Brunetto, M. Delbo, M. Marsset, F. Marchis, O. Groussin, B. Zanda, P. Lamy, L. Jorda, O. Mousis, A. Delsanti, Z. Djouadi, Z. Dionnet, F. Borondics, and B. Carry. Different Origins or Different Evolutions? Decoding the Spectral Diversity Among C-type Asteroids. *The Astronomical Journal*, 153:72, February 2017. doi: 10.3847/1538-3881/153/2/72.

J. Veverka. The surfaces of Phobos and Deimos. *Vistas in Astronomy*, 22:163–192, January 1978. doi: 10.1016/0083-6656(78)90014-4.

Channon Visscher and Jr. Fegley, Bruce. Chemistry of Impact-generated Silicate Melt-vapor Debris Disks. *The Astrophysical Journal*, 767:L12, April 2013. doi: 10.1088/2041-8205/767/1/L12.

David Vokrouhlický, William F. Bottke, and David Nesvorný. Capture of Trans-Neptunian Planetesimals in the Main Asteroid Belt. *The Astronomical Journal*, 152:39, August 2016. doi: 10.3847/0004-6256/152/2/39.

K. J. Walsh, A. Morbidelli, S. N. Raymond, D. P. O'Brien, and A. M. Mandell. A low mass for Mars from Jupiter's early gas-driven migration. *Nature*, 475: 206–209, July 2011. doi: 10.1038/nature10201.

Huapei Wang, Benjamin P. Weiss, Xue-Ning Bai, Brynna G. Downey, Jun Wang, Jiajun Wang, Clément Suavet, Roger R. Fu, and Maria E. Zucolotto. Lifetime of the solar nebula constrained by meteorite paleomagnetism. *Science*, 355:623–627, February 2017. doi: 10.1126/science.aaf5043.

W. R. Ward. Survival of Planetary Systems. *The Astrophysical Journal Letters*, 482:L211–L214, June 1997. doi: 10.1086/310701.

W. R. Ward. On the evolution of the protolunar disc. *Philosophical Transactions of the Royal Society of London Series A*, 372:20130250–20130250, August 2014. doi: 10.1098/rsta.2013.0250.

William R. Ward. On the Vertical Structure of the Protolunar Disk. *The Astrophysical Journal*, 744:140, January 2012. doi: 10.1088/0004-637X/744/2/140.

S. J. Weidenschilling. Aerodynamics of solid bodies in the solar nebula. *Monthly Notices of the Royal Astronomical Society*, 180:57–70, July 1977. doi: 10.1093/mnras/180.1.57.

K. Willner, X. Shi, and J. Oberst. Phobos' shape and topography models. *Planetary and Space Science*, 102:51–59, November 2014. doi: 10.1016/j.pss.2013.12.006.

Satoru Yamamoto, Ryosuke Nakamura, Tsuneo Matsunaga, Yoshiko Ogawa, Yoshiaki Ishihara, Tomokatsu Morota, Naru Hirata, Makiko Ohtake, Takahiro Hiroi, Yasuhiro Yokota, and Junichi Haruyama. Olivine-rich exposures in the South Pole-Aitken Basin. *Icarus*, 218:331–344, March 2012. doi: 10.1016/j.icarus.2011.12.012.

C. C. Yang, A. Johansen, and D. Carrera. Concentrating small particles in protoplanetary disks through the streaming instability. *Astronomy&Astrophysics*, 606:A80, October 2017. doi: 10.1051/0004-6361/201630106.

A. G. Yeghikyan. Irradiation of dust in molecular clouds. II. Doses produced by cosmic rays. *Astrophysics*, 54:87–99, March 2011. doi: 10.1007/s10511-011-9160-2.

A. N. Youdin and Y. Lithwick. Particle stirring in turbulent gas disks: Including orbital oscillations. *Icarus*, 192:588–604, December 2007. doi: 10.1016/j.icarus.2007.07.012.

Andrew N. Youdin and Jeremy Goodman. Streaming Instabilities in Protoplanetary Disks. *The Astrophysical Journal*, 620:459–469, February 2005. doi: 10.1086/426895.

Appendix

This section contains papers published in refereed journals during the course of this thesis and sorted in chronological order.

The Astrophysical Journal Letters, 823:L41 (5pp), 2016 June 1 doi:10.3847/2041-8205/823/2/L41

ORIGIN OF MOLECULAR OXYGEN IN COMET 67P/CHURYUMOV–GERASIMENKO

O. Mousis[1], T. Ronnet[1], B. Brugger[1], O. Ozgurel[2], F. Pauzat[2], Y. Ellinger[2], R. Maggiolo[3], P. Wurz[4], P. Vernazza[1], J. I. Lunine[5], A. Luspay-Kuti[6], K. E. Mandt[6], K. Altwegg[4], A. Bieler[4], A. Markovits[2], and M. Rubin[4]
[1] Aix Marseille Université, CNRS, LAM (Laboratoire d'Astrophysique de Marseille) UMR 7326, F-13388, Marseille, France; olivier.mousis@lam.fr
[2] Laboratoire de Chimie Théorique, Sorbonne Universités, UPMC Univ. Paris 06, CNRS UMR 7616, F-75252 Paris CEDEX 05, France
[3] Royal Institute for Space Aeronomy, 3 Avenue Circulaire, Brussels, Belgium
[4] Physikalisches Institut, University of Bern, Sidlerstrasse 5, CH-3012 Bern, Switzerland
[5] Department of Astronomy and Carl Sagan Institute, Space Sciences Building Cornell University, Ithaca, NY 14853, USA
[6] Department of Space Research, Southwest Research Institute, 6220 Culebra Rd., San Antonio, TX 78228, USA
Received 2016 March 28; revised 2016 April 25; accepted 2016 April 26; published 2016 June 1

ABSTRACT

Molecular oxygen has been detected in the coma of comet 67P/Churyumov–Gerasimenko with abundances in the 1%–10% range by the *Rosetta* Orbiter Spectrometer for Ion and Neutral Analysis-Double Focusing Mass Spectrometer instrument on board the *Rosetta* spacecraft. Here we find that the radiolysis of icy grains in low-density environments such as the presolar cloud may induce the production of large amounts of molecular oxygen. We also show that molecular oxygen can be efficiently trapped in clathrates formed in the protosolar nebula (PSN), and that its incorporation as crystalline ice is highly implausible, because this would imply much larger abundances of Ar and N_2 than those observed in the coma. Assuming that radiolysis has been the only O_2 production mechanism at work, we conclude that the formation of comet 67P/Churyumov–Gerasimenko is possible in a dense and early PSN in the framework of two extreme scenarios: (1) agglomeration from pristine amorphous icy grains/particles formed in ISM and (2) agglomeration from clathrates that formed during the disk's cooling. The former scenario is found consistent with the strong correlation between O_2 and H_2O observed in comet 67P/Churyumov-Gerasimenko's coma while the latter scenario requires that clathrates formed from ISM icy grains that crystallized when entering the PSN.

Key words: astrobiology – comets: general – comets: individual (67P/Churyumov–Gerasimenko) – methods: numerical – solid state: volatile

1. INTRODUCTION

The *Rosetta* Orbiter Spectrometer for Ion and Neutral Analysis (ROSINA) Double Focusing Mass Spectrometer (DFMS) on board the *Rosetta* spacecraft (Balsiger et al. 2007) enabled the detection of O_2 in the coma of comet 67P/Churyumov–Gerasimenko (67P/C–G) with local abundances in the 1%–10% range and a mean value of 3.80 ± 0.85% (Bieler et al. 2015). A subsequent reinvestigation of the 1P/Halley data from the Giotto Neutral Mass Spectrometer also indicates that the coma of comet 1P/Halley should contain O_2 with an abundance of 3.7 ± 1.7% with respect to water, suggesting that this molecule may be a rather common parent species in comets (Rubin et al. 2015b).

To investigate the origin of O_2 in 67P/C–G, Bieler et al. (2015) considered the possibility of O_2 production via the radiolysis of water ice incorporated within the nucleus. Based on 67P/C–G's known orbital history, they estimated that any O_2 produced during the residence time of 67P/C–G in the Kuiper Belt was quickly lost during the first pass or two around the Sun. The authors further found that radiolysis on closer orbit to the Sun would most likely only affect the top few micrometers of the nucleus' active surface. In this case, the O_2/H_2O ratio produced in these conditions would decrease with depth. Because they did not observe any variation of the O_2/H_2O ratio during the sampling period, Bieler et al. (2015) ruled out the hypothesis of O_2 production via the radiolysis and determined that O_2 must have been incorporated into 67P/C–G at the time of its formation in the protosolar nebula (PSN).

In order to explain how O_2 could have been incorporated into the ices of 67P/C–G, we investigate here the radiolysis hypothesis at epochs prior to the formation of comets, when icy grains were the dominant solid phase of the outer PSN. Furthermore, we examine the different trapping scenarios of O_2 that could explain its presence. Because some recent works suggest that this comet may have been accreted from a mixture of clathrates and pure crystalline ices formed in the PSN (Luspay-Kuti et al. 2016; Mousis et al. 2016), we study the propensity for O_2 trapping in clathrates, and also evaluate if its condensation as pure crystalline ice is consistent with the comet's inferred composition. Among all these investigated mechanisms, we find that clathration of O_2 is efficient in the PSN and that radiolysis can explain the formation of O_2 and its stabilization in icy grains. However, to produce enough O_2 molecules, the radiolysis of icy grains must have happened in a low-density environment such as the presolar cloud.

2. O_2 FORMATION VIA RADIOLYSIS

We first investigate the possibility of radiolytic production of O_2 in icy grains present in the outer PSN prior to their agglomeration by 67P/C–G. The energy available for radiolysis is provided by the galactic cosmic ray flux (CRF) impacting icy grains. In the following, since galactic CRF can penetrate into water ice down to depths of a few tens of meters (Cooper et al. 1998), we only consider icy grains with sizes below this limit, implying that no H_2O ice can be out of reach of radiolysis. In our calculations, we use the energy range and CRF distribution from Yeghikyan (2011) and Cooper et al. (2003), respectively. The CRF energy dose absorbed by icy grains located at 30 au from the Sun is within the ~(5–60) × 10^{16} eV kg^{-1} yr^{-1} range, depending on the disk's

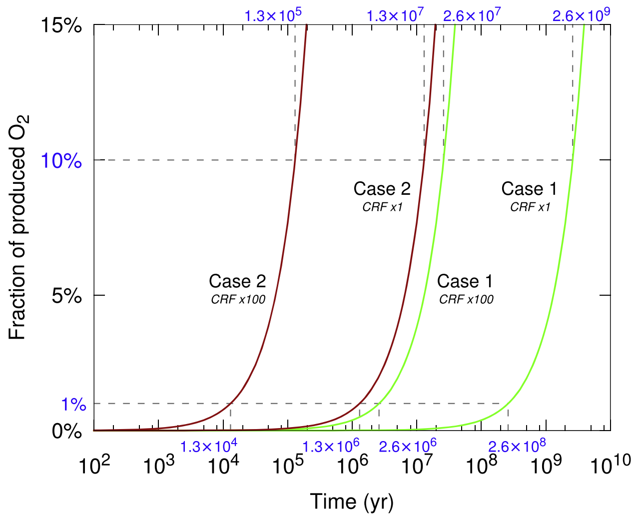

Figure 1. Time evolution of the fraction of O_2 molecules produced by cosmic rays in an icy grain. Case 1 (green curves) considers the irradiation of an icy grain placed at 30 au in the PSN. Case 2 (red curves) considers the irradiation of an icy grain located in a low-density environment ($\sim 10^{-3}$ g cm^{-2}). Two CRF values are explored in each case, namely 1 and 100 times the nominal CRF value (see the text).

surface density (between 10 and 10^3 g cm^{-2}; see Hersant et al. 2001).

O_2 is produced by radiolysis of water ice through the chemical reaction 2 $H_2O \longrightarrow 2\ H_2 + O_2$, with an amount of energy needed to alter one H_2O molecule W_r = 235 eV (Johnson 1991). H_2 is then rapidly lost from the water ice due to its fast diffusion. Further reactions with O_2 are precluded because the diffusion of these molecules is slowed down by the disk's low temperatures (Johnson 1990). We have thus assumed that all the energy absorbed by water ice is used to form O_2. To reach the molecular ratio O_2/H_2O (1%–10%) measured by Bieler et al. (2015) in 67P/C–G, cosmic rays must alter twice as many H_2O molecules in icy grains. The time τ needed to reach this ratio is then given by

$$\tau = \frac{W_r \cdot N_A}{E_{CR} \cdot M_{H_2O}} \times f_{H_2O} \quad (1)$$

where N_A (mol^{-1}) is the Avogadro constant, M_{H_2O} (kg mol^{-1}) is the molar mass of water, E_{CR} (eV kg^{-1} yr^{-1}) is the CRF energy dose received by water ice and f_{H_2O} is the fraction of altered H_2O molecules, which corresponds to two times the fraction of O_2 produced.

Figure 1 shows the results of our calculations. An O_2 fraction in the 1%–10% range is reached in ∼0.25–2.5 Gyr at the aforementioned nominal CRF value (Case 1). These extremely long time periods are incompatible with the lifetime of icy grains in the PSN (a few 10^4 year; Weidenschilling & Cuzzi 1993). If icy grains have grown to sizes larger than tens of meters in the PSN, then the deepest layers should remain unaltered. In this case, even longer timescales would be needed for O_2 formation. However, the CRF may have undergone significant enhancements throughout the history of the solar system, by a factor of ∼3 during its passages through the Milky Way's spiral arms (a few tens of Myr every 400–500 Myr; Effenberger et al. 2012; Werner et al. 2015; Alexeev 2016), or even by a factor of ∼100 during a few kyr because of a close supernova explosion (<30 pc; Fields & Ellis 1999). Such enhancements can decrease the time needed to form O_2 by up to a factor of 100, which is still too long for our consideration.

We also consider the possibility of an icy grain receiving the maximum CRF energy dose estimated by Yeghikyan (2011), namely $\sim 1.20 \times 10^{20}$ eV kg^{-1} yr^{-1}. This value leads to a time τ in the ∼1–10 Myr range (see case 2 of Figure 1), or ∼10–100 kyr with a CRF enhanced by a factor of 100. However, such a high value of E_{CR} corresponds to a surface density of 10^{-3} g cm^{-2}, which can only be reached in molecular clouds. In such environments, the column densities would be low enough to form 1%–10% of O_2 in the icy grains even on very short timescales. Therefore, to incorporate significant amounts of O_2 produced via radiolysis of icy grains, cometary grains must have formed in the presolar cloud prior to disk formation.

3. O_2 STABILITY IN WATER ICE

An important question is whether O_2 molecules produced via radiolysis of ice grains can remain stabilized within the water icy matrix of 67P/C–G. The stabilization energy is defined as the difference between the energy of the system of O_2 interacting with the ice and the sum of the energies of the pure ice and O_2 at infinite separation. To investigate this problem, a sampling of the representative structures of O_2 in solid water ice has been obtained using a strategy based on first principle periodic density functional theory quantum calculations, that has been proven to be appropriate for modeling bulk and surface ice structures (Lattelais et al. 2011, 2015; Ellinger et al. 2015). Among the different forms, we considered the apolar variety of hexagonal ice *Ih* because these structures have a balanced distribution of alternating hydrogen and oxygen avoiding computational artifacts for surface optimizations and at the same time reproduce the bulk properties (Casassa et al. 2005). How O_2 behaves as a function of the number of H_2O molecules removed is illustrative of the storage capability of the ice as a function of porosity. The results of our calculations, performed using the Vienna ab initio simulation package (Kresse & Hafner 1993, 1994), are presented below.

1. Starting with no H_2O removed, i.e., the pure cristalline ice, we found no stabilization for the inclusion of O_2 in the hexagonal lattice. It is in fact an endothermic process.
2. With one H_2O removed, and replaced by one O_2, we have a substitution structure whose stabilization, in the order of 10^{-3} eV, is meaningless.
3. With 2, 3, and 4 adjacent H_2O molecules removed from the hexagonal lattice we obtained well defined cavities that, after reconstruction, show different shapes according to the positions of the entities removed. The stabilization energies were found to be on the order of 0.2–0.3 eV, going to 0.4–0.5 eV for an embedded O_2 dimer. A typical structure of embedding is illustrated in Figure 2 where O_2 is stabilized with an energy of ∼0.23 eV. This energy is on the order of that of a water dimer, which means that the presence of O_2 should not perturb the ice structure until it is ejected into the coma via sublimation with the surrounding H_2O molecules.

It should be stressed that the formation of one O_2 requires at least the destruction of two H_2O. The present simulation is fully consistent with the aforementioned radiolysis hypothesis, where the irradiation process is at the origin of both the formation of O_2 and the development of the cavity in which it

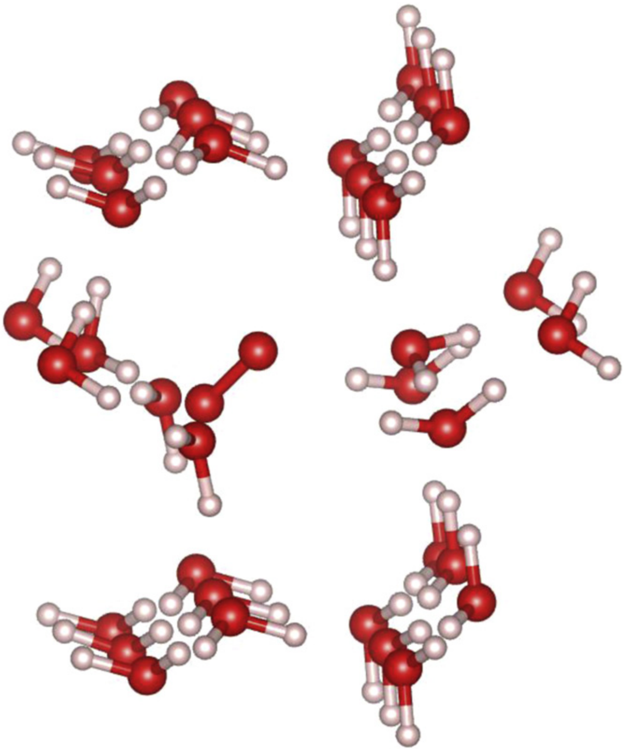

Figure 2. Side view of O_2 embedded in a cavity inside compact amorphous ice. The cavity corresponds to a void of 3 H_2O molecules from an hexagonal apolar lattice.

remains sequestered. Similar results are obtained in the case of O_2 stabilization in amorphous ice.

4. O_2 CLATHRATION IN THE PSN

One possible source of O_2 in the nucleus of 67P/C–G is the trapping of O_2 in clathrates that formed in the PSN prior to having been agglomerated by the comet as it formed. This is supported by recent works showing that the Ar/CO and N_2/CO ratios and the time variation of other volatile species measured in 67P/C–G's coma are found to be consistent with the presence of clathrates in its nucleus (Luspay-Kuti et al. 2016; Mousis et al. 2016). To investigate the amount of O_2 that could have been trapped in clathrates and now be present in 67P/C–G, we use the same statistical thermodynamic model as the one described in Mousis et al. (2010, 2016), which is used to estimate the composition of these crystalline structures formed in the PSN. To evaluate the trapping efficiency of O_2, we consider a gas constituted of O_2 and CO. After H_2O, CO is one of the dominant gases found in 67P/C–G (Le Roy et al. 2015) and in most of comets (Bockelée-Morvan et al. 2004, p. 391). The Kihara parameters for the molecule-water interactions employed in our calculations are derived from Mohammadi et al. (2003) for O_2 and from Mohammadi et al. (2005) for CO. These represent the most recent sets of data found in the literature for the two species. We refer the reader to the model description provided in Mousis et al. (2010) for further details.

When clathrates destabilize in the nucleus, the trapped volatiles are released prior to water sublimation, implying that the water vapor measured at the time of the O_2 sampling by ROSINA should be derived from the vaporization of crystalline ice layers located closer to the surface. Hence, the O_2 depletion is better quantified by comparing the O_2/CO ratio in clathrates and the coma value since these two species are expected to be released simultaneously from destabilized clathrates. Figure 3 represents the value of the O_2/CO ratio in structure I clathrates[7] as a function of the O_2/CO ratio in the coexisting gas phase at a chosen disk's temperature of ∼45 K. This value is within the temperature range needed for clathrates to form in the PSN from a gaseous mixture of protosolar composition that reproduces the Ar/CO and N_2/CO ratios measured in 67P/C–G's coma (Mousis et al. 2016). We find that, whatever the O_2/CO ratio considered for the initial PSN gas phase, it is enriched by a factor of ∼1.4–1.8 in the formed clathrate. Figure 3 also shows that the O_2/CO ratio must be in the 0.026–0.24 range in the PSN gas phase for the clathrate trapping mechanism to agree with the measured range of O_2/H_2O in the coma (∼1%), assuming that all cavities are filled by guest molecules and that the CO/H_2O abundance ratio in the coma corresponds to the sampled value (∼2.7%–21%; Le Roy et al. 2015). This range of O_2/CO ratios is consistent with values obtained at distances beyond ∼5 au in a T Tauri disk (Walsh et al. 2015). Therefore, our calculations show that the clathration of O_2 in the PSN is a realistic mechanism to account for the O_2/H_2O ratio observed by ROSINA in 67P/C–G's coma.

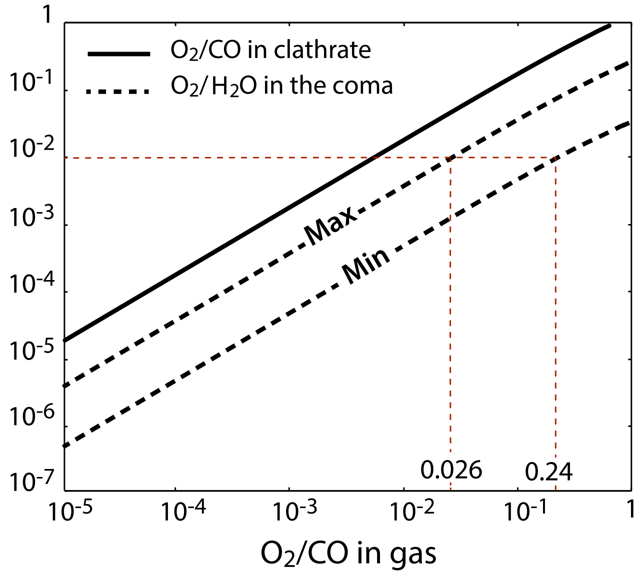

Figure 3. O_2/CO ratio in clathrates formed at 45 K and the corresponding O_2/H_2O ratio in the coma, as a function of the coexisting O_2/CO ratio in the PSN gas phase. The "Min" and "Max" labels correspond to calculations of the O_2/H_2O ratio in 67P/C–G's coma, assuming that the CO/H_2O abundance is between 2.7% and 21% (see the text). The vertical red dashed lines represent the O_2/CO ratio in the PSN gas phase needed to form clathrates giving 1% O_2 relative to H_2O in the coma.

5. O_2 CONDENSATION IN THE PSN

An alternative possibility for the observed presence of O_2 in the coma of 67P/C–G is that the O_2 could have been agglomerated as pure crystalline ice by the nucleus forming at cooler PSN temperatures than those required for clathration.

[7] Both O_2 and CO molecules are expected to form this structure (Mohammadi et al. 2003, 2005).

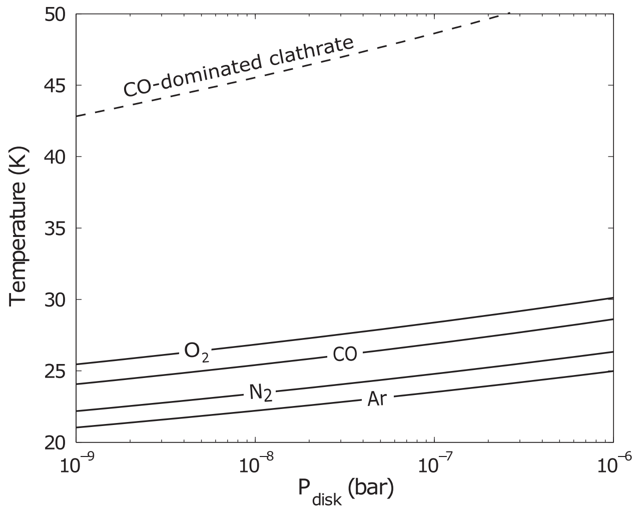

Figure 4. Solid lines: equilibrium curves of O_2, CO, N_2, and Ar pure crystalline ices as a function of total disk pressure. Dashed line: equilibrium curve of the CO-dominated clathrate as a function of total disk pressure (see the text).

To investigate this scenario, we calculated the temperature dependence of the equilibrium curves of O_2, CO, N_2, and Ar pure crystalline ices via the use of the polynomial relations reported by Fray & Schmitt (2009). To derive the partial pressures for each gas, we assumed that O, C, N, and Ar exist in protosolar abundances in the PSN (Lodders et al. 2009), with all C and all N in the forms of CO and N_2, respectively. The partial pressure of O_2 is derived from the O_2/CO gas phase ratio (~33%) predicted beyond the snowline of a T Tauri disk via an extensive chemical model (Walsh et al. 2015). The equilibrium curves of O_2, CO, N_2, and Ar pure crystalline ices are represented along with the equilibrium curve of the CO–N_2–Ar multiple guest clathrate proposed by Mousis et al. (2016) to explain 67P/C–G's composition, as a function of the total PSN pressure in Figure 4. Because the CO–N_2–Ar multiple guest clathrate is by far dominated by CO (see Figure 1 of Mousis et al. 2016), we assume that its partial pressure is the same as for CO crystalline ice. The equilibrium curve of the clathrate is taken from Lectez et al. (2015).

From the examination of the condensation sequence presented in Figure 4, we find that the hypothesis of O_2 agglomeration as pure crystalline ice is inconsistent with 67P/C–G's current composition. The fact that Ar/CO and N_2/CO ratios are found to be significantly depleted by factors of ~90 and 10 in 67P/C–G's coma, respectively, compared to the protosolar values (Balsiger et al. 2015; Rubin et al. 2015a; Mousis et al. 2016), implies that Ar and N_2 cannot form substantial amounts of pure crystalline ices at the formation location of the comet in the PSN (Mousis et al. 2016). Instead, it has been proposed that these volatiles were mostly trapped in CO-dominated clathrates (Mousis et al. 2016). Under these circumstances, because the equilibrium curve of O_2 ice is in the vicinity of those of Ar and N_2 ices, the incorporation of O_2 in this form would require the trapping of larger amounts of Ar and N_2, incidentally leading to quasi protosolar Ar/CO and N_2/CO ratios. This does not agree with the depleted ratios observed in 67P/C–G.

6. CONCLUSIONS

In this study, we have investigated several scenarios that may explain the presence of molecular oxygen in the nucleus of 67P/C–G. Our results are the following:

1. Even with a strong CRF enhancement due to the presence of a nearby supernova, we find that the radiolysis of icy grains is not fast enough in the PSN to create amounts of O_2 comparable with those observed in 67P/C–G. Instead, icy grains must be placed in low-density environments such as molecular clouds to allow radiolysis to work efficiently. The irradiation process also favors the stabilization of O_2 molecules in the icy matrix via the development of cavities and is compatible with both amorphous and crystalline ice structures.
2. O_2 can be efficiently trapped in clathrates formed in the PSN. The O_2/CO ratio in the clathrate phase is up to ~2 times the O_2/CO ratio in the coexisting PSN gas phase.
3. The incorporation of O_2 as pure crystalline ice is unlikely in 67P/C–G because the condensation of this species in the PSN would imply much larger abundances of Ar and N_2 than those observed in the coma.

Based on these results, and assuming that radiolysis has been the only mechanism for producing O_2, we find that the formation of 67P/C–G is possible in a dense and early PSN in the framework of two extreme scenarios: (1) agglomeration from pristine amorphous icy grains/particles formed in the ISM and (2) agglomeration from multiple guest clathrates including O_2 that formed during the cooling of the disk subsequent to the vaporization of the amorphous icy grains entering the PSN. However, scenario 1 was found inconsistent with ROSINA pre-perihelion observations of volatile abundances in the coma. In contrast, Mousis et al. (2016) and Luspay-Kuti et al. (2016) have shown that scenario 2 could match these data if 67P/C–G agglomerated from a mixture of clathrates and crystalline ices that condensed in the PSN. Also, scenario 2 is compatible with a possible chemical production of O_2 in the PSN gas phase (Walsh et al. 2015). In this picture, whatever the considered source, i.e., radiolysis of ISM grains or/and PSN gas phase chemistry, O_2 is efficiently entrapped in clathrates prior to their agglomeration by 67P/C–G.

On the other hand, with the incorporation of O_2 in the cavities created by CRF in the icy matrix, scenario 1 naturally provides an explanation for the strong correlation found between the O_2 and H_2O production rates observed in 67P/C–G's coma (Bieler et al. 2015). If this scenario is correct, this would make implausible the accretion of 67P/C–G from clathrates and crystalline ices originating from the PSN. Meanwhile, a way to reconcile scenario 2 with the strong O_2–H_2O correlation would be to assume that the icy grains initially formed as in scenario 1. These icy grains/particles would have then subsequently experienced an amorphous-to-crystalline phase transition in the 130–150 K temperature range when entering the disk (Kouchi et al. 1994; Maldoni et al. 2003; Ciesla 2014). In this alternative scenario, all volatiles initially adsorbed by ISM amorphous ice would be released in the PSN gas phase during phase transition. With the cooling of the disk, these volatiles would have been later trapped in the clathrates formed with the crystallized icy grains. The case of O_2 is unique because, due to its formation process, this molecule is inserted into the icy matrix. In spite of the phase transition, O_2 would remain stable within the icy matrix because the strength of the interaction between O_2 and the surrounding H_2O molecules is expected not to decrease (eventually increase) upon crystallization. In this scenario, CO, Ar, and N_2 would be trapped in clathrates with O_2 remaining embedded in water, in a way consistent with the observed correlation.

To conclude, further post-perihelion *ROSINA* data, in particular the precise measurements of the relative abundances of the different volatiles as a function of geography and time, are needed to disentangle between the existing formation scenarios. It is also possible that only the in situ sampling of a nucleus by a future lander will provide a definitive answer to the question of the formation conditions of 67P/C–G and other Jupiter Family Comets in the PSN.

O.M. acknowledges support from CNES. This work has been partly carried out thanks to the support of the A*MIDEX project (n^{o} ANR-11-IDEX-0001-02) funded by the "Investissements d'Avenir" French Government program, managed by the French National Research Agency (ANR). This work also benefited from the support of CNRS-INSU national program for planetology (PNP). R.M. was supported by the Belgian Science Policy Office through the Solar-Terrestrial Centre of Excellence and by PRODEX/ROSETTA/ROSINA PEA 4000107705. J.I.L. acknowledges support from JWST. K.E. M. acknowledges support from JPL Subcontract 1345493.

REFERENCES

Alexeev, V. A. 2016, SoSyR, 50, 24
Balsiger, H., Altwegg, K., Bar-Nun, A., et al. 2015, SciA, 1, e1500377
Balsiger, H., Altwegg, K., Bochsler, P., et al. 2007, SSRv, 128, 745
Bieler, A., Altwegg, K., Balsiger, H., et al. 2015, Natur, 526, 678
Bockelée-Morvan, D., Crovisier, J., Mumma, M. J., & Weaver, H. A. 2004, in Comets II, ed. M. C. Festou, H. U. Keller, & H. A. Weaver (Tucson, AZ: Univ. Arizona Press), 391
Casassa, S., Calatayud, M., Doll, K., Minot, C., & Pisani, C. 2005, CPL, 409, 110
Ciesla, F. J. 2014, ApJL, 784, L1
Cooper, J. F., Christian, E. R., & Johnson, R. E. 1998, AdSpR, 21, 1611
Cooper, J. F., Christian, E. R., Richardson, J. D., & Wang, C. 2003, EM&P, 92, 261
Effenberger, F., Fichtner, H., Scherer, K., & Büsching, I. 2012, A&A, 547, A120
Ellinger, Y., Pauzat, F., Mousis, O., et al. 2015, ApJL, 801, L30
Fields, B. D., & Ellis, J. 1999, NewA, 4, 419
Fray, N., & Schmitt, B. 2009, P&SS, 57, 2053
Hersant, F., Gautier, D., & Huré, J.-M. 2001, ApJ, 554, 391
Johnson, R. E. 1990, PCS, 19
Johnson, R. E. 1991, JGR, 96, 17
Kouchi, A., Yamamoto, T., Kozasa, T., Kuroda, T., & Greenberg, J. M. 1994, A&A, 290, 1009
Kresse, G., & Hafner, J. 1993, PhRvB, 48, 13115
Kresse, G., & Hafner, J. 1994, PhRvB, 49, 14251
Lattelais, M., Bertin, M., Mokrane, H., et al. 2011, A&A, 532, A12
Lattelais, M., Pauzat, F., Ellinger, Y., & Ceccarelli, C. 2015, A&A, 578, A62
Lectez, S., Simon, J.-M., Mousis, O., et al. 2015, ApJL, 805, L1
Le Roy, L., Altwegg, K., Balsiger, H., et al. 2015, A&A, 583, A1
Lodders, K., Palme, H., & Gail, H.-P. 2009, Landolt Börnstein, ed. J. E. Trümper Springer Materials
Luspay-Kuti, A., Mousis, O., Fuselier, S. A., et al. 2016, SciA, 2, e1501781
Maldoni, M. M., Egan, M. P., Smith, R. G., Robinson, G., & Wright, C. M. 2003, MNRAS, 345, 912
Mohammadi, A. H., Anderson, R., & Tohidi, B. 2005, Am. In. Chem. Eng., 51, 2825
Mohammadi, A. H., Tohidi, B., & Burgass, R. W. 2003, J. Chem. Eng. Data, 48, 612
Mousis, O., Lunine, J. I., Luspay-Kuti, A., et al. 2016, ApJL, 819, L33
Mousis, O., Lunine, J. I., Picaud, S., & Cordier, D. 2010, FaDi, 147, 509
Mumma, M. J., & Charnley, S. B. 2011, ARA&A, 49, 471
Parrish, W. R., & Prausnitz, J. M. 1972, Ind. Eng. Chem. Process Design Dev., 11, 26 (Erratum: Parrish, W. R., Prausnitz, J. M. 1972, Ind. Eng. Chem. Process Design Dev. 11, 462)
Rubin, M., Altwegg, K., Balsiger, H., et al. 2015a, Sci, 348, 232
Rubin, M., Altwegg, K., van Dishoeck, E. F., & Schwehm, G. 2015b, ApJL, 815, L11
Walsh, C., Nomura, H., & van Dishoeck, E. 2015, A&A, 582, A88
Weidenschilling, S. J., & Cuzzi, J. N. 1993, in Protostars and Planets III (Tucson, AZ: Univ. Arizona Press), 1031
Werner, M., Kissmann, R., Strong, A. W., & Reimer, O. 2015, APh, 64, 18
Yeghikyan, A. G. 2011, Ap, 54, 87

THE ASTROPHYSICAL JOURNAL, 828:109 (7pp), 2016 September 10 doi:10.3847/0004-637X/828/2/109

RECONCILING THE ORBITAL AND PHYSICAL PROPERTIES OF THE MARTIAN MOONS

T. RONNET[1], P. VERNAZZA[1], O. MOUSIS[1], B. BRUGGER[1], P. BECK[2], B. DEVOUARD[3], O. WITASSE[4], AND F. CIPRIANI[4]
[1] Aix Marseille Université, CNRS, LAM (Laboratoire d'Astrophysique de Marseille) UMR 7326, F-13388, Marseille, France; pierre.vernazza@lam.fr
[2] Univ. Grenoble Alpes, IPAG, F-38000 Grenoble, France
[3] Aix-Marseille Université, CNRS, IRD, CEREGE UM34, F-13545 Aix en Provence, France
[4] European Space Agency, ESTEC, Keplerlaan 1, 2200 AG Noordwijk, The Netherlands
Received 2016 February 26; revised 2016 May 19; accepted 2016 June 2; published 2016 September 8

ABSTRACT

The origin of Phobos and Deimos is still an open question. Currently, none of the three proposed scenarios for their origin (intact capture of two distinct outer solar system small bodies, co-accretion with Mars, and accretion within an impact-generated disk) are able to reconcile their orbital and physical properties. Here we investigate the expected mineralogical composition and size of the grains from which the moons once accreted assuming they formed within an impact-generated accretion disk. A comparison of our results with the present-day spectral properties of the moons allows us to conclude that their building blocks cannot originate from a magma phase, thus preventing their formation in the innermost part of the disk. Instead, gas-to-solid condensation of the building blocks in the outer part of an extended gaseous disk is found as a possible formation mechanism as it does allow reproducing both the spectral and physical properties of the moons. Such a scenario may finally reconcile their orbital and physical properties, alleviating the need to invoke an unlikely capture scenario to explain their physical properties.

Key words: planets and satellites: composition – planets and satellites: formation – planets and satellites: individual (Phobos, Deimos)

1. INTRODUCTION

During the 1970s and 1980s, dynamicists demonstrated that the present low eccentricity, low inclinations, and prograde orbits of Phobos and Deimos are very unlikely to have been produced following capture (Burns 1978; Pollack et al. 1979), thus favoring a formation of the moons around Mars (Goldreich 1963; Cazenave et al. 1980; Szeto 1983). Despite such early robust evidence against a capture scenario, the fact that the moons share similar physical properties (low albedo, red and featureless VNIR reflectance, low density) with outer main belt D-type asteroids has kept the capture scenario alive (Fraeman et al. 2012, 2014; Pajola et al. 2013).

Whereas the present orbits of the moons are hardly compatible with a capture scenario, they correspond to the expected outcome of an in situ formation scenario as the result of either co-accretion or a large impact. Co-accretion with Mars appears unlikely because Phobos and Deimos would consist of the same building block materials from which Mars once accreted. Those building blocks would most likely comprise water-poor chondritic meteorites (enstatite chondrites, ordinary chondrites) and/or achondrites (e.g., angrites), which are all suspected to have formed in the inner ($\leqslant$2.5 au) solar system, namely, interior to the snowline. This assumption is supported by the fact that the bulk composition of Mars can be well reproduced assuming ordinary chondrites (OCs), enstatie chondrites, and/or angrites as the main building blocks (Sanloup et al. 1999; Burbine & O'Brien 2004; Fitoussi et al. 2016). Yet OCs, as well as the remaining candidate building blocks (enstatite chondrites, angrites), are spectrally incompatible with the Martian moons, even if space weathering effects are taken into account (see panel (b) in Figure 1).

It thus appears from above that accretion from an impact-generated accretion disk remains as the only plausible mechanism at the origin of the Martian moons. As a matter of fact, the large impact theory has received growing attention in recent years (Craddock 2011; Rosenblatt & Charnoz 2012; Canup & Salmon 2014; Citron et al. 2015). This hypothesis is attractive because it naturally explains the orbital parameters of the satellites, as well as some features observed on Mars, such as (i) its excess of prograde angular momentum possibly caused by a large impact (Craddock 2011) and (ii) the existence of a large population of oblique impact craters at its surface that may record the slow orbital decay of ancient moonlets formed from the impact-generated accretion disk (Schultz & Lutz-Garihan 1982). Along these lines, Citron et al. (2015) have recently shown that a large impact (impactor with 0.01–0.02 Mars masses) would generate a circum-Mars debris disk comprising ~1%–4% of the impactor mass, thus containing enough mass to form both Phobos and Deimos. Although the impact scenario has become really attractive, it has not yet been demonstrated that it can explain the physical properties and spectral characteristics of the Martian moons.

Here we investigate the mineralogical composition and texture of the dust that would have crystallized in an impact-generated accretion disk. Since there are no firm constraints regarding the thermodynamic properties of the disk, we perform our investigation for various thermodynamic conditions and impactor compositions. We show that under a specific disk's pressure and temperature conditions, Phobos's and Deimos's physical and orbital properties can be finally reconciled.

2. FORMATION FROM A COOLING MAGMA

Because of the absence of constraints regarding the composition (Mars-dominated or impactor-dominated) and the thermodynamic conditions of the impact-generated disk, several configurations must be investigated in order to understand the formation conditions of Phobos and Deimos within such a scenario. As a first step, we considered the protolunar disk as a reference case because it is so far the most

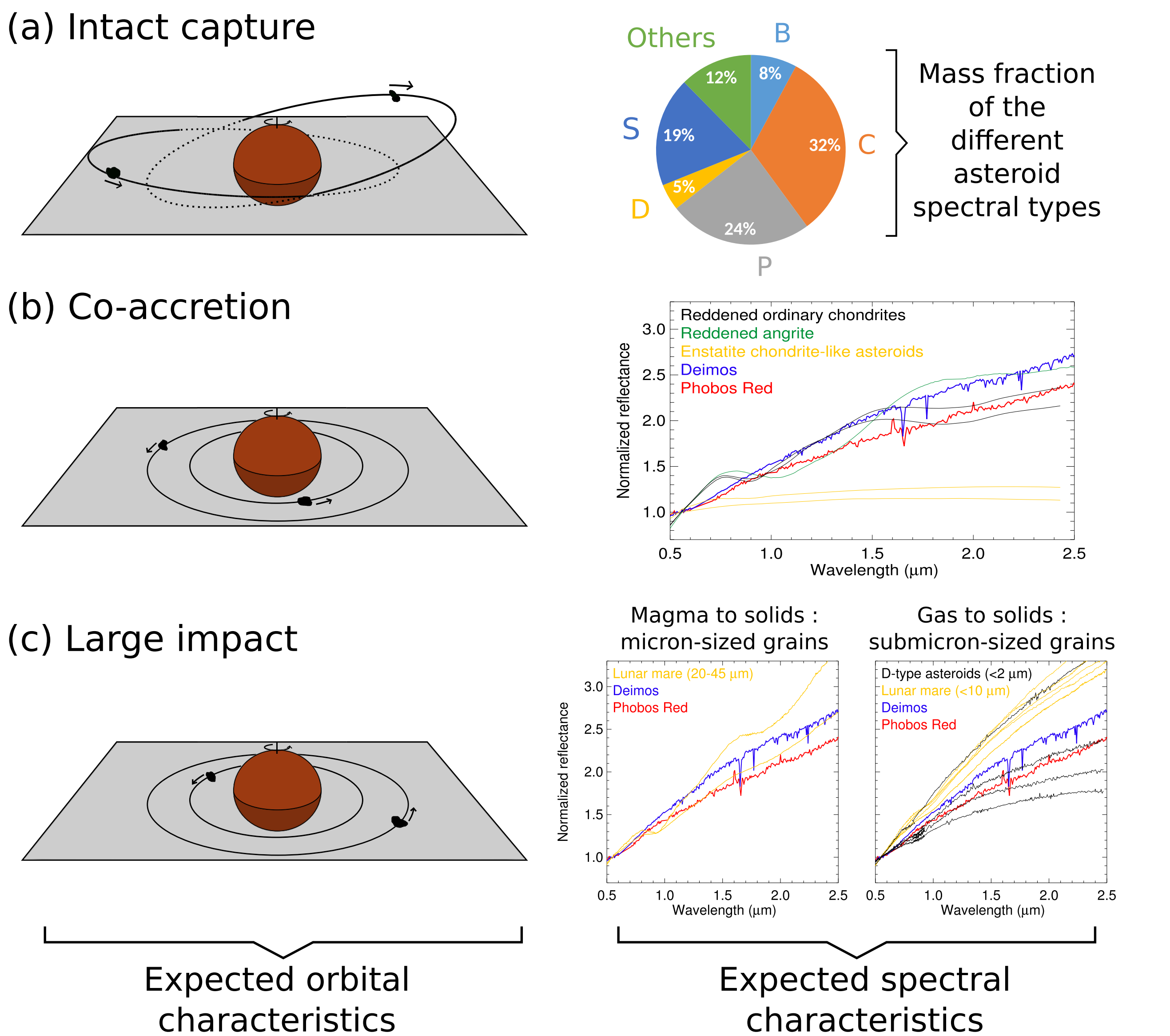

Figure 1. Schematic representation of the expected orbital (left) and spectral (right) characteristics of the Martian moons for each of the three different scenarios currently invoked for their origin. Note that in the case of Phobos, we display the average spectrum of the red region. The Phobos and Deimos spectra are CRISM/MRO data that were retrieved from PDS: http://pds-geosciences.wustl.edu/. The lunar mare spectra were retrieved from http://pgi.utk.edu/. The meteorite spectra were retrieved from RELAB: www.planetary.brown.edu/relab/. The asteroid spectra were retrieved from http://smass.mit.edu/. (a) The intact capture scenario would likely produce retrograde, large, eccentric, and inclined orbits. The nearby asteroid belt being a good proxy for the asteroid types that could have been captured, we display the spectral diversity of the latter (DeMeo & Carry 2013). Both D-type asteroids (which are the closest spectral analogs to Phobos and Deimos) and P-types are thought to have formed in the primordial trans-Neptunian disk and to have been injected in the inner solar system during the late migration of the giant planets (e.g., the Nice model; Levison et al. 2009). Such an event could have potentially led to a few of these objects being captured as moons by Mars. The problem with this scenario is that P-types are twice as abundant as D-types; the capture of two D-types around Mars rather than two P-types or even one P-type and one D-type is thus not statistically favored. Along these lines, an additional caveat of the capture scenario is that the density of the largest ($D \geqslant 200$ km) P- and D-type asteroids lies in the 0.8–1.5 g cm^{-3} range (Carry 2012). With density decreasing with asteroid size for a given composition (Carry 2012), we would expect the density of Phobos and Deimos to be somewhere in between the density of the comet 67P (~0.5 g cm^{-3}; Sierks et al. 2015) and the one of the largest P- and D-types (Carry 2012), thus clearly below the one of the Martian moons. (b) In the co-accretion scenario, circular and co-planar orbits would be expected and the spectral characteristics of the Martian moons would likely ressemble those of either reddened ordinary chondrites, reddened angrites, or enstatite chondrite-like asteroids (note: enstatite chondrites barely redden via space weathering effects; see Vernazza et al. 2009). Yet this is not the case. (c) Within the impact scenario, acondensation directly from a magma (left) would lead to the Martian moons having typical lunar-mare-like spectral properties resulting from the coexistence of fine ($\leqslant$10 μm; spectrally featureless) and of large ($\geqslant$10 μm; spectrally feature-rich) olivine and pyroxene grains at their surfaces. Alternatively, gas-to-solid condensation in the external part of the disk (right) would lead to the formation of small grains ($\leqslant$2 μm) and thus naturally explain the similarity in spectral properties between the moons and both D-type asteroids and fine-grained ($\leqslant$10 μm) lunar soils.

studied impact-generated accretion disk. Its structure has been investigated by Thompson & Stevenson (1988) and subsequently by Ward (2012, 2014). These studies have shown that the disk's midplane consists of a liquid phase surrounded by a vapor atmosphere. Beyond the Roche limit, gravitational instabilities developed and large clumps formed directly from the magma (e.g., Kokubo et al. 2000; Salmon & Canup 2012). Those clumps then agglomerated to form the Moon. In this

Table 1
Bulk Silicate Compositions Used to Model the Disk Composition

Oxide Wt%	BSM[a]	Dep. BSM[b]	Moon[c]	IDP[d]
SiO_2	45.39	17.4	44.60	47.00
MgO	29.71	20.5	35.10	16.8
MnO	⋯	⋯	⋯	0.1
NiO	⋯	⋯	⋯	1.1
Al_2O_3	2.89	2.19	3.90	1.3
TiO_2	0.14	0.09	0.17	⋯
Feo	17.21	10.55	12.40	24.4
CaO	2.36	1.81	3.30	0.9
Cr_2O_3	⋯	⋯	⋯	0.2
Na_2O	0.98	0.01	0.05	⋯
K_2O	0.11	0.01	0.004	⋯
S	⋯	⋯	⋯	7.3
Total	98.79	52.54	99.5	99.09

Notes.
[a] Bulk silicate Mars (Lodders & Fegley 2011).
[b] Depleted BSM estimated for a 50% vaporized disk (Canup et al. 2015).
[c] Bulk silicate Moon (O'Neill 1991).
[d] Interplanetary dust particle (Rietmeijer 2009).

case, because of internal evolutionary processes (differentiation, convection, etc.), the mineralogical composition and thus the spectral properties of the lunar mantle and crust will differ from the clump ones. In the Martian case, the situation is different in the sense that the clumps possess right away a mass/size comparable to that of Phobos and Deimos (Rosenblatt & Charnoz 2012). This implies that the final composition and spectral properties of the Martian moons would directly reflect those of the minerals that crystallized from the magma disk.

2.1. Methods

We considered three different compositions for the impactor (see Table 1), namely, a Mars-like composition (1), a moon-like composition (2), and an outer solar system composition (3) (i.e., TNO). The latter case would be coherent with an inward migration of a large planetesimal as a consequence of the possible late migration of the giant planets (e.g., Morbidelli et al. 2005). By analogy with the Earth-moon system, it has been suggested, however, that the impactor most probably formed near the proto-Mars (Hartmann & Davis 1975; see cases 1 and 2), but one cannot exclude that the impactor formed elsewhere (case 3).

In addition, since the relative proportions of the impactor and Martian materials are poorly constrained in the resulting disk, we considered various proportions between these two materials. We considered two cases, namely, a disk exclusively made of the impactor mantle and a half–half fraction. Case 1 complements this sequence by illustrating the case for a 100% fraction of the Martian mantle.

To estimate the composition of the solids crystallized from the magma and thus of the moons, we performed a CIPW normative mineralogy calculation (Gonzalez-Guzman 2016). This method allows determining the nature of the most abundant minerals that crystallize from an anhydrous melt at low pressure while providing at the same time a good estimate of their final proportions. The CIPW norm calculation is well

Table 2
Bulk Mineral Composition Resulting from the CIPW Norm Calculation

Minerals Wt%	BSM 100%	Dep. BSM 100%	Moon 100%	Moon/BSM 50%/50%	IDP 100%	IDP/BSM 50%/50%
Quartz	⋯	⋯	⋯	⋯	9.83	⋯
Plagioclase	11.59	10.45	10.88	11.24	3.62	9.57
Orthoclase	0.66	⋯	0.02	0.34	⋯	0.33
Diopside	6.97	⋯	4.78	5.87	0.76	5.69
Hypersthene	21.29	⋯	23.24	22.24	66.00	48.86
Olivine	59.22	84.65	60.76	60.01	⋯	27.58
Magnetite	⋯	2.97	⋯	⋯	4.01	⋯
Pyrite	⋯	⋯	⋯	⋯	15.78	7.84
Total	99.73	98.07	99.68	99.70	100	99.87

adapted to our case given that the disk supposedly cooled down slowly through radiation (Ward 2012), allowing complete crystallization of the minerals. It should be noted that we do not aim at determining the exact composition of the moons. Considering the few constraints we have on the system, our purpose is to discriminate between plausible and unplausible scenarios and thus provide new constraints for future studies.

2.2. Results

In this section, we present the inferred mineralogical composition of the moons for the three aforementioned impactor compositions (see Table 2) and for the different relative abundances of the impactor and Martian mantle.

1. *Case 1 (Mars-like impactor)*: since the impactor has a composition similar to that of Mars, we performed the calculation using a bulk silicate Mars (BSM) magma composition (taken from Lodders & Fegley 2011). The BSM is an estimate of the chemical composition of Mars's mantle. By calculating the CIPW norm, we found that both olivine and orthopyroxene (hypersthene) are the main minerals to crystallize (~59% and ~21%, respectively). Both diopside and feldspar (plagioclase) are also formed, although in significantly lower proportions (~7% and ~12%, respectively).

   Note, however, that the above results do not account for a partial vaporization of the disk. The fraction of vaporized material is speculative, although theoretical considerations advocate that it should be more than 10% in the case of the protolunar disk (Ward 2012, 2014). To emphasize the role of vaporization on the resulting composition of the building blocks of the moons, we considered the case of a half vaporized disk (see Table 1(b)). Its magma composition was derived following the results of Canup et al. (2015) for a bulk silicate Earth (BSE) disk's composition. This first-order approximation is quantitatively valid as the BSE and BSM compositions are very similar (Visscher & Fegley 2013). By applying the CIPW norm to this new magma composition, we found that significantly more olivine is crystallized (~85%), whereas both orthopyroxene and diopside do not form. The proportion of feldspar remains, however, the same (~10%).
2. *Case 2 (moon-like impactor)*: here we used the bulk silicate moon composition as a proxy for the impactor

composition. For both a 50%–50% Moon–Mars mixing ratio and a pure lunar-like composition, we found that both olivine and orthopyroxene (hypersthene) are the main crystallizing minerals (~60% and ~22%, respectively). In both cases, it thus appears that the derived bulk composition of the moons is very close to the one obtained for a BSM disk's composition. Taking into account a partial vaporization of the magma would also lead to results similar to those obtained for case 1.

3. *Case 3 (TNO-like impactor)*: here we used the composition of interplanetary dust particles (IDPs; Rietmeijer 2009) as a proxy for the composition of the TNO-like impactor. IDPs, which are the likely building blocks of comets, may also be the ones of TNOs if one follows the basic and currently accepted assumption that both populations formed in the outer solar system. However, by using directly the composition of IDP grains, we neglect the effect of differentiation that has likely occurred on a moon-sized TNO. This implies that we certainly overestimate the amount of iron in the disk.

   When considering a pure IDP-like composition, quartz crystallizes because of an excess of silica. Indeed, the amount of Mg and Fe does not allow the formation of enough olivine and pyroxene to account for all the available Si. Moreover, quartz and Mg-rich olivine being mutually exclusive minerals, the absence of one of the two is the norm if the other is formed. In this case, the resulting composition is pyroxene-rich instead of olivine-rich. A substantial amount of pyrite is also formed due to the high proportion of sulfur in IDPs. When considering a 50%–50% TNO–Mars mixing ratio, there is no longer an excess of silica. Orthopyroxene remains the most abundant mineral, but olivine is formed instead of quartz and in a larger amount.

In summary, we find that for every tested scenario the inferred mineralogical composition of the building blocks of the moons (and thus of the moons) is either olivine-rich or pyroxene-rich. Since minerals that solidify from a slow cooling magma are usually coarse grained (grain size usually in the 10 μm–1 mm range; see Section A.1.; Cashman 1993; Solomatov 2007, p. 91), our findings imply that if Phobos and Deimos actually formed from a disk of magma, then their spectra—similarly to those of either S-type asteroids or lunar mares—should display detectable 1 and 2 μm bands (see Figure 1, panel (c)—left) that are characteristic of the presence of olivine (1 μm) and pyroxene (1 and 2 μm).

Yet this is not the case. It is very unlikely that space weathering effects—which are more significant at 1 au than at 1.5 au—could suppress the olivine and pyroxene absorption bands in the Martian moons' spectra, considering that those effects are not able to suppress them in the lunar ones (Pieters et al. 2000; Yamamoto et al. 2012). We thus conclude that it is highly unlikely that Phobos and Deimos actually formed from a disk of magma. Another argument in disfavor of this scenario is given by the fact that the magma resides inside the Roche limit (at ~$4R_{\mathrm{Mars}}$), which in the Martian case is located inside the synchronous orbit (at ~$6R_{\mathrm{Mars}}$). Thus, the bodies that formed directly from the magma must have impacted Mars a long time ago as a consequence of their orbital decay due to tidal forces (Rosenblatt & Charnoz 2012).

3. FORMATION IN AN EXTENDED GASEOUS DISK

A different formation mechanism is thus required to explain both the current orbits of the moons and their spectral characteristics. Of great interest, Rosenblatt & Charnoz (2012) suggested that the moons could have formed in an extended gaseous disk farther from Mars than in the two-phase disk case. Such a disk should be initially hot so that it would thermally expand under pressure gradients and be gravitationally stable beyond the Roche limit. As the disk would thermally expand, it would cool down rapidly. The extended disk would also have a lower pressure and a larger radiative surface, allowing, again, a faster cooling than a compact disk residing inside the Roche limit.

In this scenario, the conditions under which Phobos and Deimos formed could have been similar to those that occurred in the protosolar nebula in the sense that small solid grains could have condensed directly from the gas without passing through a liquid (magma) phase (see Section A.2.). In this case, Phobos and Deimos would consist of material that has the same texture—not necessarily the same composition—as the one that has been incorporated into comets and D-type asteroids, namely, fine-grained dust (grain size $\leqslant 2\,\mu$m; see A2; Vernazza et al. 2015). It would therefore not be surprising that these objects share similar physical properties, including (i) a low albedo (pv ~ 0.06) and (ii) featureless and red spectral properties in the visible and near-infrared range (see Figure 1, panel (c)—right; Vernazza et al. 2015). It is important to stress here that there are currently no available laboratory reflectance spectra in the visible and near-infrared range for submicron-sized particles. The spectral behavior in this wavelength range can be reproduced via the Mie theory as implemented by Vernazza et al. (2015). These authors showed that a space weathered mixture of submicron-sized olivine and pyroxene grains would possess spectral properties similar to those of P- and D-type asteroids. Future laboratory measurements will be necessary in order to characterize the reflectance properties of all kinds of minerals (silicates, phyllosilicates, iron oxides, etc.) in order to provide more accurate constraints on the composition of the moons. Note that a further comparison of the Phobos and Deimos spectra with those of fine-grained lunar mare soils (grain size $\leqslant 10\,\mu$m) reinforces the idea that the moons may effectively be aggregates of submicron-sized grains. Indeed, although the average grain size of the lunar soils is small ($\leqslant 10\,\mu$m), absorption bands at 1 μm are still visible, suggesting that the grains at the surface of the Martian moons must be even smaller than these already fine-grained lunar samples.

Finally, accretion from such poorly consolidated submicron-sized material would also naturally explain the low densities (~1.86 g cm^{-3} for Phobos and ~1.48 g cm^{-3} for Deimos) and high internal porosities (~40%–50% assuming an anhydrous silicate composition) of the moons (Andert et al. 2010; Rosenblatt 2011; Willner et al. 2014). Importantly, such high porosity is not observed in the case of S-type asteroids with diameters in the 10–30 km size range (a ~20%–30% porosity is observed for these objects; Carry 2012), reinforcing the idea that the building blocks of the Martian moons must be drastically different in texture from those of S-type asteroids (i.e., OCs).

The fact that the building blocks of the moons should avoid a magma phase provides interesting constraints on the thermodynamic conditions that prevailed inside the disk. Whereas a

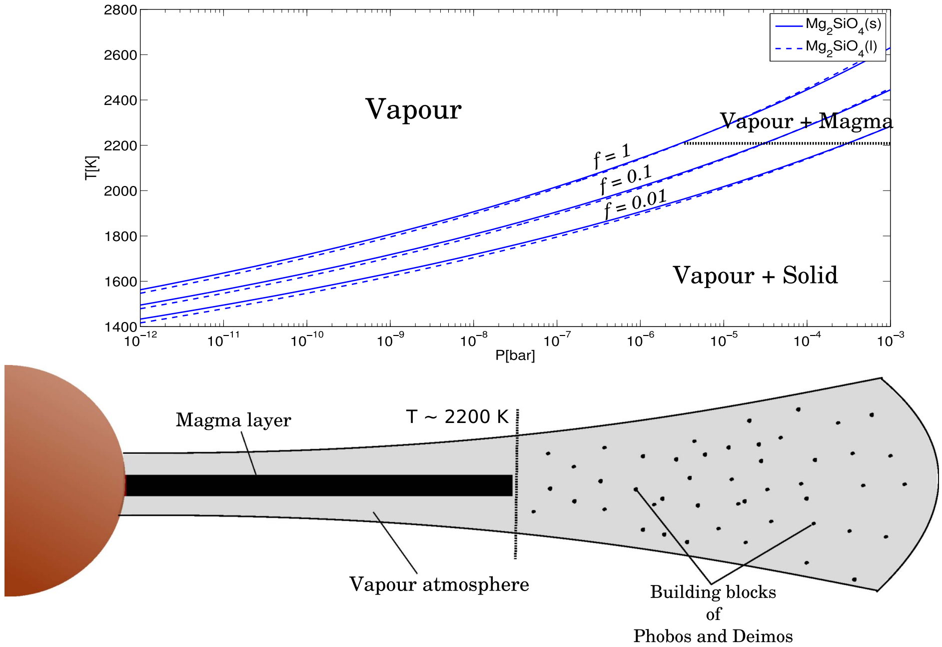

Figure 2. Schematic representation of the plausible structure of the accretion disk around Mars. The external part of the disk where Phobos and Deimos may have formed is defined as the region on the right side of the vertical line where the temperature drops below ~2200 K and solids start to condense. The location of the synchronous orbit shall lie in this extended part of the disk to prevent rapid orbital decay of the moons toward Mars. The equilibrium curves of solid (solid line) and liquid (dotted line) forsterite are shown for different fractions (f) of Mg and Si bound into MgO and SiO_2.

magma layer inside the Roche limit is not inconsistent with our findings (the moon or moons that would have formed from this layer would have impacted Mars a long time ago), future modeling of the disk should account for an extended disk where the pressure and the temperature allow for a direct condensation of the vapor into solid grains.

In order to provide constraints for future models of the Martian disk, we determined the pressure–temperature ranges where the gas would directly condense into solid grains assuming a BSM composition of the gas. We restricted our analysis to the condensation of olivine only. Gail (1998) found that olivine would first condense as nearly pure forsterite and iron might be included later on in the solution. We consequently considered the condensation of pure forsterite. The pressure up to which solid or liquid forsterite is stable for a given temperature can be calculated with the following formula:

$$P(T)^3 = \frac{1}{x_{\mathrm{MgO}}^2 x_{\mathrm{SiO_2}} e^{-\Delta G_{s,l}/RT}}, \tag{1}$$

where $\Delta G_{s,l}$ is the Gibbs free energy of formation of solid or liquid forsterite from gaseous MgO and SiO_2 (it can be calculated with the JANAF online tables), and x_{MgO} and $x_{\mathrm{SiO_2}}$ are the molar fractions of the gases. An extensive chemical model would thus be required in order to infer these molar fractions. As such detailed modeling is beyond the scope of the present work, we simply assumed that different fractions (f) of Mg and Si were bound into MgO and SiO_2 molecules in the gas phase and thus $x_{\mathrm{MgO,SiO_2}} = f\epsilon_{\mathrm{Mg,Si}}$, ϵ being the fraction of the element.

The stability curves are shown in Figure 2 for $f = 1$, 0.1, and 0.01. The last two cases are more realistic given that Mg is usually found as a free atom whereas Si is mainly found in SiO molecules. We find that the solid phase of forsterite becomes more stable than the liquid one below a temperature of ~2200 K. At this temperature, the condensation of forsterite occurs at a pressure lower than 10^{-6} to 10^{-3} bar depending on the partial pressures of MgO and SiO_2.

4. DISCUSSION

Here we have opened the possibility that gas-to-solid condensation in the external part of an extended gaseous disk is a likely formation mechanism for the Martian moons' building blocks, as it would lead to the formation of small ($\leqslant 2\ \mu$m) dust particles. Accretion from such tiny grains would naturally explain the similarity in spectral properties between D-type asteroids (or comets) and the Martian moons, as well as their low densities. It therefore appears that accretion in the external part of an impact-generated gaseous disk is a likely formation mechanism for the Martian moons that would allow reconciling their orbital and physical properties. Future work should attempt modeling the mineralogy resulting from the gas-to-solid condensation sequence and verify that a space weathered version of the derived composition sieved to submicron-sized grains is compatible with the spectral properties of the moons. Such investigation would greatly benefit from detailed numerical models that would constrain the thermodynamic properties of a circum-Mars impact-generated disk as a function of radial distance.

Finally, note that our proposed scenario is not incompatible with the presence of weak hydration features in the spectra of Phobos and Deimos (Giuranna et al. 2011; Fraeman et al. 2012, 2014). Water has been delivered to the surfaces of most if not all bodies of the inner solar system, including the moon (Sunshine et al. 2009), Mercury (Lawrence et al. 2013), and Vesta (Scully et al. 2015). It has thus become clear recently that space weathering processes operating at the surfaces of atmosphere-less inner solar system bodies not only comprise the impact of solar wind ions and micrometeorites, which tend to redden and darken the spectra of silicate-rich surfaces, but also comprise contamination and mixing with foreign materials, including water-rich ones (Pieters et al. 2014).

We warmly thank the referee for his very constructive review. P.V. and O.M. acknowledge support from CNES. This work has been partly carried out thanks to the support of the A*MIDEX project (no. ANR-11-IDEX-0001-02) funded by the "Investissements d'Avenir" French Government program, managed by the French National Research Agency (ANR).

APPENDIX

A.1. Grain Size Resulting from Magma Solidification

The grain size of a crystal resulting from magma solidification has been extensively studied and appears closely related to its cooling history. Rapid cooling ($\gtrsim 10^2$ K hr^{-1}) will lead to the formation of smaller grains ($\sim 10^{-2}$ mm), whereas slow cooling ($\lesssim 1$ K hr^{-1}) will lead to the formation of larger grains (~ 1 mm), as is observed in experimental studies and Earth's samples (Flemings et al. 1976; Ichikawa et al. 1985; Cashman & Marsh 1988; Grove 1990; Cashman 1993). This is well illustrated in the case of Earth's rocks via basalts and gabbros. These rocks possess the same composition but a very different texture. Basalts are extrusive igneous rocks that experienced rapid cooling within either Earth's atmosphere or oceans and possess a fine-grained structure. On the other end, gabbros are intrusive igneous rocks that crystallized below Earth's surface on much longer timescales and thus exhibit coarse grains.

In the present case, assuming that the temperature of the magma layer is regulated by the disk radiative cooling only, an order of magnitude of the disk cooling rate is

$$\frac{dT}{dt} = -\frac{2\pi R_{\rm disk}^2 \sigma_{\rm SB} T_{ph}^4}{M_{\rm disk} C_p} \sim -2 \text{ K hr}^{-1}, \tag{2}$$

where $R_{\rm disk} = 4R_{\rm Mars}$, which is approximately the Roche limit, $\sigma_{\rm SB} = 5.67 \times 10^{-8}$ J m^{-2} K^{-1} is the Stefan–Boltzmann constant, $T_{\rm ph} = 2000$ K is the temperature of the disk at the photosphere that is maintained at $\sim$2000 K throughout its lifetime (Ward 2012), $M_{\rm disk} = 5 \times 10^{20}$ kg following the results of Citron et al. (2015), and $C_p = 4 \times 10^3$ J kg^{-1} K^{-1} is the heat capacity of the vapor.

One may also consider that the clumps formed still molten at the Roche limit. In this case, assuming a density $\rho = 3300$ kg m^{-3} for the melt and clumps with typical sizes in the 1–10 km range, an order of magnitude of the clump cooling rate would be

$$\frac{dT}{dt} = -\frac{3\pi \sigma_{\rm SB} T_s^4}{R_{\rm clump} \rho C_p} \sim -0.2\text{–}2 \text{ K hr}^{-1}, \tag{3}$$

where the largest clumps would possess the slowest cooling rates and vice versa. In either case, the cooling timescales are comparable to those derived from laboratory experiments, and the rocks that would have crystallized from the magma should typically exhibit the same grain sizes as those found in magmatic rocks on Earth.

In a different register, it is interesting to note that chondrules, which formed as molten or partially molten droplets in space before being accreted to their parent asteroids, have typical sizes in the 0.1–1 mm range (Hutchison 2004). In summary, magma condensates appear always coarse grained (grain size in the 0.1–1 mm range), regardless of their formation mechanism.

A.2. Grain Size Resulting from Gas to Solid Condensation

The texture and size of the grains condensing directly from the vapor are, similarly to the solidification from a magma, closely related to the cooling rate of the vapor. Fast cooling will be associated with a high nucleation rate. As such, a rapid decrease of the temperature will imply the condensation of a large number of small grains. On the contrary, if the cooling rate is slow, fewer nuclei will condense, but these will grow by continuous condensation of vapor onto their surface, which will result, on average, in the development of larger grains. This process has been investigated via both theory (Gail et al. 1984; Gail & Sedlmayr 1988) and laboratory experiments (Rietmeijer & Karner 1999; Rietmeijer et al. 1999a, 1999b; Toppani et al. 2006; De Sio et al. 2016). The theoretical investigations of grain growth in stellar outflows were applied to carbon growth and resulted in grains with sizes in the 10^{-3} to 1 μm range (Gail et al. 1984). Concerning the laboratory experiments, two cases have been investigated, namely, a rapid and a slow condensation of silicate-rich vapor into solid grains. In the case of rapid condensation, which occurs in nonequilibrium, the formation of very small amorphous grains with typical sizes of a few tens to a few hundred nanometers was observed, in agreement with theoretical calculations by Gail et al. (1984). In the case of slow condensation, which occurs near equilibrium, the formation of small crystalline grains with typical sizes of a few hundred nanometers was observed (Toppani et al. 2006). It therefore appears that—in either case (slow or fast cooling)—small dust grains with typical sizes of $\sim$0.1 μm are the natural outcome of gas-to-solid condensation. This is very coherent with the typical grain sizes observed among interplanetary dust particles (Rietmeijer 2009).

REFERENCES

Andert, T. P., Rosenblatt, P., Pätzold, M., et al. 2010, GeoRL, 37, L09202
Burbine, T. H., & O'Brien, K. M. 2004, M&PS, 39, 667
Burns, J. A. 1978, VA, 22, 193
Canup, R. M., & Salmon, J. 2014, BAAS, 46, 501.09
Canup, R. M., Visscher, C., Salmon, J., & Fegley, B., Jr. 2015, NatGe, 8, 918
Carry, B. 2012, P&SS, 73, 98
Cashman, K. V. 1993, CoMP, 113, 126
Cashman, K. V., & Marsh, B. D. 1988, CoMP, 99, 292
Cazenave, A., Dobrovolskis, A., & Lago, B. 1980, Icar, 44, 730
Citron, R. I., Genda, H., & Ida, S. 2015, Icar, 252, 334
Craddock, R. A. 2011, Icar, 211, 1150
De Sio, A., Tozzetti, L., Wu, Z., et al. 2016, A&A, 589, A4
DeMeo, F. E., & Carry, B. 2013, Icar, 226, 723
Fitoussi, C., Bourdon, B., & Wang, X. 2016, E&PSL, 434, 151
Flemings, M. C., Riek, R. G., & Young, K. P. 1976, Materials Science and Engeneering, 25, 103
Fraeman, A. A., Arvidson, R. E., Murchie, S. L., et al. 2012, JGR, 117, E00J15
Fraeman, A. A., Murchie, S. L., Arvidson, R. E., et al. 2014, Icar, 229, 196
Gail, H.-P. 1998, A&A, 332, 1099
Gail, H.-P., Keller, R., & Sedlmayr, E. 1984, A&A, 133, 320
Gail, H.-P., & Sedlmayr, E. 1988, A&A, 206, 153
Giuranna, M., Roush, T. L., Duxbury, T., et al. 2011, Icar, 59, 1308
Goldreich, P. 1963, MNRAS, 126, 257
Gonzalez-Guzman, R. 2016, OJGeo, 6, 30
Grove, T. L. 1990, AmMin, 75, 544
Hartmann, W. K., & Davis, D. R. 1975, Icar, 24, 504

Hutchison, R. 2004, in Meteorites, ed. R. Hutchison (Cambridge: Cambridge Univ. Press), 520

Ichikawa, K., Kinoshita, Y., & Shimamura, S. 1985, Transactions of the Japan Institute of Metals, 26, 513

Kokubo, E., Ida, S., & Makino, J. 2000, Icar, 148, 419

Lawrence, D. J., Feldman, W. C., Goldsten, J. O., et al. 2013, Sci, 339, 292

Levison, H. F., Bottke, W. F., Gounelle, M., et al. 2009, Natur, 460, 364

Lodders, K., & Fegley, B., Jr. 2011, Chemistry of the Solar System (Cambridge: Royal Society of Chemistry)

Morbidelli, A., Levison, H. F., Tsiganis, K., & Gomes, R. 2005, Natur, 435, 462

O'Neill, H. S. C. 1991, GeCoA, 55, 1135

Pajola, M., Lazzarin, M., Dalle Ore, C. M., et al. 2013, ApJ, 777, 127

Pieters, C. M., Murchie, S., Thomas, N., & Britt, D. 2014, P&SS, 102, 144

Pieters, C. M., Taylor, L. A., Noble, S. K., et al. 2000, M&PS, 35, 1101

Pollack, J. B., Burns, J. A., & Tauber, M. E. 1979, Icar, 37, 587

Rietmeijer, F. 2009, M&PS, 44, 1589

Rietmeijer, F. J. M., & Karner, J. M. 1999, JChPh, 110, 4554

Rietmeijer, F. J. M., Nuth, J. A., III, & Karner, J. M. 1999a, ApJ, 527, 395

Rietmeijer, F. J. M., Nuth, J. A., III, & Karner, J. M. 1999b, PCCP, 1, 1511

Rosenblatt, P. 2011, A&ARv, 19, 44

Rosenblatt, P., & Charnoz, S. 2012, Icar, 221, 806

Salmon, J., & Canup, R. M. 2012, ApJ, 760, 83

Sanloup, C., Jambon, A., & Gillet, P. 1999, PEPI, 112, 43

Schultz, P. H., & Lutz-Garihan, A. B. 1982, LPSC, 13, A84

Scully, J. E. C., Russell, C. T., Yin, A., et al. 2015, E&PSL, 411, 151

Sierks, H., Barbieri, C., Lamy, P. L., et al. 2015, Sci, 347, 1044

Solomatov, V. S. 2007, in Treatise on Geophysics, Vol. 9, ed. G. Schubert (Amsterdam: Elsevier)

Sunshine, J. M., Farnham, T. L., Feaga, L. M., et al. 2009, Sci, 326, 565

Szeto, A. M. K. 1983, Icar, 55, 133

Thompson, C., & Stevenson, D. J. 1988, ApJ, 333, 452

Toppani, A., Libourel, G., Robert, F., & Ghanbaja, J. 2006, GeCoA, 70, 5035

Vernazza, P., Brunetto, R., Binzel, R. P., et al. 2009, Icar, 202, 477

Vernazza, P., Marsset, M., Beck, P., et al. 2015, ApJ, 806, 204

Visscher, C., & Fegley, B., , Jr. 2013, ApJL, 767, L12

Ward, W. R. 2012, ApJ, 744, 140

Ward, W. R. 2014, RSPTA, 372, 20130250

Willner, K., Shi, X., & Oberst, J. 2014, P&SS, 102, 51

Yamamoto, S., Nakamura, R., Matsunaga, T., et al. 2012, Icar, 218, 331

The Astrophysical Journal, 835:134 (5pp), 2017 February 1 doi:10.3847/1538-4357/aa5279

Stability of Sulphur Dimers (S_2) in Cometary Ices

O. Mousis[1], O. Ozgurel[2], J. I. Lunine[3], A. Luspay-Kuti[4], T. Ronnet[1], F. Pauzat[2], A. Markovits[2], and Y. Ellinger[2]
[1] Aix Marseille Université, CNRS, LAM (Laboratoire d'Astrophysique de Marseille) UMR 7326, F-13388, Marseille, France; olivier.mousis@lam.fr
[2] Laboratoire de Chimie Théorique, Sorbonne Universités, UPMC Univ. Paris 06, CNRS UMR 7616, F-75252 Paris CEDEX 05, France
[3] Department of Astronomy and Carl Sagan Institute, Space Sciences Building Cornell University, Ithaca, NY 14853, USA
[4] Department of Space Research, Southwest Research Institute, 6220 Culebra Road, San Antonio, TX 78228, USA
Received 2016 July 27; revised 2016 October 21; accepted 2016 December 5; published 2017 January 23

Abstract

S_2 has been observed for decades in comets, including comet 67P/Churyumov–Gerasimenko. Despite the fact that this molecule appears ubiquitous in these bodies, the nature of its source remains unknown. In this study, we assume that S_2 is formed by irradiation (photolysis and/or radiolysis) of S-bearing molecules embedded in the icy grain precursors of comets and that the cosmic ray flux simultaneously creates voids in ices within which the produced molecules can accumulate. We investigate the stability of S_2 molecules in such cavities, assuming that the surrounding ice is made of H_2S or H_2O. We show that the stabilization energy of S_2 molecules in such voids is close to that of the H_2O ice binding energy, implying that they can only leave the icy matrix when this latter sublimates. Because S_2 has a short lifetime in the vapor phase, we derive that its formation in grains via irradiation must occur only in low-density environments such as the ISM or the upper layers of the protosolar nebula, where the local temperature is extremely low. In the first case, comets would have agglomerated from icy grains that remained pristine when entering the nebula. In the second case, comets would have agglomerated from icy grains condensed in the protosolar nebula and that would have been efficiently irradiated during their turbulent transport toward the upper layers of the disk. Both scenarios are found consistent with the presence of molecular oxygen in comets.

Key words: astrobiology – comets: general – comets: individual (67P/Churyumov–Gerasimenko) – methods: numerical – solid state: volatile

1. Introduction

The nature of the source of sulphur dimers (S_2) observed in comets is still unknown. The first detection of S_2 in a celestial body was in the UV spectra of Comet IRAS-Araki-Alcock (C/1983 H1) acquired with the *International Ultraviolet Explorer* (*IUE*) space observatory (Ahearn et al. 1983). Emission bands of S_2 were subsequently identified in many comets observed with *IUE* in the eighties, including 1P/Halley (Krishna Swamy & Wallis 1987). S_2 was also identified in comets Hyakutake (C/1996 B2), Lee (C/1999 H1), and Ikeya-Zhang (C/2002 C1; Laffont et al. 1998; Kim et al. 2003; Boice & Reylé 2005). More recently, S_2 has been detected in comet 67P/Churyumov–Gerasimenko (hereafter 67P/C-G) by the ROSINA mass spectrometer on board the *Rosetta* spacecraft at a distance of ~3 au from the Sun in 2014 October (~4–13 $\times 10^{-6}$ with respect to water; Le Roy et al. 2015; Calmonte et al. 2016). All of these observations suggest that S_2 is ubiquitous in comets.

Because the lifetime of S_2 is very short in comae (approximately a few hundred seconds at most; Reylé & Boice 2003), two main scenarios have been invoked in the literature to account for its presence in comets. In the first scenario, S_2 is the product of reactions occurring in the coma. Ethylene was thus proposed to act as a catalyst allowing the formation of S_2 molecules in the inner coma (Saxena & Misra 1995; Saxena et al. 2003). Also, the presence of atomic S (as the photodissociation product of CS_2) reacting with OCS was suggested to form S_2 in comae (A'Hearn et al. 2000). However, models depicting the chemistry occurring in cometary comae show that these two mechanisms do not account for the observed levels of S_2 (Rodgers & Charnley 2006).

In the second scenario, S_2 molecules are believed to be of parent nature and reside in cometary ices (Ahearn et al. 1983; Ahearn & Feldman 1985; Feldman 1987; Grim & Greenberg 1987; A'Hearn 1992). Ahearn & Feldman (1985) proposed that the UV photolysis of S-bearing species embedded in ISM ices could form sufficient amounts of S_2 that remains trapped in the icy matrix. Since then, a number of mechanisms based on UV or X-ray irradiation have been proposed, starting mainly from H_2S (the most abundant S-bearing volatile observed in comets; Irvine et al. 2000; Bockelée-Morvan et al. 2004) and H_2S_2, and involving radicals like HS and HS_2 (Grim & Greenberg 1987; Jiménez-Escobar & Muñoz-Caro 2011; Jiménez-Escobar et al. 2012). It has also been proposed that S_2 could be formed from the radiolysis of S-bearing compounds in cometary ices (Ahearn & Feldman 1985; Calmonte et al. 2016) despite the fact that so far, there is no experimental proof showing that this mechanism is effective.

In the present study, we postulate that S_2 is formed from H_2S molecules embedded in icy grains by irradiation of UV, X-ray, and cosmic ray fluxes (CRF), whether icy grain precursors of comets formed in the protosolar nebula or the ISM. Because radiolysis generated by the impact of cosmic rays simultaneously creates voids in ices within which the produced molecules can accumulate (Carlson et al. 2009; Mousis et al. 2016b), we investigate the stability of S_2 molecules in such cavities, assuming that the surrounding ice is made of H_2S or H_2O. We show that the stabilization energy of S_2 molecules in such voids is close to that of the H_2O ice binding energy, implying that they can only leave the icy matrix when this latter sublimates. We finally discuss the implications of our results for the origin of cometary grains, with a particular emphasis on those agglomerated by comet 67P/C-G.

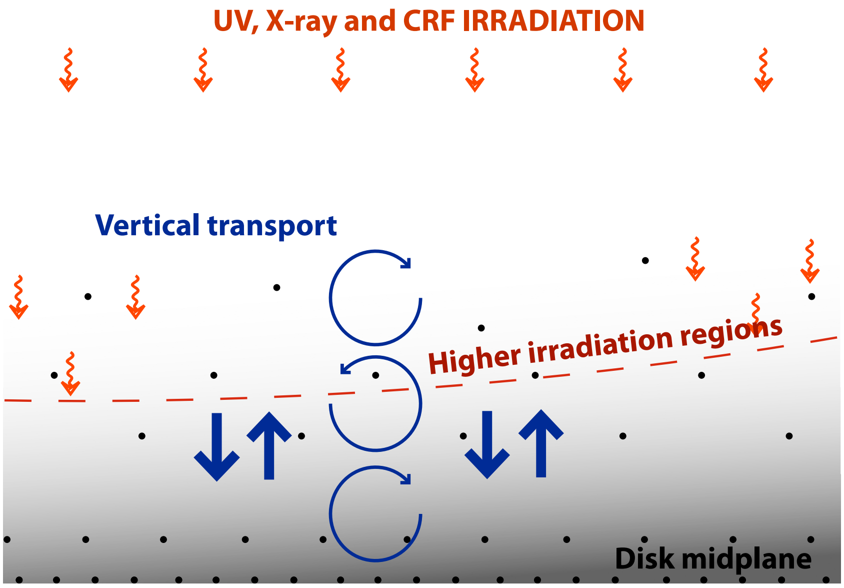

Figure 1. Illustration of the vertical transport of small icy grains toward disk regions where they are efficiently irradiated. Dust is concentrated in the midplane of the disk due to gravitational settling and gas drag. However, turbulent eddies lift the icy grains toward the upper regions and also drag them down because the direction of the velocity is random and coherent during a timecale comparable to the local keplerian period. Small dust grains finally spend a non-negligible fraction of their lifetime in the disk's upper regions, where the irradiation attenuation is low.

2. Irradiation of Icy Grains

Three irradiation mechanisms leading to the formation of S_2 are considered in this study. The first two mechanisms, namely UV and X-ray irradiation, have been proven to produce S_2 from H_2S and H_2S_2 (Grim & Greenberg 1987; Jiménez-Escobar & Muñoz-Caro 2011; Jiménez-Escobar et al. 2012). Experiments have shown that S_2 can be produced and stabilized in icy grains over thicknesses of a few tenths of microns. Despite the lack of experimental data, radiolysis has also been considered as a potential candidate for S_2 formation from S-bearing compounds in cometary icy grains (Ahearn & Feldman 1985). This mechanism has recently been proposed to explain the detection of S_2 in 67P/C-G (Calmonte et al. 2016) and is often invoked to account for its presence in Europa's exosphere (Carlson et al. 1999; Cassidy et al. 2010). Cosmic rays reach deeper layers than photon irradiation and simultaneously creates voids in which some irradiation products such as O_2 or here S_2 can be sequestrated (Mousis et al. 2016b). Whatever the irradiation process considered, we assume that, once S_2 has been created and trapped in the microscopic icy grains, the latter agglomerated and formed the building blocks of comets.

3. Stability of S_2 Molecules in an Icy Matrix

The S_2 stabilization energy arises from the electronic interaction between the host support (H_2O ice or H_2S ice) and the S_2 foreign body. The stabilization energy is evaluated as

$$E_{\rm stab} = (E_{\rm ice} + E_{S_2}) - E, \quad (1)$$

where E_{S_2} is the energy of the isolated molecule, $E_{\rm ice}$ the energy of the pristine solid host and E is the total energy of the [host + S_2] complex, with all entities optimized in isolation.

All simulations are carried out by means of the Vienna ab-initio simulation package (Kresse & Hafner 1993, 1994; Kresse & Furthmüller 1996; Kresse & Joubert 1999). The long range interactions in the solid and the hydrogen bonding being the critical parameters in the ices, we use the PBE generalized gradient approximation functional (Perdew et al. 1996), in the (PBE+D2) version corrected by Grimme et al. (2010), that has been specifically designed to deal with the present type of problem. This theoretical tool has proved to be well adapted to model bulk and surface ice structures interacting with volatile species (Lattelais et al. 2011, 2015; Ellinger et al. 2015; Mousis et al. 2016b). More details on the computational background can be found in the aforementioned publications.

Since S_2 is created well inside the icy grain mantles, the initial description of the irradiated ice is taken as that of the internal structures of ice clusters obtained from Monte-Carlo simulations of ice aggregates constituted of hundreds of water molecules. The important point in the simulations by Buch et al. (2004) is that the core of the aggregates consists in crystalline domains of apolar hexagonal ice *Ih*. However, in the present context, the irradiation creates significant defects inside the ice, namely, voids and irradiation tracks that, at least locally, modify the crystalline arrangement.

3.1. S_2 Embedded in H_2O Ice

Because H_2O is the dominant volatile in comets (Bockelée-Morvan et al. 2004), most of the cavities created by CRF irradiation are expected to be surrounded by H_2O molecules. Table 1 shows the stabilization energy of S_2 as a function of the size of these cavities. How the S_2 stabilization evolves as a function of their size is summarized below.

1. Starting with no H_2O removed, we find no stabilization for the inclusion of S_2 in the ice lattice. It is in fact an endothermic process, as it is for O_2 inclusion (Mousis et al. 2016b).
2. With one H_2O removed, we have an inclusion structure for which stabilization is negative, meaning that S_2 cannot stay in such a small cavity.
3. With somewhat larger cavities obtained by removing two to four adjacent H_2O molecules from the ice lattice, we

Table 1
Computed Stabilization Energies (eV) of S_2 Interacting with H_2O Ice or H_2S Ice

Environment	H_2O Ice	H_2S Ice
Adsorption	0.28	⋯
Inclusion ($n = 1$)[a]	−0.12	0.30
Inclusion ($n = 2$)	0.28	0.45
Inclusion ($n = 4$)	0.50	0.40
Inclusion (fine track)	0.51	0.41
Inclusion (large track)	0.53	0.50

Note.
[a] n = number of H_2O or H_2S molecules destroyed to create the void in which S_2 is trapped.

Table 2
Computed Stabilization Energies (eV) of H_2S Interacting with H_2O Ice

Environment	H_2S
Adsorption	0.61
Substitution ($n = 1$)[a]	0.77
Substitution ($n = 2$ far away)	0.73
Substitution ($n = 2$ close)	0.56
Substitution ($n = 3$ close)	0.50
Substitution (irradiation track)	0.51

Note.
[a] n = number of H_2O molecules replaced by H_2S.

obtain increasing stabilization energies from 0.3 to 0.5 eV.

4. With larger cavities that form along the irradiation track, the stabilization energies are found to be at least of the order of 0.5 eV.

In short, as soon as the space available is sufficient, the energy stabilizes around 0.5 eV. This stabilization energy is (1) higher (more stabilizing) than what is found in the case of O_2 (0.2–0.4 eV; Mousis et al. 2016b) and (2) larger than that of a water dimer (∼0.25 eV). Hence, the presence of S_2 should not perturb the ice structure until it is ejected into the coma via sublimation with the surrounding H_2O molecules. The results of our computations are consistent with the laboratory experiments of Grim & Greenberg (1987) who showed that S_2 remains trapped in icy grains until they are heated up to ∼160 K, a temperature at which water ice sublimates at PSN conditions.

3.2. *S_2 Embedded in H_2S Ice*

H_2S behaves similarly to H_2O because of its ability to establish hydrogen bonds. This implies that small domains of H_2S could have formed in the bulk of the ice and served as local sources for the formation of S_2. The stabilization of these aggregates is addressed by numerical simulations in which H_2S entities are progressively introduced by replacing an equal number of H_2O molecules in the water-ice lattice. Table 2 shows the stabilization energies with values around 0.5 and 0.75 eV for neighboring and far away H_2S, respectively. Consequently, substituting several neighboring H_2O by H_2S is a possibility to be considered if the H_2S is abundant enough, thus creating small islands of H_2S within the water ice.

If small clumps of H_2S ices in the bulk of water ice are a plausible hypothesis, as suggested by the aforementioned numbers, then the proper conditions are realized for the in situ formation of S_2 by deep irradiation. The case in which H_2S molecules replace H_2O along the irradiation track is a less favorable situation but it could be at the origin of the S_n oligomers observed in some laboratory experiments (Meyer et al. 1972; Jiménez-Escobar et al. 2012). We evaluate the stabilization of S_2 in H_2S clumps, assuming that they behave as pure condensates. The results, presented in Table 1 and summarized below, are quite close to those derived for water ice.

1. With one H_2S removed, we have a substitution structure whose stabilization is on the order of 0.30 eV.
2. With larger cavities obtained by removing two to four adjacent H_2S molecules, we obtain increasing stabilization energies between 0.40 and 0.45 eV.
3. With even larger cavities, extended in the direction of the irradiation, the stabilization energies are found to be similar to the preceding ones, between 0.40 and 0.50 eV.

Again we find that the presence of S_2 should not perturb the ice structure, even when trapped in H_2S clumps, until the latter sublimate, due to increasing local temperature.

4. Implications for Cometary Ices

It has recently been shown that the radiolysis of icy grains in low-density environments, such as the presolar cloud, may induce the production of amounts of molecular oxygen high enough to be consistent with the quantities observed in 67P/C-G (Mousis et al. 2016b). Higher density environments such as the PSN midplane were excluded because the timescales needed to produce enough O_2 in cometary grains exceeded by far their lifetimes in the disk. Also, the efficiency of ionization by cosmic rays in the PSN midplane is now questioned because of the deflection of galactic CRF by the stellar winds produced by young stars (Cleeves et al. 2013, 2014).

On the other hand, because the lifetime of S_2 is very short in the gas phase (approximately a few hundred seconds at most; Reylé & Boice 2003), its formation conditions are even more restrictive than those required for O_2. Assuming that S_2 indeed formed from H_2S or any other S-bearing molecule via UV, X-ray, or CRF irradiation, this implies that this molecule never left the icy matrix in the time interval between its formation and trapping. In other words, S_2 never condensed from the PSN before being trapped in cometary grains. This stringent constraint requires S_2 to form within icy grains irradiated by CRF in low-density environments such as ISM, where the local temperature is extremely cold. In this picture, comets, including 67P/C-G, would have agglomerated in the PSN from icy grains originating from ISM, whose compositions and structures remained pristine when entering the nebula.

Alternatively, because the CRF irradiation should be poorly attenuated in the upper layers of the PSN, these regions also constitute an adequate low-density environment, allowing the formation of S_2 in cometary grains. Turbulence plays an important role in the motion of small dust grains that are well coupled to the gas (see Figure 1). Micron-sized grains initially settled in the midplane are entrained by turbulent eddies and diffuse radially and vertically with an effective viscosity roughly equal to that of the gas for such small particles (see Ciesla 2010, 2011 for details). Consequently, solid particles follow a Gaussian distribution in the vertical direction. The scale height of dust (corresponding to the standard deviation of the distribution) is a fraction of the gas scale height, this fraction being larger and possibly equal to the gas scale height in the cases of small grains and higher degrees of turbulence (Dubrulle et al. 1995; Youdin & Lithwick 2007).

The vertical transport of solids exposes them to very different disk environments. Dust grains are stochastically transported to high altitude and low-density regions above the disk midplane. Ciesla (2010) developed a numerical simulation to integrate the motion of individual particles and showed that micron-sized grains spent $\sim$32% of their lifetime at altitudes above the scale height of the disk, including $\sim$5% at heights above four times its scale height, regardless of the distance from the Sun. In such low-density environments, photochemistry plays a primordial role, as demonstrated by Ciesla & Sandford (2012), because UV photons are weakly attenuated at those heights. This also holds for the CRF irradiation of grains that should be substantially enhanced compared to the dose received by particles residing in the midplane. Under those circumstances, the production of S_2 should be favored in icy grains over several cycles of vertical transport toward the surface of the disk. This scenario should also favor the formation of O_2 from irradiation of H_2O ice (see Mousis et al. 2016b for details).

5. Discussion and Conclusions

It is reasonable to assume that the multiple forms of irradiation hitting the microscopic icy grains in low-density environments such as ISM or the upper layers of protoplanetary disks can lead both to the formation of S_2 molecules and the development of cavities in these grains, in which the molecule remains sequestered. The same scenario has been proposed for O_2 formation and stabilization in cometary icy grains (Mousis et al. 2016b). In the case of S_2 formation, the possibility of forming the dimer via the radiolysis of S-bearing ices remains an open question. Future experimental work is needed to check the viability of this mechanism.

The possible formation of S_2 in icy grains via their irradiation in ISM, together with the short lifetime of this molecule in the gas phase, leads to the plausible possibility that comets agglomerated from pristine amorphous grains that never vaporized when entering the PSN, as already envisaged for the origin of 67P/C-G's material (Rubin et al. 2015a; Mousis et al. 2016b). On the other hand, the formation of S_2 in icy grains that migrated toward the upper layers of the disk is compatible with their condensation in the PSN midplane. This mechanism leaves open the possibility that these grains are made of crystalline ices and clathrates, as proposed by Mousis et al. (2016a) and Luspay-Kuti et al. (2016) to account for several pre-perihelion compositional measurements made by the *Rosetta* spacecraft in 67P/C-G. The same process could explain the presence of O_2 measured in situ in comets 67P/C-G and 1P/Halley (Bieler et al. 2015; Rubin et al. 2015b). Interestingly, whatever the ice structure considered for the icy grains, the voids allowing the stabilization of S_2 can be considered as analogs of clathrates in terms of cage sizes and intermolecular interactions.

The fact that one H_2S replacing one H_2O has little influence on the stability of the solid lattice is a favorable situation for the formation of a mixed ice. It is plausible that some segregation occurs with the formation of H_2S islands in the bulk of crystalline or amorphous water ice. Then, the proper conditions would be realized for the in situ formation of S_2, especially if we remember that the formation of one S_2 requires at least the destruction of two imprisoned sulphur species. The plausible formation of H_2S clumps is a strong argument in favor of a non-uniform distribution of S_2 within cometary ices. Note that in the case of irradiation of crystalline grains condensed in the PSN and transported toward the upper layers of the disk, the formed S_2 may be entrapped in clathrates (Grim & Greenberg 1987), also forming a solid phase distinct from water ice in cometary grains.

The immediate consequence of the presence of distinct S_2-bearing solid phases is the difficulty to predict the S_2 correlation with H_2O or H_2S in 67P/C-G from *Rosetta* measurements. The S_2/H_2O abundance ratio is directly linked to the region of the comet whose desorption is observed. Contrary to O_2 whose apparent good correlation with H_2O is explained by its trapping in water ice (Bieler et al. 2015; Mousis et al. 2016b), no global trend should be drawn between the variation of S_2 and H_2O abundances if S_2 is distributed within both the S-bearing and H_2O ices. Indeed, S_2 may be released simultaneously from the H_2O layer present close to the surface and from H_2S clusters localized deeper in the subsurface. Our results are supported by the ROSINA data collected between 2015 May (equinox) and 2015 August (perihelion), showing that there is no clear correlation of S_2 with H_2O or H_2S in 67P/C-G (Calmonte et al. 2016). These observations allow us to exclude the trapping of S_2 in a dominant ice reservoir. If S_2 was mainly trapped in H_2S-bearing ice, then the outgassing rates of S_2 and H_2S should have been well correlated during the period sampled by the ROSINA instrument. The same statement applies if S_2 had been essentially trapped in water ice.

O.M. acknowledges support from CNES. This work has been partly carried out thanks to the support of the A*MIDEX project (n° ANR-11-IDEX-0001-02) funded by the "Investissements d'Avenir" French Government program, managed by the French National Research Agency (A.N.R.). This work also benefited from the support of CNRS-INSU national program for planetology (P.N.P.). J.I.L. appreciates support from NASA through the *JWST* project. A.L.-K. acknowledges support from NASA JPL (subcontract no. 1496541).

References

A'Hearn, M. F. 1992, in IAU Symp. 150, Astrochemistry of Cosmic Phenomena, ed. P. D. Singh (Dordrecht: Kluwer), 415
A'Hearn, M. F., Arpigny, C., Feldman, P. D., et al. 2000, BAAS, 32, 44.01
Ahearn, M. F., & Feldman, P. D. 1985, ASIC, 156, 463
Ahearn, M. F., Schleicher, D. G., & Feldman, P. D. 1983, ApJL, 274, L99
Bieler, A., Altwegg, K., Balsiger, H., et al. 2015, Natur, 526, 678
Bockelée-Morvan, D., Crovisier, J., Mumma, M. J., & Weaver, H. A. 2004, in Comets II, ed. M. C. Festou, H. U. Keller, & H. A. Weaver (Tuscon, AZ: Univ. Arizona Press), 391
Boice, D. C., & Reylé, C. 2005, HiA, 13, 501
Buch, V., Sigurd, B., Devlin, J. P., Buck, U., & Kazimirski, J. K. 2004, IRPC, 23, 375
Calmonte, U., Altwegg, K., Balsiger, H., et al. 2016, MNRAS, 462, S253
Carlson, R. W., Calvin, W. M., Dalton, J. B., et al. 2009, in Europa, ed. R. T. Pappalardo et al. (Tucson, AZ: Univ. Arizona Press), 283
Carlson, R. W., Johnson, R. E., & Anderson, M. S. 1999, Sci, 286, 97
Cassidy, T., Coll, P., Raulin, F., et al. 2010, SSRv, 153, 299
Ciesla, F. J. 2010, ApJ, 723, 514
Ciesla, F. J. 2011, ApJ, 740, 9
Ciesla, F. J., & Sandford, S. A. 2012, Sci, 336, 452

Cleeves, L. I., Adams, F. C., & Bergin, E. A. 2013, ApJ, 772, 5
Cleeves, L. I., Bergin, E. A., Alexander, C. M. O., et al. 2014, Sci, 345, 1590
Dubrulle, B., Morfill, G., & Sterzik, M. 1995, Icar, 114, 237
Ellinger, Y., Pauzat, F., Mousis, O., et al. 2015, ApJL, 801, L30
Feldman, P. D. 1987, in IAU Symp. 120, Astrochemistry (Dordrecht: D. Reidel), 417
Grim, R. J. A., & Greenberg, J. M. 1987, ApJ, 321, L91
Grimme, S., Antony, J., Ehrlich, S., & Krieg, H. 2010, JChPh, 132, 154104
Irvine, W. M., Schloerb, F. P., Crovisier, J., Fegley, B., Jr., & Mumma, M. J. 2000, in Protostars and Planets IV, ed. V. Mannings, A. P. Boss, & S. Russell (Tuscon, AZ: Univ. Arizona Press), 1159
Jiménez-Escobar, A., & Muñoz-Caro, G. M. 2011, A&A, 536, A91
Jiménez-Escobar, A., Muñoz Caro, G. M., Ciaravella, A., et al. 2012, ApJL, 751, L40
Kim, S. J., A'Hearn, M. F., Wellnitz, D. D., Meier, R., & Lee, Y. S. 2003, Icar, 166, 157
Kresse, G., & Furthmüller, J. 1996, PhRvB, 54, 11169
Kresse, G., & Hafner, J. 1993, PhRvB, 48, 13115
Kresse, G., & Hafner, J. 1994, PhRvB, 49, 14251
Kresse, G., & Joubert, D. 1999, PhRvB, 59, 1758
Krishna Swamy, K. S., & Wallis, M. K. 1987, MNRAS, 228, 305
Laffont, C., Boice, D. C., Moreels, G., et al. 1998, GeoRL, 25, 2749
Lattelais, M., Bertin, M., Mokrane, H., et al. 2011, A&A, 532, A12
Lattelais, M., Pauzat, F., Ellinger, Y., & Ceccarelli, C. 2015, A&A, 578, A62
Le Roy, L., Altwegg, K., Balsiger, H., et al. 2015, A&A, 583, A1
Luspay-Kuti, A., Mousis, O., Hässig, M., et al. 2016, SciA, 2, e1501781
Meyer, B., Stroyer-Hansen, T., & Oommen, T. V. 1972, JMoSp, 42, 335
Mousis, O., Lunine, J. I., Luspay-Kuti, A., et al. 2016a, ApJL, 819, L33
Mousis, O., Ronnet, T., Brugger, B., et al. 2016b, ApJL, 823, L41
Perdew, J. P., Burke, K., & Ernzerhof, M. 1996, PhRvL, 77, 3865
Reylé, C., & Boice, D. C. 2003, ApJ, 587, 464
Rodgers, S. D., & Charnley, S. B. 2006, AdSpR, 38, 1928
Rubin, M., Altwegg, K., Balsiger, H., et al. 2015a, Sci, 348, 232
Rubin, M., Altwegg, K., van Dishoeck, E. F., & Schwehm, G. 2015b, ApJL, 815, L11
Saxena, P. P., & Misra, A. 1995, MNRAS, 272, 89
Saxena, P. P., Singh, M., & Bhatnagar, S. 2003, BASI, 31, 75
Youdin, A. N., & Lithwick, Y. 2007, Icar, 192, 588

The Astrophysical Journal, 845:92 (11pp), 2017 August 20 https://doi.org/10.3847/1538-4357/aa80e6

Pebble Accretion at the Origin of Water in Europa

Thomas Ronnet, Olivier Mousis, and Pierre Vernazza
Aix Marseille Univ, CNRS, LAM, Laboratoire d'Astrophysique de Marseille, Marseille, France; thomas.ronnet@lam.fr
Received 2017 April 20; revised 2017 July 17; accepted 2017 July 17; published 2017 August 16

Abstract

Despite the fact that the observed gradient in water content among the Galilean satellites is globally consistent with a formation in a circum-Jovian disk on both sides of the snowline, the mechanisms that led to a low water mass fraction in Europa (∼8%) are not yet understood. Here, we present new modeling results of solids transport in the circum-Jovian disk accounting for aerodynamic drag, turbulent diffusion, surface temperature evolution, and sublimation of water ice. We find that the water mass fraction of pebbles (e.g., solids with sizes of 10^{-2}–1 m) as they drift inward is globally consistent with the current water content of the Galilean system. This opens the possibility that each satellite could have formed through pebble accretion within a delimited region whose boundaries were defined by the position of the snowline. This further implies that the migration of the forming satellites was tied to the evolution of the snowline so that Europa fully accreted from partially dehydrated material in the region just inside of the snowline.

Key words: methods: numerical – planets and satellites: formation – planets and satellites: individual (Jupiter, Galilean satellites) – protoplanetary disks

1. Introduction

The four Galilean satellites (Io, Europa, Ganymede, and Callisto) are thought to have formed during the very late stages of Jupiter's formation, at a time when Jupiter was surrounded by a circumplanetary disk (CPD; see e.g., Canup & Ward 2009; Estrada et al. 2009). While of comparable masses, these four satellites have different densities (Io: 3527.5 ± 2.9 kg m^{-3}, Europa: 2989 ± 46 kg m^{-3}, Ganymede: 1942.0 ± 4.8 kg m^{-3}, Callisto: 1834.4 ± 3.4 kg m^{-3}; Schubert et al. 2004) due to different water mass fractions (Io: ∼0%, Europa: ∼8%, Ganymede and Callisto: ∼50%) and their density decreases (hence their water mass fraction increases) with increasing distance to Jupiter (Anderson et al. 1998; Sohl et al. 2002; Schubert et al. 2004). This gradient in water mass fraction puts a strong constraint on (1) the satellites' formation conditions and/or (2) their subsequent thermal evolution via tidal heating.

Concerning case (2), it has been proposed that the density gradient among the satellites results from increased tidal heating (Canup & Ward 2009; Dwyer et al. 2013) with decreasing distance from the planet. However, Io is currently dissipating ∼1 ton s^{-1} of material in the Jovian magnetosphere which, integrated over 4 billion years, represents only ∼0.1% of its mass. This argument alone is insufficient to fully preclude the proposed mechanism but it suggests that tidal heating is not the most likely mechanism to explain Io's or Europa's low water content (see also the discussion in Canup & Ward 2009).

Concerning case (1), the first explanation that has been proposed is an increasing relative velocity among the building blocks with decreasing distance from the planet leading to substantial water loss in the case of the most energetic impacts (Estrada & Mosqueira 2006), which occurred closer to Jupiter. Nonetheless, this scenario has been discarded by a detailed study showing that Io and Europa analogs exhibit an overabundance of water when they are formed via an *N*-body code simulating imperfect accretion and water loss during collisions (Dwyer et al. 2013). A second explanation is that the observed water gradient among the satellites results from an outwardly decreasing temperature of the CPD, leading to the existence of a snowline at a given radial distance from Jupiter (see, e.g., Lunine & Stevenson 1982). In this case, bodies that formed inward of the snowline (Io) accreted from essentially water-poor building blocks, whereas bodies that formed outward of the snowline (Ganymede, Callisto) formed from a primordial mixture of water ice and silicates (e.g., Canup & Ward 2002; Mosqueira & Estrada 2003a, 2003b; Mousis & Gautier 2004). Within this scenario, the low water content of Europa is puzzling. So far, Europa's water content has been mostly attributed to its formation both outward and inward of the snowline due to either (i) its migration inward of the snowline during formation (i.e., growth), (ii) the progressive cooling of the disk and thus inward migration of the snowline during its formation, or (iii) an interplay between the two mechanisms (Alibert et al. 2005; Canup & Ward 2009). However, the evolution of the CPD has been systematically modeled using an ad hoc parametrization of the turbulent viscous disk (the so-called α-viscosity, Shakura & Sunyaev 1973) which governs the temperature evolution and lifetime of the disk. While providing a good starting point for evolutionary disk models, this kind of parametrization has been highly questioned in recent years (Bai & Stone 2013; Simon et al. 2013; Gressel et al. 2015). Hence, using a predefined α-viscosity prescription to describe the CPD's evolution and provide hints on Europa's formation remains questionable. The same remark holds for planet (or satellite) migration, which has also been extensively studied within recent years (see, e.g., Paardekooper et al. 2010; Bitsch et al. 2014). These studies have shown that in realistic disk conditions, migrating planets can behave significantly differently from what was previously thought, i.e., a persistent inward motion (e.g., Tanaka et al. 2002), due to the existence of regions where the migration is halted and even reversed. Because the studies of satellite formation have been based so far on the migration formulation of Tanaka et al. (2002; e.g., Canup & Ward 2002, 2006; Alibert et al. 2005; Sasaki et al. 2010) their proposed growth/migration scenario is questionable.

Overall, it appears that Europa's composition (as well as those of the other Galilean moons) is the consequence of the way the satellite formed within the Jovian CPD rather than the result of some post-formation mechanism. Hence, investigating how the partial devolatilization of Europa's building blocks occurred within the circum-Jovian disk should provide important constraints on the processes that took place during its formation.

In this work, we investigate the formation conditions of the Galilean moons, and in particular those of Europa, by coupling a transport model of solids including aerodynamic drag, turbulent diffusion, surface temperature evolution, and water ice sublimation with a classical CPD prescription. Considering the fact that Dwyer et al. (2013) demonstrated the inability of classical accretion of large ($D \sim$ 10–100 km) satellitesimals to reproduce the observed density gradient among the satellites, we focus here on the evolution of the so-called pebbles ($D \sim$ 1 cm–10 m). Pebble accretion has become an attractive scenario over recent years, as it is able to explain the growth of both the planets and the small bodies in our solar system (see, e.g., Lambrechts & Johansen 2012, 2014; Morbidelli et al. 2015).

The outline of our paper is as follows. The transport model of solids and the used CPD prescription are detailed in Section 2. The results of our simulations are presented in Section 3. Sections 4 and 5 are devoted to discussion and conclusions, respectively.

2. Methods

In this section, we provide a detailed description of our model. Similarly to Canup & Ward (2002) and Sasaki et al. (2010), we used a simple quasi-stationary CPD model to (i) derive the gas density and temperature distributions and (ii) analytically determine the radial and azimuthal velocities of the gas (Section 2.1). To model the transport of solids (Section 2.2), we numerically solved the equation of motion of the solid particles, including the effect of gas drag, turbulent diffusion and sublimation of water ice.

2.1. Circumplanetary Disk Model

The gas surface density of our CPD is derived from the gas starved disk model of Canup & Ward (2002). In this concept, the CPD is fed through its upper layers from its inner edge up to the centrifugal radius r_c by gas and gas-coupled solids inflowing from the protosolar nebula (PSN). In practice, the centrifugal radius, which corresponds to the location where the angular momentum of the incoming gas is in balance with the gravitational potential of Jupiter, evolves with time and moves toward larger distances with respect to the growing Jupiter.

Here, we focused on the very late stages of Jupiter's formation when the satellites start their accretion. We thus considered the centrifugal radius at a fixed distance $r_c = 26$ $R_{\rm Jup}$ for all our simulations (see, e.g., Canup & Ward 2002; Mosqueira & Estrada 2003a; Sasaki et al. 2010). The surface density is obtained by considering an equilibrium between the mass inflowing from the PSN onto the CPD and the mass accretion rate $\dot{M}_p$ onto Jupiter (Canup & Ward 2002):

$$\Sigma_g(r) = \frac{\dot{M}_p}{3\pi\nu(r)} \begin{cases} 1 - \frac{4}{5}\sqrt{\frac{R_c}{R_d}} - \frac{1}{5}\left(\frac{r}{R_c}\right)^2 & \text{for } r \leqslant R_c \\ \frac{4}{5}\sqrt{\frac{R_c}{r}} - \frac{4}{5}\sqrt{\frac{R_c}{R_d}} & \text{for } r > R_c, \end{cases} \quad (1)$$

where R_d is the outer radius of the disk, here assumed to be equal to 150 $R_{\rm Jup}$ based on 3D hydrodynamic simulations (Tanigawa et al. 2012). ν is the turbulent viscosity given by (Shakura & Sunyaev 1973)

$$\nu = \alpha H_g^2 \Omega_K, \quad (2)$$

where α is the coefficient of turbulent viscosity, $\Omega_{\rm K}$ the keplerian orbital frequency. $H_g = c_g/\Omega_{\rm K}$ is the gas scale height derived from the isothermal gas sound speed $c_g = \sqrt{R_g T_d/\mu_g}$. R_g is the ideal gas constant, μ_g is the mean molecular weight of the gas ($\sim$2.4 g mol^{-1}), and T_d is the CPD's temperature at a given distance from the planet. The temperature profile is derived from the simple prescription of Sasaki et al. (2010):

$$T_d \simeq 225\left(\frac{r}{10\, R_{\rm Jup}}\right)^{-3/4}\left(\frac{\dot{M}_p}{10^{-7}\, M_{\rm Jup}\ {\rm yr}^{-1}}\right)^{1/4} {\rm K}. \quad (3)$$

This temperature profile is obtained from the balance between the energy provided by viscous dissipation within the CPD and the energy loss through blackbody radiation of the disk. This expression gives the temperature at the radiative surface of the disk, where energy balance is achieved. The temperature at the midplane of the disk T_m is obtained by multiplying T_d by a factor of $\left(\frac{3\tau_R}{8} + \frac{1}{2\tau_P}\right)^{1/4}$ (e.g., Hueso & Guillot 2005), where τ_R and τ_P are the Rosseland and Planck mean optical depths, respectively. This would give a slightly higher temperature than T_d. However, given the uncertainties on the opacity, the turbulence level and the mass accretion rate of the circum-Jovian disk, we follow Sasaki et al. (2010) in adopting $T_m \sim T_d$. Both the surface density and gas temperature are thereby determined from the value of the accretion rate $\dot{M}_p$. Therefore, a time evolution of the CPD can be accounted for by imposing a decrease of the mass accretion rate over time. Following Sasaki et al. (2010), this can be expressed as

$$\dot{M}_p(t) = \dot{M}_{p,0}\, e^{-\frac{t}{\tau_{\rm disk}}}, \quad (4)$$

where $\dot{M}_{p,0}$ is the initial mass accretion rate and $\tau_{\rm disk}$ is the lifetime of the nebula, which drives its evolution.

An example of surface density and temperature profiles of the CPD is presented in Figure 1 for a mass accretion rate of $10^{-7}\, M_{\rm Jup}\, {\rm yr}^{-1}$ and a turbulent parameter $\alpha = 10^{-3}$. In that case, the temperature profiles allow the survival of water ice at Ganymede and Callisto's current location.

Because this work aims at describing the interaction between solid particles and the gas, we have added a prescription computing the velocity of the CPD's gas. To do so, we considered that the gas is in hydrostatic equilibrium in the vertical direction and the vertical velocity of the gas is therefore zero (see Takeuchi & Lin (2002) for a discussion about the validity of this assumption). In the radial direction, however, the generally outward pressure gradient force causes the gas to rotate at a slightly subkeplerian velocity. The equation of motion of a gas parcel in the radial direction is given by

$$r\Omega_g^2 = \frac{GMr}{R^3} + \frac{1}{\rho_g}\frac{\partial P}{\partial r}, \quad (5)$$

where Ω_g is the rotation frequency of the gas, M is the mass of the central object, and R is the distance of the gas parcel from

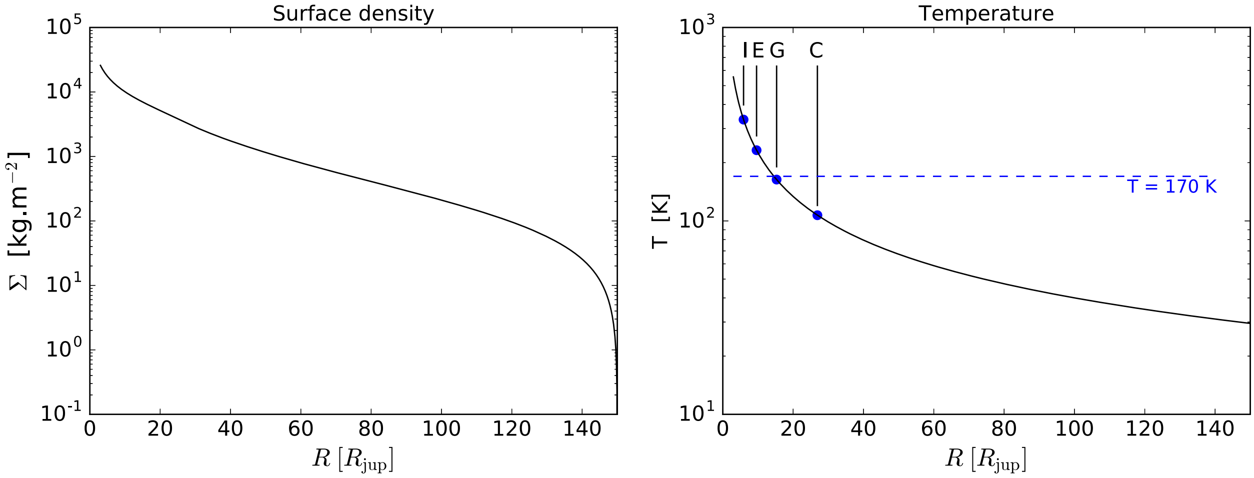

Figure 1. Surface density and temperature profiles of the CPD, with the distance from Jupiter expressed in units of Jovian radii ($R_{\rm Jup}$) calculated for $\dot{M}_p = 1 \times 10^{-7}\, M_{\rm Jup}\, {\rm yr}^{-1}$ and $\alpha = 10^{-3}$. The vertical bars designated by the letters I, E, G, and C correspond to the current orbits of Io, Europe, Ganymede, and Callisto, respectively.

this object. Assuming $P = c_g^2 \rho_g$, this gives the well-known relation for the gas orbital velocity $v_{\phi,\,g}$ (see, e.g., Weidenschilling 1977)

$$v_{\phi,g} \equiv v_{\rm K} - \eta v_{\rm K} \approx v_{\rm K} + \frac{1}{2}\frac{c_g^2}{v_{\rm K}}\frac{\partial \ln P}{\partial \ln r}, \tag{6}$$

where $v_{\rm K}$ is the keplerian orbital velocity and η is a measure of the gas pressure support.

Using the above relations, we derived the velocity of the gas in the radial direction from the azimuthal momentum equation of the viscous gas:

$$\rho_g v_{r,g}\frac{\partial}{\partial r}(r v_{\phi,g}) = \frac{1}{r}\frac{\partial}{\partial r}(r^2 T_{r\phi}) + \frac{\partial}{\partial z}(r T_{\phi z}). \tag{7}$$

where $T_{r\phi}$ and $T_{\phi z}$ are the shear stresses expressed as (e.g., Takeuchi & Lin 2002)

$$T_{r\phi} = r\nu\rho_g\frac{\partial \Omega_g}{\partial r} \text{ and } T_{\phi z} = r\nu\rho_g\frac{\partial \Omega_g}{\partial z}. \tag{8}$$

Equation (7) directly yields the expression for the radial velocity of the gas:

$$v_{r,g}(z) = \left[\frac{\partial}{\partial r}(r^2\Omega_g)\right]^{-1} \times \left[\frac{1}{r\rho_g}\frac{\partial}{\partial r}\left(r^3\nu\rho_g\frac{\partial\Omega_g}{\partial r}\right) + \frac{r^2\nu}{\rho_g}\frac{\partial}{\partial z}\left(\rho_g\frac{\partial\Omega_g}{\partial z}\right)\right], \tag{9}$$

where we used the fact that $v_{\phi,g} = r\Omega_g$ and replace the shear stresses by their expressions.

Using the assumption of vertical hydrostatic equilibrium for the gas, its density is given by

$$\rho_g(r, z) = \rho_0(r) e^{-\frac{z^2}{2H_g^2}}, \tag{10}$$

with

$$\rho_0(r) = \frac{\Sigma_g}{\sqrt{2\pi} H_g}. \tag{11}$$

This set of equations allows us to determine the radial velocity of the gas flow as a function of the distance to the planet and height above the disk midplane. Note that the density-weighted average of Equation (9) over z results in the mean accretion flow velocity $v_{\rm acc}$ derived by Lynden-Bell & Pringle (1974):

$$v_{\rm acc} = -\frac{3}{\Sigma_g r^{1/2}}\frac{\partial}{\partial r}(\nu\Sigma_g r^{1/2}). \tag{12}$$

Figure 2 represents the radial velocity vertical profiles calculated at different distances from Jupiter and for different values of α. The velocity profiles are poorly influenced by the distance from the central planet. Instead, they strongly depend on the disk's viscosity where higher levels of turbulence result in larger velocities (both inward and outward) and consequently faster evolution of the disk. The velocities are small and slightly positive (outward) close to the midplane while at greater heights, namely in the less dense parts of the disk, they become larger and negative (inward). Such profiles have already been detailed in several studies of protoplanetary disks (PPDs; e.g., Takeuchi & Lin 2002; Keller & Gail 2004; Ciesla 2009). It should be noted that such velocity profiles have not been found in turbulent simulations of disks (Fromang et al. 2011) because the magneto-rotational instability, which is the source of turbulence in these simulations, results in non-uniform effective viscosity in the vertical direction. However, the outward radial velocity in the midplane of the CPD has been evidenced in several 3D hydrodynamic simulations (Klahr & Kley 2006; Tanigawa et al. 2012) as well as in MHD simulations (Gressel et al. 2013). Moreover, only small dust grains that are well coupled with the gas can be significantly affected by its meridional circulation. The dynamics of larger grains/solids are mostly dictated by the deviation from keplerian orbital velocity of the gas (see Section 2.2). It is therefore unclear, given the current knowledge of the structure of CPDs and PPDs, whether or not the radial velocity profiles we used are realistic, but this should hardly change our general conclusions.

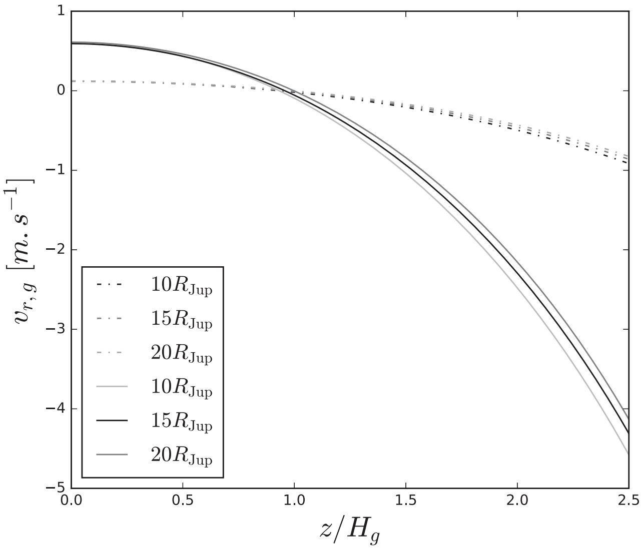

Figure 2. Radial velocity profiles of the gas as a function of the height above the midplane at different distances from Jupiter. Solid and dashed lines correspond to profiles calculated with $\alpha = 1 \times 10^{-4}$ and 5×10^{-4}, respectively.

2.2. Particles Dynamics and Thermodynamics

A lagrangian integration method is used to track the individual particles within the CPD. The transport model includes several mechanisms. Among them, the primary mechanism dictating the dynamical evolution of solids is the gas drag. Contrary to gas, solid particles are not pressure supported and their velocities do not deviate from the keplerian velocity. Solids consequently orbit around the planet faster than the gas does and feel a headwind. They transfer angular momentum to the gas via friction forces on a timescale called the stopping time of the particle t_s. This quantity generally depends on the size of the particle R_s, the gas density, and the relative velocity $v_{\rm rel}$ between the particle and the gas. Assuming that solids are spherical particles, their stopping time is (Perets & Murray-Clay 2011; Guillot et al. 2014)

$$t_s = \left(\frac{\rho_g v_{\rm th}}{\rho_s R_s} \min\left[1, \frac{3}{8}\frac{v_{\rm rel}}{v_{\rm th}} C_D(Re)\right]\right)^{-1}, \tag{13}$$

where $v_{\rm th} = \sqrt{8/\pi}\, c_g$ is the gas thermal velocity and ρ_s is the density of the solid particle, assumed to be 1 g cm^{-2} regardless of its size. The dimensionless drag coefficient C_D is a function of the Reynolds number Re of the flow around the particle (Perets & Murray-Clay 2011):

$$C_D = \frac{24}{Re}(1 + 0.27\, Re)^{0.43} + 0.47(1 - e^{-0.04 Re^{0.38}}). \tag{14}$$

The Reynolds number is given by (Supulver & Lin 2000)

$$Re = \frac{4 R_s v_{\rm rel}}{c_g l_g}, \tag{15}$$

where l_g is the mean-free path of the gas.

The stopping time is divided into two regimes. The Epstein regime is valid when the particle size is smaller than the mean-free path of the gas. In this case, the stopping time does not depend upon the relative velocity between the particle and the gas. When the particles are larger than the mean-free path of the gas, the gas should be considered to be a fluid. In such a case, the stopping time depends upon the relative velocity and the Reynolds number of the flow. In the limit $Re \ll 1$ (Guillot et al. 2014), the conditions of the widely used Stokes regime are fulfilled.

The equation of motion of the particles within the CPD is then given by

$$\frac{d\boldsymbol{v}_s}{dt} = -\frac{GM_p}{R^3}\boldsymbol{R} - \frac{1}{t_s}(\boldsymbol{v}_s - \boldsymbol{v}_g). \tag{16}$$

where M_p is the mass of the central planet (here Jupiter), $\boldsymbol{R}$ is the position vector of the particle, $\boldsymbol{v}_s$ is its velocity vector, and $\boldsymbol{v}_g$ is the velocity of the gas. The equation is integrated with an adaptive time step ODE solver[1] (Brown et al. 1989), using Adams methods for particles with sizes down to 10^{-3} m. An implicit backward differentiation formula scheme is used to integrate the motion of lower size particles whose small stopping times imply a too restrictive time step for an explicit scheme (the time step should be smaller than the stopping times of the particles).

Small dust grains ($\sim\mu$m) have very short stopping times (e.g., $t_s \ll \Omega_K^{-1}$), meaning that they quickly become coupled with the gas. On the other hand, large planetesimals (tens or hundreds of kilometers in radius) have long stopping times ($t_s \gg \Omega_K^{-1}$) and their motion is hardly affected by the friction with the gas. Intermediate planetesimals, with sizes in the $\sim$centimeter range, efficiently loose angular momentum but on timescales that are too long to allow them to become coupled with the gas. These bodies thus always feel a headwind and they continue loosing angular momentum, causing them to rapidly drift inward toward the central planet. The solids that experience the most rapid inward drift are those whose Stokes number St, namely the stopping time multiplied by the local keplerian frequency ($\Omega_{\rm K}\, t_s$), is of the order of unity.

Figure 3 represents the midplane radial velocity of particles as a function of their Stokes number (left panel) as well as the size associated with the Stokes number (right panel) for solids at a distance of 15 $R_{\rm Jup}$ from Jupiter. The left panel of Figure 3 shows a comparison of the velocity of particles in the simulation (black dots) with that derived from the analytical formula (see, e.g., Birnstiel et al. 2012):

$$v_{r,s} = -\frac{2St}{1 + St^2}\eta v_{\rm K} + \frac{1}{1 + St^2}v_{r,g}. \tag{17}$$

Almost all solids are steady in the disk compared to the very rapid dynamics of the pebbles (particles with $St \sim 1$) that drift inward at high velocities.

The other mechanism affecting the motion of solids is turbulent diffusion. Turbulent eddies can entrain particles during their cohesion timescale and would efficiently mix radially and vertically small dust grains that couple well with the gas. The motion of solids due to turbulence is modeled following Ciesla (2010, 2011) with a stochastic kick in the position of the particle (see also Charnoz et al. 2011). Additional advection terms are also added to account for the non-uniform background gas density and diffusivity of solids (see Equation (20)). For a detailed description of this kind of model, we refer the reader to the work of Ciesla (2010, 2011)

[1] The ODE solver is available at the following webpage: https://computation.llnl.gov/casc/odepack/.

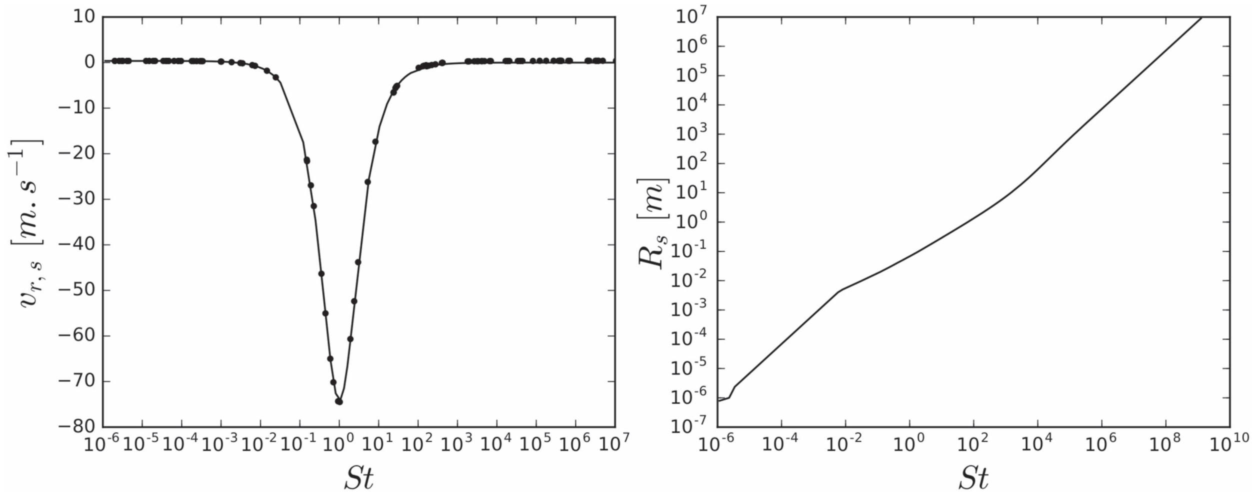

Figure 3. Left: particles' radial velocities as a function of their Stokes numbers (black dots) at 15 R_{Jup} from a Jupiter mass planet in the midplane of a CPD with $\dot{M}_p = 10^{-7}\, M_{\mathrm{Jup}}\, \mathrm{yr}^{-1}$ and $\alpha = 10^{-3}$. The solid line shows the solution of the analytical formula given by Equation (17), which fits well the results of our integration. Small dust grains with sizes smaller than $\sim 10^{-3}$ m have a slightly positive velocity, which is that of the gas at the midplane ($v_{r,g} \simeq 0.15\ \mathrm{m\ s^{-1}}$). Overall, there is more than one order of magnitude difference between the velocity of pebbles (solids with $St \sim 1$) and those of the larger ($St \gg 1$) and smaller ($St \ll 1$) particles. Right: correspondance between the Stokes number and the size of the particles.

and Charnoz et al. (2011) who comprehensively describe the physcics modeled and demonstrate how the Monte Carlo method is able to solve for the advection-diffusion equation of the solids. Accounting for all transport mechanisms, the new position of a solid particle along any axis of a cartesian coordinate system after a time step dt can be expressed as (Ciesla 2010, 2011; Charnoz et al. 2011)

$$x(t + dt) = x(t) + v_{\mathrm{adv}} dt + R_1 \left[\frac{2}{\sigma^2} D_p dt\right]^{\frac{1}{2}}, \tag{18}$$

where x stands for any cartesian coordinate, $R_1 \in [-1; 1]$ is a random number, σ^2 is the variance of the random number distribution, D_p the diffusivity of the solid particle and v_{adv} is the term accounting for the non-uniform density of the gas in which the particles diffuse as well as the non-uniform diffusivity of the particles, and the forces experienced by the particle, namely the gravitational attraction from the central planet and the gas drag (see Equation (20)). D_p is related to the gas diffusivity through the Schmidt number Sc as (Youdin & Lithwick 2007):

$$Sc \equiv \frac{\nu}{D_p} \sim 1 + \frac{St^2}{4}, \tag{19}$$

implying that solids with large Stokes number are not significantly affected by turbulence. The advective velocity v_{adv} is given by (Ciesla 2010, 2011; Charnoz et al. 2011)

$$v_{\mathrm{adv}} = \frac{D_p}{\rho_g}\frac{\partial \rho_g}{\partial x} + \frac{\partial D_p}{\partial x} + v_{s,x}, \tag{20}$$

where the two first terms account for the gradients in gas density and solid diffusivity and the last term is the velocity of the particle determined from its equation of motion (Equation (16)).

We have also included the sublimation of water ice in our model to track the evolution of the ice fraction of the solids during their transport within the CPD. This ice fraction is compared with the present water content of the Galilean satellites. The surface temperature of the solids is calculated following the prescription of D'Angelo & Podolak (2015), in which several heating and cooling mechanisms are considered. The main heat source is the radiation from the ambiant gas at the local temperature T_d. Friction, and the gas also heats up the surface of the body. Water ice sublimation on the other hand is an endothermic process that substantially lowers the temperature of the solid.

Finally, energy is radiated away from the surface at the surface temperature of the body. Taking into account all the heating and cooling sources, and considering that these processes only affect an isothermal upper layer of thickness δ_s, the evolution of the surface temperature T_s of the solid is given by (D'Angelo & Podolak 2015)

$$\begin{aligned}\frac{4}{3}\pi[R_s^3 - (R_s - \delta_s)^3]\rho_s C_s \frac{dT_s}{dt} = {}& \frac{\pi}{8} C_D \rho_g R_s^2 v_{\mathrm{rel}}^3 \\ & + 4\pi R_s^2 \epsilon_s \sigma_{\mathrm{SB}} (T_d^4 - T_s^4) \\ & + L_s \frac{dM_s}{dt},\end{aligned} \tag{21}$$

where R_s is the radius of the particle, C_s is the specific heat of the material set to $1.6 \times 10^3\ \mathrm{J\ kg^{-1}\ K^{-1}}$ (specific heat of water ice at $\sim$200 K), ϵ_s is the emissivity of the material, σ_{SB} is the Stefan–Boltzmann constant, and L_s is the latent heat of sublimation of water ice ($L_s = 2.83 \times 10^6\ \mathrm{J\ kg^{-1}}$). Usually, the heating due to gas friction has a negligible effect so that the surface temperature of the bodies tends to equal to that of the disk when water ice sublimation is not significant. On the other hand, when sublimation is important, the surface temperature can be significantly lowered (see Section 3 and Figure 5 for more details).

The resulting mass-loss rate due to water ice sublimation is then given by

$$\frac{dM_s}{dt} = -4\pi R_s^2 P_v(T_s) \sqrt{\frac{\mu_s}{2\pi R_g T_s}}, \tag{22}$$

Table 1
Coefficients for the Polynomial Relation Giving the Equilibrium Vapor Pressure of Water at a Given Temperature

i	e_i
0	20.9969665107897
1	3.72437478271362
2	−13.9205483215524
3	29.6988765013566
4	−40.1972392635944
5	29.7880481050215
6	−9.13050963547721

Note. The coefficients are taken from Fray & Schmitt (2009).

where $P_v(T_s)$ is the equilibrium vapor pressure of water over water ice at the temperature T_s, μ_s is the molecular weight of water, and R_g is the ideal gas constant. The above expression is neglecting the effect of the partial pressure of water and holds in vacuum. In practice, P_v should be replaced by $(P_v(T_s) - P_{H_2O}(r))$ in Equation (22), with $P_{H_2O}(r)$ the partial pressure of water vapor in the disk. However, we do not follow the evolution of the water vapor in this study and the initial composition of the CPD is uncertain, as water was most likely in condensed form at Jupiter's orbit. Our expression therefore yields to "colder" snowlines as the sublimation of water ice should be inhibited whenever $P_{H_2O} > P_v$ in more realistic conditions. The equilibrium vapor pressure $P_v(T_s)$ is computed from Fray & Schmitt (2009):

$$\ln\left(\frac{P_v(T)}{P_t}\right) = \frac{3}{2}\ln\left(\frac{T}{T_t}\right) + \left(1 - \frac{T_t}{T}\right)\gamma\left(\frac{T}{T_t}\right) \tag{23}$$

$$\gamma\left(\frac{T}{T_t}\right) = \sum_{i=0}^{6} e_i\left(\frac{T}{T_t}\right)^i, \tag{24}$$

where $P_t = 6.11657 \times 10^{-3}$ bar and $T_t = 273.16$ K are the pressure and temperature of the triple point of water respectively. The coefficients e_i are given in Table 1.

The thickness of the isothermal layer is given by D'Angelo & Podolak (2015) as

$$\delta_s = \min\left[R_s, 0.3\frac{K_s}{\sigma_{SB}T_s^3}\right], \tag{25}$$

where K_s is the thermal conductivity of ice ($\sim$3 W m^{-1} K^{-1} at 200 K). At a surface temperature of 150 K the thickness of the isothermal layer is $\delta_s \sim 4.7$ m while at 200 K it is reduced to $\sim$2 m. For the sake of simplicity, we do not consider here a mixture of ice and rock that would primarily have a slightly lower specific heat and a slightly higher thermal conductivity. The impact on our results focusing on the sublimation of water ice would only be minor, as D'Angelo & Podolak (2015) demonstrated that the differences in the ablation rates among completely icy and mixed composition bodies are no more than $\sim$10%.

The equations depicting the surface temperature evolution and mass ablation rate are integrated together with the equation of motion of the particle. The change in radius caused by ice ablation is taken into account during the determination of the stopping time and consequently in the motion equation of the particle. For the sake of simplicity, we assume that the density of the solids is not modified during ice ablation and the radius of the particle is therefore always given by $Rs = (3M_s/4\pi\rho_s)^{1/3}$. This is equivalent to considering that the porosity of the body increases when ice sublimates.

3. Results

Figure 4 presents the results of simulations with initial sizes of 10^{-6}, 10^{-1}, 1, 10^3, and 10^4 m, to illustrate their very different behavior in terms of dynamics and thermodynamics.

We applied our model to particles of different initial sizes (10^{-6}, 10^{-1}, 1, 10^3, and 10^4 m) and tracked the dynamical and compositional evolution over a short timespan (2700 years). Specifically, one thousand particles per size bin were initially released in the midplane of the CPD at distances ranging between 20 and 35 R_{Jup}. At the beginning of the simulation, all particles have an ice mass fraction $f_{ice} = m_{ice}/m_{tot} = 0.5$. The CPD is assumed to be in steady-state with $\dot{M}_p = 10^{-7}\,M_{Jup}\,yr^{-1}$ and $\alpha = 10^{-3}$, which gives the surface density and temperature profiles drawn in Figure 1, allowing us to focus the results on solids' evolution. The inner edge of the disk is set equal to 3.5 R_{Jup}. Solids crossing this distance are considered lost to the planet, implying that their motion is no longer integrated. In Figure 4, we display the rock mass fraction ($f_{rock} = 1 - f_{ice}$), height, and distance to Jupiter of the solids as functions of time.

The different dynamical behavior as a function of particle size is well illustrated in Figure 4. A common feature for all particle sizes is the much faster vertical than radial diffusion timescale. The first column of the figure, showing the radial and vertical position of the solids after $\sim$2.7 years of evolution, illustrates the fact that solids are already distributed vertically and this distribution does not significantly change further in time. As expected, larger solids concentrate more in the midplane of the disk whereas micron-sized dust particles are efficiently entrained by turbulence and follow the distribution of the gas. It is important to note that the vertical position of the solids (Figure 4) is represented in units of the gas scale height $H_g(r)$ at the radial position of the particle. The radial drift of the particles also follows a well-known trend with very small particles (micron-sized) being well coupled with the gas, intermediate-sized particles (1 cm–1 m) drifting inward at a high pace, and large particles ($\geqslant$1 km) drifting inward and diffusing outward at a very low pace.

Concerning the compositional evolution of the particles, some clear trends emerge (see Figure 4). It appears that size strongly influences the ability of a given particle to retain water while drifting inward. In short, larger bodies are able to retain significantly more water than the smaller ones. For example, meter-sized bodies located inside of $\sim$12 R_{Jup} have lost all their water after 27 years of evolution whereas kilometer-sized bodies (fourth row of Figure 4) have retained most of their water at the same location. The same applies for 10^3 and 10^4 m solids after 270 and 2700 years of evolution. It is also interesting to note that due to their limited inward drift and rather long sublimation timescales, water-free and water-rich kilometer-sized bodies can coexist at the same location, a feature that is not observed among the smaller particles.

The origin of such compositional evolution as a function of particle size is twofold. First, from Equation (22), one can derive that the ablation timescale at a given location of a particle is $M_s\,(dM_s/dt)^{-1} \propto R_s$, implying that larger particles retain more water than smaller ones. Second, because water ice

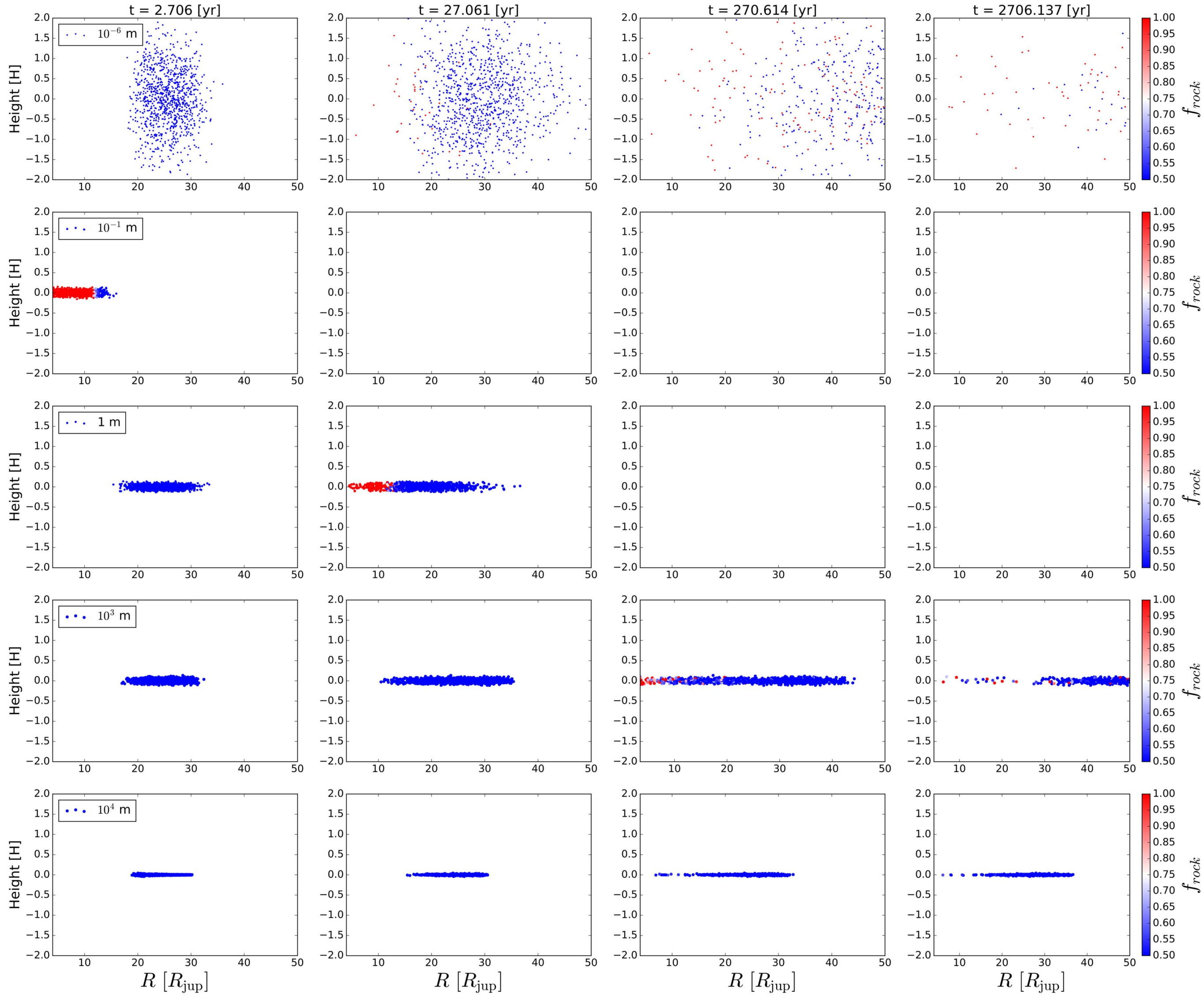

Figure 4. From left to right: snapshots of the evolution of particles at different times within a Jovian CPD with parameters $\dot{M}_p = 10^{-7}\, M_{\rm Jup}\, {\rm yr}^{-1}$ and $\alpha = 10^{-3}$. From top to bottom, each row displays the evolution of solids of different initial sizes with radii of 10^{-6}, 10^{-1}, 1, 10^3, and 10^4 m. The radial and vertical positions of the solids are expressed in $R_{\rm Jup}$ and local gas scale height respectively. The color of each particle illustrates its composition with bluer particles having a higher water ice mass fraction.

sublimation is an endothermic process, it cools down the surface temperature of large particles efficiently for longer time. Considering negligible the heating due to friction with the gas and that an equilibrium is rapidly attained, Equation (21) reduces to

$$\epsilon_s \sigma_{\rm SB}(T_d^4 - T_s^4) = L_s P_v(T_s) \sqrt{\frac{\mu_s}{2\pi R_g T_s}}. \tag{26}$$

When the release of sublimation heat is important (right-hand side of the equation), the surface temperature of the bodies departs from that of the surrounding gas.

This process is well illustrated in Figure 5, where the surface temperature of 10 km and 10 cm sized planetesimals is shown (blue and yellow dots, respectively) along with the temperature of the surrounding gas (black dashed line) and the solution of Equation (26) (red dashed line). Closer to Jupiter, where the CPD is hotter, the temperature of these bodies departs from that of the gas because a significant amount of water sublimates at their surfaces. The surface temperature given by Equation (26) slightly underestimates the temperature but is a good approximation. In spite of that, the ablation timescale of 10 cm particles remains short and their water ice is entirely sublimated when they approach at distances $\lesssim 10\, R_{\rm Jup}$. Interior to this distance, the surface temperature of the 10 cm bodies abruptly catches up with the disk temperature. The efficient cooling during water ice sublimation and the fact that the sublimation timescale scales with the size of the object allows larger bodies to retain water over much longer timescales than their smaller siblings.

Due to the very short lifetime of the solids with sizes in the 10^{-1}–1 m range, we ran another set of simulations to study in more details their evolution within the CPD. We also extended the size range down to 10^{-2} m particles.

We ran simulations using 10,000 particles, released between 25 and 35 $R_{\rm Jup}$ and we opted to randomly reinject in this region

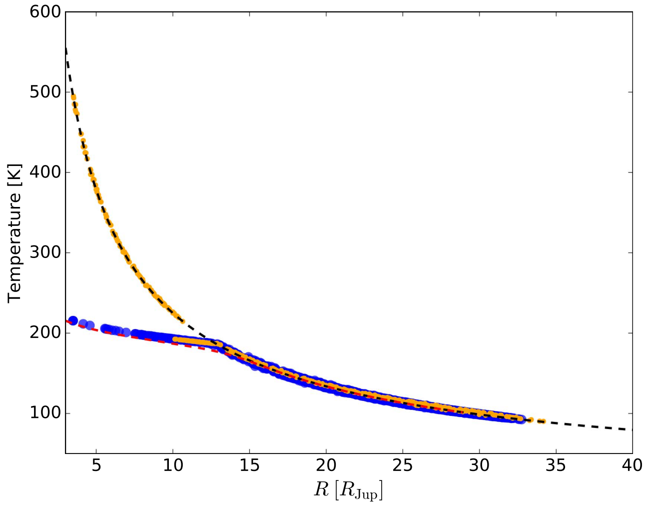

Figure 5. Surface temperature of 10 km (blue dots) and 10 cm (yellow dots) bodies as a function of the distance from Jupiter within a CPD with $\dot{M}_p = 10^{-7}\,M_{\rm jup}\,{\rm yr}^{-1}$ and $\alpha = 10^{-3}$. The black dashed line represents the temperature profile of the CPD, while the red dashed line is the solution of Equation (26). The high water ice ablation rates suffered by these bodies efficiently cools down their surface temperatures in the inner part of the disk, making them substantially depart from the ambient gas temperature. However, 10 cm bodies cannot retain water ice below $\sim 10\,R_{\rm Jup}$ so that their surface temperature is that of the ambient gas interior to this distance.

the particles that cross the inner edge of the CPD at 3.5 $R_{\rm Jup}$. In a way, we mimic a flux of pebbles that would originate from farther locations within the CPD. The parameters of the CPD are those used in the previous simulations.

Figure 6 shows the average water ice mass fraction $f_{\rm ice}$ of solids with sizes of 10^{-2}, 10^{-1}, and 1 m as a function of the distance to Jupiter. Due to the rapid dynamics of these solids and the fact that we reinject them, an equilibrium is rapidly attained, meaning that the curves shown in Figure 6 are steady in time for a stationary CPD. These curves would, however, shift toward Jupiter as the disk slowly cools down compared to the drift timescale of the pebbles. During their inward migration, solids gradually loose water ice and therefore exhibit a gradient in their water mass fraction as a function of the radial distance. The solids able to transport water the farthest inside the disk are the 10^{-1} m pebbles because of their very rapid inward motion. The solids with a size of 10^{-2} m display a very similar behavior, although their water mass fraction is shifted in the outer radial direction. This shift is due to the shorter ablation timescale of 10^{-2} m pebbles compared to that of the larger ones, although their velocity is comparable (see Figure 3). Larger meter-sized bodies exhibit a less steep gradient in their water mass fraction because of their much slower inward velocities. They spend a greater amount of time in a given environment than smaller pebbles, causing them to be more ablated and therefore they are not able to carry as much water as 10^{-1} m pebbles.

Overall, we find that the pebbles define three distinct compositional regions. In the outer region, the solids mostly retain their primordial water content because they do not suffer from substantial sublimation. In the innermost region, the solids have already lost all of their water ice and are essentially rocky. In between these two regions, the particles exhibit a gradient in their water content over an area that is $\sim 3\,R_{\rm Jup}$ wide due to the combined effect of inward drift and sublimation.

4. Discussion

Here we put into perspective the results presented in the previous section with the current composition of the Galilean system. We try to provide some constraints on the size of the building blocks of the Jovian moons and discuss the implications on different mechanisms, such as the delivery of solids to the CPD or the migration of the satellites, which were not studied here. Overall, we try to provide new insights on the formation of the satellites of Jupiter and some exploration tracks for the future.

4.1. Constraints on the Size of the Building Blocks of the Galilean Satellites

We presented in Section 3 the dynamical and compositional evolution of particles with a wide range of sizes. We find that larger objects are able to retain more water ice than smaller ones, and that the ablation timescale of planetesimals with sizes $\gtrsim 10^4$ m is significantly enhanced in hot environments due to an efficient cooling of their surfaces. While it is common to assume that solids inside the snowline are rocky whereas the ones residing outward are icy (e.g., Alibert et al. 2005; Sasaki et al. 2010), our results show that the solids embedded within Jupiter's CPD should have been (at least initially) relatively smaller than 10^3 m to ensure this. If the initial building blocks of the satellites were large ($D \geqslant 10^3$ m) icy objects ($f_{\rm ice} = 1$), Io and Europa would probably have formed with substantially more water than they possess today. This finding is also supported by the study of Dwyer et al. (2013), which demonstrated that water loss during collisions of large planetesimals is not a sufficient mechanism to account for the formation of a water-free Io and Europa with less than 10% water by mass. Conversely, if the initial building blocks of the satellites were small ($D \leqslant 10^{-6}$ m) icy particles (ice/rock = 1), Io and Europa would have formed without water and Europa should be dry today.

There is only one size range that allows the direct formation of a dry Io, of a Europa with low water content and of two icy moons (Ganymede, Callisto) in the outer region of the CPD, namely $10^{-2}\,{\rm m} \leqslant D \leqslant 1$ m. If our proposed scenario is the right one, this implies that Europa could have had any water content between 0% and 50% while forming in the intermediate region (see Figure 6). In summary, the growth of Europa could have been restricted to this "intermediate" region, where the protosatellite would have accreted partially dehydrated, drifting material. Recent studies have shown that the accretion of solids with a Stokes number close to unity, such as those solids we present in Figure 6, is very efficient (e.g., Lambrechts & Johansen 2012). These pebbles are therefore good building blocks candidates, as their composition within the Jovian CPD could have defined three distinct compositional regions coherent with the current water content of the Galilean satellites.

It should be noted that the positions of the different regions defined on Figure 6 do not match the current location of the Galilean satellites. Whereas it would be easy to adjust the mass accretion rate $\dot{M}_p$ to shift the position of the different regions, we do not want to suggest that these bodies formed in a steady disk or that they necessarily formed at the position we observe them today by doing so. These issues are further discussed in the next section.

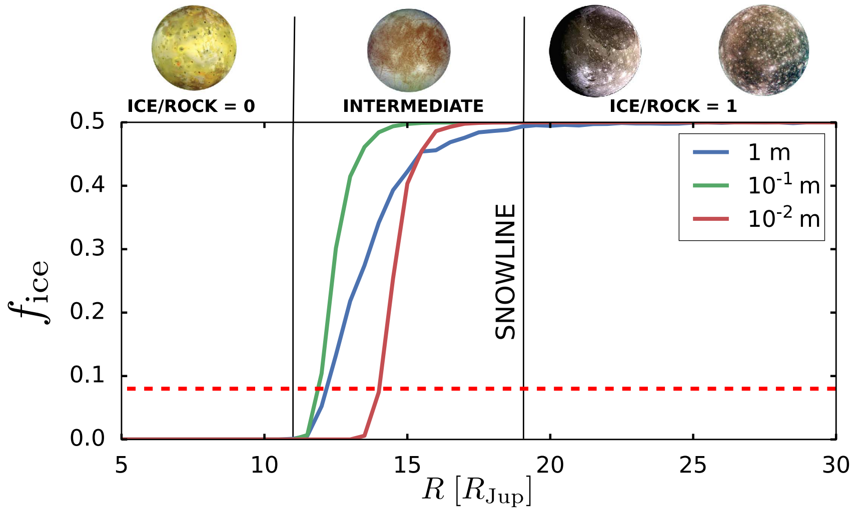

Figure 6. Average water ice mass fraction of solids as a function of radial distance from Jupiter. 10^4 particles of each size have been released in the 25–35 $R_{\rm Jup}$ region. The horizontal dashed line corresponds to Europa's estimated water mass fraction.

4.2. Caveats of the Model and Roadmap for Future Research

We discuss here some of the processes that likely played a role during the formation of the satellites and that we did not study here, and how they would fit with our findings. We also recall the assumptions of the model we used and how it affects our results.

Model assumptions—We start here by discussing the assumptions upon which our results rely and some of the processes we neglected in this study. In our simulations, we considered that solids lose water via sublimation of water ice and that the refractory part remains. This gradual sublimation of pebbles gives rise to the region suitable for the formation of Europa-like bodies. Other studies of grain sublimation suggest that solids are disrupted into small micrometer dust grains when they cross the snowline (see, e.g., Saito & Sirono 2011). In such a case, no gradient in the composition of the solids would exist, but rather a twofold population constituted of very small silicate grains inside the snowline and large icy grains outside. Whether or not disruption of the grains occurs at the snowline depends on the structure of the grains. Very porous aggregates of silicate monomers covered with ice are prone to disruption while more compact aggregates or collisional fragments of larger bodies would more likely stay intact. The structure of the solids embedded within the Jovian CPD is uncertain and would primarily depend on the delivery mechanism of solids within the CPD, which is discussed next.

In addition, our model does not consider the condensation of water vapor onto grains. Although the effect on centimeter or larger grains should be moderate, it has a great importance for the evolution of small dust grains onto which condensation will preferentially occur (Ros & Johansen 2013). As we did not include grain growth either in our model, we miss effects such as local water vapor or solids enhancement close to the snowline (e.g., Ciesla & Cuzzi 2006). This is, however, beyond the scope of this study and would only be relevant if the solids within the CPD built-up from small dust grains. This depends, again, on wether solids are primarily brought to the CPD in the form of small, well coupled grains or in the form of larger, already decoupled aggregates. As we discuss below, this question remains to be investigated but our results would be more consistent with the delivery of already decoupled and rather compact solids.

Delivery mechanism of solids—The main origin of solids in the Jovian CPD, which is deeply connected with the formation of Jupiter, is still debated. Two different mechanisms have been proposed to feed the CPD. Canup & Ward (2002) proposed that small dust grains that couple with the gas are entrained with the inflow onto the CPD whereas Mosqueira & Estrada (2003a, 2003b) and Estrada & Mosqueira (2006) argued that larger planetesimals crossing Jupiter's orbit could be captured through gas drag within the CPD.

While the first mechanism has not been quantitatively studied, we can note some important caveats. It is expected that dust grains can grow up to decoupling sizes with Stokes numbers $\gtrsim 10^{-2}$ in the regions where the giant planets formed and that the population of larger grains carry most of the mass (e.g., Birnstiel et al. 2011, 2012). This is also required to rapidly grow the cores of giant planets through pebble accretion (Lambrechts & Johansen 2014). It results that most of the solids mass should reside close to the midplane of the PPD in decoupled solids. This is hard to reconcile with the view of Canup & Ward (2002) who advocated a fiducial dust-to-gas ratio of 1% in the Jovian CPD. It is more likely that the gas accreted by Jupiter and its disk, which proceeded through the heights of the PPD as demonstrated by 3D hydrodynamic simulations (Tanigawa et al. 2012; Szulágyi et al. 2016), was depleted in dust. Interestingly, this depletion in dust benefits giant planet formation, as this would substantially reduce the opacity of their envelope, allowing a much faster contraction of the envelope and triggering runaway gas accretion more rapidly (Lambrechts et al. 2014; Bitsch et al. 2015).

Concerning the second mechanism, Estrada & Mosqueira (2006) and Mosqueira et al. (2010) argued that at the time of the formation of the satellites, planetesimals in heliocentric orbits would have their eccentricities and inclinations excited by almost completely formed nearby giant planets. Collisions among these excited planetesimals would have led to intense collisional grinding and resulting bodies in the meter to kilometer size range (Charnoz & Morbidelli 2003). This would provide suitable conditions for the capture of planetesimals by the CPD, as their high inclinations and eccentricities would place them onto Jupiter crossing orbits. The capture of these collisional fragments in the meter to kilometer size range is more in line with our study than the inflow of small grains, and as we mentioned, with the timing required to accrete Jupiter's envelope. It is also in agreement with the fact that starting out with large icy bodies (tens or hundreds of kilometers) would lead to the formation of hydrated inner satellites as neither collisions, as demonstrated by Dwyer et al. (2013), nor sublimation, as we pointed out in this study, seem efficient enough mechanisms to dehydrate such large building blocks. This capture scenario, however, remains to be investigated and quantified. A better knowledge of the initial solids size and mass distribution within the Jovian CPD is crucial to disentangle from different formation mechanisms of the Galilean satellites. The key question here being to determine whether enough mass in the meter to tens of meters range can be brought within the CPD for pebble accretion to be relevant.

Time evolution of the CPD and migration of the satellites—Here we briefly discuss the time evolution and cooling of the CPD, which we have neglected to focus on the evolution of the solids only. Although its structure and evolution timescale are very poorly constrained, the disk surrounding Jupiter likely evolved with time. Depending on the viscosity and mass accretion rate, the evolution of the CPD could have occurred on timescales ranging from $\sim 10^4$ to 10^6 years (Miguel & Ida 2016). The evolution and cooling of the CPD was therefore very slow compared to the inward drift of pebbles. It results that the composition of these solids would not be directly affected by the cooling of the disk. Provided that icy pebbles come from the outer parts of the CPD and drift toward its inner regions, they should always exhibit a gradient in composition when crossing the snowline. The disk's evolution would only affect the location of the snowline, namely the region where the gradient exists.

The question that remains to be elucidated is then whether or not the complete formation of the satellites, and particularly Europa, could have occurred in a given region matching their composition. This would depend on the ratio of their growth/migration timescale to the CPD's evolution timescale. Fully forming Europa in the region inside the snowline would either imply that (i) its growth timescale was much faster than its migration timescale and the cooling timescale of the CPD or (ii) its migration timescale was comparable to the disk evolution timescale so that Europa migrated inward together with the snowline as the CPD cooled over time. While (i) could be hard to reconcile with the fact that Callisto migth not be fully differentiated, implying a formation timescale of $\sim 10^5$ years (see, e.g., Canup & Ward 2002), several recent studies have shown that planet traps, i.e., regions where migration is halted, are associated with the water snowline inside PPDs (Baillié et al. 2015, 2016; Bitsch et al. 2015; Bitsch & Johansen 2016), making scenario (ii) a promising one. As the snowline moves inward over time, so does the migration trap, offering the possibility to tie the migration of a body to the evolution of the snowline.

5. Conclusions

In this study, we have shown that the overall bulk composition of the Galilean satellites could be naturally accounted for in a pebble accretion scenario. The strong inward drift of these solids leads to the rapid emergence of well defined regions in terms of composition that can reproduce the gradient in water mass fraction existing among the satellites. The strongest implications of this scenario are the existence of pebbles that do not completely fragment when crossing the snowline and the fact that each satellite fully accreted in a given region. The latter implies that the migration of the satellites must have been somehow tied to the evolution of the snowline, as its position determines the location of the different regions. Though it needs to be investigated in the case of the Jovian CPD; the existence of a relationship between migration and snowlines seems to be supported by recent theoritical developments about type I migration (e.g., Paardekooper et al. 2010; Bitsch et al. 2014, see also Section 4).

It is very delicate to determine whether the Jovian moon's density gradient results directly from a gradient in the water mass fraction of the solids they accreted or from a more complicated interplay among their growth, migration, and CPD's evolution given our current knowledge of these processes. While recent developments in 3D hydrodynamics simulations help better understand the accretion of gas onto the CPD (e.g., Tanigawa et al. 2012), more realistic equations of state are needed to constrain the density and temperature of the CPD (see, e.g., Szulágyi et al. 2016). A better understanding of the formation and structure of CPDs and the delivery mechanisms of solids is crucial for further developments of the Galilean satellites' formation models.

We wish to warmly thank the referee for the very careful review of the paper. T.R. and O.M. acknowledge support from the A*MIDEX project (n° ANR-11-IDEX-0001-02) funded by the "Investissements d'Avenir" French Government program, managed by the French National Research Agency (ANR). O.M. also acknowledges support from CNES.

References

Alibert, Y., Mousis, O., & Benz, W. 2005, A&A, 439, 1205
Anderson, J. D., Schubert, G., Jacobson, R. A., et al. 1998, Sci, 281, 2019
Bai, X.-N., & Stone, J. M. 2013, ApJ, 769, 76
Baillié, K., Charnoz, S., & Pantin, E. 2015, A&A, 577, A65
Baillié, K., Charnoz, S., & Pantin, E. 2016, A&A, 590, A60
Birnstiel, T., Klahr, H., & Ercolano, B. 2012, A&A, 539, A148
Birnstiel, T., Ormel, C. W., & Dullemond, C. P. 2011, A&A, 525, A11
Bitsch, B., & Johansen, A. 2016, A&A, 590, A101
Bitsch, B., Lambrechts, M., & Johansen, A. 2015, A&A, 582, A112
Bitsch, B., Morbidelli, A., Lega, E., Kretke, K., & Crida, A. 2014, A&A, 570, A75
Brown, P. N., Byrne, G. D., & Hindmarsh, A. C. 1989, SIAM J. Sci. Stat. Comput., 10, 1038
Canup, R. M., & Ward, W. R. 2002, AJ, 124, 3404
Canup, R. M., & Ward, W. R. 2006, Natur, 441, 834
Canup, R. M., & Ward, W. R. 2009, in Europa, ed. R. T. Pappalardo, W. B. McKinnon, & K. K. Khurana (Tucson, AZ: Univ. Arizona Press), 59
Charnoz, S., Fouchet, L., Aleon, J., & Moreira, M. 2011, ApJ, 737, 33
Charnoz, S., & Morbidelli, A. 2003, Icar, 166, 141
Ciesla, F. J. 2009, Icar, 200, 655
Ciesla, F. J. 2010, ApJ, 723, 514
Ciesla, F. J. 2011, ApJ, 740, 9
Ciesla, F. J., & Cuzzi, J. N. 2006, Icar, 181, 178
D'Angelo, G., & Podolak, M. 2015, ApJ, 806, 203
Drążkowska, J., Alibert, Y., & Moore, B. 2016, A&A, 594, A105
Dwyer, C. A., Nimmo, F., Ogihara, M., & Ida, S. 2013, Icar, 225, 390
Estrada, P. R., & Mosqueira, I. 2006, Icar, 181, 486
Estrada, P. R., Mosqueira, I., Lissauer, J. J., D'Angelo, G., & Cruikshank, D. P. 2009, in Europa, ed. R. T. Pappalardo, W. B. McKinnon, & K. K. Khurana (Tucson, AZ: Univ. Arizona Press), 27
Fray, N., & Schmitt, B. 2009, P&SS, 57, 2053
Fromang, S., Lyra, W., & Masset, F. 2011, A&A, 534, A107
Fujita, T., Ohtsuki, K., Tanigawa, T., & Suetsugu, R. 2013, AJ, 146, 140
Greenzweig, Y., & Lissauer, J. J. 1990, Icar, 87, 40

Gressel, O., Nelson, R. P., Turner, N. J., & Ziegler, U. 2013, ApJ, 779, 59
Gressel, O., Turner, N. J., Nelson, R. P., & McNally, C. P. 2015, ApJ, 801, 84
Guillot, T., Ida, S., & Ormel, C. W. 2014, A&A, 572, A72
Hueso, R., & Guillot, T. 2005, A&A, 442, 703
Johansen, A., Blum, J., Tanaka, H., et al. 2014, in Protostars and Planets VI, ed. H. Beuther et al. (Tucson, AZ: Univ. of Arizona Press), 547
Johansen, A., Oishi, J. S., Mac Low, M.-M., et al. 2007, Natur, 448, 1022
Keller, C., & Gail, H.-P. 2004, A&A, 415, 1177
Klahr, H., & Kley, W. 2006, A&A, 445, 747
Kobayashi, H., Ormel, C. W., & Ida, S. 2012, ApJ, 756, 70
Lambrechts, M., & Johansen, A. 2012, A&A, 544, A32
Lambrechts, M., & Johansen, A. 2014, A&A, 572, A107
Lambrechts, M., Johansen, A., & Morbidelli, A. 2014, A&A, 572, A35
Levison, H. F., Kretke, K. A., & Duncan, M. J. 2015, Natur, 524, 322
Lunine, J. I., & Stevenson, D. J. 1982, Icar, 52, 14
Lynden-Bell, D., & Pringle, J. E. 1974, MNRAS, 168, 603
Masset, F. S., Morbidelli, A., Crida, A., & Ferreira, J. 2006, ApJ, 642, 478
McKinnon, W. B. 1997, Icar, 130, 540
McKinnon, W. B. 2007, in Io After Galileo: A New View of Jupiter's Volcanic Moon, ed. R. M. C. Lopes & J. R. Spencer (Berlin: Springer), 61
Miguel, Y., & Ida, S. 2016, Icar, 266, 1
Morbidelli, A., Lambrechts, M., Jacobson, S., & Bitsch, B. 2015, Icar, 258, 418
Mosqueira, I., & Estrada, P. R. 2003a, Icar, 163, 198
Mosqueira, I., & Estrada, P. R. 2003b, Icar, 163, 232
Mosqueira, I., Estrada, P. R., & Charnoz, S. 2010, Icar, 207, 448
Mousis, O., & Gautier, D. 2004, P&SS, 52, 361
Ogihara, M., & Ida, S. 2012, ApJ, 753, 60
Paardekooper, S.-J. 2007, A&A, 462, 355
Paardekooper, S.-J., Baruteau, C., Crida, A., & Kley, W. 2010, MNRAS, 401, 1950
Perets, H. B., & Murray-Clay, R. A. 2011, ApJ, 733, 56
Ros, K., & Johansen, A. 2013, A&A, 552, A137
Saito, E., & Sirono, S.-I. 2011, ApJ, 728, 20
Sasaki, T., Stewart, G. R., & Ida, S. 2010, ApJ, 714, 1052
Schubert, G., Anderson, J. D., Spohn, T., & McKinnon, W. B. 2004, in Jupiter. The Planet, Satellites, and Magnetosphere, ed. F. Bagenal, T. E. Dowling, & W. B. McKinnon (Cambridge: Cambridge Univ. Press), 281
Shakura, N. I., & Sunyaev, R. A. 1973, A&A, 24, 337
Simon, J. B., Bai, X.-N., Stone, J. M., Armitage, P. J., & Beckwith, K. 2013, ApJ, 764, 66
Sohl, F., Spohn, T., Breuer, D., & Nagel, K. 2002, Icar, 157, 104
Supulver, K. D., & Lin, D. N. C. 2000, Icar, 146, 525
Szulágyi, J., Masset, F., Lega, E., et al. 2016, MNRAS, 460, 2853
Szulágyi, J., Morbidelli, A., Crida, A., & Masset, F. 2014, ApJ, 782, 65
Takeuchi, T., & Lin, D. N. C. 2002, ApJ, 581, 1344
Tanaka, H., & Ida, S. 1999, Icar, 139, 350
Tanaka, H., Takeuchi, T., & Ward, W. R. 2002, ApJ, 565, 1257
Tanigawa, T., Maruta, A., & Machida, M. N. 2014, ApJ, 784, 109
Tanigawa, T., Ohtsuki, K., & Machida, M. N. 2012, ApJ, 747, 47
Weidenschilling, S. J. 1977, MNRAS, 180, 57
Youdin, A. N., & Lithwick, Y. 2007, Icar, 192, 588

The Astronomical Journal, 155:224 (13pp), 2018 May https://doi.org/10.3847/1538-3881/aabcc7

Saturn's Formation and Early Evolution at the Origin of Jupiter's Massive Moons

T. Ronnet[1], O. Mousis[1], P. Vernazza[1], J. I. Lunine[2], and A. Crida[3,4]
[1] Aix Marseille Univ, CNRS, LAM, Laboratoire d'Astrophysique de Marseille, Marseille, France; thomas.ronnet@lam.fr
[2] Department of Astronomy and Carl Sagan Institute, Cornell University, Ithaca, NY 14853, USA
[3] Université Côte d'Azur/Observatoire de la Côte d'Azur, Laboratoire Lagrange (UMR7293), Boulevard de l'Observatoire, CS 34229, F-06300 Nice, France
[4] Institut Universitaire de France, 103 Boulevard Saint-Michel, F-75005 Paris, France
Received 2017 December 23; revised 2018 April 6; accepted 2018 April 7; published 2018 May 3

Abstract

The four massive Galilean satellites are believed to have formed within a circumplanetary disk during the last stages of Jupiter's formation. While the existence of a circum-Jovian disk is supported by hydrodynamic simulations, no consensus exists regarding the origin and delivery mechanisms of the building blocks of the forming satellites. The opening of a gap in the circumsolar disk would have efficiently isolated Jupiter from the main sources of solid material. However, a reservoir of planetesimals should have existed at the outer edge of Jupiter's gap, where solids were trapped and accumulated over time. Here we show that the formation of Saturn's core within this reservoir, or its prompt inward migration, allows planetesimals to be redistributed from this reservoir toward Jupiter and the inner Solar System, thereby providing enough material to form the Galilean satellites and to populate the Main Belt with primitive asteroids. We find that the orbit of planetesimals captured within the circum-Jovian disk are circularized through friction with gas in a compact system comparable to the current radial extent of the Galilean satellites. The decisive role of Saturn in the delivery mechanism has strong implications for the occurrence of massive moons around extrasolar giant planets as they would preferentially form around planets within multiple planet systems.

Key words: methods: numerical – planets and satellites: formation – planets and satellites: individual (Jupiter, Saturn, Galilean satellites) – protoplanetary disks

1. Introduction

All four giant planets of the Solar System possess regular satellites that likely formed in situ (Peale & Canup 2015). The origin of the satellite systems can therefore provide hints about the conditions prevailing during the epoch of their formation. Whereas the regular satellites of Saturn, Uranus, and Neptune may well have formed after their host planets by the spreading of massive rings (Crida & Charnoz 2012), the Galilean satellites are generally seen as a by-product of Jupiter's formation (e.g., Lunine & Stevenson 1982; Coradini et al. 1995; Canup & Ward 2002; Mosqueira & Estrada 2003a, 2003b; Mousis & Gautier 2004) and could therefore help in better understanding how, where and when the giant planet formed. Moreover, the inferred existence of a water ocean underneath the icy crust of Europa and likely within Ganymede and Callisto make the Galilean system of peculiar interest from an astrobiological point of view and motivate the search for potentially habitable extrasolar moons (for a review, see, e.g., Heller et al. 2014). Yet, some crucial steps need to be unveiled to assess the origin of the Galilean satellites and the likelihood of finding similar objects around giant exoplanets.

In the current paradigm, the Jovian satellites would have formed within a circumplanetary disk (CPD) that surrounded Jupiter at the very end of its formation (see, e.g., Canup & Ward 2009; Estrada et al. 2009, for a review). Although the development phase of a CPD and its precise structure are not well constrained, its existence around a Jupiter-mass planet has been well established through numerical experiments (e.g., Machida et al. 2008; Tanigawa et al. 2012). However, the fundamental issue of the origin of the solids embedded within the Jovian CPD remains. Although several mechanisms of solids delivery have been proposed, no consensus currently exists. This is problematic because how solids are brought to the CPD in turn dictates their initial mass and size distributions, which then essentially determine the accretion timescale of the satellites and their final masses.

Formation models of the Galilean satellites generally fall in two distinct classes, the so-called gas-starved model (e.g., Canup & Ward 2002) and the minimum mass subnebula model (e.g., Lunine & Stevenson 1982; Mosqueira & Estrada 2003a, 2003b), each being associated with a different source of solids and delivery mechanism. In the starved-disk model of Canup & Ward (2002), Jupiter is still feeding from the circumsolar disk at the formation epoch of its satellites and its CPD is constantly replenished with fresh material. Canup & Ward argue that small solids are entrained with the gas inflow onto the CPD and provide the bulk material necessary to form the satellites over a timespan of 10^5–10^6 years. Minimum mass models, on the other hand, are ad hoc constructions of a disk where sufficient condensable material to form the satellites is augmented with gas upon reaching a solar composition. Contrary to starved-disk models, this yields very dense gaseous disks and a rapid assemblage of the satellites in 10^2–10^4 years (Lunine & Stevenson 1982). Mosqueira & Estrada (2003a, 2003b) revisited such models by enhancing the solid mass fraction by a factor of 3–4 to account for the enrichment over solar abundances observed in Jupiter's atmosphere and adding an extended outer disk leading to a longer formation timescale of the satellites (especially Callisto). They argued that a dense CPD provides suitable conditions for the capture/ablation of planetesimals ($\gtrsim$10 m) on initially heliocentric orbits close to Jupiter, which would have provided the bulk material necessary to form the satellites (see also the discussion in Estrada et al. 2009).

In both scenarios, the delivery of solids to the CPD is tightly linked to the formation history of Jupiter and the distribution of dust/planetesimals in its vicinity. In recent years, large strides have been made in the theory of planet formation. Of particular interest are numerous recent studies that have demonstrated the efficiency of the so-called pebble accretion, i.e., the gas drag assisted accretion of approximately centimeter-sized solids, in growing the giant planets cores (Johansen & Lacerda 2010; Ormel & Klahr 2010; Lambrechts & Johansen 2012, 2014; Levison et al. 2015). This new formation paradigm implies that most of the solid mass budget in the forming giant planet region was contained in pebbles and not in larger planetesimals. As the pebbles are very sensitive to aerodynamic drag, their distribution within the disk does not necessarily follow a power-law distribution, such as that advocated in the widely used minimum mass solar nebula model (e.g., Hayashi 1981), and is affected by pressure perturbations. This issue is crucial for understanding the origin of the Jovian massive moons as the spatial and size distributions of the solids in the vicinity of Jupiter set the conditions of their delivery to the CPD.

Moreover, it is now established that the growth and dynamics of the giant planets have a tremendous influence on the distribution of small bodies within the Solar System (see, e.g., Gomes et al. 2005; Morbidelli et al. 2005; Levison et al. 2009; Walsh et al. 2011; Vokrouhlický et al. 2016; Raymond & Izidoro 2017). Despite this fact, the formation of the Jovian moons in the broader context of the early history of the giant planets in the protoplanetary disk (PPD) has not been quantitatively investigated.

These considerations motivated the present study, in which we attempt to address the delivery of solid material to the circum-Jovian disk in light of the recent theories of giant planet formation (e.g., Ormel & Klahr 2010; Lambrechts & Johansen 2014; Lambrechts et al. 2014; Levison et al. 2015). In Section 2, we discuss some of the limitations of the proposed delivery mechanisms and introduce our framework. We thus propose that the building blocks of the Galilean satellites originated from a reservoir of planetesimals located at the outer edge of the gap opened by Jupiter in the circumsolar disk. However, because this reservoir remains mainly out of Jupiter's reach, in Section 3, we show the decisive role of Saturn's growth and early evolution. We show that the forming Saturn had the potential to perturb the planetesimals' orbits and to allow their delivery to both the Jovian CPD and the inner Solar System. In Section 4, we investigate the subsequent evolution of the planetesimals within the circum-Jovian disk. The implications of our results along with some additional considerations raised by the model are discussed in Section 5 and our findings are summarized in Section 6.

2. Sources of Solid Material

Here we briefly present the prevailing scenarios for the origin of the building blocks of the Galilean satellites and discuss some of their limitations. Considering the hurdles of the proposed mechanisms, we argue for the existence of a reservoir of material located at the outer edge of Jupiter's gap. This reservoir likely provided the bulk of the material for the Galilean satellites as will be shown in the next sections.

2.1. Inflow of Small Dust Grains

Canup & Ward (2002) postulated that the Galilean satellites formed while Jupiter was still feeding from the circumsolar disk via the replenishment of its CPD with a mixture of gas and dust in solar proportions. This model was originally proposed to circumvent some weak points of the minimum mass models, specifically the long accretion timescale needed to match the internal structure of Callisto and the survival of satellites against gas-driven migration.

However, the scenario of Canup & Ward (2002) requires that the solids brought to the CPD were in the form of perfectly coupled dust grains that have not settled toward the midplane of the disk. Indeed, hydrodynamic simulations demonstrated that the gas eventually falling onto the CPD resides well above the midplane of the circumsolar disk (Machida et al. 2008; Tanigawa et al. 2012; Morbidelli et al. 2014; Szulágyi et al. 2014). The dust grains that substantially grew up and settled toward the midplane of the disk due to gas drag would therefore not be able to reach the CPD with the characteristics defined by Canup & Ward (2002). Paardekooper & Mellema (2006) and Paardekooper (2007) have shown that only particles with sizes $\leqslant 10$ μm could be entrained with the gas flow once Jupiter opened up a gap in the circumsolar disk. Birnstiel et al. (2011, 2012) precisely investigated dust growth within PPDs and found that it is efficient at least up to partially decoupled sizes (millimeters to centimeters, depending on the turbulence level and location in the disk), implying a substantial settling of dust grains toward the disk's midplane. Considering the results of Birnstiel et al. (2011), Zhu et al. (2012) estimated the dust-to-gas ratio within the gap opened by a Jupiter-mass planet to be 10^{-4}, which is two orders of magnitude lower than the protosolar value. On the other hand, Shibaike et al. (2017) studied grain growth within CPDs and find that the dust-to-gas ratio must be $\gtrsim 1$ in order to grow satellitesimals via direct collision or streaming instability (i.e., the collapse of a cloud of pebbles concentrated through gas drag into $\sim$100 km objects, Johansen et al. 2015).

Considered together, it is difficult to reconcile these results with the scenario envisioned by Canup & Ward (2002). The gas accreted by Jupiter and the CPD was most likely depleted in dust and might not have provided the bulk of the material necessary to form the satellites.

2.2. Capture of Large Planetesimals

Another potential mechanism to deliver solid material to the CPD is the capture/ablation of larger planetesimals located in the vicinity of Jupiter due to either collisions in a gas poor environment (Estrada & Mosqueira 2006) or gas drag within a gas rich CPD (Mosqueira et al. 2010). The latter process has been numerically investigated by several authors (Fujita et al. 2013; D'Angelo & Podolak 2015; Suetsugu et al. 2016; Suetsugu & Ohtsuki 2017). However, the existence of planetesimals in the close vicinity of Jupiter is questionable. It is now well known that a planet as massive as Jupiter should have carved a deep gap in the circumsolar disk (e.g., Lin & Papaloizou 1986). The opening of a gap in the planetesimal or dust distribution will predate the opening of a deep gap in the gas distribution (e.g., Paardekooper 2007; Levison et al. 2010; Lambrechts et al. 2014; Dipierro et al. 2016; Dipierro & Laibe 2017). Unless subject to a replenishment mechanism, the feeding zone of Jupiter should have been rapidly devoid of solid material. As a matter of fact, Suetsugu & Ohtsuki (2017) pointed out that if a gap existed in the planetesimal distribution beyond the orbit of Jupiter, the accretion of material onto the CPD would be greatly reduced, if not suppressed. This is a crucial issue considering that the Galilean satellites should have formed in the later stages of Jupiter's formation (e.g., Canup & Ward 2009; Estrada et al. 2009).

The existence of a sea of planetesimals in the giant planet region to feed Jupiter's disk also remains hypothetical. In the current paradigm of planetesimal formation (see e.g., Johansen et al. 2014), specific conditions need to be fulfilled for large bodies to form, resulting in potentially very localized regions of efficient planetesimal formation (Drążkowska et al. 2016; Carrera et al. 2017; Schoonenberg & Ormel 2017). At first sight, it seems that the opening of a gap by Jupiter is problematic for the formation of its satellites as this would have substantially isolated the giant planet from any source of solid material.

2.3. Existence of a Reservoir of Planetesimals Close to Jupiter

Recent developments in the theory of giant planet formation suggest that the rapid formation of a solid core of several Earth masses is facilitated if the solid mass budget of PPDs is carried by dust grains only partially decoupled from gas, designated as pebbles, with sizes in the millimeters to centimeters range[5] (Lambrechts & Johansen 2012, 2014; Levison et al. 2015). The very efficient accretion of pebbles leads to high mass accretion rates and substantial heating of the envelope that prevents its rapid contraction onto the core. Pebble accretion is however halted when the core becomes massive enough so that it significantly perturbs the surrounding gas distribution, creating a pressure maximum outside its orbit that acts as a barrier (Lambrechts et al. 2014). After reaching this mass threshold, the accretional heating of the core's envelope ceases, allowing a rapid contraction of the atmosphere of the protoplanet and its subsequent growth toward becoming a gas giant.

Once Jupiter reached the pebble isolation mass (estimated to be $\sim 20\,M_\oplus$; Lambrechts et al. 2014), pebbles remained trapped at the outer edge of its gap and accumulated over time (e.g., Gonzalez et al. 2015). The accumulation of solids at this particular place would have lead to an enhanced dust-to-gas ratio and therefore likely provided suitable conditions to trigger the formation of large planetesimals via direct sticking or gravitational instability. Therefore, a reservoir of planetesimals should have built up over time just outside Jupiter's orbit, while the close vicinity of the planet was devoid of solid material. This reservoir is potentially so massive that Kobayashi et al. (2012) proposed that Saturn's core actually grew at the outer edge of Jupiter's gap (an hypothesis also mentioned by Lambrechts et al. 2014).

It would be surprising were such a reservoir to have existed close to Jupiter and not play any role in the formation of its regular satellites, the origin of whose building blocks remains elusive. Yet, as demonstrated by Suetsugu & Ohtsuki (2017), if the objects of the reservoir were on circular and coplanar orbits, as expected from their formation process, they would have mainly remained out of Jupiter's reach. However, there is now little doubt that Saturn once was orbiting much closer to Jupiter than it is currently (see, e.g., Deienno et al. 2017, and references therein). Saturn could therefore have had a great influence on the dynamics of the planetesimals residing at the outer edge of Jupiter's gap, exciting their orbits and potentially allowing their delivery to the Jovian CPD. This idea constitutes the cornerstone of the present study.

[5] We stress that the sizes given here are mere indications as pebbles are defined by their aerodynamic properties and not their sizes.

3. Delivering Planetesimals from the Reservoir

Here we investigate the orbital evolution of the planetesimals trapped at the outer edge of Jupiter's gap and under the influence of both the planet itself (assumed to have acquired essentially its current mass) and the forming Saturn.

Jupiter is assumed to be located at a heliocentric distance of ~ 5.4 au, in agreement with the dynamical evolution of the giant planets after the dispersal of the circumsolar disk (Deienno et al. 2017, and references therein). This does not imply that Jupiter never suffered from any migration within the disk. Rather, the planet migration rate was substantially lowered when it opened up a gap in the disk (Lin & Papaloizou 1986; Crida & Bitsch 2017), so that the reservoir of planetesimals could have built up over time.

Regarding Saturn, we explored two different evolution pathways, first because of the many unknowns of its formation history and second, to show that the redistribution of solids from the reservoir is a natural outcome and does not necessarily require very specific configurations of Jupiter and Saturn. In Section 3.1, we investigate a scenario where the core of Saturn is formed at the outer edge of Jupiter's gap, as proposed by Kobayashi et al. (2012). Alternatively, Saturn could have formed further from Jupiter and migrated inward until being caught in resonance with Jupiter (e.g., Bitsch et al. 2015b). We explore this possibility in Section 3.2.

The orbital integrations were performed using the hybrid `HERMES` integrator available with the open source `REBOUND` package.[6] Each simulation included 5000 planetesimals as test particles and the orbits were integrated with a timestep of $10^{-2}/2\pi$ year.[7] In each case, we included the eccentricity damping of the giant planets due to interaction with the gas disk using fictitious forces (Appendix A). We used disk profiles including a Jupiter-mass planet and associated gap obtained from 2D hydrodynamic simulations performed with FARGO (Masset 2000). Figure 1 shows the gas distribution obtained after 300 orbits of Jupiter. We normalized the disk profiles so that the surface density at 1 au is $\sim 300\,\mathrm{g\,cm^{-2}}$, which corresponds to a moderately evolved disk (Bitsch et al. 2015a). We included the effect of aerodynamic drag in the equation of motion of the planetesimals, considering they have a radius of 100 km and a density of $1\,\mathrm{g\,cm^{-3}}$ (see Appendix A). When planetesimals were found at a distance $r \leqslant 150\ R_{\mathrm{Jup}}$ from Jupiter, the aerodynamic drag was computed with respect to a CPD profile derived from the parameterization of Sasaki et al. (2010). A description of the CPD model is provided in Appendix B.

We consider that planetesimals are captured within the circum-Jovian disk when they are found on a bound orbit with a semimajor axis with respect to Jupiter that is less than $0.2\ R_{\mathrm{Hill}}$, where $R_{\mathrm{Hill}} = a_{\mathrm{Jup}}(M_{\mathrm{Jup}}/3\,M_\odot)^{1/3}$ is the Hill's radius of Jupiter. This quite arbitrary threshold was chosen because it corresponds roughly to the extension of the circum-Jovian disk and is plausibly deep enough in Jupiter's potential to consider the objects as permanently captured within the CPD. More details about the capture of planetesimals and a test of the validity of the threshold are presented in Appendix C. The orbital parameters of the planetesimals with respect to the Sun

[6] Available at http://github.com/hannorein/rebound.

[7] We note that this is the timestep for the simplectic integrator only. Close encounters with the massive planets are handled with the high-order adaptive time-stepping `IAS15` integrator (Rein & Spiegel 2015; Rein & Tamayo 2015).

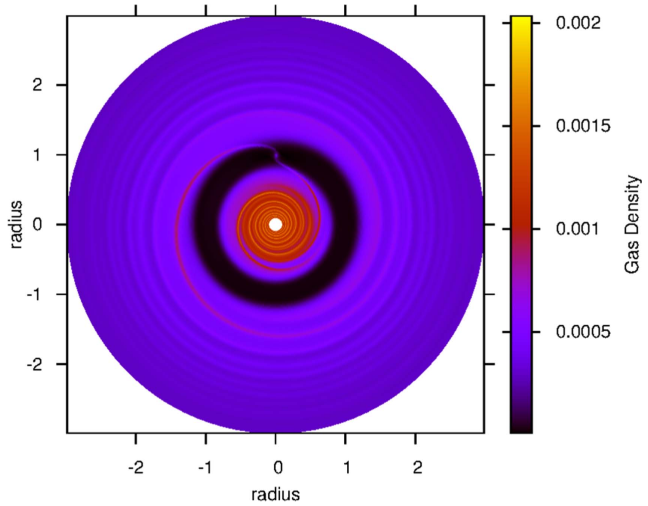

Figure 1. Fargo simulation of a Jupiter-mass planet in a viscous disk with a constant aspect ratio of 0.05 (i.e., the scale height of the disk normalized by the orbital distance). The turbulent viscosity was accounted for following the prescription of Shakura & Sunyaev (1973) with $\alpha = 2 \times 10^{-3}$. The radius is expressed in terms of the giant planet's semimajor axis and the gas density is in arbitrary units. This gas distribution is obtained after 300 orbits of the planet.

or Jupiter are computed using the dedicated tools provided in the REBOUND package. Captured planetesimals are removed from the simulation to save computing power and their orbital parameters with respect to Jupiter are stored.

3.1. Case 1: Growth of Saturn at the Edge of Jupiter's Gap

Here we present the results of simulations considering the growth of a body from a mass of $\sim 1\,M_\oplus$ up to the mass of Saturn and located at a heliocentric distance of 7 au (with Jupiter placed at 5.4 au). The mass of the protoplanet, $M_{\rm Sat}$, is increased on a timescale $\tau_{\rm growth}$ ranging between 10^5 and 10^6 years following

$$M_{\rm Sat}(t) = M_i + \Delta M[1 - \exp(-t/\tau_{\rm growth})], \quad (1)$$

where M_i is the initial mass of the core and ΔM is the difference between the initial core mass and the final mass of Saturn. This evolution pathway is very simplified compared to the core accretion model where an envelope is slowly contracted until a rapid runaway gas accretion is triggered and then followed by a slower accretion phase when the planet carves a gap in the disk (e.g., Pollack et al. 1996). However, the classical picture of core accretion might be inaccurate due to the fact that the gas and solids distributions are significantly perturbed in the particular case considered here. Detailed investigations would be needed to obtain a more realistic growth pattern but we do not aim here at studying the precise evolution of Saturn. We nevertheless varied the growth timescale to see whether some trends stand out in the final planetesimals distribution.

Figure 2 shows the orbital evolution in the semimajor axis-eccentricity plane obtained from a simulation with Saturn growing over a timescale $\tau_{\rm growth} = 5 \times 10^5$ years. The eccentricity of the planetesimals is excited by Jupiter and the growing core, allowing them to cross Jupiter's orbit and be redistributed inward or outward. Some of the planetesimals are implanted in the main asteroid belt, whose boundaries are illustrated by the dotted box in Figure 2, and others have orbits that cross the region of terrestrial planets embryos (which were not included in the simulation) marked by the dashed line (see figure legend for details). Issues regarding the implantation of objects in the inner Solar System are further discussed in Section 5. Here, we are more concerned with the capture of planetesimals within the circum-Jovian disk.

A matter of critical importance is the relative number of objects captured by Jupiter with respect to that of objects implanted in the Main Belt. Currently, the mass of the asteroid belt is estimated to be $\sim 5 \times 10^{-4}\,M_\oplus$ (Krasinsky et al. 2002) whereas the mass of the Galilean system is approximately $\sim 6 \times 10^{-2}\,M_\oplus$. Although it is expected that the asteroid belt has been depleted in mass throughout its history (Morbidelli et al. 2015), a scenario where more mass is implanted in the asteroid belt than in the CPD would be hardly reconcilable with the two orders of magnitude more massive Galilean system observed today. Moreover, it is very likely that the accretion of the Jovian moons was far from being perfectly efficient, implying that more than the current mass of the Galilean system should have been embedded within the CPD.

The results of the simulations with different growth timescales are summarized in Table 1. The CPD capture and Main Belt implantation efficiencies are expressed as a percentage of the total number of objects initially located at the outer edge of Jupiter's gap. In all the cases investigated, we find that approximately one order of magnitude more objects end up captured within the CPD rather than being implanted in the Main Belt. We also note that some planetesimals directly collide with Jupiter in our simulations and would be subsequently ablated in its envelope, in proportions similar to that of the captured objects. The higher capture efficiency was obtained for Saturn growing on a 5×10^5 years timescale. In this case, considering that a mass equivalent to that of the Galilean system ($\sim 6 \times 10^{-2}\,M_\oplus$) was captured by Jupiter implies an initial mass of planetesimals of $\sim 0.41\,M_\oplus$ in the reservoir and $\sim 5.3 \times 10^{-3}\,M_\oplus$ of material implanted in the main asteroid belt. Considering the efficiencies obtained from different growth timescales yield very similar results with an initial reservoir mass varying from ~ 0.41 to $0.69\,M_\oplus$ and a mass implanted in the asteroid belt varying from $\sim 5.3 \times 10^{-3}$ to $\sim 9.2 \times 10^{-3}\,M_\oplus$. These values are crude order-of-magnitude estimates as the mass captured within the CPD should be higher than that of the Galilean satellites, unless the accretion was perfectly efficient. The mass implanted in the asteroid belt nevertheless compares well with that estimated in the Grand Tack scenario of Walsh et al. (2011). These authors find a final asteroid belt containing $\sim 4 \times 10^{-3}\,M_\oplus$ of planetesimals originating from beyond Jupiter's orbit.

3.2. Case 2: Migration of Saturn Toward Jupiter

Another plausible scenario is that Saturn formed further from Jupiter and migrated inward rapidly (before possibly opening its own gap), thereby catching up with Jupiter until the giants were caught in a mean motion resonance (MMR). Contrary to Case 1, this scenario does not constrain a precise location for the formation of Saturn. The formation of Saturn in the more distant regions of the disk could be the mere result of the initial distribution of material in the disk and the stochastic nature of accretion (e.g., Levison et al. 2015) or it could be the result of self-organization in the disk when Hall effect is considered. The self-organization results in zonal flows, which naturally

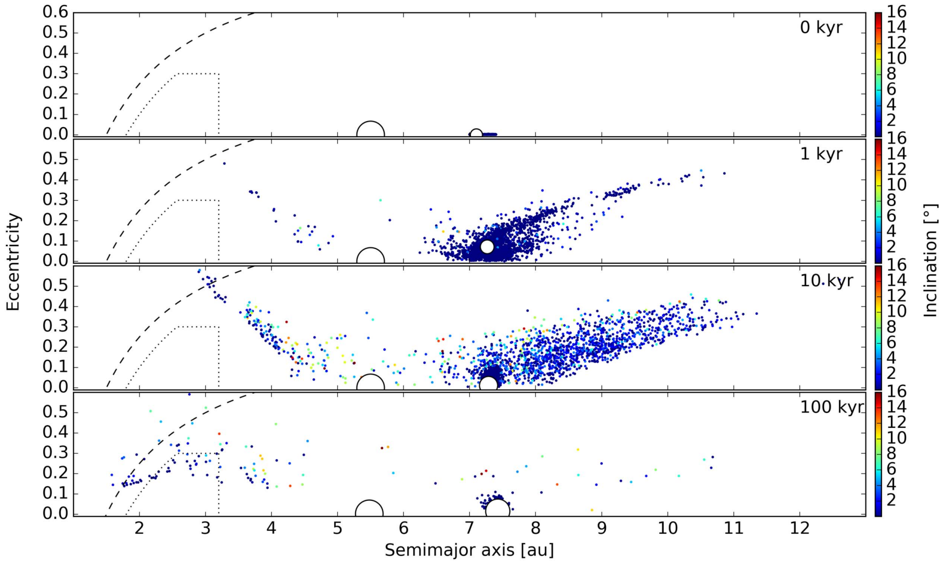

Figure 2. Orbital evolution of the planetesimals with Saturn growing at the outer edge of the gap over a timescale $\tau_{\rm growth} = 5 \times 10^5$ year. The orbits of the planetesimals, initially nearly circular, are excited by the growing planet and scattered both inward and outward. The excitation of the eccentricity of the planetesimals allows their capture within the circum-Jovian disk and injection in the inner Solar System. The dotted box roughly represents the extension of the asteroid belt while the dashed line marks the orbits with $q = 1.5$ au. Planetesimals with a perihelion $q \leqslant 1.5$ au would interact with the embryos of the terrestrial planets and potentially deliver water to them.

Table 1
CPD Capture and Main Belt Implantation Efficiencies for Case 1 Scenario

$\tau_{\rm growth}$ (year)	Capture	Implantation
1×10^5	8.7%	0.9%
5×10^5	14.8%	1.3%
1×10^6	11.8%	1.8%

creates axisymmetric dust traps at different radial distances whose number and locations depends on the magnetic flux and intensity of the Hall effect (Béthune et al. 2016).

To investigate such a scenario, we conducted simulations where Saturn started at 12 au and then migrated on different timescales toward Jupiter. We considered a fully formed Saturn to highlight the effect of the migration timescale on the final distribution of planetesimals. We mimicked the migration of Saturn by applying a fictitious force acting on a timescale $\tau_{\rm mig}$, which yields the following acceleration term (e.g., Cresswell & Nelson 2008):

$$\boldsymbol{a}_{\rm mig} = -\frac{\boldsymbol{v}}{\tau_{\rm mig}}. \tag{2}$$

For the sake of simplicity, we turned off the force when Saturn is caught in the 2:1 MMR with Jupiter to avoid unphysical crossing of the resonance. Whether Jupiter and Saturn end up in their mutual 2:1 or 3:2 MMR is nevertheless not critical for the delivery of planetesimals, as shown below. Also, given the many uncertainties in the formation history of the giant planets and considering our very simplified model, we do not aim here at exploring the full range of possible parameters.

Figure 3 shows snapshots of the evolution of the system with Saturn migrating on a timescale $\tau_{\rm mig} = 10^5$ years. The sweeping of the reservoir of planetesimals by the 2:1 and 3:2 MMRs with Saturn excites the planetesimals' orbits and allows their delivery to the Jovian CPD and the inner Solar System. The vast majority of planetesimals have been redistributed after the passage of the 3:2 MMR with Saturn across the reservoir.

The percentage of objects captured within the CPD and implanted in the main asteroid belt at the end of the simulations for different migration timescales of Saturn are summarized in Table 2. The capture efficiencies differ from case to case due to the fact that the excitation of the eccentricity of the planetesimals in MMR with Saturn depends on the velocity of the giant planet. In the case where Saturn migrates on a 5×10^5 years timescale, the planetesimals are efficiently captured in the 2:1 MMR and reach very high eccentricities.

In the other cases, the planetesimals are only excited by the 2:1 MMR, they are not captured, and reach lower eccentricities. Therefore, more objects with lower eccentricities remain when the 3:2 MMR with Saturn sweeps the reservoir and this yields slightly higher capture efficiencies. Nevertheless, the differences are not dramatic. The percentage of captured objects varies from ~14.4% in the most favorable case down to ~9% for the slow migration case, assessing the robustness of the mechanism against the range of plausible migration rates of Saturn. The implantation of objects in the Main Belt is also comparable for each investigated migration rate with efficiencies that are more than one order of magnitude lower than the CPD capture efficiencies. Similarly to the Case 1 scenario, we find that a number of objects equivalent to that of the captured planetesimals directly collide with Jupiter.

We find that a migration rate $\tau_{\rm mig} = 10^5$ years yields the highest capture efficiency within the circum-Jovian disk with ~14.4% of planetesimals from the reservoir captured. Considering the captured objects represent the mass of the Galilean system (~$6 \times 10^{-2}\,M_\oplus$), the initial reservoir should have had a mass of ~$0.42\,M_\oplus$ and the mass implanted in the asteroid belt would be ~$1.7 \times 10^{-3}\,M_\oplus$. With the different efficiencies derived, we find that the intial mass of the reservoir would vary from ~0.42 to 0.67 $M_\oplus$ and the mass implanted in the asteroid belt from ~1.7×10^{-3} to 3.3×10^{-3} $M_\oplus$. These results are

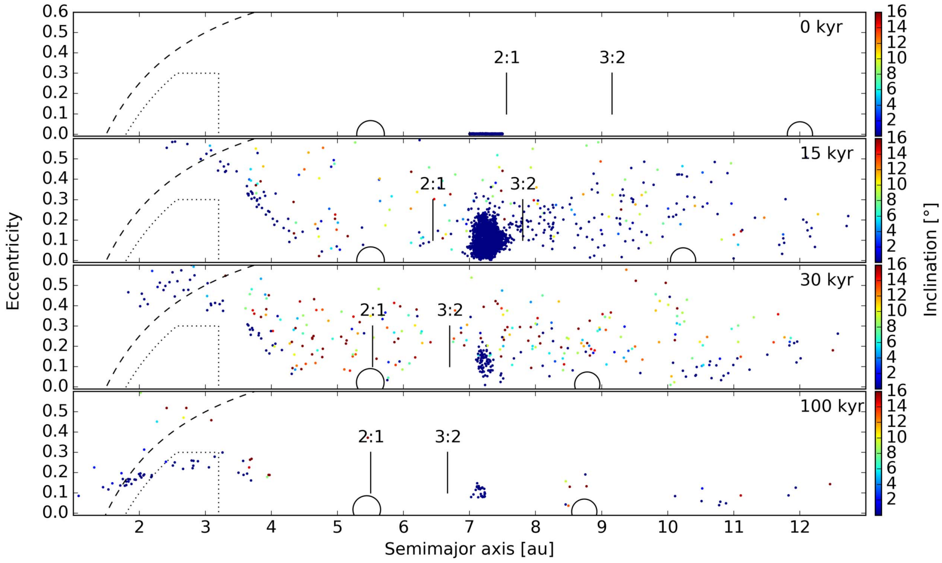

Figure 3. Orbital evolution of planetesimals with Saturn migrating toward Jupiter over a timescale $\tau_{\rm mig} = 10^5$ years. The small vertical lines, labeled 2:1 and 3:2, show the positions of the corresponding MMRs with Saturn. The dashed line and the dotted box are equivalent to those of Figure 2. The planetesimals are excited when the reservoir is swept out by the 2:1 and 3:2 MMRs with Saturn after 15 and 30 kyr, respectively.

Table 2
CPD Capture and Main Belt Implantation Efficiencies for Case 2 Scenario

$\tau_{\rm mig}$ (year)	Capture	Implantation
5×10^4	12.9%	0.6%
1×10^5	14.4%	0.4%
5×10^5	9.0%	0.5%

very similar to those obtained in the Case 1 scenario with the notable difference that the implantation of objects in the asteroid belt is less efficient.

4. Evolution of Captured Planetesimals

We now investigate the evolution of the planetesimals captured in orbits around Jupiter. For all cases considered, the planetesimals captured within the CPD have initially very eccentric and inclined orbits at large distances from Jupiter. Slightly less than one-half of the objects captured are actually found in retrograde orbits. Figure 4 shows that the distributions of orbital parameters of the objects at the time of their capture are quite similar in the most favorable scenarios of cases 1 and 2. Similar trends were obtained by Suetsugu & Ohtsuki (2017) although they considered that planetesimals initially populate the close vicinity of Jupiter (i.e., the region inside of Jupiter's gap in our configuration) and no other massive object but Jupiter perturbed their orbits. It should be noted that the distribution of objects in Figure 4 is not representative of the system at a particular time because the planetesimals were not all captured concurrently. The delivery of planetesimals actually spans $\sim 10^4$–10^5 years depending on the adopted parameters (see Figure 5).

To illustrate the subsequent evolution of the captured planetesimals, we conducted simulations centered on Jupiter as the only massive object and integrated the orbits of the planetesimals within the CPD for the most favorable scenario of Case 1. The simulation started at the time of capture of the

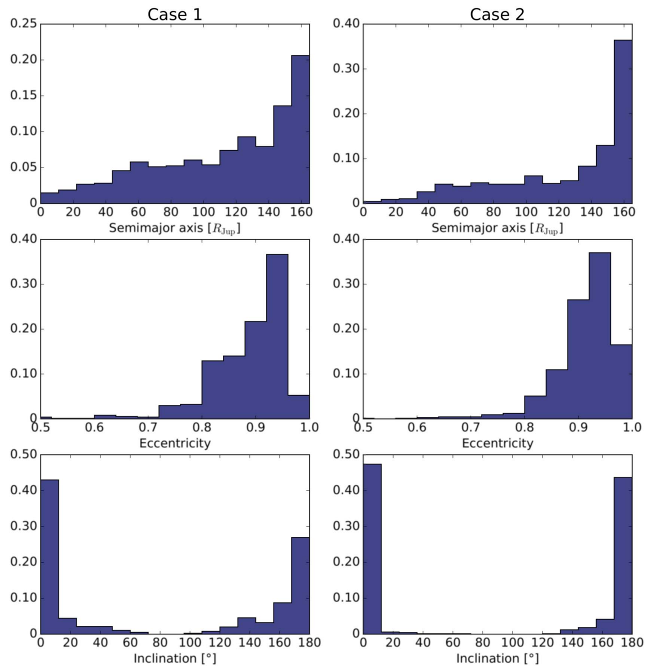

Figure 4. Comparison of the orbital parameters of the captured objects in Case 1 with $\tau_{\rm growth} = 5 \times 10^5$ years (left) and in Case 2 with $\tau_{\rm mig} = 10^5$ years (right). The histograms are normalized according to the total number of captured objects. Both cases exhibit very similar trends with planetesimals initially captured on large, very eccentric, and inclined orbits.

first planetesimal and objects were subsequently added at their corresponding capture time as the simulation evolves. We also assumed a slightly sub-Keplerian velocity of the gas around Jupiter ($v_{\rm orb} = (1 - \eta)\ v_{\rm kep}$, where η is a measure of the pressure support of the disk and we used $\eta = 0.005$, typical for Keplerian disks, Johansen et al. 2014) to account for the potential loss of objects through inward drift due to gas drag. Figure 6 shows the distribution of the planetesimals as a function of their distance from Jupiter at different epochs of the CPD's evolution. Objects that are captured on initially

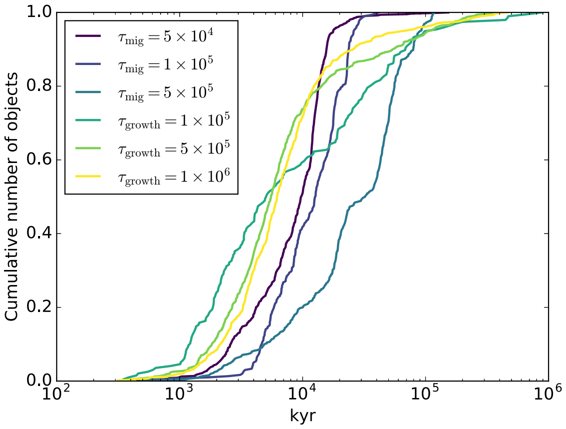

Figure 5. Time evolution of the cumulative number of objects captured within Jupiter's CPD in Case 1 (formation of Saturn at the gap) and in Case 2 (migration of Saturn toward Jupiter) for different parameters investigated. In each scenario, the delivery of planetesimals to the circum-Jovian disk spans a few 10^5 years.

retrograde orbits are rapidly lost to Jupiter due to gas drag. On the other hand, the planetesimals initially captured on prograde orbits with large eccentricities and inclinations rapidly circularize and pile up in the inner part of the CPD (c.f., the histogram drawing the distribution of captured objects after 5 kyr of evolution). The hatched region of Figure 6 illustrates the current extension of the Galilean system with the inner and outer radial boundaries being the position of Io and Callisto, respectively. Interestingly, the region where planetesimals pile up matches well that where the Galilean satellites orbit.

After having rapidly reached a maximum at $\sim$5 kyr, the number of objects in the CPD slowly decreases as the planetesimals drift inward due to gas drag faster than the replenishment due to the capture of new objects. The decay is nevertheless slow compared to the orbital period of the objects, which is $\sim$2 days at Io's orbit and $\sim$17 days at Callisto's orbit. The timescale of orbital decay due to gas drag can be estimated as $\tau_{\rm drag} = r\frac{dt}{dr}$ with $\frac{dr}{dt} = \frac{2{\rm St}}{1+{\rm St}^2}\eta v_{\rm kep}$ (e.g., Weidenschilling 1977), with St the Stokes number of the planetesimal (i.e., the stopping time normalized by the Keplerian frequency; see Appendix A for an expression of the stopping time). Considering that St $\gg 1$, relevant for large planetesimals, the decay timescale can be expressed as:

$$\tau_{\rm drag} \sim \frac{1}{2}{\rm St}\frac{T_{\rm orb}}{2\pi\eta} \sim 1.6 \times 10^7 \left(\frac{\rm St}{10^6}\right)\left(\frac{0.005}{\eta}\right) T_{\rm orb}. \tag{3}$$

In the above expression, $T_{\rm orb}$ is the orbital period of the object. On the other hand, Canup & Ward (2002) approximate a satellite's growth timescale as:

$$\tau_{\rm acc} \sim 8 \times 10^6 \left(\frac{\rho_s}{2\ {\rm g\ cm^{-3}}}\right)\left(\frac{R_{\rm sat}}{2500\ {\rm km}}\right)\left(\frac{1\ {\rm g\ cm^{-2}}}{\Sigma_s}\right)\left(\frac{10}{F_g}\right) T_{\rm orb}. \tag{4}$$

In the latter expression, ρ_s is the mass density of the satellite, $R_{\rm sat}$ its radius, Σ_s is the surface density of solids within the CPD and $F_g = 1 + (v_{\rm esc}/v_{\rm rel})^2$ is the gravitational focusing factor with $v_{\rm rel}$ the relative velocity between satellitesimals and $v_{\rm esc}$ their mutual escape velocity. Therefore, the collisional growth of the objects should have been efficient provided that

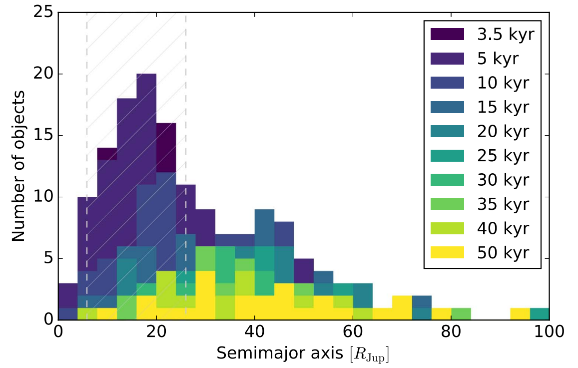

Figure 6. Distribution of planetesimals at different epochs in Case 1 with $\tau_{\rm growth} = 5 \times 10^5$ years. Each bin is 4 $R_{\rm Jup}$ wide. The hatched region indicates the present day extension of the Galilean system, with the inner and outer edges being the radial positions of Io ($\sim$5.9 $R_{\rm Jup}$) and Callisto ($\sim$26 $R_{\rm Jup}$).

the surface density of solids was at least of the order of $1\ {\rm g\ cm^{-2}}$, which is a rather low value appropriate for starved-disk formation models.

5. Discussion

5.1. Implantation of Planetesimals in the Asteroid Belt

In Section 3, we have shown that, for both the formation of Saturn at the outer edge of Jupiter's gap and at further distances, planetesimals from the reservoir are redistributed across the inner Solar System. Recently Raymond & Izidoro (2017) proposed that the redistribution of planetesimals by the gas giants is a natural outcome of their formation, providing an explanation for the delivery of water to the terrestrial planets and the presence of primitive C-type asteroids in the outer asteroid belt. The authors demonstrated that some planetesimals were always scattered inward of Jupiter's orbit regardless of the precise growth timescale or migration rates of Jupiter and Saturn in their simulations. However, the planetesimals were initially spread between 2 and 20 au in their simulations, which is quite different from the distribution we consider in this work. Our results therefore support the findings of Raymond & Izidoro (2017), showing them to be robust against more specific initial conditions and accounting for the fact that objects might be captured by Jupiter instead of being scattered inward of its orbit.

Figure 7 represents the trajectories of planetesimals in the semimajor axis-eccentricity plane in the 1.2–4.0 au region, along with important MMRs with Jupiter and the different regions of the main asteroid belt (inner, middle, and outer belt). Our simulations show that planetesimals are not preferentially implanted in the outer region of the Main Belt, where the majority of C-type asteroids are found today. This result should nevertheless be considered with caution for several reasons. First, planetary embryos were not included in our simulations. The planetesimals ending up in the inner parts of the asteroid belt have trajectories that cross the embryos' region, marked by the dashed line in Figure 7. The final distribution of objects in the inner belt might be inaccurate due to the fact that the influence of embryos was not accounted for in this work. Second, the C-type spectral group embraces a great diversity of objects with potentially very different origins or formation times (e.g., Vernazza et al. 2017). If the diversity among C-type asteroids indeed traces different origins, it is likely that the different populations were not implanted at the same time or

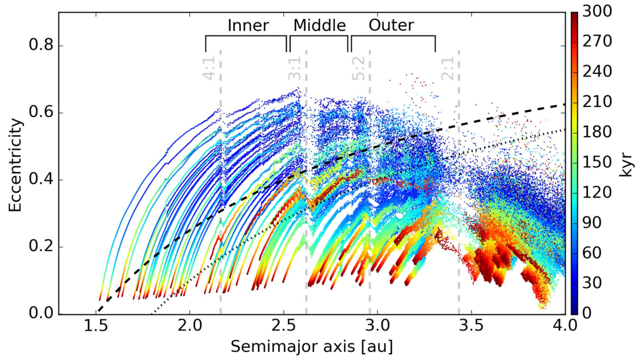

Figure 7. Trajectories of planetesimals in the semimajor axis-eccentricity plane of the asteroid belt region. The colors of the dots give an indication of the time. The dotted and dashed lines mark the limit where the periapsis of the orbit is $q = 1.8$ au (roughly the edge of the asteroid belt) and $q = 1.5$ au (region of the terrestrial planets' embryos), respectively. The positions of major mean motion resonances with Jupiter are represented by the vertical dashed lines. These are the resonances that define today's asteroid belt regions, labeled Inner, Middle, and Outer in the figure. The different regions are shifted inward as compared to the position of the MMRs because Jupiter is orbiting at ~5.4 au at the end of the simulation, consistently with models of later dynamical evolution of the outer Solar System.

that some C-type asteroids have formed in situ so that not all of the objects from this group were actually implanted in the belt. Finally, we have not implemented the decay of the gas density due to the viscous evolution of the PPD and/or the photoevaporation of the disk. As the density decays, the damping due to gas drag is less efficient and planetesimals can reach more distant regions in the inner solar system (Raymond & Izidoro 2017). As we used a constant surface density, the planetesimals were implanted quite homogeneously from 1.5 to 3.5 au in our simulations.

Instead of reasoning in terms of spectral types, Kruijer et al. (2017) proposed that the observed dichotomy in the isotopic ratios of carbonaceous and non-carbonaceous meteorites is due to the separation of the formation regions of the parent bodies of these meteorites by Jupiter's core. This way, the two reservoirs of objects could not mix and their isotopic differences were preserved. The authors were able to put new constraints on the formation timescales of the carbonaceous chondrites that would have formed beyond Jupiter's orbit. They showed that the formation of the parent bodies of the carbonaceous meteorites started ~1 My after the condensation of the CAIs (Carbon and Aluminium rich Inclusions) and ended ~4 My after CAIs, implying that the reservoir of carbonaceous material has been separated from that of non-carbonaceous material for ~3 My. These constraints can be matched in the framework of our scenario, suggesting that the formation of the parent bodies of carbonaceous chondrites was triggered by the end of the accretion of solid material onto Jupiter's core. From this moment, solids (in the form of pebbles) accumulated at the pressure perturbation induced by the forming planet and eventually collapsed into larger objects. Their injection in the inner solar system was then triggered by either the formation of Saturn's core or its migration in the vicinity of Jupiter. This would naturally account for the delay between the formation of the carbonaceous meteorites parent bodies and their mixing with the non-carbonaceous meteorites parent bodies, which formed and remained inside of Jupiter's orbit and were not included in our simulations.

5.2. *Accretion of the Galilean Satellites*

In Section 6, we have shown that the planetesimals rapidly pile up in the region where the Galilean satellites are found today. This could provide suitable conditions for the rapid formation of satellite seeds in this region. The satellites would then fully accrete on longer timescales (~10^5 years, Figure 5), limited by the capture of new objects by Jupiter and the slow orbital decay of the planetesimals that have been circularized on wider orbits. Such a scenario would be consistent with a partially differentiated Callisto (Barr & Canup 2008).

In a previous study, Ronnet et al. (2017) have shown that the compositional gradient among the Galilean satellites could be accounted for if they accreted from pebbles with sizes in the range of 1–10^2 cm. This scenario, however, implies that the pebbles do not disintegrate as their water ice starts to sublimate when crossing the snowline and the migration of Europa was tied to the evolution of the snowline. In the present study, we used objects with a radius of 100 km as typical planetesimals, a choice motivated by the existence of such large primitive objects in the asteroid belt, pointing toward the existence of a planetesimal reservoir outside of Jupiter's orbit. At first sight, this seems contradictory with the pebble accretion scenario proposed by Ronnet et al. (2017). However the planetesimals captured within the CPD being initially on very excited, both prograde and retrogade orbits, violent impacts could have led to an intense grinding of the planetesimals. It is therefore plausible that a non-negligible amount of material was found in objects with a size in the meter range and below and were subsequently efficiently accreted by the larger objects that did not suffer disruptive collisions. This would also be favorable to the formation of an only partially differentiated Callisto as noted by several authors (e.g., Lunine & Stevenson 1982; Barr & Canup 2008). It should be also noted that, considering the dynamical state of the reservoir, disruptive collisions within the reservoir might have provided an important source of dust grains. Shibaike et al. (2017) pointed out in their study the difficulty in growing large objects from dust grains within CPDs, hinting toward the existence of already large objects that would act as the seeds of the protosatellites. The Galilean satellites might well have grown through a combination of planetesimal and pebble accretion.

5.3. *Effect of the Surface Density of the CPD*

Our nominal set of simulations was performed using a CPD with a surface density that is approximately one order of magnitude higher than that of the gas-starved disk proposed by Canup & Ward (2002, 2006), with a peak surface density at ~10^4 g cm^{-2}. Such surface densities are still lower than that adopted in the minimum mass model (surface density peak at ~10^6 g cm^{-2}, Mosqueira & Estrada 2003a, 2003b). The disk profile we used is likely representative of the stage when Jupiter is still feeding from the surrounding nebula (e.g., Fujii et al. 2017). However, as the PPD's density is supposedly decaying and Jupiter's gap deepening over time, the surface density of the CPD would also decay, leading to a less efficient capture of planetesimals through gas drag. Therefore, the capture efficiencies may be lower than those obtained here.

To investigate whether our results are realistic, we ran the Case 1 and Case 2 scenarios with the optimal parameters, namely $\tau_{\rm growth} = 5 \times 10^5$ years for Case 1 and $\tau_{\rm mig} = 10^5$ years for Case 2, with a CPD profile identical to that of

Sasaki et al. (2010) (cf. Appendix B). These authors investigated the growth of the Galilean satellites with a semi-analytical model in the context of a slightly modified starved-disk scenario. In both simulations, the CPD capture efficiencies dropped to $\sim$8%. Such efficiencies are still in the range of values obtained by varying Saturn's growth or migration timescale.

In Section 4, we showed that planetesimals are delivered over an $\sim 10^5$ years timescale. The capture of large planetesimals would therefore remain efficient if the CPD's surface density does not decay significantly during this timescale (i.e., Jupiter is still accreting gas from the PPD and/or the viscous evolution of the CPD is slow). A more subtle effect that has been ignored in the present study is that planetesimals with different sizes would have different capture efficiencies due to a more or less efficient gas drag braking within the circum-Jovian disk. The evolution of the CPD's surface density would likely result in an evolution of the size distribution of captured objects, which could affect the subsequent growth of the satellites. More detailed studies, including plausible planetesimals size distributions at the outer edge of Jupiter's gap and evolution of the circum-Jovian disk, are needed to determine more realistic conditions of accretion of the Galilean satellites.

5.4. Influence of Saturn's Growth Track

Although we varied Saturn's growth timescale by an order of magnitude when investigating the dynamical evolution of planetesimals in Section 3.1, the use of Equation (1) always implies that the mass doubling timescale of the planet is shorter in the early phases of its growth. As demonstrated by Shiraishi & Ida (2008), a growing planet generally experiences more close encounters with nearby planetesimals if its mass doubling timescale is shorter because the expansion of its Hill sphere is then fast compared to the gap opening timescale in the planetesimals' disk. If the growth of Saturn was initially slow enough, the protoplanet might have carved a gap in the planetesimal's distribution, which would have prevented an efficient scattering and delivery of the planetesimals toward Jupiter. Hence, the use of Equation (1) might overestimate the ability of Saturn's core to scatter nearby planetesimals in the early phases of its growth. We note, however, that if Saturn's core had grown through pebble accretion, its mass doubling timescale would have indeed been shorter in the early phases of its growth (due to the sublinear dependance of the pebbles' accretion rate on the mass of the core, Lambrechts & Johansen 2012) and certainly shorter than the gap opening timescale in the planetesimals' disk.

To assess the robustness of the redistribution of planetesimals against Saturn's growth track, we ran an additional simulation with a qualitatively different growth rate for Saturn. In this simulation, we let Saturn grow according to $M_{\rm sat}/\dot{M}_{\rm sat} = 10^6$ years, which yields a very slow initial growth (the mass of the protoplanet is $\sim 2\,M_\oplus$ after $\sim 5 \times 10^5$ years) and a rapid final assemblage of the planet. The capture efficiency within the CPD obtained was $\sim$11%, which compares well with the results obtained using Equation (1). This is due to the fact that the opening of a gap within the planetesimals' disk by the growing core is prevented by nearby Jupiter, which stirs the orbits of the objects in the reservoir, maintaining high eccentricities. It is therefore the combined influence of Jupiter and growing Saturn, and not uniquely Saturn's growth, that allows for an efficient redistribution of the planetesimals. The precise growth of Saturn hence has little effect on its ability to scatter nearby planetesimals. We note that an effect that might damp the eccentricities of the planetesimals and was not included in our simulations is collisions among the objects. Taking collisions into account would, however, require the assumption of an initial mass of the reservoir, considered as unknown in the present study. We leave such a different approach to the problem, and the investigation of the effects of collisions, to future work.

5.5. Formation of Saturn's Satellite System

Saturn possesses a unique assemblage of regular satellites with a possible dual origin. The small satellites orbiting close to Saturn are thought to have formed from the spreading of ring material across the Roche radius while Titan and Iapetus could have formed via a mechanism similar to those invoked for the formation of the Galilean satellites (Charnoz et al. 2010; Crida & Charnoz 2012; Salmon & Canup 2017). When the two gas giants were close together within the PPD (in their mutual 2:1 or 3:2 MMR), they would have opened a unique and large gap in the disk (Morbidelli & Crida 2007; Pierens et al. 2014). The solids would then be trapped outside of Saturn's orbit, at the outer edge of the common gap opened by Jupiter and Saturn. If enough material remained in the form of pebbles at this time in the PPD, a new reservoir of planetesimals could have built up there. Either the formation of the cores of Uranus and Neptune at the gap or their migration toward Saturn could have allowed the delivery of planetesimals from this new reservoir to Saturn's CPD to build Titan and Iapetus.

5.6. Implications for the Formation of Extrasolar Moons

In this study, we have pointed out that the gap opened by a giant planet in a PPD efficiently isolates it from the main sources of solid material. In our proposed scenario, the delivery of solids to the giant planet's CPD results from the interaction of a massive object with a reservoir of planetesimals. From this perspective, it is to be expected that the formation of massive moons is not ubiquitous, especially in systems with single or isolated giant planets. Moreover, if a giant planet is orbiting close to its host star, its Hill sphere is reduced and the capture rate of planetesimals could be lowered due to larger orbital velocities, therefore acting against the formation of a massive satellite system.

6. Summary

An important step in understanding the formation of the giant planet's satellite systems is to elucidate the origin and delivery mechanism of the solid material needed to build the moons. Here we attempted to revisit the origin and delivery of the building blocks of the Galilean satellites, based on our current understanding of giant planet formation. Our findings can be summarized as follows:

1. Based on studies by Suetsugu & Ohtsuki (2017), Paardekooper (2007), and Zhu et al. (2012), we concluded that the gap opened by Jupiter efficiently isolated the giant planet and its CPD from sources of solid material such as pebbles or planetesimals. However, the accumulation of solids at the outer edge of the gap likely translated into a planetesimal reservoir there.

2. The planetesimals' orbits were then excited by the formation of Saturn at Jupiter's gap or during its migration toward Jupiter.
3. This triggered the redistribution of planetesimals from the reservoir to the circum-Jovian disk and the inner Solar System, with a moderate dependency on the input parameters of our model such as the growth timescale of Saturn or its migration rate. Therefore, we find there exists a link between primitive asteroids of the Main Belt and the Galilean satellites, as they shared a common reservoir. This link could be a testable constraint of our scenario by future missions to the Jovian system, such as the ESA Juice mission, as some isotopic correspondences (e.g., the D/H ratio in water) should exist between the satellites and the asteroids.
4. We find that the planetesimals are initially captured on very eccentric, both prograde and retrograde, orbits within the circum-Jovian disk. The subsequent gas drag damping of the orbits results in an accumulation of objects in the region where the Galilean satellites are found today.
5. The decisive role of Saturn in the delivery of material to the Jovian disk has severe implications for the occurence of massive moons around extrasolar giant planets. If our proposed scenario is correct, massive satellites would preferentially form around giant planets in multiple planet systems.

Finally, it appears difficult to disentangle the formation of Saturn at the outer edge of the gap opened by Jupiter from its formation further from Jupiter and subsequent migration considering only the implications for the formation of the Galilean moons. Both scenarios provide quite similar results, although we believe that our so-called Case 1 scenario provides a more consistent model for Saturn's formation. Additional constraints should come from more detailed studies of Saturn's growth and the implications of the different formation scenarios on its final composition. In the present study, we left aside some important issues such as the size distribution of planetesimals, the evolution of the circum-Jovian disk, or the accretion of the satellites. More detailed simulations are needed to assess realistic conditions for the accretion of Jupiter's massive moons.

The authors thank the anonymous referee for their comments that helped reinforce the present study. This work has been partly carried out thanks to the support of the A*MIDEX project (n° ANR-11-IDEX-0001-02) funded by the "Investissements d'Avenir" French Government program, managed by the French National Research Agency (ANR). O.M. acknowledges support from CNES. J.I.L. acknowledges support from the Juno project.

Appendix A
Additional Forces for Planets and Planetesimals

Here we describe the effects of aerodynamic drag and eccentricity/semimajor axis damping that were included in our simulations. Following Cresswell & Nelson (2008), we included the effects of eccentricity and semimajor axis damping of the planets due to interactions with the gas disk through the following acceleration term:

$$\boldsymbol{a}_{\rm mig} = -\frac{\boldsymbol{v}}{\tau_{\rm mig}}, \tag{5}$$

$$\boldsymbol{a}_{\rm e} = -2\frac{(\boldsymbol{v}\cdot\boldsymbol{r})\boldsymbol{r}}{r^2\tau_{\rm e}}. \tag{6}$$

In the above expressions, $\boldsymbol{v}$ is the velocity vector of the planet, $\boldsymbol{r}$ its position vector and r the distance to the star. In the case of Saturn, the eccentricity damping timescale $\tau_{\rm e}$ was taken to be $0.01\ \tau_{\rm mig}$ (e.g., Lee & Peale 2002). As we did not consider any radial migration of Jupiter, we always used an eccentricity damping timescale of $\tau_{\rm e} = 5\times10^3$ years and no semimajor axis damping for this planet. These are simplified prescriptions that do not take into account the structure of the disk. However the purpose of this study is not to investigate the precise migration of the giant planets within the disk.

We accounted for the aerodynamic drag effects on the planetesimals. This was implemented in a similar fashion as in Ronnet et al. (2017) by adding the following acceleration term:

$$\boldsymbol{a}_{\rm drag} = -\frac{1}{t_s}(\boldsymbol{v} - \boldsymbol{v}_g). \tag{7}$$

In the above expression, $\boldsymbol{v}_g$ is the velocity of the gas given by the hydrodynamic simulation when planetesimals are far from Jupiter. When planetesimals are at a distance of 150 $R_{\rm Jup}$ from Jupiter or closer, the gas velocity is found assuming a Keplerian velocity around the giant planet to model the interaction with the CPD. The stopping time t_s, is computed using the following expression (Perets & Murray-Clay 2011; Guillot et al. 2014):

$$t_s = \left(\frac{\rho_g v_{\rm th}}{\rho_s R_s}\min\left[1, \frac{3}{8}\frac{v_{\rm rel}}{v_{\rm th}}C_D(Re)\right]\right)^{-1}. \tag{8}$$

In this expression, R_s is the size of the planetesimal and $\rho_s = 1\ {\rm g\ cm^{-3}}$ its density. The gas density ρ_g is obtained by assuming hydrostatic equilibrium in the vertical direction with an aspect ratio of the disk $h = 0.05$ in the case of the PPD or it is given by the CPD prescription described in Appendix B when planetesimals are close to Jupiter. The gas thermal velocity is $v_{\rm th} = \sqrt{8/\pi}\,c_g$, c_g is the isothermal sound speed and $v_{\rm rel}$ is the relative velocity between the gas and the planetesimal, either in the CPD or the PPD. The dimensionless drag coefficient C_D is computed as a function of the Reynolds number Re of the flow around the planetesimal (Perets & Murray-Clay 2011):

$$C_D = \frac{24}{Re}(1 + 0.27Re)^{0.43} + 0.47(1 - e^{-0.04Re^{0.38}}), \tag{9}$$

$$Re = \frac{4R_s v_{\rm rel}}{c_g l_g}. \tag{10}$$

The mean free path of the gas l_g is taken from the prescription of Supulver & Lin (2000).

Appendix B
The CPD Model

Our model is based on the simple prescription of Sasaki et al. (2010), which was constructed from the gas-starved model of

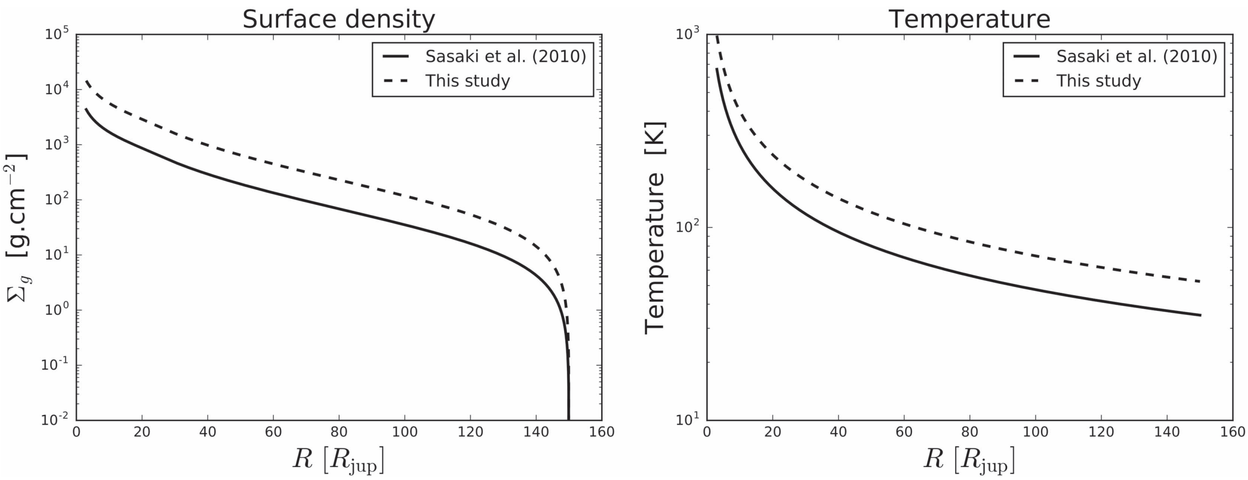

Figure 8. Left. Comparison between the surface density profile used by Sasaki et al. (2010) (solid line) obtained with $\dot{M}_p = 2 \times 10^{-7}\,M_{\rm Jup}\ \ {\rm yr}^{-1}$ and the profile used in this study (dashed line) obtained with $\dot{M}_p = 1 \times 10^{-6}\,M_{\rm Jup}\ \ {\rm yr}^{-1}$. Right. Comparison between the temperature profiles assumed in this study (dashed line) and that assumed by Sasaki et al. (2010).

Canup & Ward (2002). The surface density of the disk is found by considering an equilibrium between the mass accreted from the PPD to the CPD and the mass accretion rate onto Jupiter $\dot{M}_p$. The gas accreted from the PPD is considered to fall uniformly from the inner edge of the disk out to the centrifugal radius R_c, which is set at 26 $R_{\rm Jup}$. This gives the following expression for the surface density of the CPD (e.g., Canup & Ward 2002):

$$\Sigma_g(r) = \frac{\dot{M}_p}{3\pi\nu(r)}\begin{cases} 1 - \dfrac{4}{5}\sqrt{\dfrac{R_c}{R_d}} - \dfrac{1}{5}\left(\dfrac{r}{R_c}\right)^2 & \text{for } r \leqslant R_c \\ \dfrac{4}{5}\sqrt{\dfrac{R_c}{r}} - \dfrac{4}{5}\sqrt{\dfrac{R_c}{R_d}} & \text{for } r > R_c. \end{cases} \quad (11)$$

Here, $R_d = 150\ \ R_{\rm Jup}$ is the outer radius of the disk and ν is the turbulent viscosity parameterized with the α equivalent turbulence $\nu = \alpha H_g^2 \Omega_K$ (Shakura & Sunyaev 1973) and $\alpha = 10^{-3}$, where $H_g = c_s/\Omega_K$ is the disk scale height, $c_s = \sqrt{R_g T_d/\mu}$ is the gas isothermal sound speed with R_g the ideal gas constant, $\mu = 2.4$ g mol^{-1} the molecular weight of the gas, T_d the temperature of the disk, and Ω_K the Keplerian frequency. The temperature profile of the disk is given by a balance between viscous dissipation and energy radiated away. Using the simplifications introduced by Sasaki et al. (2010), the temperature profile can be expressed as a function of the mass accretion rate:

$$T_d \simeq 225\left(\frac{r}{10\ R_{\rm Jup}}\right)^{-3/4}\left(\frac{\dot{M}_p}{10^{-7}\ M_{\rm Jup}\ {\rm yr}^{-1}}\right)^{1/4}\ {\rm K}. \quad (12)$$

More details can be found in the work by Sasaki et al. (2010) (see also, Ronnet et al. 2017). Both the surface density and the temperature are therefore determined by the mass accretion rate onto Jupiter $\dot{M}_p$. The nominal value of the accretion rate at the time of Galilean satellites formation assumed by Sasaki et al. (2010) was $2 \times 10^{-7}\ M_{\rm jup}\ {\rm yr}^{-1}$. In this work, we have assumed a mass accretion rate onto Jupiter $\dot{M}_p = 10^{-6}\,M_{\rm jup}\ {\rm yr}^{-1}$, resulting in a denser and hotter disk. We used this parameter because a denser disk allows a higher capture rate and this is also in line with the results of 3D hydrodynamic simulations where denser disks are found (see, e.g., Tanigawa et al. 2012). The results of hydrodynamic simulations should be considered with caution and could be more representative of the very early phase of the CPD. Nevertheless, Fujii et al. (2017) show that the turbulence of the disk should be weak due to an inefficient ionization of the gas. A lower turbulence results in a denser CPD for a given accretion rate. Therefore, it seems likely that the disk had a surface density slightly higher than that advocated in the starved model of Canup & Ward (2002). Figure 8 shows a comparison between the surface density and temperature profiles we used and those of the study by Sasaki et al. (2010).

Appendix C
Capture of Planetesimals

We present here further details about the capture of planetesimals within the circum-Jovian disk. More detailed investigations on the capture process can be found in the studies by Fujita et al. (2013), Suetsugu et al. (2016), and Suetsugu & Ohtsuki (2017). Gas drag is not efficient enough to allow for the direct capture within the circum-Jovian disk of large planetesimals, such as those investigated in the present study, over a single passage through the CPD. Therefore, planetesimals experience a phase where they are captured on large orbits with respect to the extension of the CPD. During this phase, they cross the circum-Jovian disk multiple times and their orbit gradually shrinks. Because the drag experienced by a planetesimal having a retrograde orbit with respect to Jupiter is much more efficient than that experienced in the case of prograde orbits (due to the lower relative velocity between the gas and the planetesimal in the latter case), planetesimals on retrograde orbits are more rapidly captured inside the CPD. They are however subsequently rapidly lost to Jupiter due to their fast orbital decay (see Section 4). This is illustrated in Figure 9 where the orbits of planetesimals captured in the prograde (left panel) and retrograde (right panel) directions are showed. The orbits of these objects were integrated until they were found on bound orbits with a semimajor axis with respect to Jupiter that is smaller than 0.1 $R_{\rm Hill}$. The orbits were

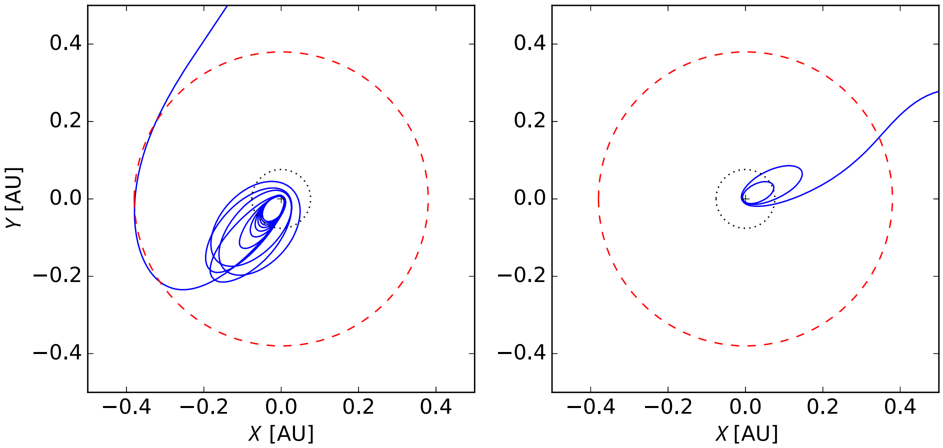

Figure 9. Orbits of captured planetesimals in a cartesian plane centered on Jupiter. The dashed red circle is Jupiter's Hill sphere whereas the dotted black circle shows the extension of the CPD. Left: Orbit of a planetesimal captured in the prograde direction with respect to Jupiter. Right: Orbit of a planetesimal captured in the retrograde direction.

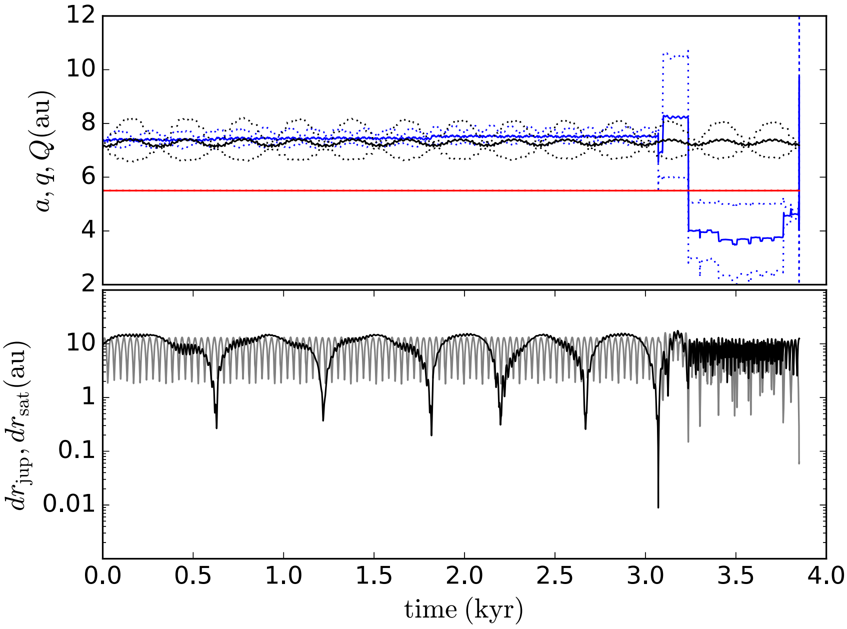

Figure 10. Top: Evolution of the semimajor axis (a), perihelion distance (q), and aphelion distance (Q) of Jupiter (red), Saturn's core (black), and a planetesimal (blue) finally captured by Jupiter. Bottom: Evolution of the radial distance of the planetesimal relative to Jupiter (gray) and Saturn (black).

taken from a Case 1 simulation with Saturn growing on a 5.5×10^5 year timescale. The planetesimal captured in the prograde direction clearly experienced many more CPD-crossing orbits before reaching our capture threshold than its sibling captured on a retrograde orbit. We note that the capture of large planetesimals, although dependent on their initial energy, generally requires that the object approach Jupiter at a distance $\lesssim 10^{-2}\ R_{\rm Hill}$ for the CPD's parameters adopted here. To test the sensitivity of the capture efficiencies presented in the main text on the capture threshold imposed, we ran a full Case 1 simulation with a 0.1 $R_{\rm Hill}$ capture threshold. We obtained a capture efficiency of 14.6%, in very good agreement with the results obtained using the less restrictive threshold presented in Section 3.1.

Figure 10 shows an exemple of the heliocentric orbital evolution of a planetesimal before it is captured within the Jovian CPD. The top panel shows the evolution of the semimajor axis (solid lines), perihelion, and aphelion distances (dotted lines) of Jupiter (red), Saturn's core (black), and the planetesimal (blue). The bottom panel shows the corresponding evolution of the radial distance of the planetesimal relative to Jupiter (gray line) and Saturn's core (black line). Initially, the semimajor axis and the eccentricity of both Saturn's core and the planetesimal oscillate due to their proximity with the outer 3:2 MMR with Jupiter located at ∼7.2 au. The planetesimal experiences a close encounter with Saturn's core after ∼3.05 kyr, which can be identified in the bottom panel of Figure 10. This interaction yields an abrupt change of the semimajor axis of the planetesimal, from ∼7.5 to ∼6.9 au, and an increase of the eccentricity, originally varying around a value of ∼0.03, up to a value of ∼0.13. This event triggers a more chaotic evolution of the planetesimal, which interacts with Jupiter several times, further increasing its eccentricity to values close to 0.4 after it is scattered inward of Jupiter's orbit at 3.24 kyr. Interestingly, the planetesimal experiences two encounters with Jupiter soon before it is captured, at 3.76 and 3.81 kyr, both bringing its semimajor axis closer to that of Jupiter and reducing its eccentricity down to a value of ∼0.04. Due to the chaotic evolution of the planetesimals before their capture, a typical evolution is not easy to define but we find that captured planetesimals generally experience a close encounter with Saturn's core, triggering a chaotic phase of evolution during which their eccentricity is high and they interact several times with Jupiter. We find that the eccentricity of a planetesimal is often reduced following a close encounter with Jupiter right before the object is captured and is generally $\lesssim$0.2 then.

References

Barr, A. C., & Canup, R. M. 2008, Icar, 198, 163
Béthune, W., Lesur, G., & Ferreira, J. 2016, A&A, 589, A87
Birnstiel, T., Klahr, H., & Ercolano, B. 2012, A&A, 539, A148
Birnstiel, T., Ormel, C. W., & Dullemond, C. P. 2011, A&A, 525, A11
Bitsch, B., Johansen, A., Lambrechts, M., & Morbidelli, A. 2015a, A&A, 575, A28
Bitsch, B., Lambrechts, M., & Johansen, A. 2015b, A&A, 582, A112
Canup, R. M., & Ward, W. R. 2002, AJ, 124, 3404
Canup, R. M., & Ward, W. R. 2006, Natur, 441, 834
Canup, R. M., & Ward, W. R. 2009, in Europa, ed. R. T. Pappalardo, W. B. McKinnon, & K. K. Khurana (Tucson, AZ: Univ. Arizona Press), 59
Carrera, D., Gorti, U., Johansen, A., & Davies, M. B. 2017, ApJ, 839, 16
Charnoz, S., Salmon, J., & Crida, A. 2010, Natur, 465, 752
Coradini, A., Federico, C., Forni, O., & Magni, G. 1995, SGeo, 16, 533
Cresswell, P., & Nelson, R. P. 2008, A&A, 482, 677
Crida, A., & Bitsch, B. 2017, Icar, 285, 145
Crida, A., & Charnoz, S. 2012, Sci, 338, 1196
D'Angelo, G., & Podolak, M. 2015, ApJ, 806, 203
Deienno, R., Morbidelli, A., Gomes, R. S., & Nesvorný, D. 2017, AJ, 153, 153
Deienno, R., Nesvorný, D., Vokrouhlický, D., & Yokoyama, T. 2014, AJ, 148, 25
Dipierro, G., & Laibe, G. 2017, MNRAS, 469, 1932
Dipierro, G., Laibe, G., Price, D. J., & Lodato, G. 2016, MNRAS, 459, L1
Drążkowska, J., Alibert, Y., & Moore, B. 2016, A&A, 594, A105
Estrada, P. R., & Mosqueira, I. 2006, Icar, 181, 486
Estrada, P. R., Mosqueira, I., Lissauer, J. J., D'Angelo, G., & Cruikshank, D. P. 2009, in Europa, ed. R. T. Pappalardo, W. B. McKinnon, & K. K. Khurana (Tucson, AZ: Univ. Arizona Press), 27
Fujii, Y. I., Kobayashi, H., Takahashi, S. Z., & Gressel, O. 2017, AJ, 153, 194
Fujita, T., Ohtsuki, K., Tanigawa, T., & Suetsugu, R. 2013, AJ, 146, 140
Gomes, R., Levison, H. F., Tsiganis, K., & Morbidelli, A. 2005, Natur, 435, 466
Gonzalez, J.-F., Laibe, G., Maddison, S. T., Pinte, C., & Ménard, F. 2015, P&SS, 116, 48
Guillot, T., Ida, S., & Ormel, C. W. 2014, A&A, 572, A72
Hayashi, C. 1981, PThPS, 70, 35
Heller, R., Williams, D., Kipping, D., et al. 2014, AsBio, 14, 798
Johansen, A., Blum, J., Tanaka, H., et al. 2014, in Protostars and Planets VI, ed. H. Beuther et al. (Tucson, AZ: Univ. Arizona Press), 547
Johansen, A., & Lacerda, P. 2010, MNRAS, 404, 475
Johansen, A., Mac Low, M.-M., Lacerda, P., & Bizzarro, M. 2015, SciA, 1, 1500109
Kobayashi, H., Ormel, C. W., & Ida, S. 2012, ApJ, 756, 70
Krasinsky, G. A., Pitjeva, E. V., Vasilyev, M. V., & Yagudina, E. I. 2002, Icar, 158, 98
Kruijer, T. S., Burkhardt, C., Budde, G., & Kleine, T. 2017, PNAS, 114, 6712
Lambrechts, M., & Johansen, A. 2012, A&A, 544, A32
Lambrechts, M., & Johansen, A. 2014, A&A, 572, A107
Lambrechts, M., Johansen, A., & Morbidelli, A. 2014, A&A, 572, A35
Lee, M. H., & Peale, S. J. 2002, ApJ, 567, 596
Levison, H. F., Bottke, W. F., Gounelle, M., et al. 2009, Natur, 460, 364
Levison, H. F., Kretke, K. A., & Duncan, M. J. 2015, Natur, 524, 322
Levison, H. F., Thommes, E., & Duncan, M. J. 2010, AJ, 139, 1297
Lin, D. N. C., & Papaloizou, J. 1986, ApJ, 309, 846
Lunine, J. I., & Stevenson, D. J. 1982, Icar, 52, 14
Machida, M. N., Kokubo, E., Inutsuka, S.-i., & Matsumoto, T. 2008, ApJ, 685, 1220
Masset, F. 2000, A&AS, 141, 165
Morbidelli, A., & Crida, A. 2007, Icar, 191, 158
Morbidelli, A., Levison, H. F., Tsiganis, K., & Gomes, R. 2005, Natur, 435, 462
Morbidelli, A., Szulágyi, J., Crida, A., et al. 2014, Icar, 232, 266
Morbidelli, A., Walsh, K. J., O'Brien, D. P., Minton, D. A., & Bottke, W. F. 2015, in Asteroids IV, ed. P. Michel, F. DeMeo, & W. F. Bottke (Tucson, AZ: Univ. Arizona Press), 493
Mosqueira, I., & Estrada, P. R. 2003a, Icar, 163, 198
Mosqueira, I., & Estrada, P. R. 2003b, Icar, 163, 232
Mosqueira, I., Estrada, P. R., & Charnoz, S. 2010, Icar, 207, 448
Mousis, O., & Gautier, D. 2004, P&SS, 52, 361
Ormel, C. W., & Klahr, H. H. 2010, A&A, 520, A43
Paardekooper, S.-J. 2007, A&A, 462, 355
Paardekooper, S.-J., & Mellema, G. 2006, A&A, 453, 1129
Peale, S. J., & Canup, R. M. 2015, Treatise on Geophysics (2nd ed.; Oxford: Elsevier)
Perets, H. B., & Murray-Clay, R. A. 2011, ApJ, 733, 56
Pierens, A., Raymond, S. N., Nesvorny, D., & Morbidelli, A. 2014, ApJL, 795, L11
Pollack, J. B., Hubickyj, O., Bodenheimer, P., et al. 1996, Icar, 124, 62
Raymond, S. N., & Izidoro, A. 2017, Icar, 297, 134
Rein, H., & Spiegel, D. S. 2015, MNRAS, 446, 1424
Rein, H., & Tamayo, D. 2015, MNRAS, 452, 376
Ronnet, T., Mousis, O., & Vernazza, P. 2017, ApJ, 845, 92
Salmon, J., & Canup, R. M. 2017, ApJ, 836, 109
Sasaki, T., Stewart, G. R., & Ida, S. 2010, ApJ, 714, 1052
Schoonenberg, D., & Ormel, C. W. 2017, A&A, 602, A21
Shakura, N. I., & Sunyaev, R. A. 1973, A&A, 24, 337
Shibaike, Y., Okuzumi, S., Sasaki, T., & Ida, S. 2017, ApJ, 846, 81
Shiraishi, M., & Ida, S. 2008, ApJ, 684, 1416
Suetsugu, R., & Ohtsuki, K. 2017, ApJ, 839, 66
Suetsugu, R., Ohtsuki, K., & Fujita, T. 2016, AJ, 151, 140
Supulver, K. D., & Lin, D. N. C. 2000, Icar, 146, 525
Szulágyi, J., Morbidelli, A., Crida, A., & Masset, F. 2014, ApJ, 782, 65
Tanigawa, T., Ohtsuki, K., & Machida, M. N. 2012, ApJ, 747, 47
Teachey, A., Kipping, D. M., & Schmitt, A. R. 2017, arXiv:1707.08563
Vernazza, P., Castillo-Rogez, J., Beck, P., et al. 2017, AJ, 153, 72
Vokrouhlický, D., Bottke, W. F., & Nesvorný, D. 2016, AJ, 152, 39
Walsh, K. J., Morbidelli, A., Raymond, S. N., O'Brien, D. P., & Mandell, A. M. 2011, Natur, 475, 206
Weidenschilling, S. J. 1977, MNRAS, 180, 57
Zhu, Z., Nelson, R. P., Dong, R., Espaillat, C., & Hartmann, L. 2012, ApJ, 755, 6

The Astrophysical Journal, 858:66 (5pp), 2018 May 1 https://doi.org/10.3847/1538-4357/aab6b9

Synthesis of Molecular Oxygen via Irradiation of Ice Grains in the Protosolar Nebula

O. Mousis[1], T. Ronnet[1], J. I. Lunine[2], R. Maggiolo[3], P. Wurz[4], G. Danger[5], and A. Bouquet[6]
[1] Aix Marseille Univ, CNRS, CNES, LAM, Marseille, France; olivier.mousis@lam.fr
[2] Department of Astronomy, Cornell University, Ithaca, NY 14853, USA
[3] Royal Belgian Institute for Space Aeronomy, BIRA-IASB, Ringlaan 3, B-1180 Brussels, Belgium
[4] Physikalisches Institut, University of Bern, Sidlerstrasse 5, CH-3012 Bern, Switzerland
[5] Aix-Marseille Université, PIIM UMR-CNRS 7345, F-13397 Marseille, France
[6] Department of Space Research, Southwest Research Institute, 6220 Culebra Rd., San Antonio, TX 78228, USA
Received 2017 December 18; revised 2018 March 9; accepted 2018 March 12; published 2018 May 4

Abstract

Molecular oxygen has been detected in the coma of comet 67P/Churyumov–Gerasimenko with a mean abundance of 3.80 ± 0.85% by the ROSINA mass spectrometer on board the *Rosetta* spacecraft. To account for the presence of this species in comet 67P/Churyumov–Gerasimenko, it has been shown that the radiolysis of ice grain precursors of comets is a viable mechanism in low-density environments, such as molecular clouds. Here, we investigate the alternative possibility that the icy grains present in the midplane of the protosolar nebula were irradiated during their vertical transport between the midplane and the upper layers over a large number of cycles, as a result of turbulent mixing. Consequently, these grains spent a non-negligible fraction of their lifetime in the disk's upper regions, where the irradiation by cosmic rays was strong. To do so, we used a coupled disk-transport-irradiation model to calculate the time evolution of the molecular oxygen abundance radiolytically produced in ice grains. Our computations show that, even if a significant fraction of the icy particles has followed a back and forth cycle toward the upper layers of the disk over tens of millions of years, a timespan far exceeding the formation timescale of comet 67P/Churyumov–Gerasimenko, the amount of produced molecular oxygen is at least two orders of magnitude lower than the *Rosetta* observations. We conclude that the most likely scenario remains the formation of molecular oxygen in low-density environments, such as the presolar cloud, prior to the genesis of the protosolar nebula.

Key words: astrobiology – comets: general – comets: individual (67P/Churyumov–Gerasimenko) – methods: numerical – solid state: volatile

1. Introduction

Molecular oxygen (O_2) has been detected in the coma of comet 67P/Churyumov–Gerasimenko (67P/C–G) with abundances in the 1%–10% range and a mean value of 3.80 ± 0.85% by the *Rosetta* Orbiter Spectrometer for Ion and Neutral Analysis-Double Focusing Mass Spectrometer (ROSINA) instrument on board the *Rosetta* spacecraft (Bieler et al. 2015). Moreover, the production rate of O_2 has been found to be remarkably correlated with that of H_2O in 67P/C–G's coma, suggesting that both molecules come from the same icy phase (Bieler et al. 2015). A subsequent reanalysis of the Giotto mass spectrometry data shows that O_2 was also present in the coma of comet 1P/Halley with an abundance of 3.7 ± 1.7% with respect to water at the time of its encounter with the ESA spacecraft, suggesting that this species could be a common parent species in comets (Rubin et al. 2015).

To account for the O_2 abundance and the correlation of its production rate with that of H_2O in 67P/C–G, it has been shown that the radiolysis of ice grains in low-density environments, such as molecular clouds, is a mechanism capable of producing large amounts of O_2 from solid H_2O (Mousis et al. 2016). Meanwhile, it was also found that the radiolysis of icy grains in higher density environments, such as the midplane of protoplanetary disks, is not efficient enough to create amounts of O_2 comparable with those observed in 67P/C–G and 1P/Halley in timescales shorter than the lifetime of the protosolar nebula, even in the case of a strong cosmic-ray flux (CRF) engendered by the presence of a nearby supernova (Mousis et al. 2016). It was then concluded that, if O_2 is an irradiation product of ice, this molecule was probably formed in the interstellar medium, prior to the formation of the PSN.

Here, we consider the alternative possibility that the icy grains present in the midplane of the PSN were irradiated during their transport toward its upper layers (see the illustration in Figure 1). This idea has been introduced in Mousis et al. (2017b) but never investigated to quantitatively estimate the fraction of O_2 produced during the vertical transport of grains. Due to turbulent mixing, the ice grains present in the midplane were lifted toward the upper layers of the disk and dragged down over a large number of cycles (Ciesla & Sandford 2012; Mousis et al. 2017b). Consequently, these grains spent a non-negligible fraction of their lifetime in the disk's upper regions, where the irradiation by cosmic rays was strong. This irradiation, integrated over the disk lifetime, might cause some potentially significant production of O_2, the extent of which is explored in the present work.

2. Disk Model and Transport Module

To mimic the vertical motion of particles, we used a simple description of the PSN structure (Chiang & Goldreich 1997; Hartmann et al. 1998; Ciesla & Sandford 2012). The gas surface density Σ_g, namely the gas column density integrated through the disk plane, and temperature T_d profiles of the disk model are given by

$$\Sigma_g(r) = 2000\left(\frac{r}{1\ \mathrm{au}}\right)^{-1} \mathrm{g\ cm^{-2}} \quad (1)$$

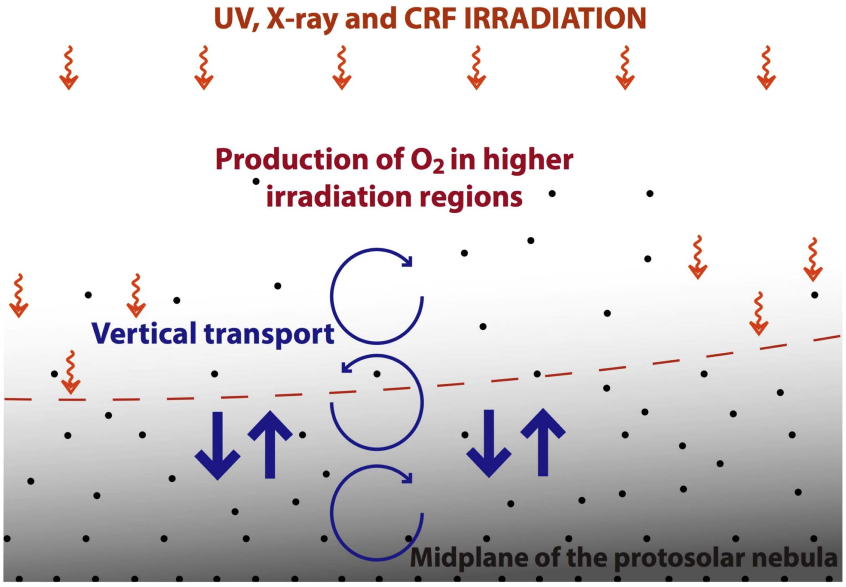

Figure 1. Illustration of the vertical transport of small icy grains toward disk regions where irradiation is strong and favors the formation of O_2. Grains remain concentrated in the midplane of the disk because of gravitational settling and gas drag.

and

$$T_d(r) = 280\left(\frac{r}{1\ \mathrm{au}}\right)^{-1/2}\mathrm{K}, \quad (2)$$

where r is the heliocentric distance. These prescriptions are appropriate for flared disks around young T Tauri stars.

Using the assumption of vertical hydrostatic equilibrium for the gas, the disk's density is expressed as a function of heliocentric distance r and altitude z above the midplane as

$$\rho_g(r, z) = \rho_0(r)e^{-\frac{z^2}{2H_g^2}}, \quad (3)$$

with

$$\rho_0(r) = \frac{\Sigma_g(r)}{\sqrt{2\pi}H_g}, \quad (4)$$

where $H_g = c_g/\Omega_K$ is the gas scale height derived from the isothermal gas sound speed $c_g = \sqrt{R_g T_d/\mu_g}$ and the keplerian orbital frequency Ω_K. R_g is the ideal gas constant and μ_g is the mean molecular weight of the gas ($\sim$2.4 g mol^{-1}).

Below we briefly outline the main aspects of the transport model used in our computations. We refer the reader to the work of Ronnet et al. (2017) for a full description. We consider the diffusion of dust grains onto the background disk gas using a Lagrangian approach where individual grains are tracked. Because our study only addresses the influence of irradiation during the vertical transport of grains, we opted not to follow their radial evolution. Small dust grains are strongly coupled and have a radial velocity similar to that of the background gas (and follow the accretion flow onto the star), whereas larger, partially decoupled grains, rapidly drift inward due to gas drag (e.g., Weidenschilling 1977). Considering the vertical hydrostatic equilibrium of the gas disk, we assume the gas has no net vertical velocity (see Takeuchi & Lin 2002 for a discussion of this assumption).

The vertical motion of the grains is therefore ruled by the turbulent diffusion that lifts them toward the upper layers of the disk and the settling toward the midplane due to gas drag and the gravity of the central star. The latter is given by the equation of motion of the dust grains in the vertical direction, which is solved following the approach developed in Ronnet et al. (2017):

$$\frac{dv_{d,z}}{dt} = -\frac{GMz}{r^3} - \frac{v_{d,z}}{t_s}, \quad (5)$$

where $v_{d,z}$ is the dust vertical velocity, $M = 1\,M_\odot$ is the mass of the central star, z is the vertical position of the dust grain, and t_s is the stopping time. The stopping time is a measure of the timescale on which the gas transfers its angular momentum to dust and can be expressed as (Perets & Murray-Clay 2011)

$$t_s = \left(\frac{\rho_g v_{\mathrm{th}}}{\rho_s R_s}\min\left[1, \frac{3}{8}\frac{v_{\mathrm{rel}}}{v_{\mathrm{th}}}C_D(Re)\right]\right)^{-1}, \quad (6)$$

where $v_{\mathrm{th}} = \sqrt{8/\pi}\,c_g$ is the gas thermal velocity, R_s is the radius of the solid particle, ρ_s is its density, assumed to be 1 g cm^{-3} regardless of the size, and v_{rel} is the relative velocity between the gas and the dust grain. The dimensionless drag coefficient C_D is a function of the Reynolds number Re of the flow around the particle and derives from an empirical law fitted on recent experimental data (Perets & Murray-Clay 2011):

$$C_D = \frac{24}{Re}(1 + 0.27Re)^{0.43} + 0.47(1 - e^{-0.04Re^{0.38}}), \quad (7)$$

where Re is the Reynolds number. It is given by (Supulver & Lin 2000)

$$Re = \frac{4R_s v_{\mathrm{rel}}}{c_g l_g}, \quad (8)$$

where l_g is the mean-free path of the gas.

The turbulent diffusion of the grains is modeled using a Monte-Carlo scheme where individual particles are given random impulses to mimic the stochastic transport due to turbulent eddies (see, e.g., Ciesla 2010, 2011). Overall, the new position z_d of a dust grain after a timestep dt is computed as follows in the vertical direction:

$$z_d(t + dt) = z_d(t) + v_{\rm adv}dt + R_1\left[\frac{2}{\sigma^2}D_p dt\right]^{\frac{1}{2}}, \quad (9)$$

where $R_1 \in [-1; 1]$ is a random number, σ^2 is the variance of the random number distribution, D_p is the diffusivity of the solid particle, and $v_{\rm adv}$ is the term accounting for the nonuniform density of the gas in which the particles diffuse as well as the nonuniform diffusivity of the particles, and the forces experienced by the particle (see Equation (11)). The diffusivity of the dust grains D_p is related to the gas diffusivity through the Schmidt number Sc as (Youdin & Lithwick 2007):

$$Sc \equiv \frac{\nu}{D_p} \sim 1 + St^2. \quad (10)$$

where $\nu = \alpha H_g^2 \Omega_K$ is the turbulent viscosity of the gas (assumed to be equivalent to the gas diffusivity) expressed through the nondimensional α parameter measuring the level of turbulence within the disk (Shakura & Sunyaev 1973) and St is the Stokes number, corresponding to the stopping time multiplied by the local Keplerian frequency. Larger values of α yield a more efficient redistribution of the dust grains through turbulent diffusion. Finally, the advection term in the transport equation is given by Ciesla (2010, 2011) as

$$v_{\rm adv} = \frac{D_p}{\rho_g}\frac{\partial \rho_g}{\partial z} + \frac{\partial D_p}{\partial z} + v_{d,z}. \quad (11)$$

This set of equations allows us to derive the vertical position z_d of individual particles at each timestep and to subsequently estimate the dose of irradiation they received.

3. Irradiation of Grains

The energy received by water molecules per unit time due to cosmic-ray irradiation $W_{\rm irr}(n)$ as a function of the column density of gas n above the particle is taken from Yeghikyan (2011). These authors computed this term by using the cosmic-ray intensity $I(E)$ (cm^{-2} s^{-1}st^{-1} MeV^{-1}) from Cooper et al. (2003) and considering a planar geometry. This leads to a differential flux spectrum inside the disk $F(E)$ given by

$$F(E) = \pi I(E)({\rm cm}^{-2}\,{\rm s}^{-1}\,{\rm MeV}^{-1}). \quad (12)$$

$W_{\rm irr}(n)$ is then derived from the molecular cloud material stopping power $S(E)$, i.e., its capability to absorb the cosmic-ray energy, as estimated from the Stopping and Range of Ions in Matter program (Ziegler et al. 2010). Note that the stopping power mostly depends on the mass density and not on the intrinsic composition or structure of the material. The computation is made for the proton component of the cosmic rays and the contribution of the alpha particles is estimated approximately, while the contribution of heavier cosmic-ray particles is neglected. We consider that the approach of Yeghikyan (2011) provides the best prescription of $W_{\rm irr}(n)$ in the literature because (i) this term weakly depends on the composition, (ii) the planar hypothesis is consistent with the geometry of the disk, and (iii) the CRF derived from Cooper et al. (2003) is the best proxy available for the one received by the PSN.

At each timestep, the column density of gas above a given particle p is calculated as

$$n = \frac{N_{\rm A}}{\mu_g}\int_{|Z_p|}^{+\infty} \rho_g(z)dz, \quad (13)$$

where $N_{\rm A}$ is Avogadro's number. The energy deposited onto water molecules during the timestep dt is then given by

$$E_{\rm dep} = W_{\rm irr}(n)\,dt. \quad (14)$$

O_2 is produced by radiolysis of water ice through the chemical reaction $2H_2O \rightarrow 2H_2 + O_2$, with an amount of energy E_w needed to alter one H_2O molecule being $E_w =$ 235 eV (Johnson 1991). The fraction of O_2 produced by the alteration of two water molecules, assuming a full efficiency, is then

$$\frac{[O_2]}{[H_2O]} = \frac{E_{\rm dep}(t)}{2E_W}. \quad (15)$$

Note that the value of $E_w = 235$ eV is a lower limit, and that the "full efficiency" assumption may be too generous. In fact, Teolis et al. (2017) find for highly penetrating radiation (such as cosmic rays penetrating through grains) that average G-values for O_2 have an approximate inverse dependence on particle penetration range (see their Figure 2).

4. Results

Turbulence plays an important role in the motion of gas-coupled small particles. Here, micron-sized grains that initially settled in the midplane are entrained by turbulent eddies and diffuse both radially and vertically with an effective viscosity roughly equal to that of the gas (Ciesla & Sandford 2012). Consequently, solid particles follow a Gaussian distribution in the vertical direction. The scale height of dust (corresponding to the standard deviation of the distribution) is a fraction of the gas scale height, this fraction being larger and possibly equal to the gas scale height H_g in the cases of small grains and higher degrees of turbulence.

Figure 2 represents the vertical distribution of 10^{-6}, 10^{-4}, and 10^{-2} m particles computed at a fixed distance of 30 au from the Sun with our disk model with vertical transport, assuming a coefficient of turbulent viscosity $\alpha = 10^{-3}$. The vertical transport of 2000 particles is simulated in each case. The figure shows that vertical spreading is more important in the cases of 10^{-6} and 10^{-4} m particles and can reach up to 2–3 gas scale heights. In contrast, because of their larger size, 10^{-2} m particles are much less affected by turbulence and do not spread more than ~0.1 scale heights above the midplane. Figure 3 displays the vertical evolution of a 10^{-6} m particle integrated over 1 Myr at 30 au in the PSN. It also shows that this particle spends a non-negligible amount of time in the regions above the disk midplane, where irradiation is more significant. 10^{-4} m particles display similar behaviors to a slightly lower extent while 10^{-2} m particles remain mostly close to the disk midplane.

Figure 4 shows the time evolution of the O_2/H_2O ratio in 10^{-6}, 10^{-4}, and 10^{-2} grains irradiated along their vertical

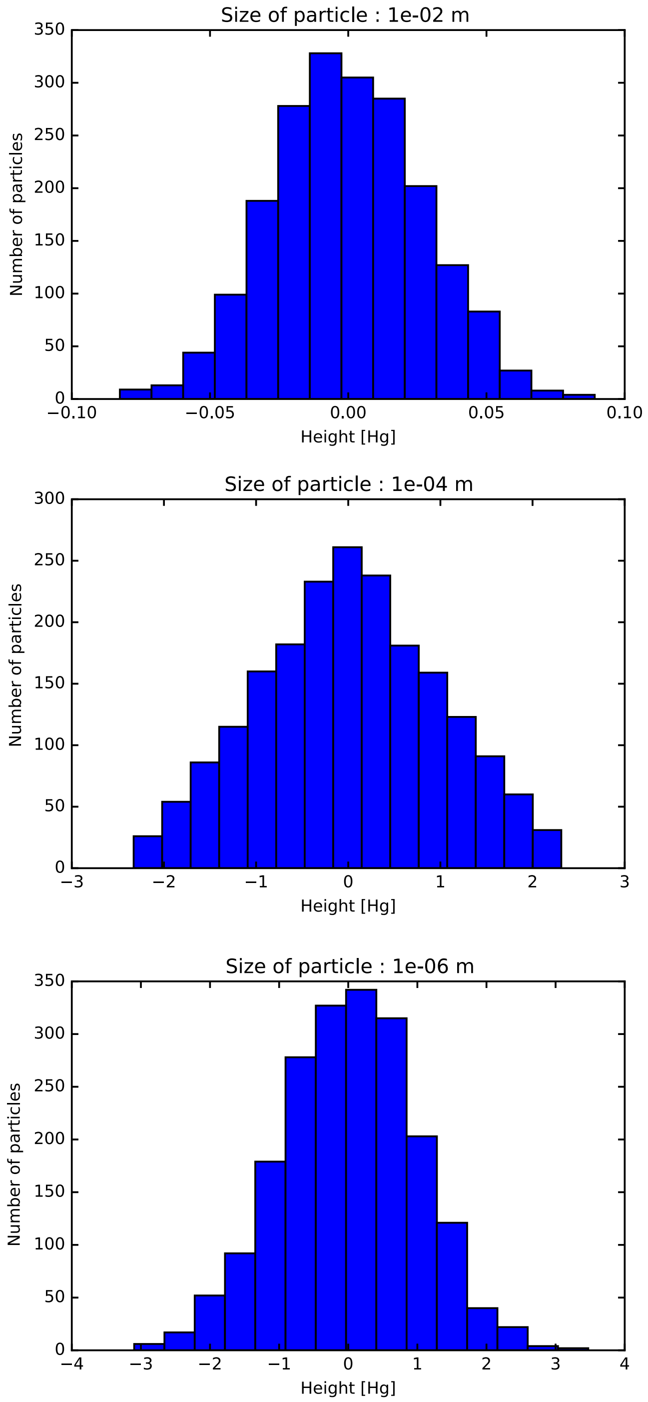

Figure 2. Vertical distribution of 10^{-6}, 10^{-4}, and 10^{-2} m particles at 30 au in the PSN. The height above the disk is expressed in function of the disk's gas scale height (H_g).

trajectories and for a turbulent viscosity α equal to 10^{-3} and 10^{-2}, namely two typical values for the disk's viscosity parameter (Drouart et al. 1999). The resulting O_2/H_2O ratio in 10^{-6} m particles (the most favorable case) is at best $\sim 10^{-5}$, namely three orders of magnitude lower than the one observed in 67P/C–G by the *Rosetta* spacecraft, after 1 Myr of vertical transport in the PSN, irrespective of the adopted α value. After the same timespan, the O_2/H_2O ratio reaches no more than $\sim 10^{-6}$ in 10^{-2} m particles, while the one obtained in 10^{-4} m grains is in the $\sim 2–6 \times 10^{-6}$ range, depending on the chosen

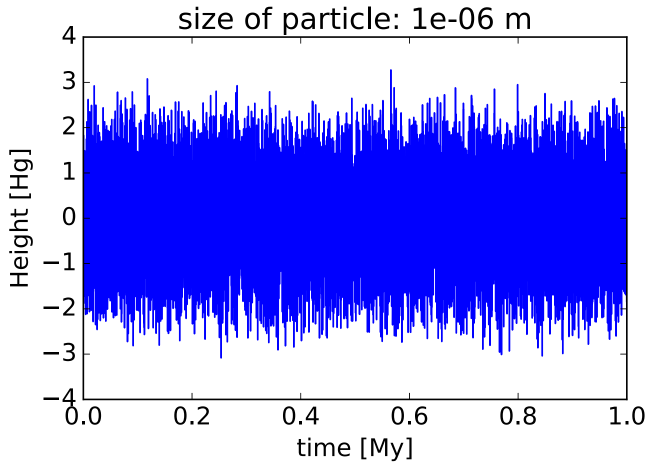

Figure 3. Vertical evolution of a 10^{-6} m particle as a function of time at 30 au in the PSN.

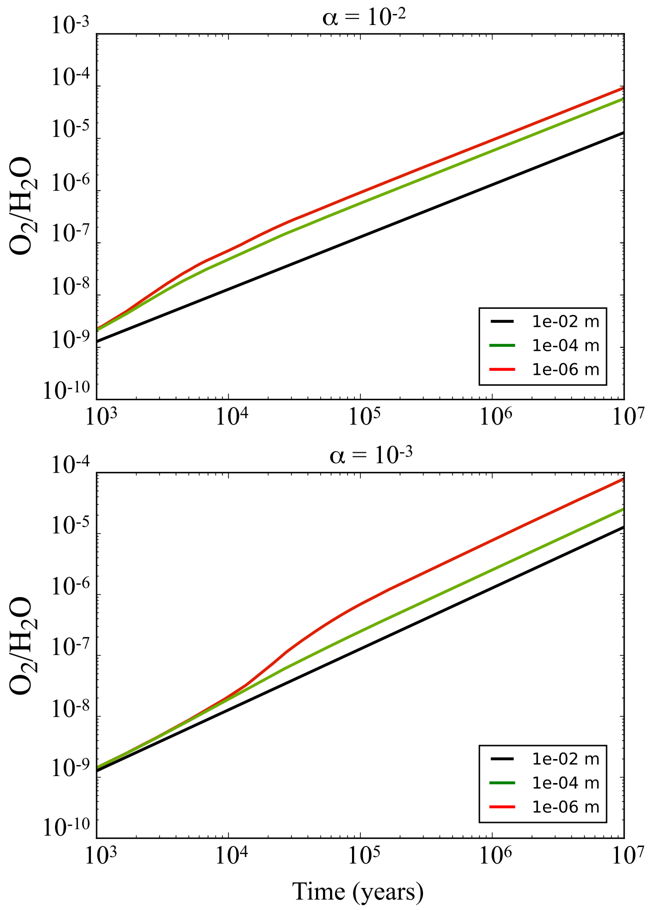

Figure 4. Abundance of O_2 relative to H_2O in 10^{-6}, 10^{-4}, and 10^{-2} m particles as a function of time in the PSN and for α values equal to 10^{-2} (top panel) and 10^{-3} (bottom panel).

value of α. After 10 Myr of vertical transport, the O_2/H_2O ratio only increases by one order of magnitude in each considered case, leading to a O_2/H_2O ratio of $\sim 10^{-4}$ in the most favorable situation (10^{-6} m particles), which is still two orders of magnitude lower than the value observed in 67P/C–G.

5. Discussion

Our computations suggest that, even if a significant fraction of the icy particles has followed a back and forth cycle toward the upper layers of the disk over tens of millions of years in a static PSN, the amount of O_2 created via radiolysis is at least ~two orders of magnitude lower than the *Rosetta* observations. This timespan exceeds by far the formation timescale of 67P/C–G, which has been estimated to range between 2.2 and 7.7 Myr after the formation of Ca–Al-rich inclusions in the PSN (Mousis et al. 2017a). The O_2/H_2O ratios derived from our simulations at 1 Myr can already be considered as optimistic since the particles most likely grew and decoupled from gas after a few dozens of thousands of years of the disk evolution (Weidenschilling & Cuzzi 1993). In this case, once the icy grains have grown up to sizes larger than a few meters in the PSN, the bulk of the ice should remain unaltered by irradiation. Also, an increase of the CRF up to a factor of ~100 due to a close supernova explosion would not substantially change the O_2/H_2O ratio in icy grains because the timespan of such an event (a few kyr) is too short (Mousis et al. 2016).

Several alternative mechanisms have recently been investigated in the literature to account for the O_2 detection in 67P/C–G. Among them, Taquet et al. (2016) have proposed that O_2 could be produced in dark clouds via a combination of gas-phase and solid-state chemical reactions leading to its formation and destruction, in agreement with the ROSINA observations and the conclusions of Mousis et al. (2016). Another mechanism, proposed by Dulieu et al. (2017), consists of the production of O_2 through dismutation of H_2O_2 during water ice desorption from the nucleus. However, this mechanism requires the incorporation of large amounts of primordial H_2O_2 into the nucleus and its complete conversion into O_2 to be consistent with the low levels of H_2O_2 observed in the coma. Another scenario investigated by Yao & Giapis (2017) is the possible present-day production of O_2 via an Eley–Rideal reaction mechanism in the coma. This reaction between energetic water ions and adsorbed O-atoms, produces highly excited oxywater (H_2O_2), which undergoes delayed fragmentation to form HO_2 as the precursor for O_2. However, at a close distance to the Sun, the solar wind strengthens and increases the ionization and water ion flux to the surface of the nucleus, and consequently produces more O_2 if the Eley–Rideal reaction mechanism is effective. According to this mechanism, the O_2/H_2O ratio should increase at perihelion, a trend that has not been seen by the ROSINA instrument.

Our results thus favor the mechanism of radiolysis of icy grains in low-density environments such as the presolar cloud, shown by Mousis et al. (2016) to be capable of producing the O_2 abundance observed in 67P/C–G. They suggested that O_2 may be trapped in the grains in radiation defects/cavities, and subsequently delivered to the PSN either in the solid or gas phase, depending on the disk's thermodynamic structure. The constant O_2/H_2O ratio observed in 67P/C–G requires that both O_2 and H_2O were released from the same solid phase and supports the hypothesis suggesting that comets formed from water ice coming from ISM without suffering from vaporization when entering the PSN.[7] Relaxing this constraint would leave alternative delivery scenarios of O_2 to comets, among which the desorption of this molecule during the amorphous-to-crystalline ice phase transition was encompassed by presolar grains that entered into the disk. The O_2 released via this manner could have been subsequently trapped in clathrates during the cooling of the PSN before being incorporated in the building blocks of comets. Finally, we note that, in addition to O_2 formation in low-density environments at epochs prior to the genesis of the protosolar nebula, an endogenic radiolytic source due to radionuclides present in the dusty component of the comet nucleus may have contributed at the percent level to the total O_2 budget in comets (Bouquet et al. 2017).

We thank the anonymous referee for helpful comments. O.M. acknowledges support from CNES. O.M. and T.R. acknowledge support from the A*MIDEX project (n° ANR-11-IDEX-0001-02) funded by the "Investissements d'Avenir" French Government program, managed by the French National Research Agency (ANR). J.I.L. was supported by the *JWST* project through a grant from NASA/GSFC.

ORCID iDs

R. Maggiolo https://orcid.org/0000-0002-5658-1313
P. Wurz https://orcid.org/0000-0002-2603-1169
A. Bouquet https://orcid.org/0000-0001-8262-9678

References

Bieler, A., Altwegg, K., Balsiger, H., et al. 2015, Natur, 526, 678
Bouquet, A., Mousis, O., Teolis, B., et al. 2017, ApJL, submitted
Chiang, E. I., & Goldreich, P. 1997, ApJ, 490, 368
Ciesla, F. J. 2010, ApJ, 723, 514
Ciesla, F. J. 2011, ApJ, 740, 9
Ciesla, F. J., & Sandford, S. A. 2012, Sci, 336, 452
Cooper, J. F., Christian, E. R., Richardson, J. D., & Wang, C. 2003, EM&P, 92, 261
Drouart, A., Dubrulle, B., Gautier, D., & Robert, F. 1999, Icar, 140, 129
Dulieu, F., Minissale, M., & Bockelée-Morvan, D. 2017, A&A, 597, A56
Hartmann, L., Calvet, N., Gullbring, E., & D'Alessio, P. 1998, ApJ, 495, 385
Johnson, R. E. 1991, JGR, 96, 17
Mousis, O., Drouard, A., Vernazza, P., et al. 2017a, ApJL, 839, L4
Mousis, O., Ozgurel, O., Lunine, J. I., et al. 2017b, ApJ, 835, 134
Mousis, O., Ronnet, T., Brugger, B., et al. 2016, ApJL, 823, L41
Perets, H. B., & Murray-Clay, R. A. 2011, ApJ, 733, 56
Ronnet, T., Mousis, O., & Vernazza, P. 2017, ApJ, 845, 92
Rubin, M., Altwegg, K., van Dishoeck, E. F., & Schwehm, G. 2015, ApJL, 815, L11
Shakura, N. I., & Sunyaev, R. A. 1973, A&A, 24, 337
Supulver, K. D., & Lin, D. N. C. 2000, Icar, 146, 525
Takeuchi, T., & Lin, D. N. C. 2002, ApJ, 581, 1344
Taquet, V., Furuya, K., Walsh, C., & van Dishoeck, E. F. 2016, MNRAS, 462, S99
Teolis, B. D., Plainaki, C., Cassidy, T. A., & Raut, U. 2017, JGRE, 122, 1996
Weidenschilling, S. J. 1977, MNRAS, 180, 57
Weidenschilling, S. J., & Cuzzi, J. N. 1993, in Protostars and Planets III, ed. E. H. Levy & J. I. Lunine (Tucson, AZ: Univ. Arizona Press), 1031
Yao, Y., & Giapis, K. P. 2017, NatCo, 8, 15298
Yeghikyan, A. G. 2011, Ap, 54, 87
Youdin, A. N., & Lithwick, Y. 2007, Icar, 192, 588
Ziegler, J. F., Ziegler, M. D., & Biersack, J. P. 2010, NIMPB, 268, 1818

[7] This scenario does not preclude a possible amorphous-to-crystalline ice phase transition due to a moderate PSN temperature along the migration path of the grains (Mousis et al. 2016).